International Committee for Future Accelerators

Sponsored by the Particles and Fields Commission of IUPAP

Beam Dynamics Newsletter

No. 59

Issue Editor:
J. M. Byrd

Editor in Chief:
W. Chou

December 2012

Contents

1 Foreword

1.1 From the Chairman

Weiren Chou, Fermilab
Mail to: chou@fnal.gov

2013 will be an important and interesting year for the world high-energy physics (HEP) community.

First, the Large Hadron Collider (LHC) at CERN will complete its very successful run at 4×4 TeV with an integrated luminosity of 23 fb^{-1}. Then, an 24-month-long shutdown (LS1) will begin to repair machine faults and prepare for the next 6.5×6.5 TeV run when the LHC restarts in 2015.

Second, the ILC GDE will deliver a *Technical Design Report* (TDR) and a *Detector Baseline Design* (DBD) to ICFA and thus complete its mission. The linear collider community will undergo reorganization by combining the ILC, CLIC and detectors together in a single organization under the leadership of Lyn Evans, the Linear Collider Director. The present ILC Steering Committee (ILCSC) will also be replaced by a Linear Collider Board (LCB).

Third, the three regions – North America, Europe and Asia – will each carry out strategic planning for HEP's future. This includes the U.S. Snowmass 2013 meeting (July 29 – August 6, 2013 at Univ. of Minnesota), European Strategy Updates meetings (January 21-25, 2013 at Erice, March 18-22, 2013 at CERN, and a special CERN Council meeting on May 23, 2013 in Brussels), as well as HEP roadmap studies in Japan and China.

Last but not least, the discovery announced by CERN on July 4th, 2012 of a Higgs-like boson could potentially be a game-changer in the HEP field. Because of its light mass (126 GeV), many options are now on the table as potential candidates for a Higgs Factory, including linear e+e- colliders, circular e+e- colliders, muon colliders and photon colliders. For the linear e+e- colliders, not only superconducting RF (for the ILC) and two-beam acceleration (for the CLIC), but also the x-band klystron based technology (which was previously heavily studied for the NLC and JLC) is back for re-consideration. 2013 will be an interesting year to see how these new developments will evolve. An ICFA beam dynamics workshop on "*Accelerators for a Higgs Factory: Linear vs. Circular*" (HF2012) was organized in November 14-16, 2012 at Fermilab. (http://conferences.fnal.gov/hf2012/) A summary report will be published in the next issue of this newsletter (no. 60, April 2013).

The Seventh International Accelerator School for Linear Colliders was held from November 27 to December 8, 2012 at the Radisson Blu Hotel, Indore, India. It was hosted by the Raja Ramanna Center for Advanced Technology (RRCAT). A school report can be found in Section 2.1. All lecture materials and homework problems are posted on the school web site: http://www.linearcollider.org/school/2012.

The Editor of this issue is John Byrd, an accelerator physicist from LBNL and a panel member. The theme is "*Femtosecond Beams*." This is an important topic in the advanced photon source field. John collected 11 well-written articles to present a

comprehensive review of the field. This issue also contains a workshop report (HB2012), four recent doctorial theses abstracts (Y.I. Levinsen, G.A. Marcus, H. Qian and A. Marinelli) and five workshop announcements (BB2013, Higgs2013, COOL'13, SRF2013 and Space Charge 2013).

I thank John for editing and producing a valuable newsletter for our accelerator community.

1.2 From the Editor

John Byrd, Lawrence Berkeley National Laboratory
Mail to: JMByrd@lbl.gov

The theme of this issue of the ICFA Beam Dynamics Newsletter is "*Femtosecond Beams.*" This is a topic that has emerged into the mainstream of accelerator physics over the past two decades with the remarkable convergence of several new technologies and ideas in accelerator physics combined with the spreading excitement for new opportunities in ultrafast science. Among the technologies are the widespread availability and adoption of high peak power optical lasers integrated with accelerators and the development of high brightness electron sources. Coupled with concepts such as free electron lasers and laser-plasma accelerators, femtosecond (fsec) beams are now a reality and the basis for a number of new accelerator projects around the world.

X-ray FELs have been established as the first wave in the next generation of light sources. Besides the increase in photon brightness of *more than 10 orders of magnitude* over existing x-ray sources, x-ray FELs produce inherently short pulses ranging from several hundred femtoseconds down to a few femtoseconds. Several schemes for producing *attosecond* x-ray pulses have already been proposed. As the x-ray pulse durations become comparable to the time for motion of a valence electron in an atomic or molecular system, the x-ray pulse can be used as a strobe to create movies of atomic and molecular reactions.

Another technique for creating molecular movies in the ultrafast field is ultrafast electron diffraction (UED) where the instantaneous structure of a material can be measured directly from diffraction of an electron bunch. The excellent performance of high brightness electron guns has been a pivotal development in making this a possibility. This subject is discussed in a contribution by **Pietro Musumeci** and **Renkai Li**.

Another revolution has taken place in accelerators with the development of laser plasma accelerators. Electrons have already been accelerated to the GeV level with GV/m gradients by excited oscillations in a plasma with a high peak power laser. Because the plasma frequency is typically several hundred GHz, the acceleration process produces electron bunches with lengths of a few femtoseconds. This subject is discussed in a contribution by **Carl Schroeder, Eric Esarey, and Wim Leemans**.

With the ability to create femtosecond beams comes the need to manipulate, measure, and control them. This need has motivated an amazing level of innovation in accelerator physics and technology. We are approaching an era where we can control optical frequencies with the same precision as we now use RF and microwave frequencies. With the broad availability of mode-locked lasers, there has been tremendous innovation in manipulating electron beams with light. By mixing multiple

optical frequencies on the beam, there are possibilities for creating attosecond structures on the beam. This subject is discussed by **Dao Xiang**.

The most exciting area to me is the incredible progress in the ability to measure and control fsec beams. This subject has been approached in the time-tested manner: adopt the best techniques and technologies from other fields. The developments in ultrafast optical science have been adopted wherever possible and accelerator science has attracted a whole new range of talented scientists and engineers to the field. We have several contributions in this area. One the primary tools for measuring fsec beams is the use of a deflecting cavity for "streaking" the beam and transforming the longitudinal beam distribution into a transverse deflection at a screen. The contribution from **Christopher Behrens** and **Christopher Gerth** describe a wide variety of applications of this type diagnostics of the longitudinal phase space to the control and understanding of fsec beams with many of the experimental results measured at FLASH. There is another contribution from **Yuantao Ding** which describes several advances in generating and measuring femtosecond beams at the LCLS.

The temporal resolution of deflecting cavities is proportional to the frequency with most microwave cavities operating at S-band frequencies. **Gerard Andonian** and collaborators describe the use of a CO_2 laser to provide the deflection with sub-fsec resolution.

Another technique that has been adopted from ultrafast optics is the Frequency Resolved Optical Gating (FROG) which was pioneered by Rick Trebino. **Gabriel Marcus** describes use of this method to measure the temporal characteristics of FEL pulses at the SPARC facility at INFN Frascati.

Electro-optic (EO) sampling of coherent terahertz radiation has emerged as one of the techniques used to measure sub-100 fsec pulses over the past decade. However, many of the EO crystals used have inherent limitations in time resolution because of their limited bandwidth. Another approach is to directly observe the modulation in the spectral domain. This approach is described by **Jeroen Van Tilborg** and colleagues where he has observed direct modulation of coherent terahertz onto an optical carrier.

The wide interest in time domain spectroscopy of terahertz pulses has led to a wide variety of techniques based on EO sampling with increasing performance. A new technique, named Temporal Electric-field Cross-correlation, or TEX, is described by its inventor, **Nicholas Matlis**. This technique uses a chirped optical pulse as the probe upon which the THz field is encoded. The innovation is using the interference between the encoded pulse and a short optical pulse as a reader. This technique does not require high peak power lasers.

As mentioned above, one of the exciting applications of fsec x-ray pulses is the use as a strobe light to illuminate the electron dynamics of molecular and chemical reactions with the ultimate goal of making "molecular movies". The technique involves initiating a non-equilibrium condition in a sample using an optical pump laser and probing the dynamics a known time later with the x-ray pulse. Each shot creates a "frame" of the "movie". In order to sort the movie frames, high precision synchronization is required between the optical and x-ray pulses. **John Byrd, Russell Wilcox, Larry Doolittle,** and **Gang Huang** provide a description of the advances in femtosecond synchronization for FELs.

One of the primary applications of high brightness beams is the enhance lasing at nm to sub-Angstrom wavelengths. However, it also becomes possible for the beams to spontaneously bunch and radiate and optical and longer wavelengths. This

microbunching can reduce the electron beam brightness before it reaches the x-ray laser and seriously degrade the performance of the FEL. This effect is known as the microbunching instability. **Daniel Ratner** provides a review of the instability along with recent measurements and mitigation schemes.

I would like to thank all of the contributors for their hard work and excellent contributions to this edition of the newsletter. I would also like to thank the many people who contributed useful suggestions for contributions.

2 International Linear Collider (ILC)

2.1 Seventh International Accelerator School for Linear Colliders

Barry Barish and Weiren Chou
mail to: barish@ligo.caltech.edu, chou@fnal.gov

The Seventh International Accelerator School for Linear Colliders took place from November 27 to December 8, 2012 at the Radisson Blu Hotel, Indore, India (http://www.linearcollider.org/school/2012/) This school continued the successful series: 2006 in Japan, 2007 in Italy, 2008 in the U.S., 2009 in China, 2010 in Switzerland and 2011 in the U.S. This year's school was jointly organized by the ILC GDE, CLIC and the ICFA Beam Dynamics Panel. The Raja Ramanna Center for Advanced Technology (RRCAT) hosted the school.

The school was aimed at PhD students, postdocs and young researchers, especially young experimentalists. The response to the school was overwhelming. We received 304 applications from 40 countries; most of the candidates presented strong credentials. However, the school could only accommodate a limited number. Through a difficult and rigorous selection process, the Curriculum Committee accepted 60 students from 17 countries. The committee members carefully read the CV and recommendation letter of each applicant, and only after discussion made the decision to admit or reject an applicant. For personal reasons six admitted students did not come. Another nine students from China, US and UK did not receive a visa from India and could not come. The forty-five students who attended the school were a talented and highly motivated group. We were glad that for the first time the school admitted a student from Africa. These students successfully met the challenge of an intensive 11-day education program and did well in the final examination.

The curriculum consisted of lectures, homework assignments and a final exam. The first three days were plenary sessions with introductory lectures: introduction, ILC, CLIC, muon collider, linac basics and beam instrumentation. The introduction lecture was different from previous years. In addition to physics, it also introduced various types of future colliders – not only linear e+e- colliders (such as the ILC and CLIC) and the muon collider, but also circular e+e- colliders, the $\gamma\gamma$ collider and plasma accelerators. This gave the students a wider vision of the entire field and could help when they choose their career path. After the plenary sessions the students were divided into two parallel classes. Class A, accelerator physics, had 29 students and included four lectures: e+ and e- sources, linacs, damping rings and ring colliders, and beam delivery systems. Class B, RF technology, had 16 students and included three lectures: room

temperature RF, superconducting RF, high power and low level RF. All lecturers were carefully chosen and are renowned scientists in their respective fields. They not only gave lectures during the day, but also gave tutorials and helped students with their homework in the evenings. They designed the examination problems and graded them. The final exam on the last day lasted four-and-a-half hours. All 45 students took the final exam. The lecture slides and homework problems can be found on the school web site.

The exam problems were different for Class A and B but were equally challenging. Most students did well as shown in the figures of exam scores. The top 8 students (5 from Class A and 3 from Class B) were honored at the banquet and each was awarded a certificate and a book (*Reviews of Accelerator Science and Technology*, Volume 4, edited by A. Chao and W. Chou, and published by World Scientific in 2011).

In addition to lectures, the students paid a site visit to the RRCAT. They visited two light sources – Indus-1 and Indus-2 – and also the superconducting RF research center. They had the opportunity to perform three hands-on experiments: (1) single-cell superconducting RF cavity measurement using a bead-pull setup, (2) characterization of solid state RF amplifier and associated co-axial components, and (3) beam profile measurements using digital image processing techniques. These experiments were very well organized and gave the students valuable hands-on training. The students also went on an excursion to visit the beautiful Lal Bagh Palace, which gave them a much needed break during their busy school work.

Throughout the school period, the students were encouraged to make new friends since this was a once-in-a-lifetime opportunity for many of them to meet with other young talented people from different origins who shared the same interest (accelerators) and career goals (future colliders). Some of the friendships nurtured at the school will last a lifetime.

Prof. P.D. Gupta, Director of RRCAT, gave strong support to the school. The Local Committee (LC) was chaired by Dr. Satish Joshi. He did an excellent job in looking after every school detail. Many RRCAT colleagues also came to help, including P.K. Gupta, P.R. Hannurkar, S.C. Joshi, S.K. Shukla, S.B. Roy, S.S. Kulkarni, A. Rawat, M. Lad, A.R. Narpharake, V. Kumar, P. Ravindran, G.V. Kane, A. Thora, A.D. Ghodke, H. Vaswani, S. Raghavendra, N. Tiwari, A. Sharma, P. Jain and many others. Raghu and Asif were responsible for the duplication of lecture slides, computer setup and networking. Prof. Atul Gurtu from the TIFR spearheaded the initiative to hold this school in India. The founding director of RRCAT, Prof. Dilip Bhawalkar attended the banquet and presented the award certificate to the top students. Cynthia Sazama and Suzanne Weber from the Fermilab Conference Office played a pivotal role in making the school a success. We are thankful to all of them for their dedication and wonderful work.

The school received generous sponsorship from a number of funding agencies and institutions from all over the world: U.S. DOE Office of Science, NSF, Fermilab, SLAC, ILC GDE, CERN, DESY, CPAN, INFN and KEK.

We carried out a student survey on the last day of school. The results will be given to the lecturers and committee members for improvements for future schools.

Based on the interest, demand and success of the first seven schools, it was decided to continue in 2013. The eighth school will take place in Europe. The venue and dates are yet to be chosen.

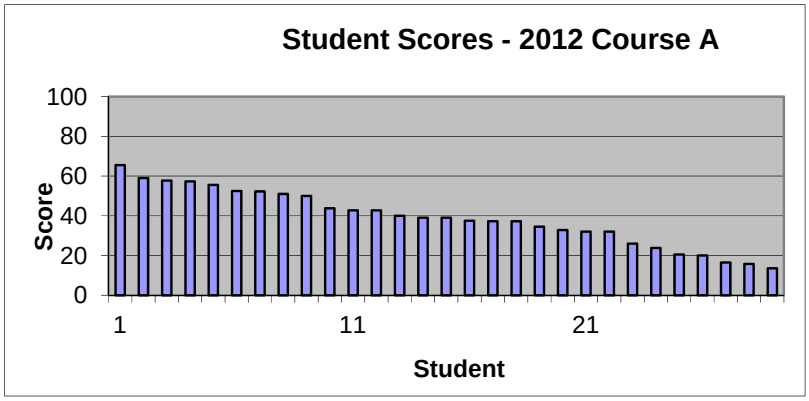
Student Scores - 2012 Course A
100
80
60
40
20
0
Score
1
11
21
Student

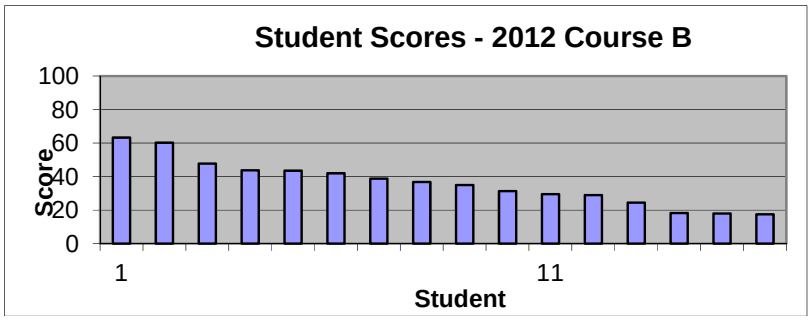
Student Scores - 2012 Course B
100
80
60
40
20
0
Score
1
11
Student


Seventh International Accelerator School for Linear Colliders,
27 November - 8 December 2012, Indore, India

3 Theme: Femtosecond Beams

3.1 Femtosecond Relativistic Electron Diffraction

P. Musumeci and R. K. Li
UCLA Department of Physics and Astronomy
475 Portola Plaza, Los Angeles, CA 90095 USA
Mail to: musumeci@physics.ucla.edu

3.1.1 Introduction

This report is intended to review the application of high brightness femtosecond electron beams to the direct investigation of structural changes in matter at atomic length scale with sub-ps resolution by time-resolved electron diffraction (ED). As we will discuss, the development of this application demands excellent beam quality both in the transverse and longitudinal phase spaces, thus requiring sources capable of generating beams of exquisitely high 6D brightness. Expertise from the low energy microscopy and diffraction community [1-3] have merged with recent advances made in relativistic electron sources for high energy particle accelerators and 4th generation light sources [4] in the quest of creating and delivering electron beams with these characteristics.

The main goal for time-resolved electron diffraction is to obtain real time resolution of atomic motion -one of the great open challenges in modern science- which promises the possibility to understand at the most basic levels various processes in the study of molecules, materials, and biological systems. The progress in laser technology has enabled the generation of optical pulses of time duration comparable to the time-scale of atomic and molecular motion (<100 fs). But ultrafast optical laser pulses can only give indirect spectroscopic information on the structural dynamics of the samples under study, and x-ray photons or fast electrons are required to resolve spatially atomic motion.

Various schemes that take advantage of the ultrashort laser pulses to generate short bursts of x-ray or electron beam suitable for ultrafast probing of materials have been developed. For an interesting review on ultrashort x-ray pulses see [5]. In contrast with expensive and large size x-ray sources, ultrafast electron diffraction (UED) offers a relatively cheap, compact and effective solution to the problem of following in real-time atomic motion, particularly suited for smaller size laboratories. Due to the large difference between the Rutherford (charge particles) and Thompson (photons) cross sections, probing with 10^6-10^7 electrons is equivalent (i.e. yields the same number of scattered particles) to a probe pulse of 10^{12} x-ray photons. The stronger interaction of the charged particles makes electrons the preferred choice to study thin layers, surface effects, or gas phase samples, whenever the number or the density of scattering centers is limited.

The use of ultrashort electron beams to probe ultrafast processes has already produced ground-breaking results in understanding solid state phase transitions [6-8], determining the transient species in gas phase [9,10], studying strongly coupled systems [11-13] and following surface dynamics [14,15]. Conventional UED setups employs non-relativistic 30-100 keV photogun electron sources which suffer from severe bunch

lengthening in the propagation region after the cathode due to the strong space charge repulsion at these low energies [16-17]. This effect seriously degrades the temporal resolution available at the sample and significant efforts have been recently directed towards improving the temporal resolution to the sub-ps level [13,18-22]. In the past researchers have been able to achieve sub-ps resolutions only by greatly reducing the number of electrons (down to 10^4 particles per pulse) with the compromise of integrating over multiple shots to collect a single diffraction image. Such stroboscopic approach has allowed the study of a large number of physical systems and reversible fast processes. But in order to capture the information concerning the transient structures with a single sub-picosecond pulse and hence enable the study of irreversible phenomena, the highest possible beam intensity must be maintained. With conventional electron diffraction guns it is simply impossible to generate an electron pulse with enough electrons ($> 10^5$) in a width shorter than 1 ps. Using rf compression has been proposed to reduce the bunch length, and initial exciting results show the possibility of capturing a diffraction pattern (DP) with <100 fs rms bunch length and ~10^6 electrons per pulse at 100 keV [20-22]. A more direct approach is to increase the electron beam energy to MeV level where space charge forces are largely suppressed and pose a lesser challenge to the bunch lengthening and beam quality preservation [23-24].

In the following we will review the most important developments which led to femtosecond relativistic electron diffraction (FRED) [25-29], its advantages compared to traditional non-relativistic electron diffraction, illustrate the main recent technological advances in FRED and the first time-resolved studies of an ultrafast process by single-shot diffraction patterns [30]. We will then spend some time to introduce a promising variation of FRED: RF streak-camera assisted continuously time-resolved electron diffraction and describe the unique advantages of this mode of operation [31-33]. We will also look at employing RF compression to show the possibility for <10 fs temporal resolution for MeV electron sources [34]. Finally we'll outline future directions in this field which include the development of ps-MeV electron microscopy.

3.1.2 **RF Photoinjector-based Femtosecond Relativistic Electron Diffraction**

Before going into the details of the development of FRED, let us briefly summarize the main differences between non-relativistic and relativistic electron beams for diffraction applications.

Table 1: Comparison between non-relativistic and relativistic electron diffraction.

Parameter	***keV UED***	***FRED***
Beam Kinetic Energy	20-100 keV	3-5 MeV
Accelerating field	10 MV/m	80-120 MV/m
number of particles	10^4	10^8
Bragg angle	10 mrad	0.5 mrad
Elastic mean free path (in Al)	20 nm	200 nm
Normalized transv. emittance	0.1 mm-mrad	0.1 mm-mrad
Relative energy spread	10^{-5}	10^{-3}

Important advantages of using relativistic energy ctrons include: i) a 3-4 orders of magnitude larger number of particles per pulse which allows the possibility of acquiring single shot diffraction patterns thus enabling the study of irreversible and low repetition rate ultrafast processes; ii) the large accelerating gradients coupled with radiofrequency bunch compression schemes enable bunch lengths shorter than 50 fs at the sample; iii) the relativistic speed of the probe particles eliminate the group velocity mismatch problem which causes a degrade in the temporal resolution of the technique. For gas phase or plasma studies where the probed sample thickness is on the order of a mm, the time resolution for non-relativistic particles is inherently limited to few ps just due to the group velocity difference of the pump laser and the probe electron beams in the sample; iv) the longer penetration depth of MeV electrons allows a larger variety in sample thickness and geometry. One interesting option is to use MeV electrons to probe biologically and chemically interesting samples in liquid phase between ultrathin membranes.

Known issues related to the higher beam energy include: i) the percent level charge and pointing fluctuations of the MeV beam. Since in single-shot mode it is not possible to average out over multiple pulses, any fluctuation poses a limit on the smallest observable structural change; ii) the dark current from the gun provides spurious electrons which degrade the signal-to-noise ratio in the diffraction images; iii) the RF amplitude and phase induced time-jitter sets a ~100 fs limit on the temporal resolution.

Over the years, issues that initially had been identified as critical for the success of FRED have been successfully resolved as we will describe later in this paper. These include the poor quality of the diffraction patterns and the lack of very high efficiency electron detection for FRED. Another point that has been brought against the use of high energy electrons for probing biological materials is related to the knock-on damage effect which affects the operation of high voltage electron microscopes. In FRED this problem is completely removed since the diffraction signal is acquired well before any structural change due to the damage can take place, in an approach similar to the diffract-and-destroy technique employed in 4th generation light sources [36].

3.1.2.1 ***Background***

Already in 2000 X. J. Wang et al had proposed the idea to solve the space charge problem in non-relativistic ED using the high brightness MeV RF photoinjector [23,24]. This kind of electron gun (a particular version is shown in Fig. 1) is widely accepted as the state-of-the-art source for high brightness electron beams and in fact it constitutes one of the key components of most of the short pulse x-ray free-electron laser (FEL) projects operating or planned for construction around the world. An important step in acknowledging this possibility was made in the paper by King et al. discussing evolution of sources for time-resolved diffraction and microscopy [1].

When optimized for UED applications, rf photoinjectors could easily deliver up to 10^7 -10^8 electrons packed in bunches of sub-100 fs length. There are two fundamental reasons for the (at least) three orders of magnitude increase in number of electrons when using relativistic (3-5 MeVs) beams. The gradient in an RF photoinjector is ~100 MV/m almost an order of magnitude larger than what achievable in DC guns. This ensures that the particles are immediately accelerated to relativistic energies leaving as quickly as possible the region close to the cathode where most of the bunch lengthening happens. Further, the space charge forces are strongly reduced as γ (the beam energy) increases.

This can be understood as the bunch is much longer in its own rest frame due to the relativistic dilation; consequently its own self-repulsion is suppressed.

Hastings et al. in 2006 demonstrated for the first time the possibility of acquiring single shot diffraction patterns using MeV beams from an RF photoinjector [25]. Since then a number of groups worldwide have joined this research field. Together with the efforts at UCLA which we will describe in more detail later, we should mention here the Tsinghua MeV electron diffraction setup which led to the first single shot high quality diffraction patterns [32], and the setups at Osaka University and Brookhaven National Laboratory which reported respectively time-resolved studies of silicon [37] and of charge density wave dynamics [38]. A more recent development is the REGAE injector at DESY Hamburg [39].

In Fig.1b we show the measurement of the bunch length of the electron beam at the UCLA Pegasus laboratory for various charges and initial cathode spot sizes. It appears evident that sub-100 fs temporal resolution is possible using a low charge electron beam. It should be noted here that for very short electron bunches, the measurement of the temporal beam profile is a challenge and a research subject in its own right. For typical FRED beam parameters, frequency-domain methods like the measurement of coherent beam radiation spectral content are not feasible because of the very low beam charge Q and the unforgiving scaling of the signal as Q^2. The best measurements are obtained by streaking directly the electron beam using an rf deflecting cavity. In principle this technique could yield unprecedented time resolution. At Pegasus, a 9.6 GHz 9-cell standing wave deflecting mode cavity with a maximum 500 kV deflecting voltage was used to obtain 35 fs resolution during these measurements.

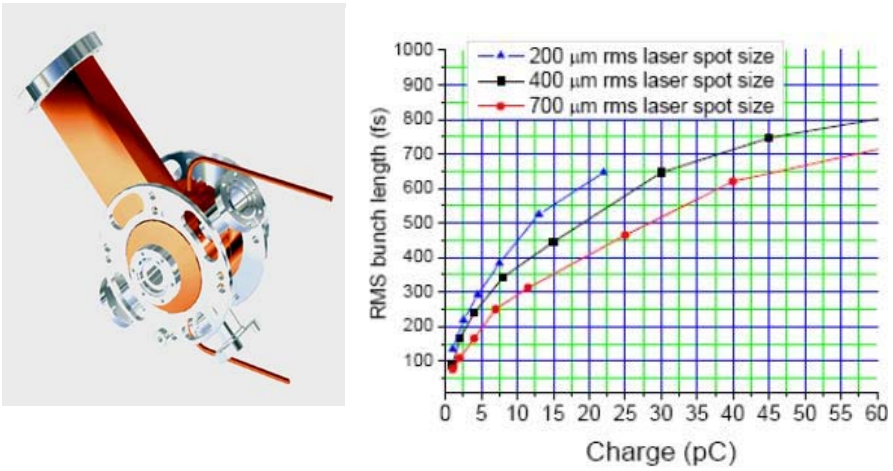

Figure 1. Left: 1.6 cell SLAC/UCLA/BNL type RF photoinjector. Right: Bunch length vs. charge measured with an RF deflecting cavity.

3.1.2.2 *Beam Brightness: Figure of Merit for FRED*

Many of the concerns on the possibility of using a relativistic electron source like an RF photoinjector for FRED arise when considering the spatial quality of the patterns. The De Broglie wavelength associated with the beam ($\lambda = h/p$ where h is the Planck constant and p is the beam momentum) is 0.3 pm for 4 MeV beam. For a typical inter-atomic distance d = 2 Å the scattering (Bragg) angle is only θ_B =1.6 mrad (to make a

comparison for a 30 keV beam, $\lambda = 7$ pm and $\theta_B = 35$ mrad). In order to be able to distinguish the scattered particles from the un-diffracted beam core, θ_B has to be much larger than the intrinsic root mean square (rms) spread in beam divergence angles at the sample σ_θ -- i.e. $\sigma_\theta < \theta_B = \lambda/d$, posing a stringent limit on the beam emittance.

A perfectly equivalent way of formulating the problem is by introducing the concept of the transverse coherence length. Transverse coherence length is defined as $L_c = \lambda /2\pi\sigma_\theta$, and it has to be compared with the structure interplanar distance d. If the beam is not coherent over few unit cells of the observed structure (i.e. $L_c > d$), then no constructive interference can be obtained and the visibility of the diffraction peaks is strongly reduced.

We can quantify these statements by calculating the resolving power of the diffraction camera. This quantity is defined as $\mathsf{R} = R/\Delta R$ where R is the radius of the diffraction rings on the detector screen and ΔR is the smallest distance between two neighboring rings which can just be discriminated. A typical long-exposure time electron microscope diffraction camera has $\mathsf{R} = 10^3$ or more. A resolving power of $\mathsf{R} > 10$ guarantees a good quality diffraction pattern and provides enough spatial resolution to adequately resolve typical ultrafast structural rearrangements. With a proper choice of beam optics, it is possible to image the angular distribution on the screen and obtain $\mathsf{R} = \lambda/(2d\sigma_\theta)$. Since $\sigma_\theta = \varepsilon_n/ \beta\gamma \sigma_{x0}$, where σ_{x0} is the spot at the sample (which is assumed here to be located in the plane of a beam waist), we can write

$$\Re = \frac{h}{2m_0 cd}\frac{\sigma_{x0}}{\varepsilon_n}$$

Note that even though the De Broglie wavelength λ for 4 MeV electrons is >20 times shorter than the one for non-relativistic particles, the coherence length and the resolving power of the diffraction camera depend only on the normalized emittance of the source and are in fact *independent* of the beam momentum. In order to keep $\mathsf{R} > 10$ with a wavelength $\lambda = 0.3$ pm and d = 2 Å, it is necessary to have at the target $\sigma_\theta < 80$ μrad. For FRED, the limiting effect to the diffraction camera resolving power is the intrinsic spread in beam angles due to the beam emittance. To make a comparison, the contribution from the rms beam energy spread $\Delta\gamma/\gamma$ –– typically smaller than 1 % -- would give $\mathsf{R} = R/\Delta R = \gamma/\Delta\gamma > 100$.

In order to obtain a high quality diffraction pattern, the small spread in divergence angles has to be obtained in conjunction with a small transverse beam size at the sample plane. This is mainly due to the typical size of the ultrathin samples required to operate in transmission mode. Another issue limiting the transverse extent of the probe beam is related to the requirements on the pump laser fluence. With a limited amount of energy per pulse available from the laser system the pump spot size needs to be typically sub-mm on the sample to reach fluences of interest for irreversible material processes (0.1-1 J/cm^2). In order to ensure that the probe beam sees a uniformly pumped area, its spot size should be much smaller spot (typically few hundred microns or less) than the laser pump transverse. This sets a tight upper limit on the beam transverse emittance.

The beam charge is set by the requirement of having enough scattered electrons to be able to detect the Bragg peaks. The milestone time-resolved electron diffraction results on Al melting have been obtained using 150 shots of 6000 electrons each, that is a total of 1 million electrons per image [7]. If an extremely high efficiency detector is

available this is the minimum charge per bunch that is required to obtain a high contrast diffraction pattern.

Assuming then 5×10^6 electrons in an rms bunch length of 100 fs, an angular divergence of 0.08 mrad and an rms beam size of 0.4 mm at 4 MeV energy, the source has to be able to generate a state-of-the-art beam with normalized brightness of $B = 2I/\varepsilon_n^2 > 10^{14}A/m^2$. To give a sense for the order of magnitude of the required brightness, the RF photoinjector source for the LCLS x-ray FEL reportedly generated beams of 20 pC, 0.13 mm-mrad emittance and 5 ps bunch length with brightness $\sim 4.5\times10^{14}A/m^2$ [41].

It is possible to get an analytical estimate for the brightness of a beam from an RF photoinjector operating in the pancake regime. In a 1D model, which assumes that the beam remains a pancake in its rest frame during propagation, the final bunch length can be analytically calculated and it is equal to $\tau = mc\sigma/\varepsilon_0 eE_0^2$, where σ is the surface charge density and E_0 is the accelerating field. Combining this with the limits on the max surface charge density set by the extraction gradient (i.e. $\sigma=Q/2\pi\sigma^2_{laser}\approx\varepsilon_0E_0$), we obtain for the max beam brightness $B \cong 4\pi\varepsilon_0 ecE_0^2/E_k$ depending only on the cathode temperature and the accelerating electric field. For a copper cathode illuminated by a 266 nm UV laser pulse ($(E_k/mc^2)^{1/2} \sim 0.8$ mrad) in a 100 MV/m field we can calculate $B = 10^{15}A/m^2$. This value should be taken as a first estimate since the assumptions of the 1D calculation are not always valid in the propagation after the gun. The beam in fact quickly reaches a point in its evolution where its rest frame longitudinal size becomes comparable with the transverse dimensions. At this point the space-charge driven expansion ceases to be only longitudinal and the model assumptions break. 3D simulations are then required to understand and optimize the beam dynamics. Different RF structures could be employed to improve various aspects of the beam propagation [42]. Nevertheless these quick estimates confirm the possibility for an RF photoinjector beam to have high enough quality to enable the study of irreversible structural changes by single shot diffraction patterns with sub-100 fs temporal resolution.

3.1.2.3 *Elements in RF Photoinjector Beamlines for FRED*

Advancing FRED can be considered a very active worldwide effort undertaken by multiple research groups as confirmed by the diverse presentations/publications in various Particle Accelerator Conferences/ refereed journals in the last 5 years. In the following of this report, we will consider the UCLA setup as an example to outline the major technical advances which led to the first time-resolved study of an ultrafast process by single-shot diffraction patterns. The setup has strong similarities with the ones developed at Tsinghua University and Brookhaven National Laboratory. An important unique feature of the Osaka University setup is the implementation of three solenoid lenses to control the diffraction camera length [37]. Unique characteristics of the Pegasus beamline include the EOS-based time-of-arrival monitor [43] and the x-band deflecting cavity for diagnostics and continuously time-resolved UED [33].

A cartoon of the UCLA Pegasus beamline for electron diffraction is shown in Fig. 2. The samples are inserted in the beamline at a plane located 80 cm from the cathode using a VGScienta sample holder capable of controlling the sample temperature from 1000 ºK (resistive heating) to 160 ºK (liquid nitrogen cooling). A smaller propagation distance from the cathode would allow reaching shorter bunch lengths at the interaction point, but the need for various beamline elements (gun solenoid, gate valve, injection

laser mirror box, detection screens, time-of-arrival screen) usually prevent placing the sample closer than 60-70 cm from the cathode. A pinhole can be inserted few cms before the sample plane to improve the quality of the diffraction patterns as it will be explained in the next sub-section. A novel high efficiency detector has been developed to maximize the signal-to-noise in the diffraction images[34].

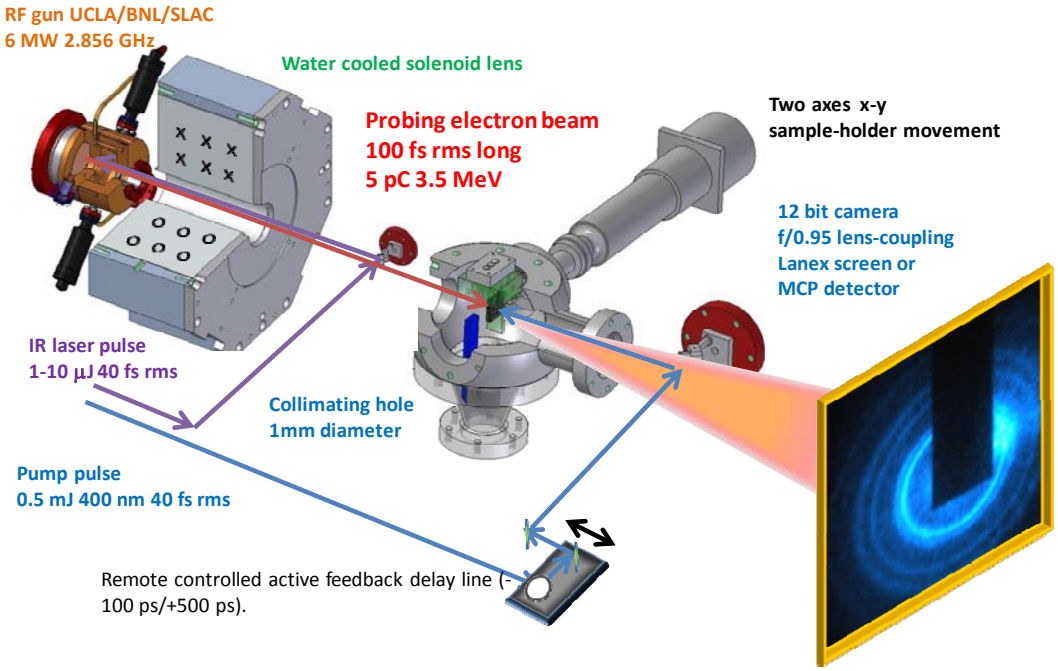

Figure 2. Setup for FRED at the UCLA Pegasus Laboratory.

3.1.2.3.1 Pinhole

An important element that was found to significantly improve the spatial resolution and signal-to-noise ratio in the diffraction patterns is a collimating pinhole aperture just before the sample plane. The dimensions of the hole are optimized in order to let 10^6-10^7 particles go through thus preserving the ability to record the diffraction pattern in a single shot. This aperture serves multiple purposes.

Without the collimator, the dimensions of the probe beam depend on the beam dynamics and are sensitive to many operating parameters. By using a fixed aperture the probe area has a well-defined size easing matching to the pump laser and alignment. During operation, collimation has the significant advantage of removing the dark current background that constitutes a large source of noise in FRED patterns.

Most importantly, the solid curve in Fig. 3 shows the transverse beam spot size when the beam charge extracted from the cathode is 10 pC with an initial laser spot size of 500 um and a collimating hole is used. The collimated beam charge hitting the sample is 1.6 pC. The spot size at the screen is almost three times smaller than what we would achieve without the hole. Since R is inversely proportional to the spot size at the detection screen, this is a significant improvement in the spatial resolution. To give an idea of the importance of this, we note that to resolve the <111> and <200> rings in the Debye–Scherrer pattern of polycrystalline gold, R has to be larger than 4, which would

not be possible without the hole. The collimating aperture effectively removes the high-emittance particles from the beam, thereby cleaning up the transverse phase space.

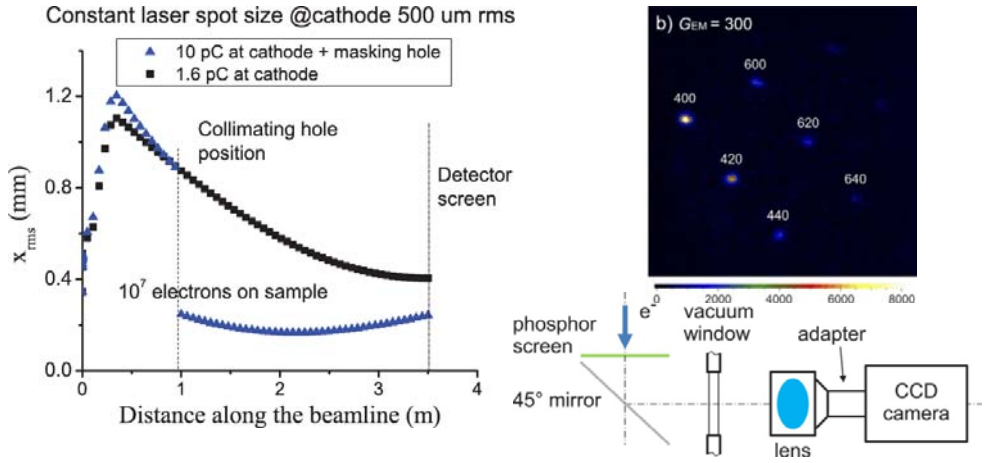

Figure 3. a) GPT simulations of beam dynamics with and without collimating aperture. b) Diffraction pattern obtained with high efficiency detector showing high order Bragg peaks from a single crystal gold sample. c) Scheme of high efficiency detector.

3.1.2.3.2 Start-to-End Simulations

In order to allow the optimization of the diffraction patterns and the spatial resolution of the technique a new General Particle Tracer module has been developed. In the kinematical diffraction approximation the module can calculate the scattering probabilities of few MeV electrons in a thin sample foil and apply the angular kicks to the particle distribution. Only few metal choices and a limited amount of diffraction order have been implemented at this time on the code [44]. Nevertheless it is important to be able to run a fully consistent start-to-end model of the experiment. GPT can follow the particles in three dimensions and has a powerful algorithm for space charge field calculations. This simulation can be very useful to study the effect of space charge effects on the spatial resolution of the technique. For example it has been shown that if the non-diffracted beam remains intense the radius of the diffraction rings is perturbed due to space charge repulsion and a systematic correction needs to be applied.

3.1.2.3.3 Detector

In conventional non-relativistic ED micro-channel plates (MCP) are used to directly image keV electrons or amplify the flux of low energy electrons inside an image-intensifier. The amplified electron flux is then converted by a scintillator to visible photons which are subsequently fiber-optically coupled to a high efficiency charge-coupled device (CCD) camera. It is relatively straightforward to achieve single-electron detection capability due to the large gain of the MCP and the high light collection efficiency of the fiber-optics coupling.

MCPs have also been tested for MeV electrons and high quality single-shot DPs were obtained [45]. Blurring of the DP was observed as a result of the large penetration depth of MeV electrons and the resulting excitation of secondary electrons in many surrounding micro-channels. It was also found that due to the active amplification process the signal from the MCP has larger fluctuations which may be a concern in single-shot measurements where very small changes in the DP are to be detected.

Performance degradation of the MCP and fiber-optics after long term exposure to MeV electrons was not observed.

An effective alternative for the detection of MeV electrons is the use of optimized passive scintillator screens which are low cost and provide high electron-to-photon conversion efficiency and improved spatial resolution. A phosphor screen yields as many as a few thousand photons for each MeV electron due to the large penetration depth of MeV electrons. As an example, two recent papers reported calibration measurements showing greater than 10^3 photons per MeV electron from a Lanex Fine screen [46,47]. In fact, considering an energy loss rate of 1.2–1.5 MeV cm^2/g for 1–4 MeV electrons and a screen density of 34 mg/cm^2, the total energy deposition by each electron is approximately $E_{loss} = 50$ keV. For an optimal choice of phosphor material and screen composition, the efficiency in conversion of this energy into output visible photons is on the order of $\eta = 15\%–25\%$. Approximately half of these photons will exit from the screen side facing the CCD camera while roughly an equal amount exits from the back side. Since the photon spectrum is narrowly peaked a$t\ h\nu = 2.27$ eV (545 nm), we have $n_{scr} = 1/2\ E_{loss}\ \eta\ /\ h\nu\ = 1.7 – 2.8 \times 10^3$ as an estimate of the number of photons emitted from each side of the screen per incident MeV electron. With a properly designed lens coupling system whose collection efficiency is higher than 1% and a state-of-the-art CCD camera capable of single-photon detection, single-electron imaging is possible. This was demonstrated recently [34] where up to the <800> diffraction spot was detected in a single shot.

More advances on the detector side are expected in the next few years. The spatial resolution and dynamic range are important figures-of-merit for a detector as well and these are yet to be optimized in our prototype detector. Currently the size of the point spread function (PSF) at Pegasus is ~100 μm, and in the future, as beam quality improves, it could become the limit on the spatial resolution of the pattern. Phosphor screens with larger density (higher electron-to-photon conversion efficiency) and smaller thicknesses (yielding smaller PSF sizes), such as the DRZ standard screen, could be used. The other issue is related to the saturation in the diffraction pattern. The electron multiplication gain is set at a high level to achieve high detection efficiency, but the camera well depth is a fixed value, one should note that the effective dynamic range is actually suppressed. To cover the large intensity ratio between the direct beam and high order spots, an effective solution is to coat a radially symmetric, variable neutral-density apodizing optical filter on the output side the phosphor screen, extending the dynamic range over 7 orders of magnitude.

3.1.2.3.4 Time Stamping

Obtaining the shortest possible electron bunch length has undoubtedly been the main direction of research efforts in the development of new electron sources. Nevertheless the temporal resolution of the FRED technique has various contributions. In particular the uncertainty in the relative time-of-arrival (TOA) between the pump laser and the probe beam constitutes a major concern when bunch lengths fall below 100 fs.

For rf-based particle accelerators, the jitter on the pump-probe TOA can be usually related to the phase jitter introduced in the rf amplification chain and typically amounts to a few tenths of a degree of the rf frequency. The synchronization accuracy between the photoinjector drive laser and radiofrequency low level oscillators adds another contribution to the total jitter. Furthermore, for low energy beams, rf amplitude

fluctuations carry a significant contribution to the arrival time of the electron beam relative to an external laser pulse. The combination of these effects limits the temporal resolution of pump-probe techniques to a few hundred femtoseconds when using an S-band rf photoinjector. A possible path to increase the temporal resolution in ultrafast dynamics studies is to time stamp each shot and then perform an offline temporal rearrangement of the data. A similar setup was proposed and successfully tested at the short pulse photon source beam line at SLAC [49], where a one-to-one correlation between the electro-optic sampling (EOS) TOA stamp and the evolution of an ultrafast phase transformation (the nonthermal melting of an InSb crystal [50]) was obtained.

At Pegasus we developed a novel 90 degrees non-collinear EOS geometry to spatially encode the signal from the electron beam onto the transverse profile of a laser pulse, as shown in Fig. 4 [43]. Notably the ZnTe crystal used in the experiment can be kept far enough from the axis of the beamline to avoid any beam intercept so this is a non-destructive diagnostics. In the Pegasus setup the crystal is housed in the cross just before the diffraction sample chamber. Accurate timing determination with sub-50 fs temporal resolution can be obtained in a single shot from few pC beam charge.

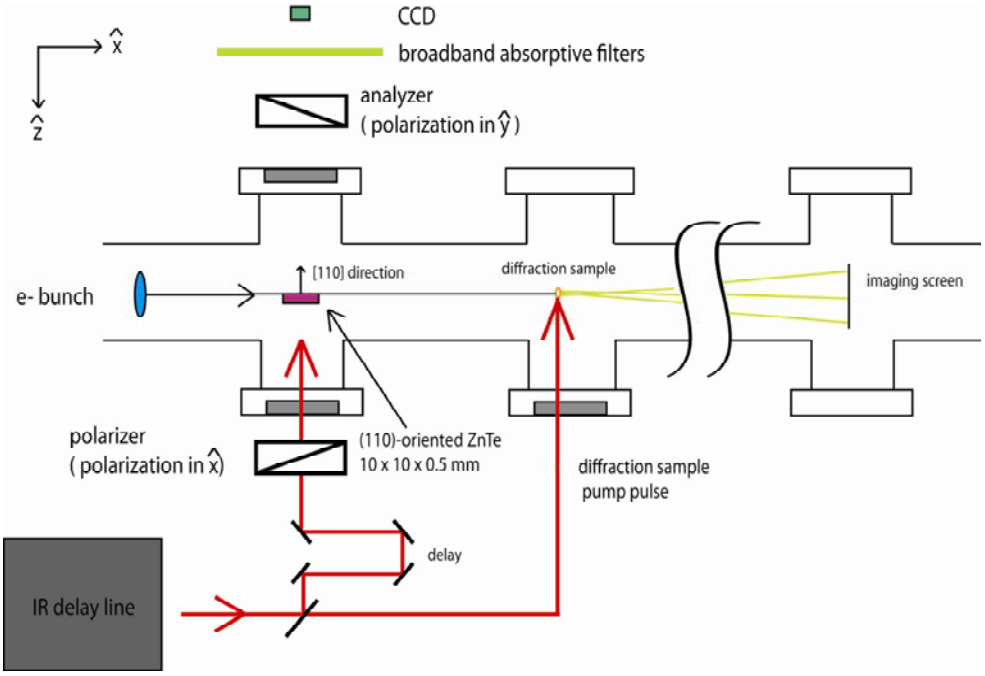

Figure 4. Scheme for non-destructive single shot TOA determination. A clear signal was obtained using less than 1 pC of beam charge in the main beam.

The infrared (ir) pulse used for the EOS is split just before the last mirror in the pump arm in order to guarantee that the EOS pulse carries a faithfully replica of the timing information for the pump pulse. The TOA jitter measured using this technique is larger than 700 fs rms. This is probably due to an aging high power RF system at the UCLA Pegasus Laboratory. Nevertheless, even at state-of-the-art facilities, it is virtually impossible to reduce the jitter between a high power pulsed RF source like a klystron and the laser to < 100 fs. This would set a strong limit on the achievable temporal resolution in electron probing techniques.

A fast algorithm processes the images and extracts a TOA number for each beam shot, which is used to time-stamp the diffraction patterns. The limit in this approach comes from the fact that a minimum charge of ~1 pC is required in order to extract in a non-destructive way a timing signal from the relativistic beam. This could be improved for example using the non-diffracted beam after the interaction and a destructive diagnostics. Using different electro-optic crystals with larger non-linear coefficients could also improve the signal-to-noise ratio of the technique.

3.1.3 A Test Process: Ultrafast Laser-induced Heating and Melting of a Gold Sample

As a benchmark for the technique, we demonstrated the use of MeV electrons from an RF photo-injector to directly detect the changes in the structure of a crystal with fine temporal resolution [30]. The test process we have chosen for this demonstration is the laser-induced melting of a single crystal 20 nm thick gold sample. Single-shot diffraction patterns are shown in Fig. 5. It is worth stressing that each diffraction pattern is obtained using a single sub-200 fs electron bunch.

For each diffraction spot, we use a two dimensional Gaussian fit to calculate its amplitude, the center position and the width. Fluctuations in the electron beam parameters are responsible for a variation in the normalized amplitude for each Bragg peak of less than 1%. This can be seen by the stability of the trace in Fig. 5 for the time delays when the laser arrives after the electron beam.

The observed behavior of the Bragg peak amplitudes is a direct test of our understanding of the laser-induced heating and melting processes in a metallic single crystal sample. The laser energy is absorbed within an optical skin depth (7-8 nm) creating a population of fast electrons which ballistically moves across the sample at Fermi velocities [50]. Due to the strong electron-electron scattering, the electron distribution thermalizes quickly. Hence, shortly (<100 fs) after illumination it is possible to define an electron temperature homogeneous across the sample. At this point, with a time scale controlled by the electron-phonon coupling constant, diffusive heat transfer to the lattice subsystem takes place leading to electron and lattice temperature equilibration. A good approximation valid after the initial few hundred fs is to include the ballistic electron transport simply modifying the penetration depth of the laser energy term and treat the problem with the two temperature model (TTM) [51].

The lattice temperature increase is the origin of the loss of coherence of the Bragg peaks. The thermal random motion induced by the electron-phonon coupling acts as a blur of the atomic positions in the crystal and decreases the Bragg peak amplitudes (Debye-Waller effect). The predictions for the variation of the Bragg peak amplitudes obtained using a TTM for the Au lattice are shown in Fig. 5. The model fits well the data when the electron phonon coupling constant, an important parameter in the theory of superconductivity, is $\lambda = 0.15$ in excellent agreement with the value reported in the literature [52]. The data also shows that the higher diffraction orders disappear faster than the lower ones, consistent with the scattering vector dependence in the Debye-Waller factor

When the illuminating pump fluence is raised to 35 mJ/cm^2, the lattice temperature goes above the melting point, the solid becomes superheated at first and then the phase transition takes place. This can be observed by the departure from the Debye-Waller factor TTM scaling in the peak amplitudes between 12-18 ps from the time when the

laser hits the sample. During the same time interval, by integrating the diffraction pattern over regions where the signal is not shadowed by diffraction spots, and again comparing with the results from the laser-off images, it is possible to observe the rise of the liquid correlation function peak at around 0.42 $Å^{-1}$. This experiment was an important benchmark for the technique since it showed for the first time the possibility of completing a time-resolved measurements using single-shot diffraction patterns. Since then more time-resolved studies using MeV electrons have been reported and MeV FRED is expected to make an impact whenever irreversible structural changes or very high temporal resolution are requested.

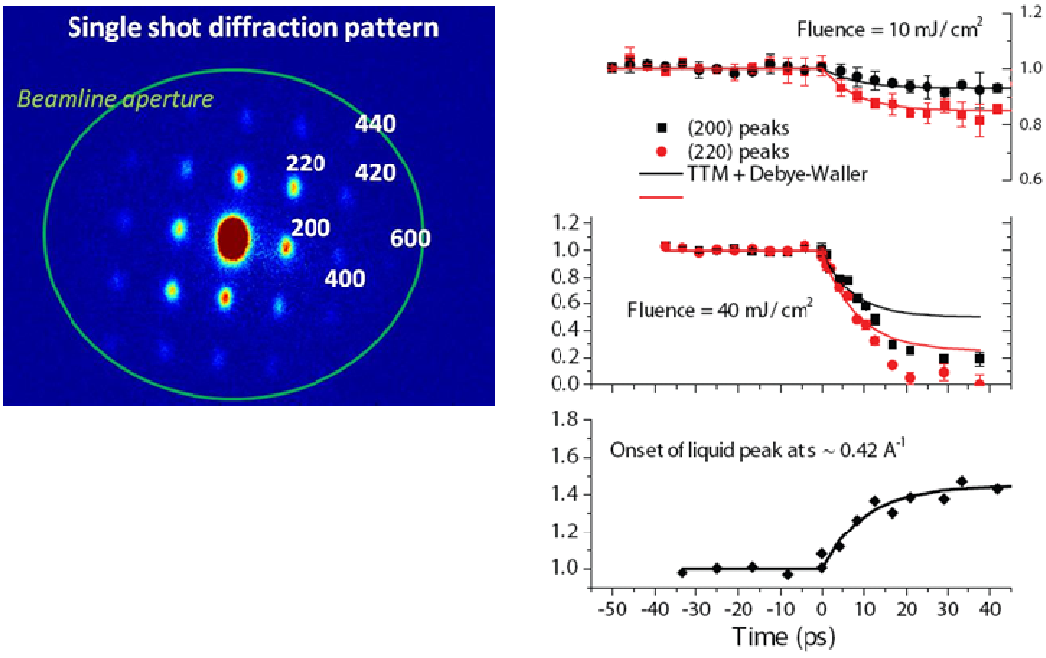

Figure 5. Laser induced heating and melting of single crystal gold sample studied by single shot MeV electron diffraction patterns (from Ref. [30]). Left) Single shot diffraction pattern from single crystal gold sample. Right) Evolution of Bragg peaks for low and high fluence as a function of time. Each point is taken after moving the pump-probe delay line stage.

3.1.4 **Continuously Time-resolved UED**

A different mode of operation for FRED is given by continuously time-resolved ED. Even in the early days of UED, researchers recognized the possibility of an alternative setup in which the diffracted electron beam is streaked using deflecting plates to record the time evolution of the changing pattern [6]. The advantage in such configuration is that a short electron bunch is no longer required and the temporal resolution is determined by the sweeping speed of the plates or more generally by the resolution of the streak camera system. The large (few ps) jitter in the photoconductive switch providing the synchronization between the beam and the deflecting voltage, and the slow sweeping speed achievable have made this approach less favorable compared to the more conventional pump and probe scheme characterized by time-delay scans. An interesting scheme to bypass the streaking plates issue was proposed by Baum and

Zewail [19]. It takes advantage of the strong chirp (time-energy correlation) that electron pulses naturally develop in the propagation from the cathode due to the space charge forces. In this promising scheme, which is currently awaiting an experimental demonstration, an energy filtering device (a spectrometer) takes the role of the streaking plates and is used to effectively analyze in time the diffraction signal.

Recently, there has been renewed interest in streak camera based UED in the context of RF (radiofrequency) photoinjector based FRED [31,32]. Using an RF resonant cavity for the deflection allows for much higher deflecting voltages which together with a relatively high oscillation frequency offer faster sweeping speeds than what is possible with traditional sweeping plates. The other key ingredient of the technique is the use of intense relativistic electron beams. The peak current in a 3-4 MeV electron beam from an RF photoinjector can be in the tens of Amps range. With 10^7-10^8 particles per pulse in a 15-20~ps long electron beam in fact it becomes possible to acquire the entire time-history of the ultrafast process within a single pump-and-probe event using only one sample. Employing MeV beams in conjunction with an RF deflector eliminates the need for time-delay scanning and offers the possibility of truly single shot studies of irreversible processes in ultrafast structural dynamics.

In a 2010 paper we demonstrated this variation of FRED and recorded streaked diffraction patterns using a 16 ps long electron beam showing the melting of the gold sample in a single shot [33]. More recently we have improved the temporal resolution of the technique to < 35 fs by improving the beam quality and using a quadrupole to narrow the width of the unstreaked spot size [53].

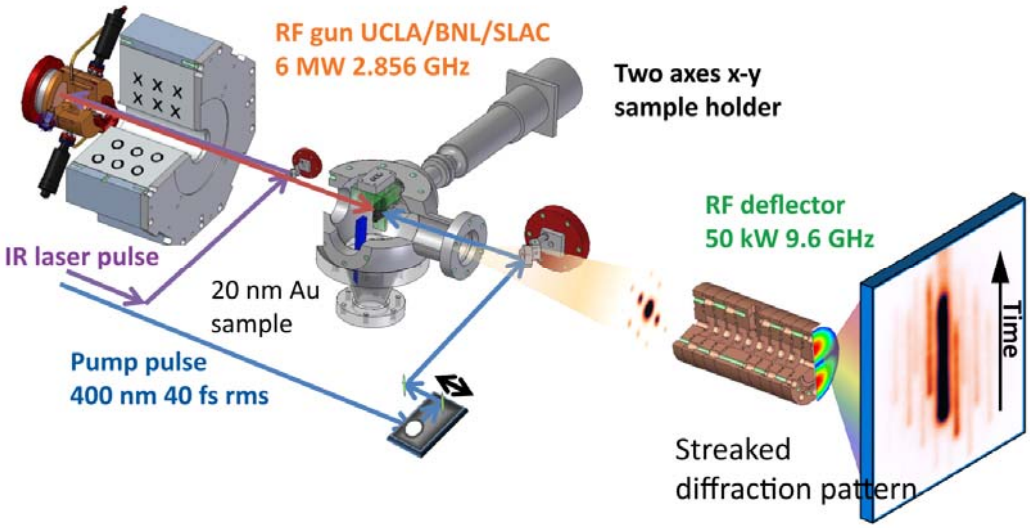

Figure 6. Streaked MeV electron diffraction cartoon.

The extension of this technique to nonrelativistic electron sources is an interesting possibility[54]. In this regard, it is important to notice that if one is looking for single shot data acquisition, the number of particles per interval of temporal resolution has to be relatively large (>10^6) to be able to resolve each diffraction peak for different time slices. The issue to be verified is if the transverse beam quality (i.e., normalized emittance) can be preserved at these relatively high currents for the lower beam energies.

3.1.5 **Compression for UED**

The 1.6 cell S-band photocathode rf gun alone can generate sub-50 fs rms electron pulses with adequate bunch charge and beam quality to take single-shot DPs. However, to observe faster processes such as coherent phonon oscillations, even shorter (~10 fs rms) electron pulses are required. In this section we discuss a scheme to generate sub-5 fs rms electron pulses based on applying the rf compression scheme proposed by Van Oudheusden et al. [20,22] to a relativistic electron source. Simulation results show that a 50 fC electron pulse can be compressed using velocity bunching in a short linac section to 4 fs rms and the transverse beam quality is preserved.

An S-band dual slot resonance linac (DSRL) has being constructed and installed at the Pegasus Laboratory in collaboration with Fartech [55]. The DSRL consists of 10 full cells plus the entrance and exit half cells, and its total length is 60 cm. It will be placed 1.1 m from the gun cathode, and the collimation hole and diffraction sample will be moved to 1.9 m position. The linac has now been conditioned up to 2 MW and with this input power the maximum energy gain of DSRL is 10 MeV. Instead of running the DSRL on the crest of the rf phase for high energy gain, it is possible to adjust its phase and amplitude to impart a negative energy(velocity)-position correlation on the beam longitudinal phase space. By letting the beam propagate through a short drift section after the DSRL, its phase space rotates in the upright position and maximum compression is achieved.

The evolution of the pulse length along the beamline is shown in Fig. 7. The locations of the DSRL and the collimation hole are also shown. Before entering DSRL the electron pulse is slightly positively chirped (head electrons have higher energies), and the pulse length increases. Since the energy gain through the DSRL is time-dependent, it is possible to reverse the energy chirp by choosing appropriately the rf phase of the DSRL. At position b inside the DSRL the energy chirp is minimized and the pulse length reaches the maximum. Once the tailing electrons have higher energies (hence travel faster) they tend to catch up the leading ones and the pulse length decreases.

The combined actions of the rf induced energy chirp and the longitudinal space charge (LSC) effects determined the dynamics of the longitudinal compression and the location of the shortest pulse length. Due to the transverse dependence of the LSC force, different radial positions in the beam arrive at the optimal longitudinal compression at different times. We use a collimation hole to select the core region of the beam where the compression dynamics is more homogeneous. The minimum pulse length at the sample is only 4 fs rms and limited by the residual curvature in the longitudinal phase space.

Table 2: Beam parameters at the sample plane for the velocity bunching scheme

Parameter	***MeV UED***
Beam Kinetic Energy	3.5 MeV
Rms energy spread	10^{-3}
Bunch charge	50 fC
Normalized emittance	0.08 mm-mrad
Transverse spot size	250 um
Rms pulse length	4 fs

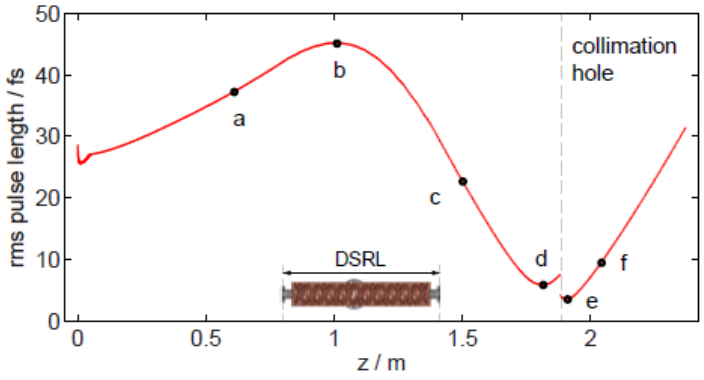

Figure 7. The evolution of the electron beam bunch length in the compressed FRED scheme.

The beam in our compression scheme is characterized by a relatively symmetric profile. This is due to the fact that by using blow-out regime of operation of RF photoinjector, the beam out of the gun is short (sub-100 fs) and with a relatively linear longitudinal phase [56]. This limits the curvature imparted by the radiofrequency accelerating wave in the linac which is usually the source of long tails after compression. At the longitudinal focus, it is only the residual space charge force nonlinearities that set the minimum pulse length.

We conclude this section by quantifying the role of the longitudinal pulse profile on the possibility to resolve a structural change of a given decay time or oscillation period. This is an important point as different communities quote different parameters to characterize bunch length such as rms or full width at half maximum (fwhm). For well defined longitudinal beam shapes, e.g. rectangular or Gaussian distributions, the rms and fwhm values only differ by a fixed shape-dependent constant. But as a result of compression schemes, longitudinal beam profiles become more complicated. In many cases they are characterized by sharp spikes and long tails, especially when a relatively long pulse is compressed and the final compression is dominated by the RF curvature. It then becomes important to understand how to quantify the temporal resolution. In electron diffraction each electron in the beam will contribute to the signal on the detection screen. The situation is different for example if the ultrashort compressed beams are used to drive Free-Electron Laser amplifiers. In this case, the instability amplification process selects the brightest part in the beam (the spike in beam current) and greatly enhances the contrast with the low current portions of the beam.

We compare our pulse shape (denoted by G) with different ones characterized by the same rms or FWHM bunch length. An interesting case to consider is a pulse shape (denoted by C) where 80% of the electrons are bunched into a 4 fs fwhm peak but the remaining 20% extended in a long tail trailing the beam so that the rms width of the entire pulse is 20 fs. This mimics the typical case when the rf induced non linearities dominate the final bunch length. A rectangular pulse shape (denoted by R) is also considered.

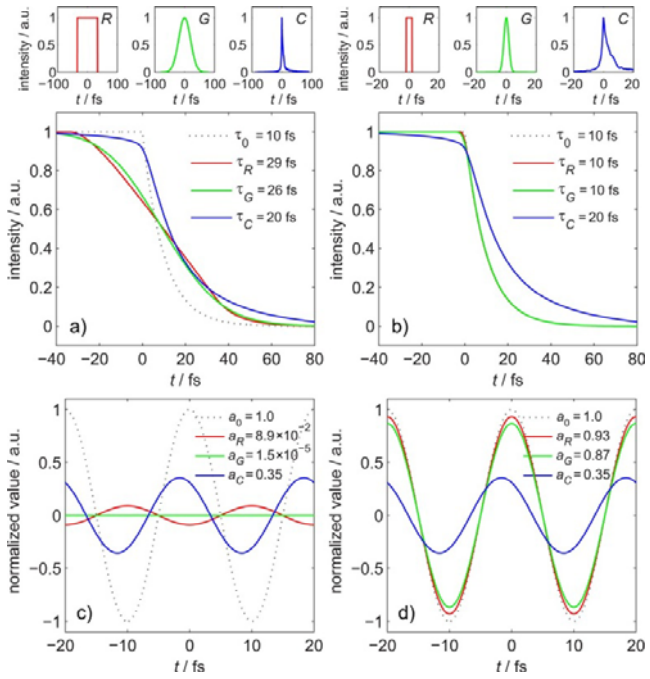

Figure 8. A longitudinally rectangular (R, red), a Gaussian (G, green) and a complicated shaped (C, blue, the insect in (a), see text for detail) pulses are used to measure a (a-b) exponentially decay and (c-d) oscillating structural changes. In (a) and (c) the three pulse have the same rms widths of 20 fs, and in (b) and (d) the pulses have equal fwhm widths of 4 fs.

The signal obtained when using these beams for electron diffraction is given by the convolution of the time-response of the system under study and the longitudinal beam profiles. In Fig.8(a) and (b) we show the results of a process with 10 fs time-constant measured by the C, R and G-shaped pulses with same rms values (20 fs) and same fwhm values (4 fs), together with the intrinsic and measured time constants. Although the C-shaped pulse has a very sharp peak, the trailing electrons sample the structures over a large time window which lead to the decrease in the observed slope. Deconvolution technique may be used to retrieve the intrinsic time constant from the measurement results if the longitudinal beam profile can be mapped with high precision.

For cases where the time-response of the system under study is an oscillation with a period of τ_0 and an amplitude a_0, using an electron beam with a finite pulse length will cause a drop in the observed oscillation amplitudes. Fig.8 (c) and (d) show the intrinsic oscillation (black dashed line) and the measured ones again using various pulse shapes with same rms values (20 fs) and same fwhm values (4 fs). In this case the C-shaped pulse is advantageous over other more smoothed shapes since the long tail extend over many oscillation periods and tend to average out. In order to keep the normalized amplitude a/a_0 at a considerable level (~0.1) so that the observable amplitude stays above the measurement error, generally the rms pulse length have to be 3-4 times shorter than the oscillation period, but a sharp peak can relax this requirement depending on the width and the fraction of number of electrons in the peak.

3.1.6 **Future Directions**

An ambitious goal of the community is to push the limit of current technology and take advantage of the high brightness of the intense MeV electron beam from the RF photoinjector source for imaging applications. Currently the only solution to the problem of capturing electron microscope images with ultrafast temporal resolution (ps or lower) is represented by Caltech Zewail's group stroboscopic approach [57,58] where the electron images are formed using single-electron pulses, thus completely removing the problems associated with space charge effects. This approach has produced exciting results, but it is limited to the study of processes that can be repeatedly excited many million times. If single shot images are required, one has to trade off spatial resolution for temporal resolution as demonstrated in the DTEM at LLNL which has ns temporal resolution and 10 nm spatial resolution [59].

Another possible solution is to increase the energy of the beam to MeV level to take advantage of the relativistic suppression of the space charge forces and capture a TEM image in a single shot. There are two major limitations in expanding the capabilities of the MeV diffraction camera towards high spatial resolution imaging mode: i) the limited beam coherence from the metal photocathodes in the RF gun and ii) the technical difficulties associated with building strong lenses for relativistic energy beams.

Recently we have demonstrated at the UCLA Pegasus Laboratory a new regime of operation of the RF photoinjector where the laser is focused on the cathode to a very small spot (< 30 micron rms) and at the same time the longitudinal profile of the beam is stretched to a parabolic shape (rms bunch length ~1 ps) [60]. In this regime the beam undergoes a mainly transverse space charge expansion which leads to the creation of a nearly ideal uniformly filled ellipsoidal distribution, characterized by linear fields in each direction. In these conditions, the space charge induced emittance growth, associated with the non-linearities of the beam self-fields, can be minimized. Moreover, the small size of the source allows the possibility of generating from the beginning a beam with very small emittance (and equivalently high transverse coherence).

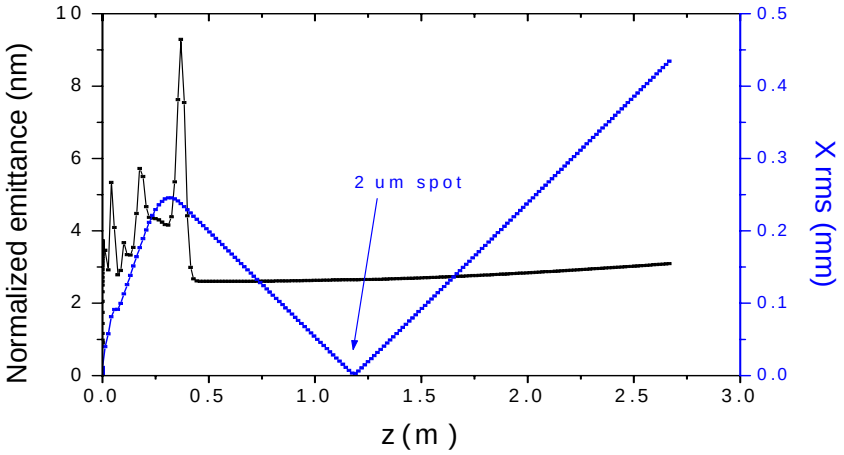

Figure 9. The evolution of the normalized emittance and spot size along the beamline in the proposed imaging mode.

First measurements of the beam emittance with pepper-pot technique indicate normalized emittance values lower than 50 nm. By further reducing the spot size on the cathode to < 20 μm rms, taking advantage of progress in cathode research to reduce the

thermal energy spread below 0.1 eV, particle tracking simulations (shown in the Fig. 9) predict MeV beams with <10 nm-rad normalized emittance.

In Table 3, we show the parameters for the imaging mode of operation of the RF photoinjector. The main differences consist in the format of the laser pulse on the cathode. For diffraction, one would like a very short electron beam and so the tendency is to decrease the surface charge at the cathode spreading the laser over a larger transverse area. For imaging, we focus the laser down to a very small spot to obtain a vanishing small thermal emittance.

Table 3. Parameters of operation of the Pegasus photoinjector for electron diffraction and microscopy experiments.

Parameter	Diffraction setup	Proposed Microscopy setup
Laser pulse length	35 fs (rms)	3 ps (rms)
Laser spot size on cathode	200 μm (rms)	20 μm (rms)
Peak field on the cathode	100 MV/m	120 MV/m
Beam energy	5 MeV	6 MeV
Beam charge	0.2 pC (1.25×10^{p} e^{-})	1 pC (6×10^{p} e^{-})
Normalized emittance	0.1 mm-mrad	10 nm-rad
Pulse length	100 fs rms	2 ps rms
Injection phase	30 degrees	30 degrees

The other ingredient in achieving high spatial resolution images with the electron beam is the availability of low-aberration strong lenses. For example, using an electron lens with a focal distance of 2 cm, simulations suggest that the Pegasus beam can be focused down to below 2 micron rms spot size, with an intrinsic divergence still smaller than the average Bragg angle. Expanding the beam to few cm spot size on the screen will allow magnification factor in excess of ×1000.

Electromagnetic solenoids for MeV electron beams on the other hand are bulky and limited in the focal length by the current density and the required cooling power. In order to approach imaging mode we propose to introduce in the column first order focusing elements such as permanent magnet quadrupoles (PMQ). UCLA has a considerable experience in building very strong quadrupole lenses based on permanent magnet technology, using the so-called Halbach configuration (shown in Fig. 8). With a gradient of > 500 T/m and an effective length of 1 cm, the effective focal distance of a PMQ triplet can be very short yielding sub 5-μm spot sizes. Another intrinsic advantage of using quadrupole magnet instead of cylindrical solenoidal lenses is that the intermediate waists between the object plane and the detector plane will be elliptical and so less prone to degradation of the image quality by stochastic Coulomb effects.

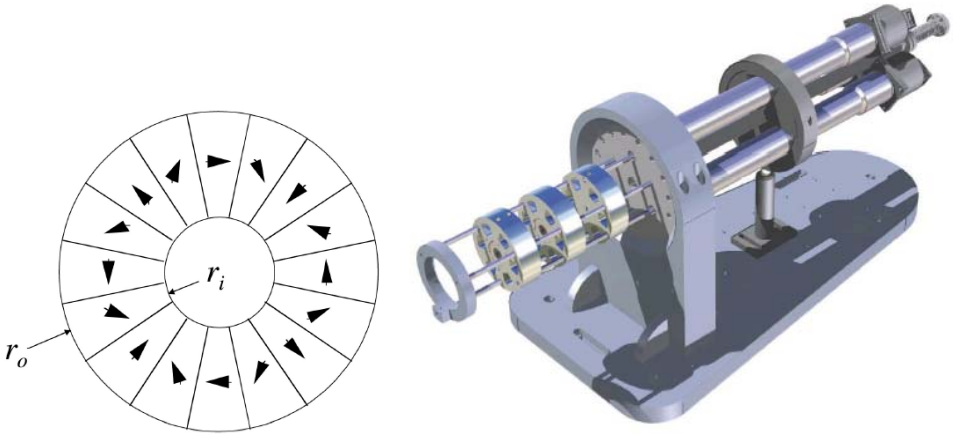

Figure 10. Left) Halbach 'pizza-pie' PMQ configuration. Right) CAD drawing of the UCLA-designed PMQ triplet assembly.

The spatial resolution of the relativistic electron imaging system will be up to one order of magnitude better than what can be achieved with conventional light microscopes. There are several very good reasons for pursuing the imaging configuration on our MeV electron camera in the context of materials in extreme conditions. These include getting access to the diffraction contrast mechanisms of TEM, which are unavailable in conventional light microscopes, obtaining moderate-resolution real-space imaging and variable diffraction camera lengths in a single system and leading the way towards further developments of ultrafast imaging capabilities for transmission electron microscopes.

3.1.7 **Conclusions**

Femtosecond relativistic electron diffraction is a novel technique which holds the promise to yield real-time atomic resolution of ultrafast structural rearrangements in matter. Many research groups are now joining this field as it becomes clear that the continuous progress in high brightness electron sources stimulated by the recent successes of X-ray FELs finds immediate application to the direct investigation of matter by electron diffraction. The first scientific studies of ultrafast science with MeV electrons have been recently completed and further progress is expected as the cross-fertilization between electron microscopy, ultrafast structural dynamics and electron sources goes on. The high peak brightness of MeV beams as well the increased penetrating power of the high energy electrons are unique features of a relativistic electron probe beam.

Interesting variations on this technique include continuously time-resolved electron diffraction and ps-MeV electron microscopy. A workshop on ultrafast electron sources for diffraction and microscopy will be held at UCLA on Dec 12-14, 2012 [35] with the charge of putting together experts from different communities to discuss the future of ultrafast electron sources for diffraction and microscopy applications.

3.1.8 **References**

1. W. E. King, G. H. Campbell, A. Frank, B. Reed, J. F. Schmerge, B. J. Siwick, B. C. Stuart, and P. M. Weber, J. Appl. Phys. **97**, 111101 (2005).

2. A. H. Zewail, Annu. Rev. Phys. Chem. **57**, 65 (2006).–
3. German Sciaini and R. J. Dwayne Miller, Rep. Prog. Phys. **74**, 096101 (2011).
4. ICFA Beam Dynamics Newsletter No. 46, edited by M. A. Furman, 2008, http://icfa-usa.jlab.org/archive/newsletter/icfa_bd_nl_46.pdf
5. Majed Chergui and Ahmed H. Zewail, Chem. Phys. **10**, 28 (2009).
6. G. Mourou and S. Williamson, Appl. Phys. Lett. **41**, 44 (1982).
7. B. J. Siwick, J. R. Dwyer, R. E. Jordan, and R. J. D. Miller, Science **202**, 1382 (2003).
8. R. Ernstorfer et al., Science, **323**, 1033 (2009)
9. R. C. Dudek and P. M. Weber, J. Phys. Chem A **105**, 4167 (2001).
10. H. Ihee, V A. Lobastov, U. M. Gomez, B. M. Goodson, R. Srinivasan, C. Ruan and A. H. Zewail, Science **291**, 458 (2001).
11. N. Gedik, D. S. Yang, G. Logvenov, I. Bozovic, and A. H. Zewail, Science **316**,425 (2007).
12. F. Carbone, P. Baum, P. Rudolf and A. H. Zewail, Phys. Rev. Lett. **100**, 035501 (2008).
13. M. Eichberger, et al. Nature, **468**, 799 (2010)
14. C. Ruan et al., Science **304**, 80 (2004).
15. B. Krenzer et al., New Journal of physics, **8**, 190 (2006)
16. B. J. Siwick, J. R. Dwyer, R. E. Jordan, and R. J. Dwayne Miller, Journal of Appl. Phys. **92** , 1643 (2002).
17. B. W. Reed, Journal of Applied Physics **100**, 034916 (2006)
18. J. Cao, Z. Hao, H. Park, C. Tao, D. Kau, and L. Blaszczyk, Appl. Phys. Lett. **83**, 1044 (2003).
19. P. Baum and A. H. Zewail, Proc. Of Nat. Acad. Of Sci, **103**, 16105 (2006).
20. T. vanOudheusden, E. F. de Jong, S. B. van der Geer, W. P. E. M. Op 't Root, O. J. Luiten and B. J. Siwick. Journal of Applied Physics **102,** 093501, (2007).
21. T. van Oudheusden, P. L. E. M. Pasmans, S. B. van der Geer, M. J. de Loos, M. J. van der Wiel, and O. J. Luiten, Phys. Rev. Lett. **105**, 0264801 (2010).
22. R. P. Chatelain, Applied Physics Letters, **101**, 081901 (2012)
23. X. J. Wang, Z. Wu and H. Ihee, Proceedings of 2003 Particle Accelerator Conference, Portland, Or (2003).
24. X. J. Wang, D. Xiang, T. J. Kim and H. Ihee, J. of Korean Physical Society, **48**, 390 (2006).
25. J. B. Hastings, F. M. Rudakov, D. H. Dowell, J. F. Schmerge, J. D. Cardoza, J. M. Castro, S. M. Gierman, H. Loos, P. M. Weber, Appl. Phys. Lett. **89**, 184109 (2006).
26. P. Musumeci et al., Ultramicroscopy, **108**, 1450 (2008).
27. R. K. Li, C. X. Tang, Y. C. Du, W. H. Huang, Q. Du, J. R. Shi, L. X. Yan, and X. Wang. Rev. Sci. Instrum. **80**, 083303 (2009).
28. P. Musumeci, J. T. Moody, C. M. Scoby, M. S. Gutierrez, H. A. Bender, and N. S. Wilcox, Rev. Sci. Instrum. **81**, 013306 (2010).
29. Y. Murooka, N. Naruse, S. Sakakihara, M. Ishimaru, J. Yang, and K. Tanimura, Appl. Phys. Lett. **98**, 251903 (2011).
30. P. Musumeci, J. T. Moody, C. M. Scoby, M. S. Gutierrez, and M. Westfall, Appl. Phys. Lett. **97**, 063502, (2010).
31. P. Musumeci, J. T. Moody, C. M. Scoby, Review of Scientific Instr. **80**, 013302 (2009).
32. R. K. Li *et al.*, Rev. Sci. Instrum. **81**, 036110 (2010).
33. P. Musumeci, J. T. Moody, C. M. Scoby, M. S. Gutierrez, M. Westfall, and R. K. Li, J Appl. Phys. **108**, 114513 (2010).
34. R. K. Li, P. Musumeci, H. A. Bender, N. S. Wilcox, and M. Wu, J Appl. Phys. **110**, 074512 (2011).
35. Workshop on Ultrafast Electron Sources for Diffraction and Microscopy (UESDM), http://pbpl.physics.ucla.edu/UESDM_2012
36. H. N. Chapman et al., Nature Physics **2**, 839 (2006).

37. N. Naruse, Y. Murooka, J. Yang, and K. Tanimura, presented at the 2012 Banff Meeting on Structural Dynamics, Banff, Alberta, Canada, 2012.
38. P. F. Zhu, J. Cao, Y. Hidaka, J. P. Hill, Y. Shen, R. I. Tobey, Y. Zhu, and X. J. Wang, at International Conference on Ultrafast Structural Dynamics (ICUSD), Berlin, Germany, March 2012.
39. K. Floettmann et al., presented at the 2012 Banff Meeting on Structural Dynamics, Banff, Alberta, Canada, 2012.
40. P. Grivet, "Electron Optics", Pergamon, Oxford, 1965.
41. Y. Ding et al., Phys. Rev. Lett. **102**, 254801 (2009).
42. P. Musumeci et al. Microscopy and Microanalysis, **15**, 290 (2009).
43. C. M. Scoby et al. Phys. Rev. STAB, **13**, 022801 (2010)
44. *www.pulsar.nl/download/aldiffr.c*
45. P. Musumeci**,** J.T. Moody**,** C.M. Scoby**,** M.S. Gutierrez**,** H.A. Bender**,** B. Hilko**,** C.A. Kruschwitz and N.S. Wilcox, Nuclear Instrum. Methods Phys. Res. Sec. A, 637, S12, (2011).
46. Y. Glinec, J. Faure, A. Guemnie-Tafo, V. Malka, H. Monard, J. P. Larbre, V. De Waele, J. L. Marignier, and M. Mostafavi, Rev. Sci. Instrum. 77, 103301 (2006).
47. A. Buck, K. Zeil, A. Popp, K. Schmid, A. Jochmann, S. D. Kraft, B. Hidding, T. Kudyakov, C. M. S. Sears, L. Veisz, S. Karsch, J. Pawelke, R. Sauerbrey, T. Cowan, F. Krausz, and U. Schramm, Rev. Sci. Instrum. 81, 033301 (2010).
48. A. L. Cavalieri et al., Phys. Rev. Lett. 94, 114801 (2005).
49. K. J. Gaffney et al., Phys. Rev. Lett. 95, 125701 (2005).
50. S. D. Brorson, J. G. Fujimoto, and E. P. Ippen, Phys. Rev. Lett. 59, 1962 (1987).
51. S. I. Anisimov, B. L. Kapeliovich, and T. L. Perel'man, Sov. Phys. JETP 39, 375 (1974).
52. P. B. Allen, Phys. Rev. Lett. 59, 1460 (1987).
53. C. M. Scoby et al. submitted to Applied Physics Letters
54. L. Faillace et al. Proceedings of 2012 IPAC conference, New Orleans, LA (2012)
55. D. J. Newsham, N. Barov, and R. H. Miller, in the Proceedings of the 2011 Particle Accelerator Conference (IEEE, New York, 2011) p. WEP220.
56. P. Musumeci, J. T. Moody, R. J. England, J. B. Rosenzweig, and T. Tran, Phys. Rev. Lett. 100, 244801 (2008).
57. V. A. Lobastov, R. Srinivasan, and A. H. Zewail, PNAS 102, 7069 (2005).
58. A. H. Zewail, Science 328, 187 (2010).
59. N. D. Browning, G. H. Campbell, J. E. Evans, T. B. LaGrange, K. L. Jungjohann, J. S. Kim, D. J. Masiel, and B. W. Reed, Dynamic Transmission Electron Microscopy, First Edition. Edited by G.Van Tendeloo, D. Van Dyck, and S. J. Pennycook, Wiley-VCH Verlag GmbH & Co. KGaA, 2012.
60. R. K. Li, K. G. Roberts, C. M. Scoby, H. To, and P. Musumeci, Phys. Rev. ST Accel. Beams 15, 090702 (2012).

3.2 High-Brightness, Femtosecond Electron Beam Generation Using Laser-Plasma Accelerators

Carl B. Schroeder, Eric Esarey, Jeroen van Tilborg, Wim Leemans
Lawrence Berkeley National Laboratory, Berkeley, CA 94720 USA
Mail to: CBSchroeder@lbl.gov

3.2.1 Introduction

Laser-plasma accelerators (LPAs) have attracted considerable attention owing to their ability to generate ultrahigh accelerating gradients, enabling compact accelerators. Laser-plasma acceleration is realized by using a high-intensity laser to ponderomotively drive a large plasma wave (or wakefield) in an underdense plasma [1]. The plasma wave has relativistic phase velocity, approximately the group velocity of the laser, and can support large electric fields in the direction of the laser propagation. When the laser pulse is approximately resonant (pulse duration on the order of the plasma period) and the laser intensity is relativistic, with normalized laser vector potential $a = eA/m_e c^2 \sim 1$, the size of the accelerating field supported by the plasma is on the order of $E_0 = m_e c^2 k_p/e$, or

$$E_0[\mathrm{V/m}] \cong 96\sqrt{n_0[\mathrm{cm}^{-3}]}, \tag{1}$$

where ck_p is the electron plasma frequency, n_0 is the ambient electron number density, m_e and e are the electronic mass and charge, respectively, and c is the speed of light in vacuum. For example, an accelerating gradient of $E_0 \sim 100$ GV/m is achieved operating at a plasma density of $n_0 \sim 10^{18}$ cm^{-3}, which is several orders of magnitude larger than conventional technology. Owing to these ultrahigh accelerating gradients, LPAs are actively being researched as compact sources of energetic beams for high-peak brightness light sources [2-6] and future linear colliders [7].

In addition to extremely large accelerating gradients, plasma-based accelerators intrinsically produce ultra-short (fs) electron bunches that are a fraction of the plasma wavelength, $L_b < \lambda_p/4$, where L_b is the beam length and

$$\lambda_p[\mu\mathrm{m}] \cong \frac{3.3\times 10^{10}}{\sqrt{n_0[\mathrm{cm}^{-3}]}} \tag{2}$$

is the plasma wavelength. As we discuss in this newsletter, recent experiments have measured LPA bunch durations that are a few femtoseconds. Because of the short beam durations, LPAs are sources of high-peak current beams ($I \sim 1$–10 kA), and, hence, it is natural to consider fs LPA electron beams as drivers for producing high-peak brightness radiation (e.g., free-electron lasers). LPA electron beams have been coupled into undulators to produce undulator radiation in the visible [8] and soft-x-ray [9] wavelengths. These fs beams are also intrinsically synchronized to the drive laser pulse, enabling a wide variation of pump-probe applications.

In this newsletter we report on recent measurements characterizing the fs LPA electron beam phase space.

3.2.2 **Laser-Plasma Accelerator Beam Phase Space Characteristics**

Rapid progress in laser-plasma accelerator research has been made over the past decade (see [1] for a review). In particular, the production of high-quality GeV electron beams over cm-scale plasmas was achieved in 2006 at Lawrence Berkeley National Laboratory [10]. Since 2006, several laser facilities worldwide have demonstrated quasi-monoenergetic LPA beams with GeV-level energies [11, 12].

High-quality electron beams up to 1 GeV have been experimentally demonstrated using 40 TW lasers interacting in centimeter-scale plasma channels [10]. Figure 1 shows a single-shot spectrum of a 1 GeV electron beam generated using the LPA at LBNL. In Fig. 1, a 1.5 J, 0.8-micron laser interacts with a 310-micron diameter H-discharge capillary with on-axis density $4\text{x}10^{18}$ cm^{-3}. The H-discharge capillary forms a plasma channel for guiding the laser. LPAs are capable of compactly producing GeV beams with tens of pC of charge, few percent-level relative energy spread, and mrad divergences. Recent experimental effort in the plasma-based accelerator community has been focused on improved diagnostics and measurements of the LPA electron beam phase space, and, in particular, measurements of the beam transverse emittance and the beam duration.

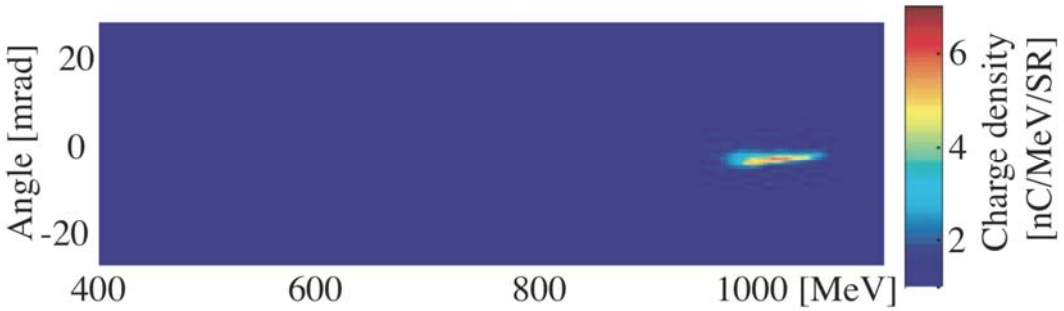

Figure 1: Single-shot electron beam spectrum from a 310-micron diameter H-discharge capillary with on-axis density $4\text{x}10^{18}$ cm^{-3} and a 1.5 J, 46 fs laser. The H-discharge capillary forms a plasma channel for guiding the laser. The 1012 MeV electron beam contained 30 pC of charge, with 2.9% (rms) energy spread and 1.7 mrad (rms) divergence.

3.2.2.1 ***Transverse Emittance Measurement***

As the electron beam is accelerated in the wakefield of the laser, it undergoes betatron motion in the strong focusing forces ($F_r \sim eE_0k_pr$) of the plasma wave, and emits fs, hard x-rays [13]. The beam transverse size in the plasma wave can be determined by measuring the spectrum of betatron x-rays produced by the beam [14-16]. The effective wiggler strength parameter $a_\beta = \gamma_z k_\beta r_\beta$ is typically large $a_\beta >> 1$ (where γ_z is the Lorentz factor of the longitudinal momentum, k_β the betatron wavenumber, and r_β the amplitude of the electron betatron orbit), and the x-ray spectrum is broad. The spectrum is characterized by the critical frequency $\omega_c = 3a_\beta\gamma_z^2k_\beta c$. Owing to the strength of the transverse focusing force in the plasma wave, the beam emits hard x-rays (~10 keV). By measuring the spectrum (i.e., ω_c), the amplitude of the betatron oscillation r_β (i.e., the beam radius) may be estimated. This measurement is a non-invasive, in situ, single-shot diagnostic of the beam size and, combined with a divergence measurement, may be used to estimate the beam transverse emittance. This diagnostic was implemented at LBNL [14], where a 463 MeV beam

was generated, with 2.8% (rms) energy spread and 1.2 mrad (rms) divergence, and the x-ray betatron spectrum was measured indicating a beam radius of 0.1 micron and an estimated normalized transverse emittance 0.1 mm mrad.

Quadrupole scan measurements of LPA electron beams have also been performed at MPQ [17]. Using this technique a normalized transverse emittance of 0.2 mm mrad was measured at 245 MeV electron beams.

3.2.2.2 *Bunch Duration Measurement*

The bunch duration of the LPA beam has recently been measured with fs resolution [18, 19]. Previous LPA bunch duration measurements based on electro-optic sampling techniques were limited in resolution to tens of fs [20]. One method for determining the bunch temporal profile relies on measuring the spectrum of coherent transition radiation (CTR) generated as the beam passed through a foil following the plasma. Analysis of the CTR spectrum (in the optical wavelength regime) generated by the electron beams (produced using colliding pulse injection, as described below) indicated a bunch duration of τ_b=1.4 fs (rms), with a peak current of I=4 kA [18].

LPA electron beam duration measurements have also been performed using an ultra-short optical probe [19]. In this single-shot, non-invasive, in-situ diagnostic, the azimuthal magnetic field generated by the beam was probed in the plasma using Faraday rotation. Here an ultra-short laser propagates orthogonal to the LPA electron beam propagation direction. The probe rays passing above and below the beam have their polarization rotated in opposite directions, and the beam duration is determined using time-resolved polarimetry. Using this technique the LPA beam (produced using self-trapping with a single laser pulse) duration was measured as τ_b=5.8 fs (FWHM) [19].

3.2.2.3 *Controlled Injection*

To control the LPA beam phase space characteristics, and potentially produce shorter bunches, research has focused on methods to provide detailed control of the injection of background plasma electrons into the plasma wave. Controlled injection is also critical to improve the shot-to-shot stability and tunability of the LPA beam parameters. One method to trigger injection into the plasma wave is to collide laser pulses in the plasma [21]. In this colliding pulse injection technique, two lasers overlap in space and time, generating a localized beat wave that imparts momentum to the plasma electrons and enables trapping in the plasma wave. This technique was experimentally realized at LOA [22], where stable beams with energy spreads as low as 1% (FWHM) have been produced [23].

Another promising method is to rely on plasma density tailoring, where a short (~mm), high (~10^{19} cm^{-3}) plasma density region to serve as a localized plasma injector, is followed by a long (~cm), low (~10^{18} cm^{-3}) plasma density region to serve as a dark-current-free accelerator stage [24]. This approach relies on locally slowing the plasma wave phase velocity to facilitate trapping of background plasma electrons. The wave phase velocity is controlled via the plasma density gradient [25] and the increasing laser intensity [26] (generated by the relativistic self-focusing produced in the high plasma density region). Using density tailoring to control injection into a subsequent plasma accelerator was experimentally realized at LBNL by integrating a gas jet into a discharge capillary. The electron trapping and energy gain was controlled by varying

the gas jet density and the laser focal position. This method of triggered injection produced greatly improved stability (percent-level) of the LPA beam properties [24].

3.2.2.4 *Beam Brightness*

With the recent measurements of the LPA beam characteristics described above, the six-dimensional (6D) beam brightness of the LPA electron beam can be estimated. The 6D beam brightness may be defined as

$$B_{6\mathrm{D}} = \frac{N}{\varepsilon_{nx}\varepsilon_{ny}\varepsilon_{nz}} \cong \frac{I/I_A}{r_e\varepsilon_n^2\sigma_\gamma} = b\lambda_C^{-3}, \qquad (2)$$

where I is the peak current, N the number of beam electrons, $m_ec^2\sigma_\gamma$ the beam energy spread, and ε_{nz}, ε_{nx}, and ε_{ny} the normalized longitudinal and transverse emittances. Here $I_A=m_ec^3/e$ is the Alfven current, $r_e= e^2/ m_ec^2$ is the classical electron radius, and λ_C the Compton wavelength. For an LPA with typical beam parameters (e.g., 0.5 GeV energy, I=4 kA peak current, ε_n=0.1 mm mrad normalized transverse emittance, and σ_γ/γ = 0.04 relative energy spread) the normalized 6D brightness is $b\sim10^{-11}$. This 6D brightness is comparable to conventional accelerators. For example, the LCLS beam at SLAC, with 13.6 GeV, I=3.4 kA, σ_γ/γ =10^{-4}, and ε_n=0.4 mm mrad, has a normalized 6D brightness of $b\sim10^{-11}$. Therefore, one may consider emittance exchange or beam phase space manipulation to enable application of LPA beams. For example, although the relative energy spread of the LPA beam presently hinders application to free-electron lasers, post-LPA beam manipulation may provide a path toward lasing [5, 6].

3.2.3 **Conclusions**

Laser-plasma accelerators are presently able to compactly generate GeV-class electron beams, accelerated over cm-scale plasmas, using 100 TW-class short pulse laser systems (operating at 1-10 Hz). These beams typically contain tens of pC of charge, few percent-level relative energy spread, and mrad divergences. Recent measurements have shown that LPA beams have low transverse emittance (~0.1 mm mrad) and have few-fs bunch durations. The fs electron beams have multi-kA peak current and are therefore well-suited as drivers for high-peak brightness radiation generation for ultrafast science. These fs beams are also intrinsically synchronized to the drive laser pulse, enabling a wide variation of pump-probe applications. Controlled injection techniques are actively being researched to improve the LPA beam quality and reproducibility. In parallel to LPA research, laser technology is undergoing rapid development, and it is anticipated that ~1 J, short-pulse laser systems operating at kHz repetition rates will become available in the next several years. If LPA research and development continues to be successful, LPAs will enable the generation of ultra-compact, multi-GeV, fs beams for the next generation of ultrafast light sources.

3.2.4 **References**

1. E. Esarey, C. B. Schroeder, and W. P. Leemans, “Physics of laser-driven plasma-based electron accelerators”, Rev. Mod. Phys. 81, 1229 (2009).
2. C. B. Schroeder, W. M. Fawley, F. Grüner, M. Bakeman, K. Nakamura, K. E. Robinson, Cs. Toth, E. Esarey, and W. P. Leemans, “Free-electron laser driven by the

LBNL laser-plasma accelerator", proceedings of the 2008 *Advanced Accelerator Concepts Workshop*, Santa Cruz, CA (2008).

3. F. Grüner, S. Becker, U. Schramm, T. Eichner, M. Fuchs, R. Weingartner, D. Habs, J. Meyer-ter-Vehn, M. Geissler, M. Ferrario, L. Serafini, B. van der Geer, H. Backe, W. Lauth, and S. Reiche, "Design considerations for table-top, laser-based VUV and X-ray free electron lasers", *Appl. Phys*. B **86**, 431 (2007).
4. C. B. Schroeder, W. M. Fawley, F. Grüner, M. Bakeman, K. Nakamura, K. E. Robinson, Cs. Toth, E. Esarey, and W. P. Leemans, "Free-electron laser driven by the LBNL laser-plasma accelerator", proceedings of the 2008 *Advanced Accelerator Concepts Workshop*, Santa Cruz, CA (2008).
5. A. R. Maier, A. Meseck, S. Reiche, C. B. Schroeder, T. Seggebrock, and F. Grüner", "Demonstration scheme for a laser-plasma-driven free-electron laser", *Phys. Rev. X*, **2**, 031019 (2012).
6. Z. Huang, Y. Ding, and C. B. Schroeder, "Compact x-ray free electron laser from a laser-plasma accelerator using transverse gradient undulator", *Phys. Rev. Lett*., **109**, 204801 (2012).
7. C.B. Schroeder, E. Esarey, C.G.R. Geddes, C. Benedetti, and W.P. Leemans, "Physics considerations for laser-plasma linear colliders " *Phys. Rev. ST Accel. Beams* **13**, 101301 (2010).
8. H.-P. Schlenvoigt, K. Haupt, A. Debus, F. Budde, O. Jäckel, S. Pfotenhauer, H. Schwoerer, E. Rohwer, J. G. Gallacher, E. Brunetti, R. P. Shanks, S. M. Wiggins, and D. A. Jaroszynski, "A compact synchrotron radiation source driven by a laser-plasma wakefield accelerator", *Nature Phys*. **4**, 130 (2008).
9. M. Fuchs, R. Weingartner, A. Popp, Zs. Major, S. Becker, J. Osterhoff, I. Cortrie, R. Hörlein, G. D. Tsakiris, U. Schramm, T. P. Rowlands-Rees, S. M. Hooker, D. Habs, F. Krausz, S. Karsch, and F. Grüner, "Laser-driven soft-x-ray undulator source", *Nature Phys*. **5**, 826 (2009).
10. W.P. Leemans, B. Nagler, A. J. Gonsalves, C. Toth, K. Nakamura, C. G. R. Geddes, E. Esarey, C. B. Schroeder, and S. M. Hooker, "GeV electron beams from a centimetre-scale accelerator", *Nature Physics* **2**, 696 (2006).
11. S. Kneip, S. R. Nagel, S. F. Martins, S. P. D. Mangles, C. Bellei, O. Chekhlov, R. Clarke, N. Delerue, E. J. Divall, G. Doucas, K. Ertel, F. Fiuza, R. Fonseca, P. Foster, S. Hawkes, C. Hooker, K. Krushelnick, W. B. Mori, C. Palmer, K. T. Phuoc, P. P. Rajeev, J. Schreiber, M. Streeter, D. Urner, J. Vieira, L. O. Silva, and Z. Najmudin, "Near-GeV acceleration of electrons by a nonlinear plasma wave driven by a self-guided laser pulse", *Phys. Rev. Lett*. **103**, 035002 (2009).
12. J. S. Liu, C. Q. Xia, W. T. Wang, H. Y. Lu, C. Wang, A. H. Deng, W. T. Li, H. Zhang, X. Y. Liang, Y. X. Leng, X. M. Lu, C. Wang, J. Z. Wang, K. Nakajima, R. X. Li, and Z. Z. Xu, "All-optical cascaded laser wakefield accelerator using ionization-induced injection", *Phys. Rev. Lett*. **107**, 035001 (2011).
13. E. Esarey, B. A. Shadwick, P. Catravas, and W. P. Leemans, "Synchrotron radiation from electron beams in plasma-focusing channels", *Phys. Rev.* E, **65**, 056505 (2002).
14. G. R. Plateau, C. G. R. Geddes, D. B. Thorn, M. Chen, C. Benedetti, E. Esarey, A. J. Gonsalves, N. H. Matlis, K. Nakamura, C. B. Schroeder, S. Shiraishi, T. Sokollik, J. van Tilborg, Cs. Toth, S. Trotsenko, T. S. Kim, M. Battaglia, T. Stöhlker, and W. P. Leemans, "Ultra-low-emittance electron bunches from a laser-plasma accelerator measured using single-shot x-ray spectroscopy", *Phys. Rev. Lett*. **109**, 064802 (2012).
15. M. Schnell, A. Sävert, B. Landgraf, M. Reuter, M. Nicolai, O. Jäckel, C. Peth, T. Thiele, O. Jansen, A. Pukhov, O. Willi, M. C. Kaluza, and C. Spielmann, "Deducing the electron-beam diameter in a laser-plasma accelerator using x-ray betatron radiation", *Phys. Rev. Lett*. **108**, 075001 (2012).
16. S. Kneip, C. McGuffey, J. L. Martins, M. S. Bloom, V. Chvykov, F. Dollar, R. Fonseca, S. Jolly, G. Kalintchenko, K. Krushelnick, A. Maksimchuk, S. P. D. Mangles, Z.

Najmudin, C. A. J. Palmer, K. T. Phuoc, W. Schumaker, L. O. Silva, J. Vieira, V. Yanovsky, and A. G. R. Thomas, "Characterization of transverse beam emittance of electrons from a laser-plasma wakefield accelerator in the bubble regime using betatron x-ray radiation", *Phys. Rev. ST Accel. Beams* **15**, 021302 (2012).
17. R. Weingartner, S. Raith, A. Popp, S. Chou, J. Wenz, K. Khrennikov, M. Heigoldt, A. R. Maier, N. Kajumba, M. Fuchs, B. Zeitler, F. Krausz, S. Karsch, and F. Grüner, "Ultralow emittance electron beams from a laser-wakefield accelerator", *Phys. Rev. ST Accel. Beams* **15**, 111302 (2012).
18. O. Lundh, J. Lim, C. Rechatin, L. Ammoura, A. Ben-Ismail, X. Davoine, G. Gallot, J. Goddet, E. Lefebvre, V. Malka, and J. Faure, "Few femtosecond, few kiloampere electron bunch produced by a laser–plasma accelerator", *Nature Phys*. **7**, 219 (2011).
19. A. Buck, M. Nicolai, K. Schmid, C. M. S. Sears, A. Sävert, J. M. Mikhailova, F. Krausz, M. C. Kaluza, and L. Veisz, "Real-time observation of laser-driven electron acceleration", *Nature Phys*. **7**, 543 (2011).
20. J. van Tilborg, C. B. Schroeder, C. V. Filip, Cs. Toth, C. G. R. Geddes, G. Fubiani, R. Huber, R. A. Kaindl, E. Esarey, and W. P. Leemans, "Temporal characterization of femtosecond laser-plasma-accelerated electron bunches using terahertz radiation", *Phys. Rev. Lett*. **96**, 014801 (2006).
21. E. Esarey, R. F. Hubbard, W. P. Leemans, A. Ting, and P. Sprangle, "Electron injection into plasma wake fields by colliding laser pulses", *Phys. Rev. Lett*. **79**, 2682 (1997).
22. J. Faure, C. Rechatin, A. Norlin, A. Lifschitz, Y. Glinec, and V. Malka. "Controlled injection and acceleration of electrons in plasma wakefields by colliding laser pulses", *Nature* **444**, 737 (2006).
23. C. Rechatin, J. Faure, A. Ben-Ismail, J. Lim, R. Fitour, A. Specka, H. Videau, A. Tafzi, F. Burgy, and V. Malka, "Controlling the phase-space volume of injected electrons in a laser-plasma accelerator", *Phys. Rev. Lett*. **102**, 164801, (2009).
24. A. J. Gonsalves, K. Nakamura, C. Lin, D. Panasenko, S. Shiraishi, T. Sokollik, C. Benedetti, C. B. Schroeder, C. G. R. Geddes, J. van Tilborg, J. Osterhoff, E. Esarey, C. Toth, and W. P. Leemans, "Tunable laser plasma accelerator based on longitudinal density tailoring", *Nature Phys*. **7**, 862 (2011).
25. S. Bulanov, N. Naumova, F. Pegoraro, and J. Sakai, "Particle injection into the wave acceleration phase due to nonlinear wake wave breaking", *Phys. Rev. E*, **58**, R5257 (1998).
26. C. B. Schroeder, C. Benedetti, E. Esarey, and W. P. Leemans, "Nonlinear pulse propagation and phase velocity of laser-driven plasma waves", *Phys. Rev. Lett*. **106**, 135002 (2011).

3.3 Creating Attosecond Structures in Femtosecond Beams

Dao Xiang, SLAC National Accelerator Laboratory, USA
Mail to: dxiang@SLAC. Stanford.edu

3.3.1 Introduction

Generation of microstructures in relativistic electron beams with varying periods ranging from millimeters to Ångstroms is of fundamental interest in accelerator physics. An x-ray free-electron laser (FEL) is an example where the electrons are packed into micro-bunches with equal spacing in the x-ray wavelength range from the sustained electron-radiation interaction in a long undulator [1-3]. This density modulation allows the electrons to radiate in phase which leads to orders of magnitude enhancement in the

radiation power compared to the spontaneous radiation, making FELs unique in providing tunable high-power short-wavelength radiation for various areas of science.

For structures well above the optical wavelength, the drive laser as required in a photocathode rf gun may be shaped accordingly to generate the desired pattern in beam current distribution, taking advantage of the promptness of the photoemission process [4-6]. It is also possible to use a transverse mask to generate fine structures in beam transverse distribution, and then use emittance exchange technique to convert the spatial structures into time structures [7-8]. However, it is technically challenging to extend these techniques for generation of attosecond structures in electron beams.

In this article we describe the techniques to create attosecond structures ranging from a few nanometer (nm) to a few hundred nm in femtosecond beams. These techniques typically involve using lasers, undulators and chicanes: lasers and undulators allow one to imprint short-scale energy modulation (sinusoidal energy chirp); and chicanes force the particles to follow energy-dependent paths such that particle's longitudinal positions can be rearranged. We will show how one can create attosecond structures with various patterns in femosecond beams and how these fine structures can enhance the performance of electron beam based facilities.

3.3.2 **Concept of Introducing Micro-Structures with Lasers**

Creating short-scale structures in an electron beam with lasers is analogous to the overall manipulation of electron bunch length in a magnetic bunch compressor, except that the energy chirp is imprinted by lasers rather than rf cavities.

The process of bunch compression, to the first order, can be described as a linear transformation where the bunch length is reduced while the energy spread (conservation of phase space area) and peak current (conservation of charge) are increased. This is achieved by first accelerating the beam off-crest in rf cavities to establish a correlation between a particle's energy and its longitudinal position, and then sending the beam through a dispersive chicane. The particles with lower energy are bent more in the chicane and they will have a longer path length. On the contrary, particles with higher energy have shorter path length because they are bent less. As a result, the low energy electrons slip back while the high energy electrons catch up, which leads to bunch compression.

Replacing the rf cavity with lasers allow one to create local fine structure in an electron beam while keeping the overall beam shape unchanged. Since the laser wavelength is typically much shorter than the beam duration, on average the laser does not give beam a net energy chirp. As a result, the overall bunch duration is kept constant. On the other hand, the time-varying laser field imprints a sinusoidal energy chirp (called energy modulation) on the beam phase space which leads to varying local compression/decompression in the beam current that eventually results in attosecond structures in beam current distribution.

3.3.3 **Single Modulator-Chicane System**

The scheme to create attosecond structure in an electron beam via a single modulator-chicane module is illustrated in Fig. 1.

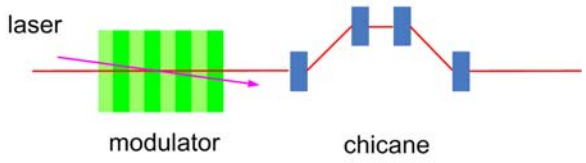

Figure 1: Creating attosecond structure in beam with a single modulator-chicane module.

For an electron beam with uniform density distribution (this assumption is justified for the general case when beam duration is much larger than laser wavelength), its longitudinal phase space distribution can be written as $f_0(p) = N_0(2\pi)^{-1/2} e^{-p^2/2}$, where N_0 is the number of electrons per unit length, $p = (E - E_0)/\sigma_E$ is the energy deviation of a particle normalized to the intrinsic beam energy spread σ_E, and E_0 is the average beam energy. After interacting with a laser with wave number k in an undulator, the particle's energy changes to $p' = p + A\sin kz$, where $A = \Delta E/\sigma_E$ is the dimensionless energy modulation, and z is the longitudinal coordinate in the beam. The distribution function after the interaction with the laser becomes,

$$f_1(z,p) = N_0(2\pi)^{-1/2} \exp\left[-\left(p - A\sin kz\right)^2/2\right] \tag{1}$$

After passing through a chicane with momentum compaction R_{56}, a particle's longitudinal position changes to $z' = z + R_{56}p\sigma_E/E_0$ and yields the distribution function,

$$f_2(z,p) = N_0(2\pi)^{-1/2} \exp\left[-\frac{1}{2}\left[p - A\sin(kz - pR_{56}k\sigma_E/E_0)\right]^2\right] \tag{2}$$

Integration of Eq. (2) over p gives the beam density N as a function of z, $N(z) = \int_{-\infty}^{\infty} dp f_2(z,p)$. Analysis shows the beam density distribution can be expanded into Fourier series

$$N(z) = N_0\left[1 + \sum_{n=1}^{\infty} 2b_n \cos\left(nkz + \varphi_n\right)\right] \tag{3}$$

where $b_n = \left|\left\langle e^{-inkz} N(z)\right\rangle\right| / N_0$ is the bunching factor used to characterize the density modulation, n is the harmonic number, and the brackets denote averaging over the coordinate z. In general, after the laser modulation and a further passage through a chicane, a beam that initially has constant density now consists of many bumps equally separated by the laser wavelength (creation of optical micro-bunches). The bunching factor has an analytical form [9],

$$b_n = \left|J_n(nkR_{56}\Delta E/E_0)\right| \exp\left[-\frac{1}{2}\left(nkR_{56}\sigma_E/E_0\right)^2\right] \tag{4}$$

By properly choosing the energy modulation amplitude to match the chicane momentum compaction, the bunching factor at a specific harmonic number may be either maximized or minimized. For instance, at a high harmonic number (large n), the bunching factor is maximized when $kR_{56}\Delta E / E_0 \approx 1$. The phase space evolution in this scenario is illustrated in Fig. 2. A laser first interacts with the beam in an undulator to generate sinusoidal energy modulation (Fig. 2b); After passing through a small chicane, half of the particles that have negative energy chirp (blue particles in Fig. 2b and Fig. 2c) are fully compressed, while the other half that have positive energy chirp (red particles in Fig. 2b and Fig. 2c) are decompressed. As a result of this transformation, energy modulation is effectively converted into density modulation to create optical micro-bunches (see Fig. 2d, now the beam density consists of many bumps equally separated by the laser wavelength) that contain frequency components at both the laser fundamental frequency and harmonic frequency.

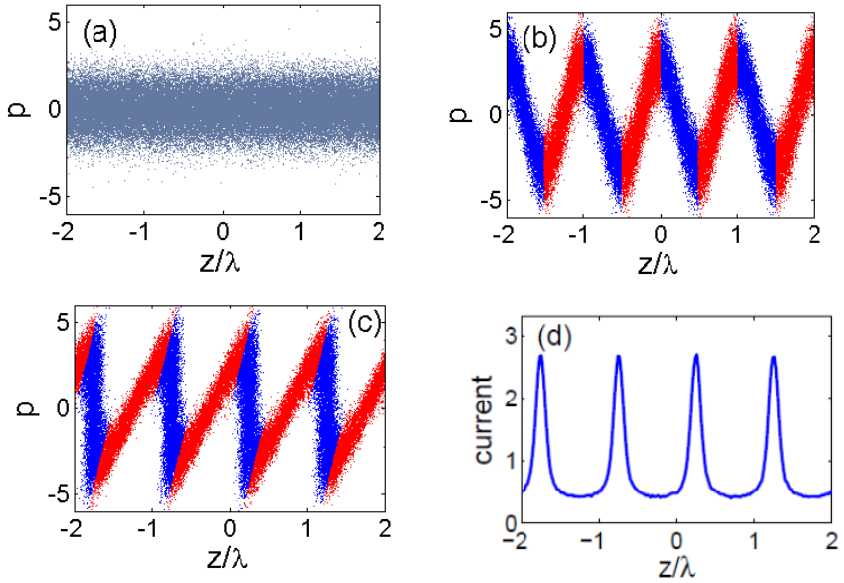

Figure 2: Beam longitudinal phase space before laser modulation (a); after laser modulation (b); after the chicane (c); final current distribution (d). The horizontal axis is the beam longitudinal position normalized to the laser wavelength and the vertical axis is particle's energy deviation with respect to the reference particle normalized to the rms slice energy spread of the beam.

As stated earlier, one can vary the energy modulation and chicane momentum compaction to tune the frequency components of the optical micro-bunches. Let's consider a beam with energy $E = 120$ MeV and slice energy spread $\sigma_E = 5$ keV; the wavelength of the laser is assumed to be $\lambda = 800\,\text{nm}$ and the momentum compaction of the chicane is $R_{56} = 1.30\,\text{mm}$. Following Eq. (4), the bunching at the 5th harmonic is maximized when $kR_{56}\Delta E / E_0 \approx 1.28$ (corresponding to $\Delta E \approx 15$ keV). In this scenario the bunching at the 5th harmonic is about 4%, significantly larger than the shot noise bunching (about $1/\sqrt{N}$, where N is the number of particles per wavelength) without laser modulation. Sending this density modulated beam through a long radiator tuned at the harmonic frequency allows generation of fully coherent radiation at the laser harmonics. This classical FEL seeding technique is called high-gain harmonic

generation (HGHG) [9] and has been experimentally demonstrated in several laboratories [10-13].

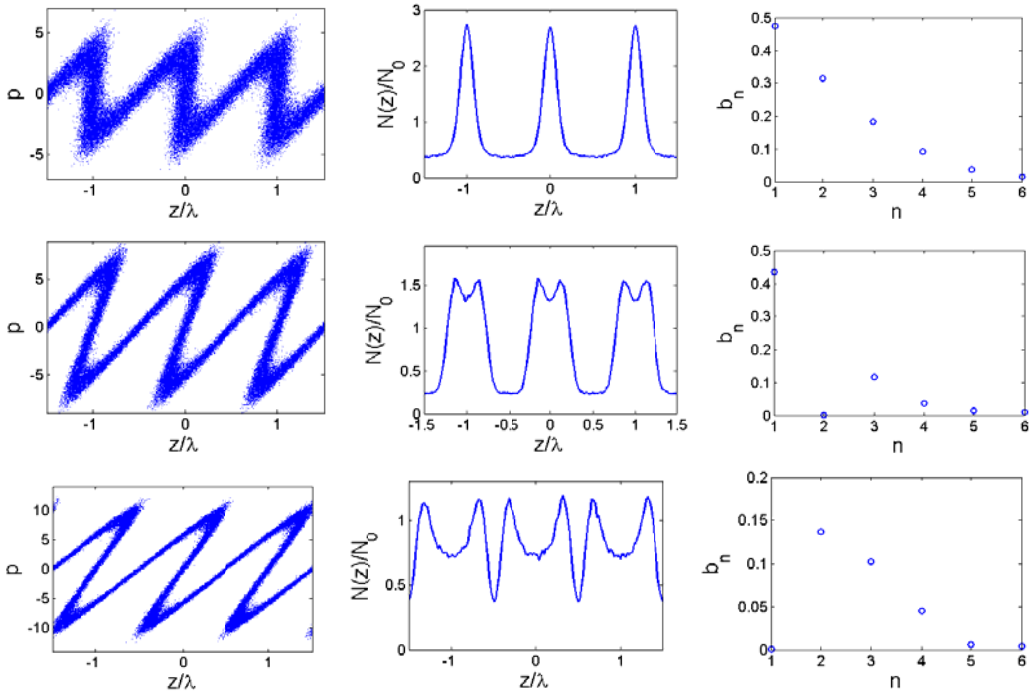

Figure 3: Longitudinal phase space (left column), beam current (middle column) and bunching factors (right column) for $\Delta E \approx 15$ keV (top row, for maximizing high harmonic bunching), $\Delta E \approx 30$ keV (middle row, for suppressing the 2nd harmonic bunching) and $\Delta E \approx 45$ keV (bottom row, for suppressing the fundamental bunching).

Slightly increasing the laser energy modulation to $\Delta E \approx 30$ keV makes $kR_{56}\Delta E / E_0 \approx 2.57$, which minimizes the bunching at the 2nd harmonic, as shown in the middle row of Fig. 3. Similarly, increasing energy modulation to $\Delta E \approx 45$ keV (corresponding to $kR_{56}\Delta E / E_0 \approx 3.83$) would suppress the bunching at the laser frequency (bottom row in Fig. 3). These exotic distributions with well-defined harmonic contents fully suppressed may be useful in specific applications. For instance, the current distribution in the middle row of Fig. 3 resembles a square wave. Sending this beam through an optical transition radiation (OTR) screen may generate radiation with instantaneous field taking a square wave form. In contrast, the conventional method to synthesize a square wave at optical wavelength involves using several lasers at different frequencies [14]. Here by creating attosecond structures with a single modulator-chicane system, an approximate square wave is produced.

As shown in the middle column in Fig. 3, by changing laser energy modulation and chicane momentum compaction, one can generate fine structures with various patterns in an electron beam to meet the demands of specific applications. It is interesting to note that the finest structure that can be created is roughly $R_{56}\sigma_E / E_0$, determined by intrinsic energy spread and chicane momentum compaction, regardless of the energy modulation amplitudes.

For generation of high harmonic bunching, the chicane momentum compaction, however, is closely connected with the energy modulation amplitude. This is because a

local full compression is required to stand the beam upright, which requires the energy modulation to match the chicane momentum compaction, i.e. $kR_{56}\Delta E / E_0 \approx 1$. In this case the finest structure has an approximate rms duration of $\lambda\sigma_E / \Delta E$, and the highest harmonic number is roughly the ratio of energy modulation to energy spread, i.e. $n \approx \Delta E / \sigma_E$. This relatively low frequency up-conversion efficiency makes it difficult to use HGHG technique in a single stage to generate harmonic with $n > 10$, because a large energy modulation as required to generate high harmonics is associated with a substantial growth in beam energy spread that may significantly degrade the beam quality. As a result, multiple stages of HGHG FELs are needed [15] in order to generate coherent x-rays from a UV laser ($n \approx 50$).

Note, by creating periodic fine structures in a femtosecond beam, the beam can emit coherent radiation at the laser fundamental frequency and the high harmonic frequencies. While the latter allows FEL seeding to up-convert the seed laser frequency to generate coherent radiation at shorter wavelengths, the coherent radiation at the laser fundamental frequency may offer new opportunity to determine electron bunch length. For instance, one can first modulate an ultrashort beam with an optical laser, and then send the density-modulated beam through an OTR screen to generate COTR. The spectrum of the COTR can be measured to infer the bunch length [16].

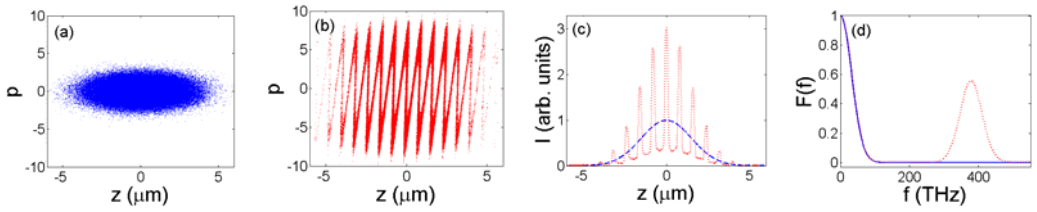

Figure 4: Initial beam phase space (a); Beam phase space after interaction with an optical laser (b); Beam current with (red) and without (blue) laser modulation (c); corresponding radiation power spectrum (d).

The idea to extract bunch length information by measuring the COTR spectrum is rather simple. For a Gaussian beam with rms length Δt, it is well known that its Fourier transform is also Gaussian with rms frequency spread Δf, and furthermore we have $\Delta t \times \Delta f = 1/2\pi$. Consider a Gaussian beam with rms length of 5 fs, its longitudinal phase space is shown in Fig. 4a. After interaction with a 795 nm laser and further passing through a chicane, the beam longitudinal phase space evolves to that in Fig. 4b. The corresponding beam current is shown with red-dashed line in Fig. 4c (the initial beam current is shown with blue-dashed line). It is justified to assume a prompt response for generation of OTR, and the pulse shape of the COTR generated when beam further strikes an OTR screen will be a replica of that of the beam current distribution. Accordingly, the COTR spectrum generated by this modulated beam will carry information about the beam current distribution. The COTR spectrum for the beam in Fig. 4c is shown in Fig. 4d where one can see that the quasi-monochromatic COTR has a central frequency at f=377 THz (corresponding central wavelength is 795 nm) with an rms frequency spread of Δf=33 THz (corresponding transform limited rms pulse width is 5 fs, which is the same as that of the electron bunch).

This method can be considered as a simplified version of the 'optical replica' scheme [17]. It is easy to implement and does not require generation of high-power

radiation for frequency-resolved optical gating measurement, yet still allows the rms length of an ultrashort bunch to be obtained.

From Fig. 4c and Fig. 4d, one can see that by creating attosecond structures in a beam with a laser, the beam envelope is imprinted to the pulse shape of COTR and the rms bunch length can be obtained through measurement of the COTR spectrum. Note, the condition $\Delta t \times \Delta f = 1/2\pi$ only applies for a Gaussian beam. In realistic conditions, the beam may deviate from a Gaussian distribution.

To see if this method can be applied to more general cases, here we show the results for 3 representative distributions: Gaussian, asymmetric Gaussian and flat-top (Fig. 5a). The corresponding COTR spectra after interaction with the laser are shown in Fig. 5b where one can see that while the detailed spectra are different, the rms frequency spread around the central frequency still has the same value. This indicates that this method can be applied to more general cases. However, it should be noted that this method may yield inaccurate results if the beam temporal profile has a very complicated distribution.

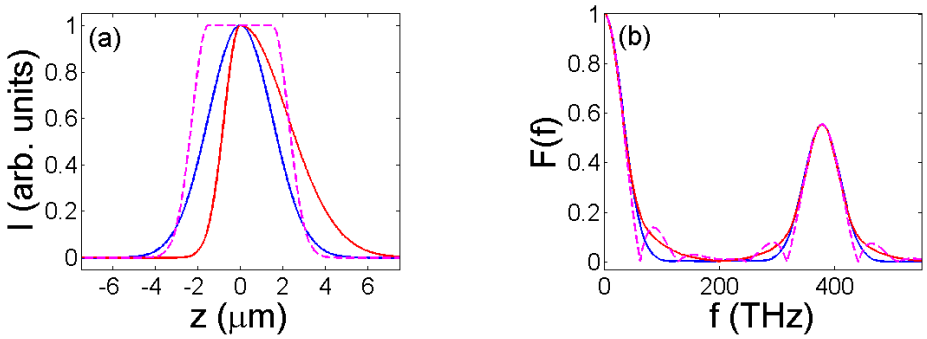

Figure 5: Various beam shapes (a) and the spectra after laser modulation (b).

3.3.4 **Double Modulator-Chicane System**

In this section we will extend our analysis to a slightly more complicated scheme with double modulator-chicane modules. We will show how cascading the modulator-chicane module offers new opportunity for creating more complicated attosecond structures in femtosecond beams.

The scheme is illustrated in Fig. 6. The beam distribution at the exit of the 2nd chicane can be easily found by applying consecutively two more transformations to Eq. (1) and (2), similar to the derivation outlined in section above. For general cases with lasers having wave number k_1 in the 1st modulator and k_2 in the 2nd modulator, the beam density contains harmonic contents at the wave number $hk_1 + mk_2$, where h and m are integers.

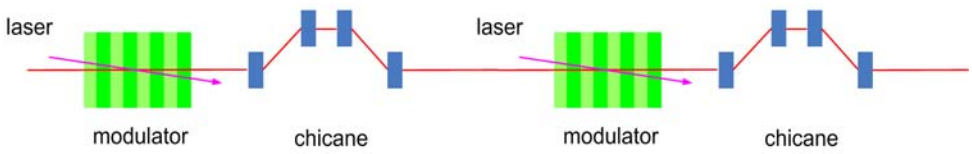

Figure 6: Double modulator-chicane modules to create attosecond structures in beams.

In general, there are 6 free parameters one can play with, i.e. laser modulation amplitudes, chicane momentum compactions, ratio of the laser wavelength and relative phase of the laser modulation. Therefore, depending on specific parameter sets, this double modulator-chicane module may work in several distinct modes.

3.3.4.1 *Reducing Beam Energy Spread in HGHG Technique*

As stated in last section, the main limitation of HGHG technique is that generation of high harmonics is typically associated with significant growth in beam energy spread that degrades FEL gain. With two modulators, the energy spread of the beam for a given harmonic bunching, however, may be reduced to some extent. For instance, in the proposed 'HGHG Silencer' scheme [18-19], a high power laser is first used to generate a large energy modulation in the 1st modulator; then as beam goes through the 2nd modulator, the energy modulation is gradually converted into density modulation with the R_{56} of the undulator; at the same time a laser with π phase shift is used in the 2nd modulator to compensate for the energy modulation in the 1st modulator. With this configuration, higher harmonics can be achieved with a reduced energy spread growth.

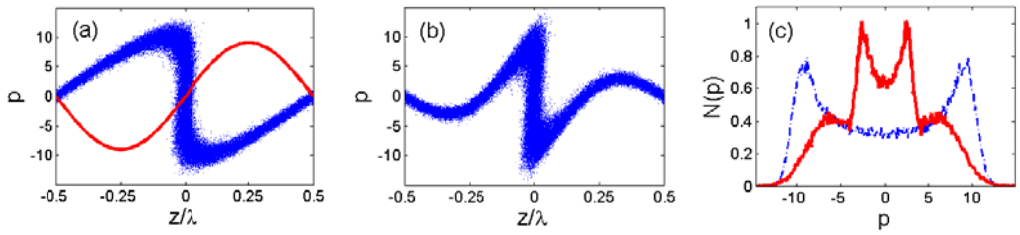

Figure 7: (a) Phase space after passing through the chicane (blue dots) and the corresponding energy modulation (red line) in a second modulator; (b) phase space after the reversed modulation in a second modulator; (c) energy distribution before (dashed blue) and after (slid red) the reverse modulation .

An alternative way to reduce the energy spread in HGHG scheme is to partially reverse the modulation in a second modulator after the beam goes through the chicane [20]. The idea is illustrated in Fig. 7. In this example, the energy modulation is 10 times larger than beam energy spread. After passing through a small chicane, half of the particles stand up to provide about 15% bunching at the 10th harmonic, as shown in Fig. 7a. A laser with π phase shift is then used in the 2nd modulator to provide a proper modulation (red line in Fig. 7a) to reduce the energy spread for the un-bunched particles, which leads to the phase space distribution shown in Fig. 7b. The histogram of the energy of the particles before and after this modulation is shown in Fig. 7c where one can clearly see that the beam energy spread is reduced (by about 40% in this example).

HGHG with two modulators to reduce beam energy spread may extend the harmonic number to $n > 10$, yet still not high enough to reach x-rays from UV laser in a single stage. This is mainly limited by the fact that the bunched particles are at the zero-crossing of the laser (see Fig. 7a) and their energy spread cannot be reduced.

3.3.4.2 *Echo-Enabled Harmonic Generation (EEHG)*

A quite different technique entitled EEHG has recently been proposed to reach soft x-rays from UV seed laser in a single stage [21-22]. This is made possible by the remarkable frequency up-conversion efficiency of EEHG. In the EEHG scheme, the beam is first energy modulated by a laser in the first modulator (Fig. 8a) and then sent through a chicane with strong momentum compaction after which the modulation obtained in the first modulator is macroscopically smeared; simultaneously, complicated fine structures are introduced into the phase space of the beam (Fig. 8b). A second laser is used to further modulate the beam energy in the second modulator (Fig. 8c) to imprint certain correlations in phase space, and after passing through a second chicane the high harmonic signal then occurs as a recoherence effect, like an echo (Fig. 8d). The key advantage of echo technique is that it can generate very high harmonics with harmonic number much larger than the ratio of energy modulation to energy spread, i.e. $n >> \Delta E / \sigma_E$. This makes it possible to generate very high harmonics (50~100) while simultaneously keeping the beam energy spread small, which allows the generation of soft x-rays from a UV seed laser in a single stage. EEHG technique has been demonstrated at SLAC's Next Linear Collider Test Accelerator (NLCTA) [23-24] and SINAP's Shanghai DUV FEL facility [25].

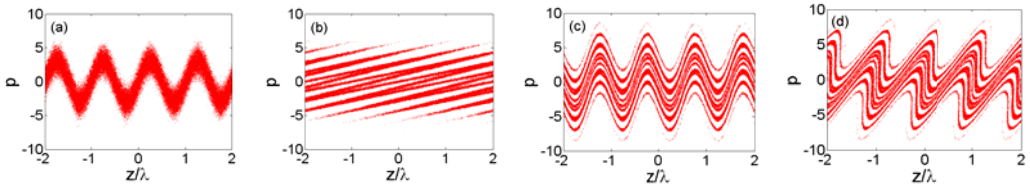

Figure 8: Evolution of the longitudinal phase space in EEHG scheme. (a) after the first modulator; (b) after the first chicane; (c) after the second modulator; (d) after the second chicane. In this example, the two lasers have the same wavelengths.

3.3.4.3 *Difference Frequency Generation for THz Emission*

In EEHG scheme, a small h and a large m is used to maximize the bunching at high harmonics. Alternatively, by choosing small h and m with opposite signs, the double modulator-chicane system may be used to down-convert the frequency of optical lasers for generation of THz structures in electron beams. For instance, with $h = 1$ and $m = -1$ (or vice versa), a density modulation at the difference frequency of the two lasers can be generated. This allows the generation of long-scale density modulations in electron beams through short-scale energy modulations [26]. This difference frequency generation scheme with relativistic electron beam as the nonlinear medium is illustrated in Fig. 9. As shown in Fig. 9a, a laser with wavelength λ_1 is first used to generate energy modulation in the beam phase space in the first modulator. After interacting with the second laser with wavelength $\lambda_2 = 0.9\lambda_1$, the beam phase space consists of fast modulation at the sum frequency and a slow modulation at the difference frequency (Fig. 9b). After passing through a chicane, the energy modulation at the difference frequency can be converted to density modulation (Fig. 9c and Fig. 9d). As a result, the beam current has density modulation with a period of about $10\lambda_1$.

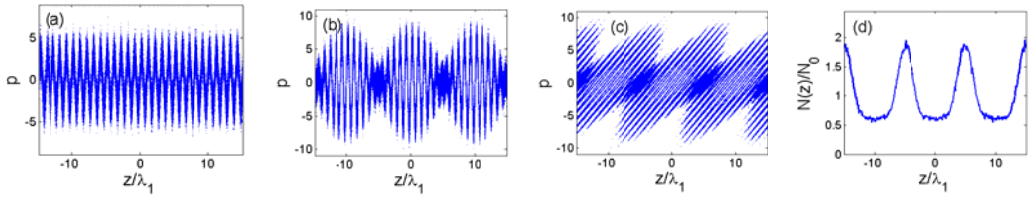

Figure 9: Evolution of the longitudinal phase space in difference frequency generation with double modulator-chicane system. (a) after the first modulator; (b) after the second modulator; (c) after the second chicane; (d) final current distribution. In this example, the momentum compaction of the first chicane is set to zero.

Once the density modulation is formed, it is then straightforward to send the beam through a bending magnet or OTR screen to generate coherent narrow-band THz radiation. Very recently, this technique has been demonstrated at SLAC's NLCTA where density modulation around 10 THz was generated by down-converting the frequencies of an 800 nm laser and a 1550 nm laser [27]. One of the many advantages of this technique is the flexibility it offers to tune the central frequency of the modulation, which can be achieved through tuning of laser wavelengths, beam energy chirp, and chicane momentum compaction. In principle, this allows one to generate coherent narrow-band THz radiation covering the whole THz range.

3.3.4.4 *Optical Waveform Synthesis*

Following Eq. (4), the maximal bunching factor that can be generated in a single modulator-chicane system is about 58% for $n=1$ and the bunching factors at high harmonics scale as $b_n \approx n^{-1/3}$ even with infinitely large energy modulation amplitude. A simple picture to explain the maximal bunching is that the sinusoidal modulation gives beam both positive and negative chirp, and as a result only half of the particles can be packed into a narrow region which limits the maximal bunching to about 50%. The sinusoidal modulation $\sin x = x - x^3/6 + \mathrm{O}(x^5)$, which deviates from a linear modulation x with dominant term x^3, is the cause for the $n^{-1/3}$ scaling at high harmonics [28]. With a double modulator-chicane system, one has more freedom to tailor the pattern of the modulation, therefore the bunching factors for either the fundamental wavelength, or the high harmonics, can be increased [29-30].

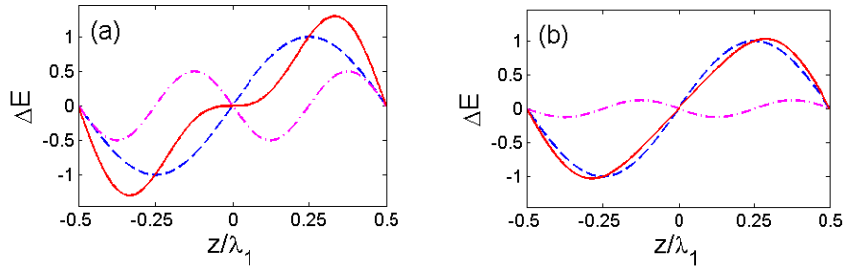

Figure 10: Energy modulation from a laser with wavelength λ_1 (dashed blue), from a laser with wavelength $\lambda_2 = 0.5\lambda_1$ (dashed magenta), and a combination of the two modulations (solid red).

Figure 10 shows how one can combine the modulation from a laser and its 2nd harmonic to increase the bunching at the fundamental frequency (Fig. 10a) and high harmonics (Fig. 10b). In Fig. 10a, the laser's second harmonic is used to give beam a sawtooth-like modulation, following the Fourier series of sawtooth function i.e. $\sin(x)-0.5\sin(2x)$. This increases b_1 to about 74%. In Fig. 10b, the laser's second harmonic is used to linearize the modulation at zero-crossing to compensate for the nonlinear energy chirp, i.e. $\sin(x)-\sin(2x)/8$. By cancellation of the x^3 term, a new scaling for high harmonic bunching as $b_n \approx n^{-1/5}$ is achieved. This leads to slower decaying of the bunching factor at high harmonics.

In addition to synthesizing a sawtooth modulation, one can also vary the phase and amplitude of the modulation from the second harmonic to form a square wave, triangular wave, etc. It is also possible to use two lasers with the same wavelength to realize this kind of manipulations [31]. Since it is obvious that adding more harmonics would yield a distribution closer to the ideal sawtooth (or square wave, triangular wave) distribution, we will discuss this synthesis technique in more detail in next section where triple modulator-chicane system will be studied.

3.3.5 **Triple Modulator-Chicane System and Beyond**

Now we proceed to analyze a triple modulator-chicane system. Here we will study a more general scheme in which the sign of the momentum compaction of each chicane can be varied with integrated quadrupoles. This scheme is illustrated in Fig. 11 where the green diamonds represent quadrupole magnets.

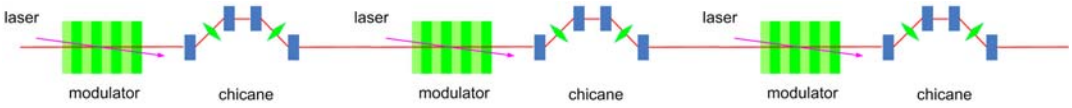

Figure 11: Triple modulator-chicane modules to create attosecond structures in beams.

The beam distribution at the exit of the 3rd chicane can be similarly found by applying consecutively four more transformations to Eq. (1) and (2). For general cases with lasers having wave number k_1, k_2 and k_3 in the 1st, 2nd and 3rd modulators, the beam density contains harmonic contents at the wave number $hk_1+mk_2+lk_3$, where h, m and l are integers. Because now there are 12 free parameters that one can play with, i.e. laser modulation wavelengths, amplitudes, phases and chicane momentum compactions, this triple modulator-chicane system can be configured in numerous modes for many different applications. Here we will briefly go through several of them.

First, we notice that by turning off the first and second chicanes, this scheme works as HGHG with 3 modulators. It is then straightforward to use the modulation at the 2nd and 3rd harmonic to tailor the modulation in the first modulator. For instance, by properly choosing the phase and amplitude of the modulation at the 2nd and 3rd harmonics, one can shape the energy modulation into $\sin(x)-0.5\sin(2x)+0.33\sin(3x)$ (following the Fourier series of sawthooth function), which will increase b_1 to about 80%. Alternatively, by shaping the energy modulation into

$\sin(x)-\sin(2x)/5+\sin(3x)/45$, the nonlinear term can be cancelled up to x^6, enabling a much better scaling of the high harmonic bunching as $b_n \approx n^{-1/7}$ [29].

In fact, inclusion of all the chicanes in the triple modulator-chicane system can produce an even higher bunching exceeding 90% at the fundamental frequency. In this scheme, the lasers have the same wavelength in the three modulators. Furthermore, the laser energy modulation increases in each modulator and accordingly R_{56} reduces in each chicane. The physics of this 'adiabatic buncher' [31] is illustrated in Fig. 12. Basically each chicane is used to rotate the local phase space so as to deposit the maximum number of particles into the phase region between peaks, i.e. $-0.25 < z/\lambda < 0.25$, after each modulation. The concept is similar to the pre-bunched enhanced EEHG scheme with a triple modulator-chicane system in [32], but is repeated in each section. By modulating the beam with increasing amplitudes, the required R_{56} for each chicane to bunch the beam is gradually reduced, which makes initially trapped particles remain trapped. Roughly speaking, in each section, only 42% of the untrapped particles remain untrapped. So with three modulator-chicane modules, the bunching factor at the fundamental frequency can be made to about 92%. This beam can then be injected into an optimized inverse FEL and efficiently accelerated to provide a high quality monoenergetic beam [33-35].

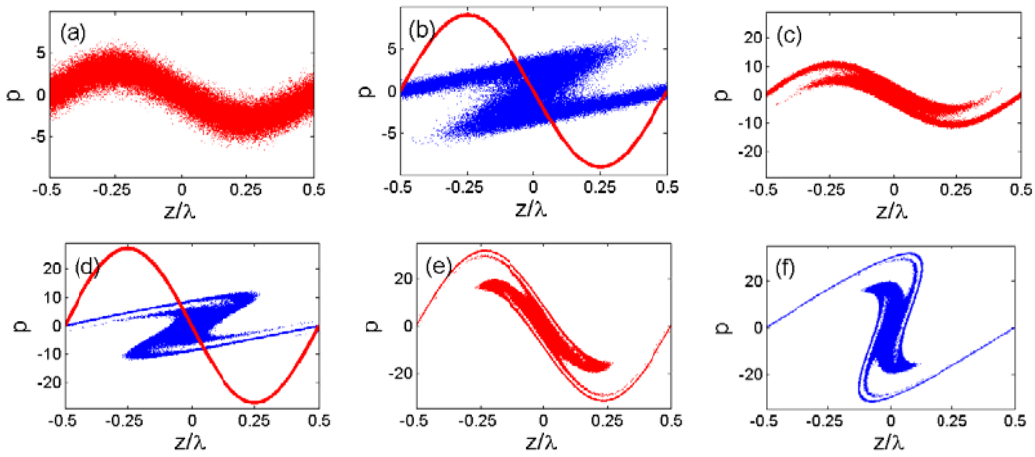

Figure 12: Beam phase space evolutions in 'adiabatic buncher' scheme. (a) after the 1st modulator; (b) after the 1st chicane (the modulation to be exerted in the 2nd modulator is shown with red line); (c) after the 2nd modulator; (d) after the 2nd chicane (the modulation to be exerted in the 3rd modulator is shown with red line); (e) after the 3rd modulator; (f) after the 3rd chicane.

For improving the high harmonic bunching in EEHG, the triple modulator-chicane system may be configured in different ways. One option is to use the first modulator-chicane to prebunch the beam and then use the rest of the components as standard EEHG [32]. One may also use the first two modulator-chicanes as the standard EEHG system, and then use the last modulator to linearize the modulation to improve the bunching. This scheme is called i-EEHG which stands for improved EEHG in [31]. A more exotic configuration that may even allow one to produce fully coherent hard x-rays has also been proposed [36]. In this scheme the 1st and 2nd chicanes have opposite R_{56}, and the 1st and 3rd lasers have the same wavelength with a π phase shift. To illustrate the physics behind this scheme, the evolution of the beam longitudinal phase space is shown in Fig. 13.

The beam phase space after interaction with the first laser is shown in Fig. 13a where the energy modulation is 3 times larger than the beam slice energy spread. Similar to the EEHG scheme, separated energy beamlets are generated (Fig. 13b) after the beam passes through the first chicane. After interaction with the second laser of which the energy modulation is 20 times smaller than beam slice energy spread, the beam phase space evolves to that in Fig. 13c. Because the energy modulation is much smaller than beam's initial energy spread, it is actually very difficult to see the difference between Fig. 13b and Fig. 13c. The second chicane with opposite momentum compaction restores the beam phase space to Fig. 13d which is similar to that in Fig. 13a. If no modulation is imposed in the 2nd modulator, the second chicane will restore beam phase space to the same distribution as that before the first chicane, because the transfer matrix from the exit of the 1st modulator to the exit of the 2nd chicane is unity. With a small energy modulation in the 2nd modulator, the second chicane will transform the beam phase space to a distribution similar to that before the first chicane with the presence of energy modulation from the 2nd modulator superimposed on the modulation from the 1st modulator (Fig. 13d). The laser in the 3rd modulator is chosen to give the beam the same modulation amplitude as that in the 1st modulator, but with π phase shift, so that the overall energy modulation in the 1st modulator is canceled in the 3rd

modulator. After the cancelation, the modulation from the 2nd modulator becomes dominant (Fig. 13e). A third chicane further converts the energy modulation into density modulation (Fig. 13f). With this configuration, the 22nd harmonic is generated with a modulation in the 2nd modulator that is 20 times smaller than beam slice energy spread and the final energy spread growth is only about 15%.

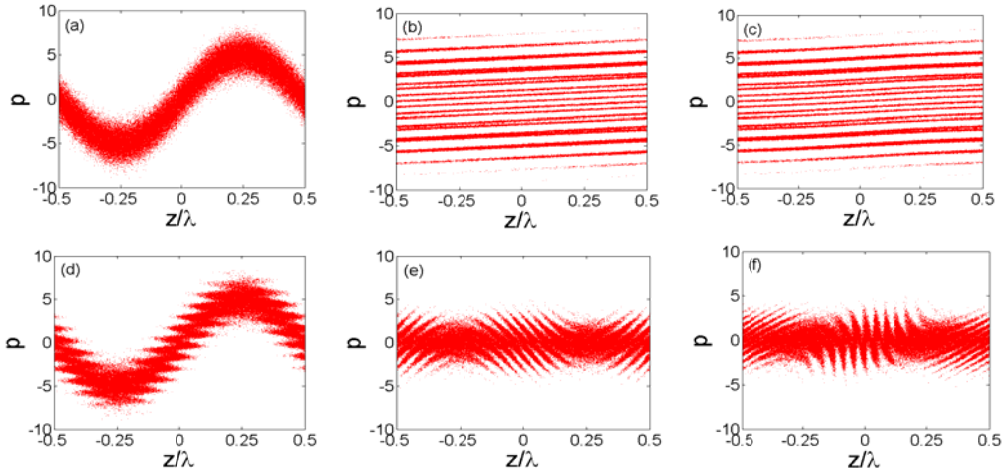

Figure 13: Beam phase space evolutions. (a) after the 1st modulator; (b) after the 1st chicane; (c) after the 2nd modulator; (d) after the 2nd chicane; (e) after the 3rd modulator; (f) after 3rd chicane.

The unique advantage of this scheme that only a small energy modulation is needed in the 2nd modulator and the 2nd chicane compresses the modulation imprinted in the 2nd modulator to shorter wavelength opens new opportunities for using low power high-order harmonic generation (HHG) source at short wavelength to seed x-ray FELs. As an example, in [36] the feasibility of generating significant bunching at 1 nm and below from a low power (~100 kW) HHG seed at 20 nm assisted by two moderate power (~100 MW) UV lasers at 200 nm while keeping the energy spread growth within 40% has been shown. The supreme up-frequency conversion efficiency together with its unique advantage in maintaining beam energy spread opens new opportunities for generating fully coherent x-rays at sub-nanometer wavelength from external seeds.

Another feature of triple modulator-chicane system is that it allows sequential piecewise manipulation of beam phase space at the optical scale. For instance, in [31] it has been shown that using only a single laser wavelength, the triple modulator-chicane scheme can act as a waveform synthesizer through linearization of local regions of phase space to generate sawtooth, triangular, and square wave-type distributions.

The idea of using cascaded modulator-chicane modules with lasers having the same wavelengths to synthesize waveforms is illustrated in Fig. 14. The energy modulation generated by a laser field creates a sinusoidal local chirp in the beam (Fig. 14a). Half of the particles have a positive chirp, whereas the other half has a negative chirp. After passage through a chicane, the region with a positive chirp becomes stretched, while the negatively chirped region is fully compressed (Fig. 14b). The decompressed region extending from $-1 < z/\lambda < 0$ forms a shape that approximates a sinusoid with twice the wavelength (red line in Fig. 14b). We see that through dispersion the original modulation at wavelength λ can now be shifted to 2λ. Similarly, with a smaller R_{56}, part of the beam can be compressed by a factor of 2, with the other half decompressed

by 50% (Fig. 14c). As a result, half of the modulation can be approximated by $\sin(2x)$ (dashed magenta in Fig. 14c) and the other half by $\sin(2x/3)$ (solid red in Fig. 14 c). With cascaded modulator-chicane modules, one can perform piecewise manipulation to the beam phase space to generate numerous patterns, e.g. forming sawtooth, triangular, and square wave, etc. The interested readers can find more details in [31].

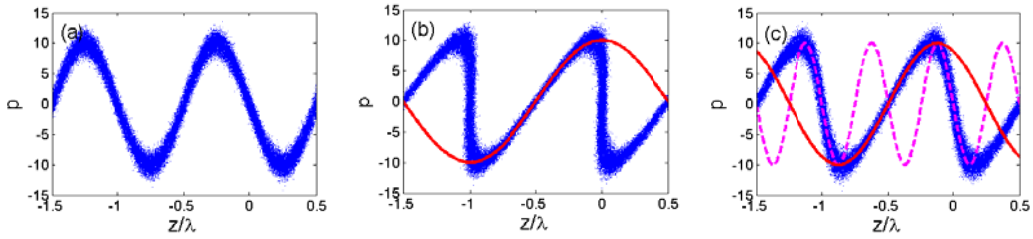

Figure 14: Effective local modulation wavelength shift through laser energy modulation and chicane. (a) phase space after a modulator; (b) after a chicane with R_{56} to fully compress part of the beam; (c) after a chicane with a smaller R_{56} to compress part of the beam by a factor of 2.

From discussions above, it is straightforward to extend the analysis to four and more modulator-chicane modules. However, it should be pointed out that while using even more modules is academically interesting, it may pose more technical challenges.

3.3.6 **Summary**

Generation of various kinds of attosecond structures in femtosecond beams is a new focus of accelerator R&D. In this article we described several techniques that use lasers, undulators and chicanes to create fine structures ranging from a few nm to a few hundred nm in electron beams. These techniques hold great promise to enhance the performance of accelerator based facilities, e.g. improving the temporal coherence in x-ray FELs, reducing the beam energy spread in inverse free electron lasers, etc.

The author would like to thank E. Hemsing and G. Stupakov for many collaborations and useful discussions. This work is supported by U.S. DOE under Contract No. DE-AC02-76SF00515.

3.3.7 **References**

1. W. Ackermann, G. Asova, V. Ayvazyan et al., “Operation of a free-electron laser from the extreme ultraviolet to the water window”, Nature Photon. 1, 336 (2007).
2. P. Emma, R. Akre, J. Arthur et al., “First lasing and operation of an ångstrom-wavelength free-electron laser”, Nature Photon. 4, 641 (2010).
3. T. Ishikawa, H. Aoyagi, T. Asaka et al., “A compact X-ray free-electron laser emitting in the sub-ångström region”, Nature Photon. 6, 540 (2012).
4. J. G. Neumann, R. B. Fiorito, P. G. O’Shea et al., “Terahertz laser modulation of electron beams”, J. Appl. Phys. 105, 053304 (2009).
5. P. Musumeci, R.K. Li and A. Marinelli, “Nonlinear Longitudinal Space Charge Oscillations in Relativistic Electron Beams”, Phys. Rev. Lett. 106, 184801 (2011).
6. Y. Shen, X. Yang, G. Carr et al., “Tunable Few-Cycle and Multicycle Coherent Terahertz Radiation from Relativistic Electrons”, Phys. Rev. Lett. 107, 204801 (2011).
7. P. Muggli, V. Yakimenko, M. Babzien et al., “Generation of Trains of Electron

Microbunches with Adjustable Subpicosecond Spacing", Phys. Rev. Lett. 101, 054801 (2008).
8. Y.-E Sun, P. Piot, A. Johnson et al., "Tunable Subpicosecond Electron-Bunch-Train Generation Using a Transverse-To-Longitudinal Phase-Space Exchange Technique", Phys. Rev. Lett. 105, 234801 (2010).
9. L.-H. Yu, "Generation of intense uv radiation by subharmonically seeded single-pass free-electron lasers", Phys. Rev. A, 44, 5178 (1991).
10. L.-H. Yu, M. Babzien, I. Ben-Zvi et al., "High-Gain Harmonic-Generation Free-Electron Laser", Science, 289, 932 (2000).
11. L. H. Yu, L. DiMauro, A. Doyuran et al., "First Ultraviolet High-Gain Harmonic-Generation Free-Electron Laser", Phys. Rev. Lett. 91, 074801 (2003).
12. M. Labat, M. Bellaveglia, M. Bougeard et al., "High-Gain Harmonic-Generation Free-Electron Laser Seeded by Harmonics Generated in Gas", Phys. Rev. Lett. 107, 224801 (2011).
13. E. Allaria, R. Appio, L. Badano et al., "Highly coherent and stable pulses from the FERMI seeded free-electron laser in the extreme ultraviolet", Nature Photon. 6, 699 (2012).
14. H.-S Chan, Z.-M Hsieh, W.-H Liang et al., "Synthesis and Measurement of Ultrafast Waveforms from Five Discrete Optical Harmonics", Science, 331, 1165 (2011).
15. J. Wu and L.-H Yu, "Coherent hard x-ray production by cascading stages of high gain harmonic generation", Nucl. Instrum. Methods Phys. Res., Sect. A, 475, 104 (2001).
16. D. Xiang, "Recent advances and new techniques in visualization of ultra-short relativistic electron bunches", proceedings of the 2012 International Particle Accelerator Conference, New Orleans, Louisiana (2012).
17. E.L. Saldin, E.A. Schneidmiller and M.V. Yurkov, "A simple method for the determination of the structure of ultrashort relativistic electron bunches", Nucl. Instrum. Methods Phys. Res., Sect. A 539, 499 (2005).
18. B. W. J. McNeil, G. R. M. Robb and M. W. Poole, "Inducing strong density modulation with small energy dispersion in particle beams and the harmonic amplifier free electron laser", proceedings of the 2005 Particle Accelerator Conference, Knoxville, Tennessee (2005).
19. E. Allaria and G. De Ninno, "Soft-X-Ray Coherent Radiation Using a Single-Cascade Free-Electron Laser", Phys. Rev. Lett. 99, 014801 (2007).
20. Q. Jia, "Enhanced high-gain harmonic generation for x-ray free-electron laser", Appl. Phys. Lett. 93, 141102 (2008).
21. G. Stupakov, "Using the Beam-Echo Effect for Generation of Short-Wavelength Radiation", Phys. Rev. Lett. 102, 074801 (2009).
22. D. Xiang and G. Stupakov, "Echo-enabled harmonic generation free electron laser", Phys. Rev. ST Accel. Beams, 12, 030702 (2009).
23. D. Xiang, E. Colby, M. Dunning et al., "Demonstration of the echo-enabled harmonic generation technique for short-wavelength seeded free electron lasers", Phys. Rev. Lett. 105, 114801 (2010).
24. D. Xiang, E. Colby, M. Dunning et al., "Evidence of high harmonics from echo-enabled harmonic generation for seeding x-ray free electron lasers", Phys. Rev. Lett. 108, 024802 (2012).
25. Z. Zhao, D. Wang, J.H. Chen et al., "First lasing of an echo-enabled harmonic generation free-electron laser", Nature Photon. 6, 360 (2012).
26. D. Xiang and G. Stupakov, "Enhanced tunable narrow-band THz emission from laser-modulated electron beams", Phys. Rev. ST Accel. Beams, 12, 080701 (2009).
27. M. Dunning, C. Hast, E. Hemsing et al., "Generating periodic terahertz structures in a relativistic electron beam through frequency down-conversion of optical lasers", Phys. Rev. Lett. 109, 074801 (2012).
28. G. Stupakov, private communications.

29. G. Stupakov and M. Zolotorev, “Using laser harmonics to increase bunching factor in EEHG”, proceedings of the 2011 Free Electron Laser Conference, Shanghai (2011).
30. D. Ratner and A. Chao, “Seeded radiation sources with sawtooth waveforms”, proceedings of the 2011 Free Electron Laser Conference, Shanghai (2011).
31. E. Hemsing and D. Xiang, “Cascaded modulator-chicane modules for optical manipulation of relativistic electron beams”, submitted to Phys. Rev. ST Accel. Beams, 2012.
32. C. Feng, D. Wang and Z. Zhao, “Pre-density modulation of the electron beam for soft x-ray FEL in the water window”, proceedings of the 2010 Free Electron Laser Conference, Malmö, Sweden (2010).
33. R.B. Palmer, “Interaction of relativistic particle and free electromagnetic waves in the presence of a static helical magnet”, J. Appl. Phys. 43, 3014 (1972).
34. W. D. Kimura, M. Babzien, I. Ben-Zvi et al., “Demonstration of High-Trapping Efficiency and Narrow Energy Spread in a Laser-Driven Accelerator”, Phys. Rev. Lett. 92, 054801 (2004).
35. J. P. Duris, P. Musumeci, and R. K. Li, “Inverse free electron laser accelerator for advanced light sources”, Phys. Rev. ST Accel. Beams, 15, 061301 (2012).
36. D. Xiang and G. Stupakov, “Triple modulator-chicane scheme for seeding sub-nanometer x-ray free-electron lasers”, New J. Phys. 13, 093028 (2011).

3.4 Recent Applications of Longitudinal Phase Space Diagnostics

Christopher Behrens and Christopher Gerth
Deutsches Elektronen-Synchrotron DESY, Notkestr. 85, 22607 Hamburg, Germany
Mail to: christopher.behrens@desy.de

3.4.1 Introduction

X-ray free-electron lasers (FELs), such as the Linac Coherent Light Source (LCLS) [1] or the Free-Electron Laser in Hamburg (FLASH) [2], open up new frontiers in photon science. In order to take full advantage of these unique accelerator-based light sources, the characterization and control of the femtosecond electron and X-ray beams is essential. The temporal profile of the FEL radiation power, neglecting the statistical properties of self-amplified spontaneous emission (SASE) radiation, is in principle determined by the parameters of the FEL driving electron beam, which can vary along the electron bunch and can show significant shot-to-shot fluctuations. Thus, in order to understand and optimize the FEL amplification process, time-resolved electron beam diagnostics with high resolution and single-shot capability are required. For typical electron bunch charges of $Q \sim 100$ pC and peak currents of $I > 1$kA, the electron bunch durations result in $T \sim Q/I < 100$ fs, which also defines the desired diagnostic accuracy.

Single-shot electron beam diagnostics with a temporal resolution of a few tens of femtoseconds and less is feasible by utilizing a transverse deflecting radio-frequency (r.f.) structure (TDS) [3,4] in combination with transverse beam profile measurements based on the imaging of incoherent optical radiation emitted by the electron beam at a view screen, e.g., a scintillator or optical transition radiation screen. However, coherent optical emission by electron beams, recently observed at present X-ray FELs, has become a severe issue for transverse beam profile diagnostics [5,6,7]. The main reason for coherent optical radiation effects is associated with the microbunching instability at FELs [8,9,10]. Furthermore, ultra-short current spikes inside bunches [7] or intrinsically

ultra-short bunches, generated at laser-plasma wakefield accelerators [11] or FELs with low-charge operation [12,13,14], can be the origin. Strategies and techniques to mitigate or even fully suppress such coherent effects are highly demanded.

Electron beams capable of driving X-ray FELs do not only require high peak currents but also low energy spreads, i.e., a high longitudinal brightness, which is a measure for the electron density in the longitudinal phase space. The longitudinal phase space is, in turn, influenced by the r.f. fields of the driving accelerator, which allow one to control and temporally shape the electron bunches and thus the X-ray FEL pulses. As is reported in Refs. [5,15,16], uniform electron bunch compression at FELs can be achieved by linearization of the longitudinal phase space using multiple, higher-harmonic r.f. frequencies. Hence, optimization and control of the bunch compression requires accurate diagnosis of the longitudinal phase space. Recently, for the characterization of the corresponding femtosecond X-ray FEL pulses on a single-shot basis, a novel concept has been proposed which is based on longitudinal phase space diagnosis of the electron bunches downstream of the FEL undulators [17].

In this beam dynamics newsletter article, we report on recent developments and results achieved within the active research field of longitudinal phase space diagnostics and applications for femtosecond electron and X-ray beams at FELs.

3.4.2 **High-Resolution Longitudinal Phase Space Diagnostics**

Several longitudinal electron beam diagnostic schemes with high temporal resolution are discussed in literature, and an excellent overview of existing techniques and recent developments is given in Ref. [18]. Here, we restrict the discussion to single-shot longitudinal phase space diagnostics that is capable of achieving high resolution in both time (longitudinal coordinate) and energy (momentum). A TDS in combination with a magnetic energy spectrometer (a typical longitudinal phase space diagnostics setup is sketched in Fig. 10) makes this possible, provided that an imaging screen is employed to get two-dimensional, transverse electron beam images.

A TDS induces a time-dependent transverse kick within the electron bunches, which can be transformed into a time-dependent transverse offset in one dimension at an imaging screen. A magnetic energy spectrometer induces an energy-dependent transverse kick that is then transformed into an energy-dependent transverse offset at the same imaging screen on the perpendicular axis if the bending plane is perpendicular to the shearing plane of the TDS. This way, the longitudinal phase space is transformed into a transverse plane, which can be measured with imaging screens. A detailed description of beam diagnostics using a TDS can be found in Refs. [19,20].

Figure 1 shows two examples of single-shot longitudinal phase space measurements performed during FEL operation at FLASH. The measured bunch currents (dotted red lines) can give reasonable estimates of expected FEL pulse durations [20]. Single-shot root mean square (r.m.s.) time resolutions of 8 fs and 13 fs have been reached for bunch charges of 150 pC and 500 pC, respectively. Future longitudinal phase space diagnostic setups, e.g., as for the LCLS (see Ref. [17]), are designed for temporal resolutions down to 1 fs (r.m.s.) at even higher electron beam energies as compared to FLASH.

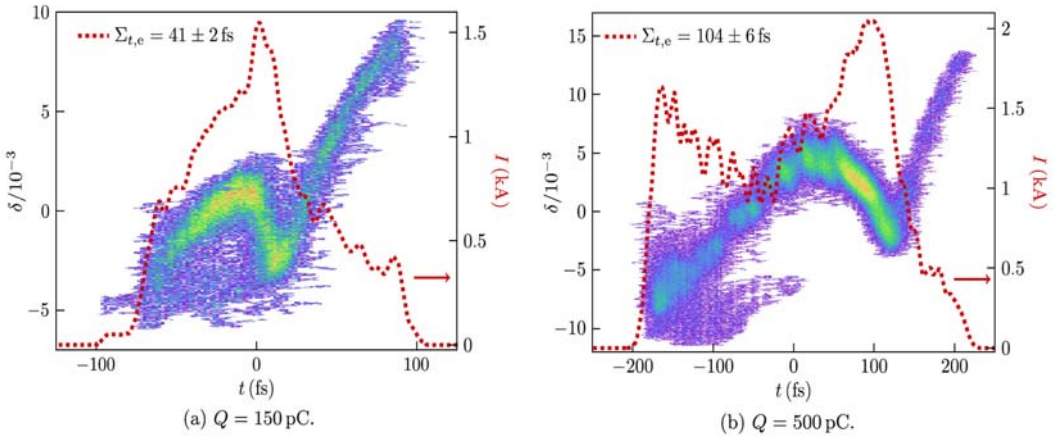

Figure 1: Single-shot longitudinal phase space measurements performed at FLASH for two bunch charges (bunch head at negative times). The dotted red lines represent the bunch current, and the corresponding r.m.s. bunch durations are given in the legends. The vertical axis on the left-hand side represents the energy deviation in relative units. Details can be found in Ref. [20].

Longitudinal bunch compression is typically accomplished by magnetic chicanes in combination with off-crest acceleration in the r.f. cavities. Hence, longitudinal phase space diagnosis is essential in order to control and manipulate the shape of the corresponding phase space for FEL operation or advanced accelerator concepts [21]. Uniform bunch compression can be accomplished by using multiple, higher-harmonic r.f. frequencies, and a longitudinal phase space linearization with the third-harmonic r.f. system of FLASH is demonstrated in Fig. 2. Throughout the rest of this article, only single-shot beam images are presented and the term 'single-shot' is thus omitted.

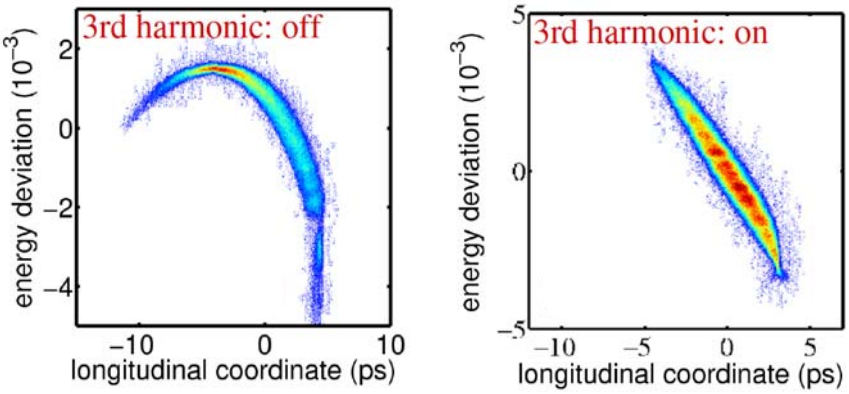

Figure 2: Demonstration of longitudinal phase space linearization utilizing the third-harmonic r.f. system at FLASH [15,16] for rather long electron bunches (bunch head at positive times).

Microbunching instabilities and corresponding electron beam diagnostic issues related to coherent emission of optical radiation (see Sec. 3.4.3) are a common observation at present X-ray FELs. This phenomenon can be studied by adequate longitudinal phase space diagnostics as is shown by the measurements in Fig. 3. These measurements were carried out during FEL operation at FLASH and clearly indicate the formation of microbunching at a characteristic time scale, compatible with analytical

calculations [10] and spectral measurements of coherent transition radiation [22]. As is presented in Sec. N.N.4, longitudinal phase space diagnostics in certain configurations can also be utilized to suppress or mitigate microbunching instabilities.

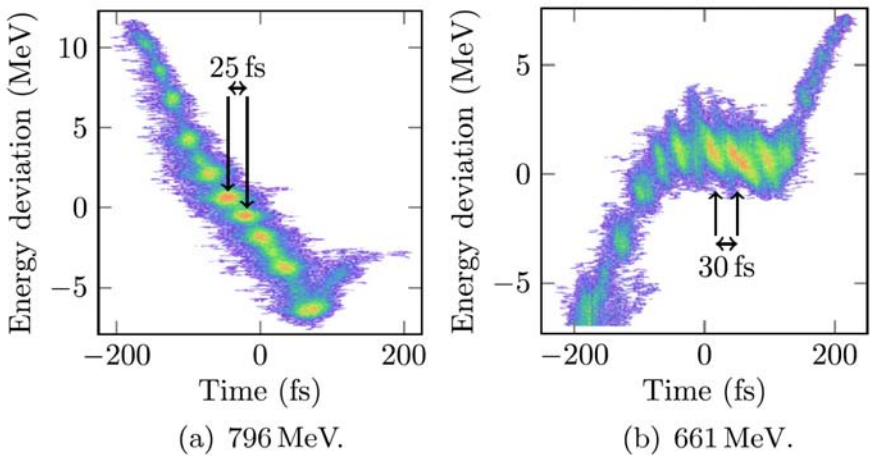

Figure 3: Longitudinal phase space measurements (bunch head at negative times) for two different compression settings and beam energies at FLASH. The formation of microbunching at characteristic time scales [10] is visible. Experimental details can be found in Ref. [7].

3.4.3 **Suppression of Coherent Optical Radiation Effects**

The main reason for coherent optical radiation effects in X-ray FELs are microbunching instabilities that can be associated with charge density modulations on the scale of optical wavelengths within the electron bunch (c.f. the article "Microbunching Review" by Daniel Ratner in this newsletter issue, and Refs. [8,9,10]). Figure 4 shows two single-shot beam images that have been recorded with a standard charged-coupled device (CCD) camera at a screen station directly upstream of the FEL undulators at FLASH. Ring-shaped structures, clearly visible in the light patterns, and a drastic increase and fluctuation in the light intensity, commonly leading to saturation in the recorded images, are characteristic indications for coherent optical radiation effects. Beam images that are dominated by coherent optical radiation are not a representation of the transverse charge distribution and hamper electron beam diagnostics that require imaging screens, e.g., longitudinal phase space diagnostics utilizing a TDS.

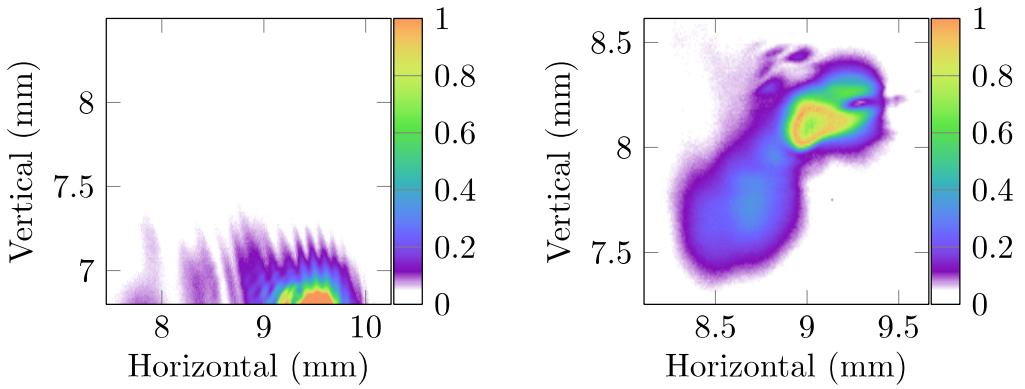

Figure 4: Single-shot electron beam images that show characteristic light patterns generated by coherent optical radiation effects [7]. Left: OTR screen. Right: LuAG scintillation screen.

For the image in Fig. 4 (left) an optical transition radiation (OTR) screen (aluminum coated silicon) was used. Transition radiation is emitted when a charged particle beam crosses the boundary between two media with different dielectric properties, and it can be described by an incoherent term that scales with the number of electrons in the bunch and by a coherent term that scales with $N^2 |F(\lambda)|^2$, where N is the number of electrons and F the wavelength-dependent longitudinal form factor, neglecting transverse beam size effects (see, e.g., Ref. [7]). The longitudinal form factor F can be expressed as the Fourier transform of the normalized longitudinal charge distribution and, hence, charge density modulations at optical wavelengths correspond to a finite longitudinal form factor, which can lead to a significant emission of coherent OTR (COTR) as $N \sim 10^8$.

By using scintillation imaging screens, coherent optical radiation effects can be mitigated. The emission of scintillation light is a stochastic process, which is completely insensitive to longitudinal density modulations and linear in the number of interacting electrons (neglecting quenching and saturation effects). Nevertheless, COTR can still be emitted at the boundary of vacuum and scintillation screen, which is demonstrated in the image of Fig. 4 (right). Here, a Ce:LuAG (cerium-doped lutetium aluminium garnet) scintillation screen was used together with a 780 nm long-pass filter, blocking completely the emitted luminescence light of LuAG that occurs below 700 nm. Hence, the light patterns in the image can solely be attributed to the emission of COTR.

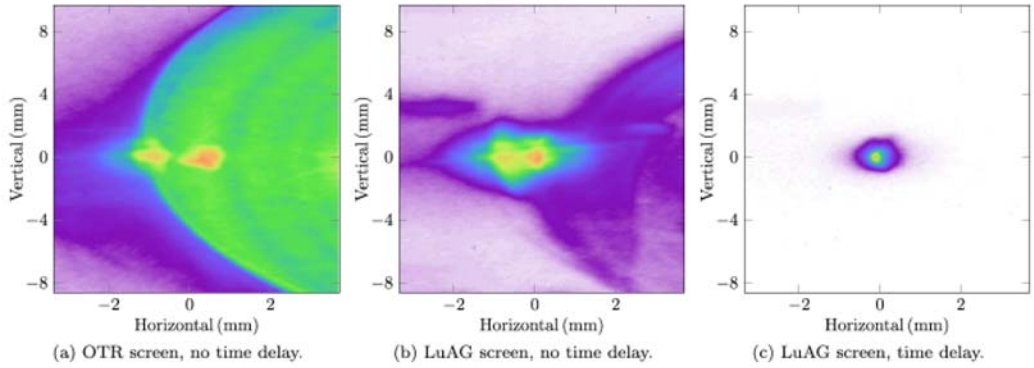

Figure 5: Temporal separation technique for the suppression of coherent optical radiation. An intensified CCD camera with an adjustable time delay of the gate for image exposure was used.

The fundamentally different light generation processes of scintillators and optical transition radiators result in clearly distinct spectral and spatial distributions as well as temporal responses. For instance, the emission duration of transition radiation from relativistic electron bunches corresponds to the bunch lengths, which is instantaneous compared to the decay times of the excited states in a scintillator. This can be exploited to fully suppress the COTR emitted at the boundary of vacuum and scintillation screen by applying the temporal separation technique, which is demonstrated in Fig. 5.

Image recording with delayed exposure can be accomplished with intensified CCD (ICCD) cameras, where a control voltage in the intensifier between photocathode and micro-channel plate allows fast gating of the image exposure. The image shown in Fig. 5(a) was recorded without a time delay of the camera gate with respect to the electron bunch using an OTR screen. The light pattern in the center of Fig. 5(a) can mainly be attributed to COTR, and the round-shaped pattern is most probably due to coherent synchrotron radiation (CSR) which was generated upstream of the OTR screen. The corresponding image taken with a time delay of 100 ns only contained background noise, which proved that the camera gate effectively suppressed the COTR and CSR.

The image in Fig. 5(b) was recorded without a time delay of the camera gate but using a LuAG screen. Figures 5(a) and 5(b) show similar patterns with the contribution from CSR slightly reduced due to the transparency of the LuAG screen. The image in Fig. 5(c), recorded with a time delay of the camera gate of 100 ns, can be attributed purely to scintillation light as COTR and CSR was fully suppressed by the camera gate which makes a quantitative analysis of the transverse beam profiles possible.

Let us now consider longitudinal phase space measurements with a TDS, which can be accomplished by recording two-dimensional, transverse beam profiles in the dispersive section of a magnetic energy spectrometer. For a simple energy spectrometer that consists of a single dipole magnet, an analytical expression can be derived that describes the evolution of the wavelength-dependent microbunching and corresponding longitudinal form factor F for a given initial bunching at the entrance of the dipole magnet. Microbunching is strongly suppressed at optical wavelengths in magnetic energy spectrometers due to the fact that transverse beam slices get sheared in the longitudinal direction inside the dipole magnet and the microbunching gets smeared out.

A suppression factor $S(\lambda)$, defined as the ratio of the bunching factors at the screen and at the entrance of the energy spectrometer, has been calculated analytically for typical parameters at FLASH and an initial density modulation with 10% peak

amplitude (see Ref. [7] for details). The result (solid red line) is shown in Fig. 6 (left) together with the result of numerical simulations (blue dots) using the particle tracking code ELEGANT [23]. The dotted green line is an approximation for which only the term that describes the shearing of beam slices, the transfer matrix element R_{51} (horizontal bending plane), was considered. A cut-off wavelength λ_c, for which the coherent and incoherent emission is of equal intensity, can be defined by $|F(\lambda_c)|^2 = 1/N^{1/2}$. For the approximation described above, a simple relation for the cut-off wavelength can be found: $\lambda_c \approx 2\pi\cdot\sigma_0\cdot\sin(\Theta)/\ln(N)^{1/2}$, where σ_0 is the beam size at the entrance of the dipole, Θ is the spectrometer bend angle, and N is the number of electrons. The cut-off wavelength in the energy spectrometer at FLASH amounts to $\lambda_c \approx 16$ µm, which manifests a strong suppression of coherent emission at optical wavelengths.

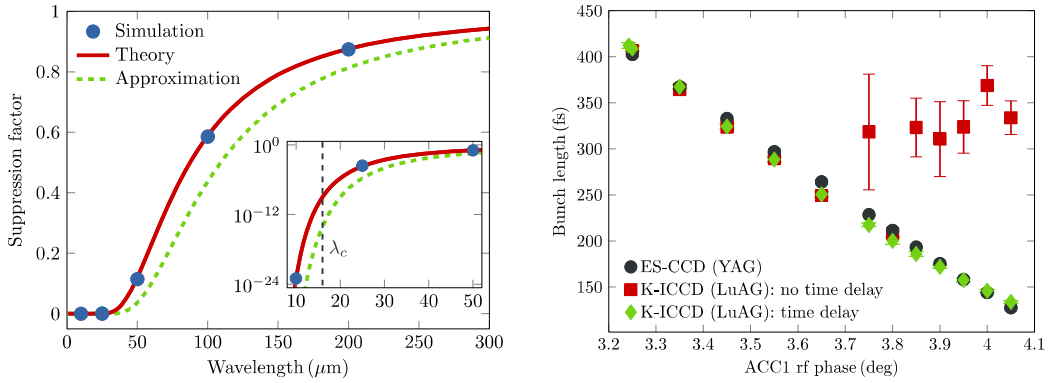

Figure 6: Left: Suppression S and cut-off wavelength λ_c for the energy spectrometer at FLASH. Right: Bunch lengths measured for various accelerating phases with three different imaging configurations: CCD camera with YAG screen in energy spectrometer (ES-CDD) and ICCD camera with and without camera delay with LuAG screen in straight beamline (K-ICCD).

To verify this finding experimentally, bunch length measurements using a TDS were carried out with a CCD camera, imaging a (yttrium aluminium garnet) YAG imaging screen in the energy spectrometer and an ICCD camera, imaging a LuAG screen in the straight beamline for various r.f. phase settings of the first accelerator module (ACC1) at FLASH. The r.f. phase of ACC1 affects the energy chirp of the electron bunches upstream of the first bunch compressor and, accordingly, the final bunch lengths.

Figure 6 (right) shows the mean r.m.s. electron bunch length of 20 single-shot images. The error bars indicate the statistical r.m.s. bunch length jitter. The bunch lengths measured in the energy spectrometer (black dots) decrease almost linearly with negligible jitter. In contrast, the measurements taken with the LuAG screen in the straight beamline without a time delay of the camera gate (red squares) show a sudden increase of the bunch length and bunch length jitter for ACC1 r.f. phases ≥ 3.75 deg which is a clear indication of the presence of coherent optical radiation effects. The corresponding electron bunch length measurements with applied temporal separation (green diamonds), i.e., the camera gate of the intensified camera was delayed, are in perfect agreement with the measurements recorded in the energy spectrometer (black dots). This proves that the emission of coherent optical radiation is suppressed in the energy spectrometer, whereas, in case of a straight beamline, separation techniques have to be applied in the imaging scheme to separate the coherent optical radiation from the incoherent scintillation light and therewith suppress coherent radiation in the detection.

3.4.4 **Reversible Beam Heating for Suppression of Microbunching Instabilities**

The required high transverse and longitudinal brightness of the electron beams at X-ray free-electron lasers are subject to various degradation effects, e.g., coherent synchrotron radiation or space charge forces, and need to be preserved during the beam transport up to the undulator section. Repulsive, transverse space charge forces inside the electron bunch can lead to a transverse beam blow-up with a corresponding increase of the transverse beam emittance. Thus, in order to maintain the small emittances provided by so-called r.f. injectors, the high electron bunch peak current required to drive an X-ray FEL is achieved by bunch compression in magnetic chicanes at relativistic energies (e.g., Ref. [24]), where the space charge forces are significantly reduced. However, the compression of high-brightness electron beams in magnetic chicanes comes along with microbunching instabilities [8,9,10], which can also degrade the electron beam brightness significantly and, furthermore, can lead to coherent optical radiation effects, hampering beam diagnostics using imaging screens (cf. Sec. N.N.3).

Microbunching instabilities associated with the bunch compression in magnetic chicanes can be suppressed by introducing additional uncorrelated energy spread within the electron bunches (so-called slice energy spread) prior to the compression [10,25]. The slice energy spread of electron bunches can be effectively increased, i.e., "heated", by making use of the resonant interaction of electrons with an optical laser in a small undulator, as has been demonstrated by the laser heater system at the LCLS [25,26]. However, the laser heater system irreversibly increases the slice energy spread and needs to be limited in order to keep the FEL performance. In comparison to existing SASE FELs, the amount of tolerable electron beam heating is particularly critical for future FELs seeded with external radiation fields, provided by external laser systems.

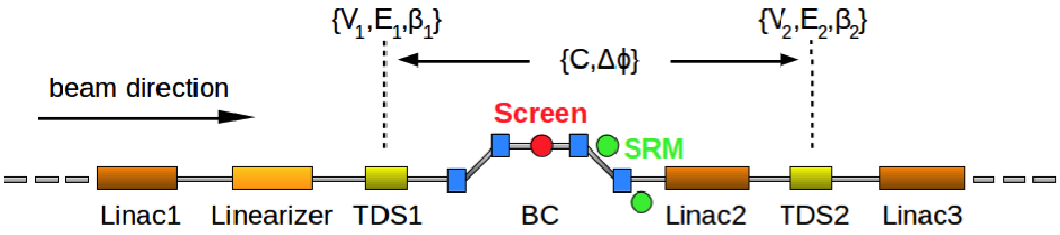

Figure 7: Layout of a reversible electron beam heater system including two TDSs located upstream and downstream of a magnetic bunch compressor (BC) chicane, and longitudinal phase space diagnostics using imaging screens and synchrotron radiation monitors. Parameters related to the reversible heater system are denoted in curly brackets (see Ref. [27] for details).

A different approach to increase the slice energy spread utilizes the characteristics of transverse deflecting r.f. structures, which are based on the Panofsky-Wenzel theorem [28]. According to this theorem, the time-dependent transverse kicks of a TDS are fundamentally related to an additional energy spread induced by the TDS [29,30]. The energy spread induced by a TDS is correlated with the transverse offsets inside the TDS during the passage, and hence the effect of an induced energy spread due to a finite transverse beam size is reversible and can be eliminated by a second TDS [27]. A scheme of two TDSs upstream and downstream of a magnetic chicane thus allows electron beam heating for suppression of microbunching instabilities and simultaneous

preservation of the slice energy spread. The additional slice energy spread is introduced in the first TDS, which suppresses the microbunching instability, and is then eliminated in the second TDS. A generic layout of such a reversible electron beam heater system is depicted in Fig. 7. The system consists of linear accelerator (linac) sections providing and accelerating high-brightness electron beams, a magnetic bunch compressor chicane in order to achieve sufficient peak currents to drive the FEL process, and two TDSs located upstream and downstream of the bunch compressor. A set of beam diagnostics, e.g., screens or synchrotron radiation monitors (SRM), complements the system.

The method of reversible electron beam heating has been thoroughly described in Ref. [27] by analytical calculations using beam optics and a matrix formalism. Here we only show the principle of the reversible heater system utilizing numerical simulations using the particle tracking code ELEGANT. The impact of CSR is not taken into account here, because the results would undergo only small modifications when including CSR effects (cf. Ref. [27] for details). Figure 8 shows the principle of the reversible beam heater system by means of simulation of the longitudinal phase space at different positions along the beamline (cf. Fig. 7). The initial slice energy spread of ~1 keV (r.m.s.) is heated up to ~10 keV (r.m.s.) in the first TDS, increased by the compression factor of 13 in the bunch compressor to ~130 keV (r.m.s.), and finally cooled down to ~13 keV (r.m.s.) by the second TDS [see Figs. 8(a)–(d)]. The heating induced by the first TDS is perfectly reversible, and the final slice energy spread is simply the initial slice energy spread scaled with the compression factor, which would be exactly the same as in the case without using the reversible beam heater system. Table 1 summarizes the main parameters used in the simulations with 5×10^5 particles.

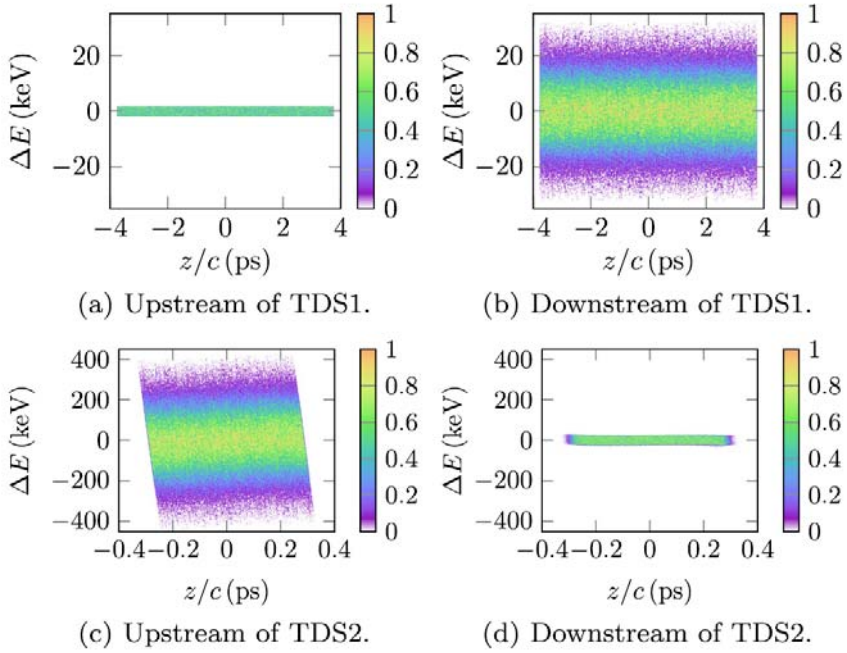

Figure 8: Simulation of the longitudinal phase space along the generic beamline depicted in Fig. 7: (a) Upstream of the first TDS, (b) directly downstream of the first TDS, (c) directly downstream of the bunch compressor and upstream of the second TDS, and (d) downstream of the second TDS. The axis scales change from (b) to (c) when bunch compression takes place.

Table 1: Parameters of the electron beam, of the bunch compressor system, and of the transverse deflecting r.f. structures used in the simulations including 5×10^5 particles.

Parameter	*Symbol*	*Value*	*Unit*
Beam energy at TDS1/2	E	350	MeV
Lorentz factor at TDS1/2	γ	685	
Initial transverse emittance	$\gamma\,\varepsilon_{x,y}$	0.6	µm
Initial slice energy spread	σ_E	~1	keV
Moment compaction factor	R_{56}	-138	mm
Compression factor	C	~13	
Final bunch compression	I_f	~520	A
TDS1/2 frequency	f	3.9	GHz
Voltage of TDS1	V_1	0.415	MV
Voltage of TDS2	V_2	5.440	MV
Length of TDS1	L_1	0.1	m
Length of TDS2	L_2	0.5	m

The principle of reversible electron beam heating has been presented in Fig. 8, now we demonstrate the microbunching gain suppression by introducing initial energy modulation with 3 keV amplitude and 50 µm wavelength. The simulations were carried out with 1×10^6 particles and including CSR effects. Figure 9 shows the longitudinal phase space downstream of the second TDS for both the reversible beam heater system switched off (left-hand side) and on (right-hand side). In the case without reversible electron beam heating, energy and density modulations at the compressed modulation wavelength appear. When switching the reversible beam heater on, the microbunching instability disappears and the resulting longitudinal phase space remains smooth.

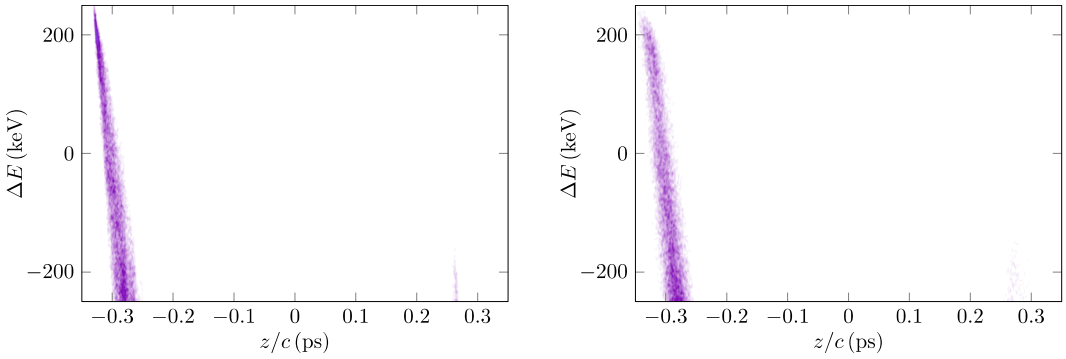

Figure 9: Simulation on suppression of microbunching instabilities due to an initial energy modulation upstream of the bunch compressor chicane. The core of the longitudinal phase space downstream of the chicane is shown for the TDS-heater system off/on (panel on the left/right).

The reversible beam heater system described here can suppress microbunching instabilities and preserve the high beam brightness at the same time. For example, this scheme significantly loosens the laser power requirements for seeding using short-wavelength high-harmonic generation sources and may strongly impact the design of future seeded FELs. In addition, the reversible heater system exhibits integrated options for diagnosis and on-line monitoring of the longitudinal phase space (cf. Fig. 7).

3.4.5 **Femtosecond X-ray FEL Pulse Characterization**

The realization and interpretation of various experiments on ultra-fast dynamics in photon science at X-ray free-electron lasers are based on the reliable generation and temporal characterization of femtosecond FEL radiation pulses. Time-resolved electron beam diagnostics demonstrated robust estimates on the upper limits of the expected FEL pulse durations [20]. However, for a more precise identification of the lasing part within the electron bunches and for actual temporal profiles of the FEL radiation power, time-domain measurements of the temporal FEL pulse profiles are required.

The principle of X-ray FELs is based on the resonant energy transfer between a relativistic electron beam and an electromagnetic (EM) wave co-propagating through a long undulator. When FEL amplification takes place, charge density modulations on the scale of the resonant wavelength develop and lead to a corresponding net energy transfer from the electrons to the EM wave. As a consequence, the FEL amplification process induces a time-dependent energy loss and spread within the electron bunches. The temporal FEL radiation pulse profile appears then as a replica pulse within the longitudinal phase space of the electron bunches downstream of the undulator [17], and can thus be measured by longitudinal phase space diagnostics for electron beams.

In order to separate the X-ray FEL radiation pulses for experiments and to finally dump the electron beams, FELs have a large dispersive beamline downstream of the undulator section, which can be utilized as a magnetic energy spectrometer. The combination of such a dispersive beamline with a TDS (see Fig. 10) allows single-shot measurements of the longitudinal phase space without affecting the FEL operation and user experiments. In fact, the acquired data, e.g., pulse duration, can be delivered to the FEL user experiments in real-time and on a single-shot basis in order to make use of it.

The operation of a TDS in combination with a magnetic energy spectrometer demonstrated temporal resolutions of sub-10 fs (cf. Sec. N.N.2), and by using X-band r.f. technology and magnetic energy spectrometers with optimized dispersion, temporal resolutions of ~1 fs (r.m.s.) and relative energy resolutions below 10^{-5} (r.m.s.) can be expected [17]. This unprecedented resolution will be sufficient to measure the FEL-induced time-dependent energy change within the electron bunches, i.e., the FEL replica pulse, making temporal characterization of the X-ray FEL pulses possible.

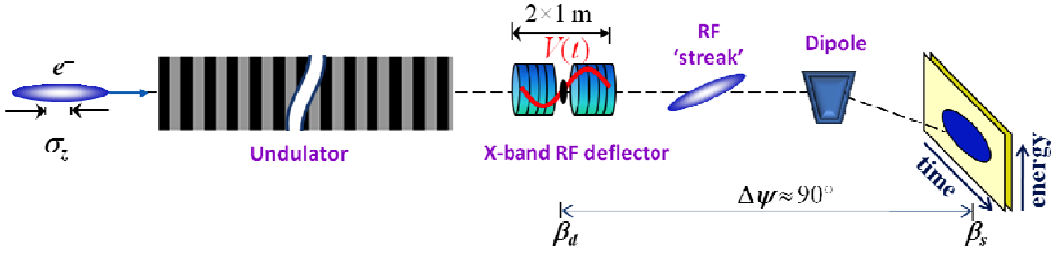

Figure 10: Schematic layout of a longitudinal phase space diagnostics downstream of an FEL undulator section with a TDS (X-band RF deflector), a magnetic (dipole) energy spectrometer, and an imaging screen [17]. This setup has been used for the simulations shown in Fig. 11.

Figure 11 presents simulated measurements of electron beam distributions (x,y) at the imaging screen with the horizontal axis x representing time and the vertical axis y representing energy. The electron beam transport upstream and downstream of the undulator has been simulated using the code ELEGANT, and for the FEL amplification

process in the undulator, the code GENESIS [31] has been used. The difference in energy (represented by the vertical axis) between FEL-on and FEL-off in Fig. 11 is clearly visible and makes the reconstruction of the temporal FEL pulses possible. The conditions FEL-on/off mean that the FEL amplification either takes place or is suppressed, respectively, where the latter can be experimentally realized by orbit kicks in the undulator. The lower right panel of Fig. 11 shows the simulated temporal FEL pulse profile in comparison with temporal profiles extracted from the longitudinal phase space of the electron beam downstream of the undulator. The temporal profile reconstruction can be done either by subtracting the mean slice energy or by subtracting in quadrature the slice energy spread. The electron beam simulations show excellent agreement with the GENESIS FEL simulation. The accuracy of this method is mainly limited by the general resolution limit of the TDS-based diagnostics, given by the r.f. system of the TDS, i.e., by the operating frequency and power, and by the electron beam optics between the TDS and the imaging screen (see Refs. [17,20] for details).

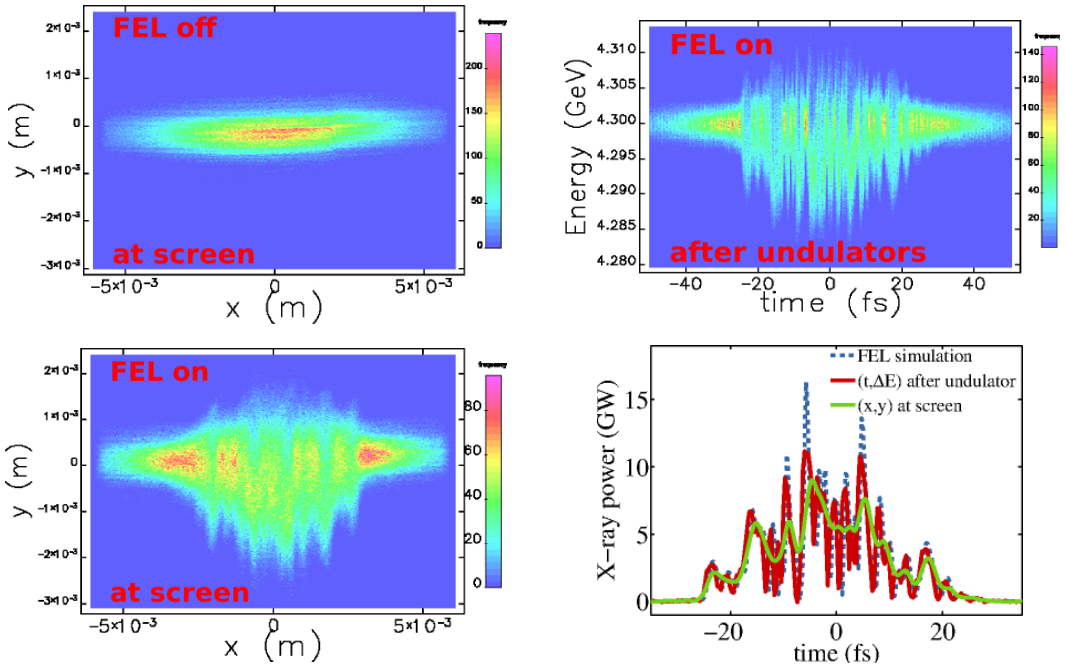

Figure 11: Simulated longitudinal phase space downstream of an FEL undulator section. The transverse beam distributions (x,y) measurable at the imaging screen are shown for FEL-off (upper left) and FEL-on (lower left). The upper right panel shows the actual longitudinal phase space (t,E) for FEL-on. The lower right panel shows the GENESIS FEL simulation (dashed blue), the reconstructed temporal FEL pulse from the actual longitudinal phase space (solid red), and the reconstructed temporal FEL pulse from the simulated measurement (solid green).

The single-shot diagnostic method described here is widely applicable to any FEL radiation wavelength, and the data can be delivered to the FEL user experiments in real-time on a single-shot basis. In addition, the electron beam parameters, e.g., peak current and energy chirp, are obtained simultaneously, providing a useful tool for detailed studies of the FEL process. We note that the article “Femtosecond electron and X-ray beams at the Linac Coherent Light Source” by Yuantao Ding in this newsletter issue discusses the method described here more detailed and for the actual case of the LCLS.

3.4.6 **Summary and Conclusions**

Measurement and control of the longitudinal phase space of femtosecond beams are essential for the operation and utilization of X-ray FELs. Within this newsletter article, recent developments and results achieved within the active research field of longitudinal phase space diagnostics have been reported, and applications for femtosecond electron and X-ray beams for current and future FELs have been discussed.

Single-shot measurements of the longitudinal phase space with sub-10 fs resolution utilizing a TDS in combination with a magnetic energy spectrometer have been presented. Longitudinal phase space linearization using accelerating fields with multiple, higher-harmonic r.f. frequencies for uniform bunch compression has been illustrated. It has been shown that the emission of coherent optical radiation effects is strongly suppressed in an energy spectrometer, which makes this configuration an ideal reference for transverse beam imaging measurements in straight beamlines. In case that coherent optical radiation effects occur in transverse electron beam profile diagnostics, scintillation screens in combination with separation techniques are required to suppress the coherent optical radiation in the imaging scheme. This has been demonstrated by applying the temporal separation technique successfully at FLASH.

Microbunching instabilities associated with the electron bunch compression in magnetic chicanes may not only lead to coherent optical radiation effects but can significantly degrade the high beam brightness required to drive a X-ray FEL. Introducing an additional energy spread upstream of the bunch compression, i.e., heating the electron beam, can effectively suppress microbunching instabilities. A scheme of two TDSs upstream and downstream of a magnetic bunch compressor chicane has been presented for reversible electron beam heating, capable to suppress microbunching instabilities and simultaneously preserve the beam brightness.

The realization and interpretation of various experiments on ultra-fast dynamics in photon science at X-ray FELs are based on the reliable generation and temporal characterization of femtosecond FEL pulses. A concept for an indirect, temporal X-ray pulse characterization has been presented, making use of the energy transfer during the FEL amplification process. The temporal FEL pulse profile appears as a replica in the longitudinal phase space of the electron bunch downstream of the undulator and can thus be measured by an appropriate longitudinal phase space diagnostics.

3.4.7 **References**

1. P. Emma *et al*., Nature Photon. **4**, 641 (2010).
2. W. Ackermann *et al*., Nature Photon. **1**, 336 (2007).
3. O. Altenmueller, R. Larsen, and G. Loew, Rev. Sci. Instrum. **35**, 438 (1964).
4. P. Emma, J. Frisch, and P. Krejcik, Technical Report No. LCLS-TN-00-12, 2000.
5. R. Akre, D. Dowell, P. Emma, J. Frisch, S. Gilevich, G. Hays, Ph. Hering, R. Iverson, C. Limborg-Deprey, H. Loos, A. Miahnahri, J. Schmerge, J. Turner, J. Welch, W. White, and J. Wu, Phys. Rev. ST Accel. Beams **11,** 030703 (2008).
6. H. Loos *et al*., Proceedings of the 30th International Free Electron Laser Conference, Gyeongju, Korea, 2008, THBAU01.
7. C. Behrens, Ch. Gerth, G. Kube, B. Schmidt, S. Wesch, and M. Yan, Phys. Rev. ST Accel. Beams **15**, 062801 (2012).
8. E.L. Saldin, E.A. Schneidmiller, and M.V. Yurkov, Nucl. Instrum. Methods Phys. Res., Sect. A **398**, 373 (1997).

9. M. Borland, Y. C. Chae, P. Emma, J. W. Lewellen, V. Bharadwaj, W. M. Fawley, P. Krejcik, C. Limborg, S. V. Milton, H.-D. Nuhn, R. Soliday, and M. Woodley, Nucl. Instrum. Methods Phys. Res., Sect. A **483**, 268 (2002).
10. E.L. Saldin, E.A. Schneidmiller, and M.V. Yurkov, Nucl. Instrum. Methods Phys. Res., Sect. A **528**, 355 (2004).
11. O. Lundh, J. Lim, C. Rechatin, L. Ammoura, A. Ben-Ismail, X. Davoine, G. Gallot, J-P. Goddet, E. Lefebvre, V. Malka, and J. Faure, Nature Physics **7**, 219 - 222 (2011).
12. Y. Ding, A. Brachmann, F.-J. Decker, D. Dowell, P. Emma, J. Frisch, S. Gilevich, G. Hays, Ph. Hering, Z. Huang, R. Iverson, H. Loos, A. Miahnahri, H.-D. Nuhn, D. Ratner, J. Turner, J. Welch, W. White, and J. Wu, Phys. Rev. Lett. **102**, 254801 (2009).
13. Z. Huang, A. Baker, C. Behrens, M. Boyes, J. Craft, F.-J. Decker, Y. Ding, P. Emma, J. Frisch, R. Iverson, J. Lipari, H. Loos, and D. Walz, Proceedings of the 24th Particle Accelerator Conference, New York, USA, THP183 (2011).
14. I. Zagorodnov, Proceedings of the 32nd International Free Electron Laser Conference, Malmö, Sweden, 2010, WEOBI2.
15. E. Vogel *et al*., Proceedings of the 1st International Particle Accelerator Conference, Kyoto, Japan, 2010, THPD0003.
16. H. Edwards, C. Behrens, and E. Harms, in Proceedings of the 25th International Linear Accelerator Conference, Tsukuba, Japan, 2010, MO304.
17. Y. Ding, C. Behrens, P. Emma, J. Frisch, Z. Huang, H. Loos, P. Krejcik, and M-H. Wang, Phys. Rev. ST Accel. Beams **14**, 120701 (2011).
18. D. Xiang, in Proceedings of the 3rd International Particle Accelerator Conference, New Orleans, USA**,** 2012, WEXB01.
19. M. Röhrs, Ch. Gerth, H. Schlarb, B. Schmidt, and P. Schmüser, Phys. Rev. ST Accel. Beams **12**, 050704 (2009).
20. C. Behrens, N. Gerasimova, Ch. Gerth, B. Schmidt, E.A. Schneidmiller, S. Serkez, S. Wesch, and M.V. Yurkov, Phys. Rev. ST Accel. Beams **15**, 030707 (2012).
21. P. Piot, C. Behrens, C. Gerth, M. Dohlus, F. Lemery, D. Mihalcea, P. Stoltz, M. Vogt, Phys. Rev. Lett. **108**, 034801 (2012).
22. B. Schmidt, C. Behrens, H. Delsim-Hashemi, P. Schmüser, and S. Wesch, Proceedings of the 24th European Particle Accelerator Conference, Genoa, Italy, 2008, MOPC029.
23. M. Borland, Advanced Photon Source Report No. LS-287, 2000.
24. I. Zagorodnov and M. Dohlus, Phys. Rev. ST Accel. Beams **14**, 014403 (2011).
25. Z. Huang, M. Borland, P. Emma, J. Wu, C. Limborg, G. Stupakov, and J. Welch, Phys. Rev. ST Accel. Beams **7**, 074401 (2004).
26. Z. Huang *et al.*, Phys. Rev. ST Accel. Beams **13**, 020703 (2010).
27. C. Behrens, Z. Huang, and D. Xiang, Phys. Rev. ST Accel. Beams **15**, 022802 (2012).
28. W.K.H. Panofsky and W.A. Wenzel, Rev. Sci. Instrum. **27,** 967 (1956).
29. S. Korepanov, M. Krasilnikov, F. Stephan, D. Alesini, and L. Ficcadenti, Proceedings of the 8th European Workshop on Beam Diagnostics and Instrumentation for Particle Accelerators, Venice, Italy, 2007, TUPB32.
30. C. Behrens and Ch. Gerth, Proceedings of the 10th European Workshop on Beam Diagnostics and Instrumentation for Particle Accelerators, Hamburg, Germany, 2011, TUPD31.
31. S. Reiche *et al*., Nucl. Instrum. Methods Phys. Res., Sect. A **429**, 243 (1999).

3.5 Longitudinal Diagnosis of Electron Beams with Sub-femtosecond Resolution

G. Andonian[1,2], E. Hemsing[3], D. Xiang[3], P. Musumeci[1], A. Murokh[2], F. O'Shea[1], J. Rosenzweig[1]
[1] Particle Beam Physics Laboratory, University of California Los Angeles, CA
[2] RadiaBeam Technologies, Santa Monica, CA
[3] SLAC National Accelerator Laboratory, Palo Alto, CA
Mail to: gerard@physics.ucla.edu

3.5.1 Introduction

Photoinjector accelerators for next generation light sources reliably produce high-current (~kA), ultra-short (< 100 fs) beams [1,2,3] using magnetic bunch compressors [4] or velocity bunching techniques [5], without comprising beam emittance. The measurement of such pulses with ultra-fast time resolution is essential for successful beam operation, performance optimization, and benchmarking to computational models. Also, the attainable diagnostic resolutions are essential to study phenomena on the ultrashort length and ultrafast time scales (e.g. space-charge driven microbunching instability [6]).

Present bunch length diagnostics rely on electro-optical techniques [7], deconvolution of the frequency spectrum of emitted radiation sources [8,9,10], or RF zero-crossing schemes [10], and have demonstrated resolutions of ~10 fs. Other proposed techniques aim to reach the femtosecond level, including the optical replica synthesizer [12], or longitudinal-transverse phase space mapping [13]. In this article, we describe a design for a bunch length diagnostic that will provide a temporal resolution on the sub-fs scale. The scheme is based on encoding the beam temporal profile information onto an angular modulation via a laser-electron beam interaction in an undulator. Using simulations, we demonstrate the viability of this diagnostic for several examples and we also propose an alternative layout to achieve sub-fs resolution.

3.5.2 Conceptual Description

The fundamental description behind the sweeping concept was rigorously developed in Ref. 14. Here we review the analytical treatment from that paper at a conceptual level to demonstrate the feasibility of the scheme. In this treatment, some assumptions and approximations are made (such as zero-length elements) for an exploratory description. However, simulations are used to complement the analytical theory and model real examples in the following section.

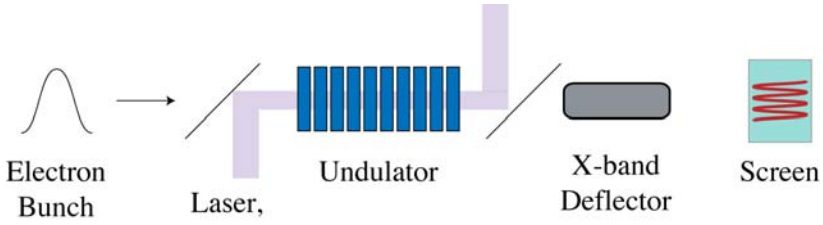

Figure 1: Conceptual design of diagnostic scheme. An angular modulation is imparted at the undulator, and a deflector provides a vertical sweep. The pattern is resolved on a screen and the curve is correlated to the beam longitudinal profile.

3.5.2.1 *Laser Modulator*

The first component of the system consists of the laser modulator, or undulator (Fig. 1). The laser interaction in the undulator provides a method to correlate the beams temporal extent to its energy and transverse angular modulation. The laser modulator is based on a concept by Zholents and Zolotorev [15] to modulate a short pulse electron beam within an undulator field and in the presence of a high-power laser operating in the TEM_{10} Hermite Gaussian mode. In our scheme, we apply a similar method using a long wavelength, high power laser, to generate an angular modulation of the electron beam via the interaction in the undulator field.

The electric field of the TEM_{10} mode is given by,

$$E_x(x,z,t) \simeq \frac{2\sqrt{2}\,E_0\,x}{w_0\left(1+\frac{z^2}{z_0^2}\right)}\sin(k(z-ct)+\phi)$$

where $k = 2\pi/\lambda$ is the laser wavenumber and λ is the laser wavelength, $w_0$is the laser waist, and z_0 is the Rayleigh range. E_0 is the field amplitude and ϕ is the phase. Here we have assumed that the transverse beam size is much smaller than the laser waist and the Rayleigh range is much larger than the interaction region.

The electron has a transverse velocity inside the undulator that is given by:

$$\beta_x = -\frac{K}{\gamma}\sin\left(\frac{2\pi\,z}{\lambda_u}\right)$$

with $K = \frac{e\,B_0\lambda_u}{2\,\pi m_0 c}$ is the undulator parameter dependent on the peak field, B_0 and the undulator period λ_u. The energy change for the electron in the presence of the laser field is given in general by,

$$\frac{d\gamma}{dt} = \frac{e}{m_0 c}E_x \cdot \beta_x$$

Combining the equations yields an expression for the energy change in the beam,

$$\frac{\Delta\,\gamma}{\gamma} = \eta_1 - \eta_0 = A\,kx_0\cos(k\,s_0)$$

where the dimensionless parameter *A* is defined as,

$$A = \frac{2K}{\gamma^2}\sqrt{\frac{P_L}{P_0}}[JJ]\,f(L_u, z_0, \nu)$$

In the expression for *A*, P_L is the laser power, [*JJ*] is the sum of Bessel functions dependent on *K*, and the function *f* is a detuning term that depends only on the undulator length, the laser Rayleigh range and the deviation from resonant energy of the beam.

This dimensionless function may also include beam emittance effects and is peaked at values of 2-3 for all practical cases.

By using an extension of the Panofsky-Wenzel theorem,

$$\frac{\partial}{\partial x}\left(\frac{\Delta\gamma}{\gamma}\right) = \frac{\partial}{\partial s}\Delta x'$$

the angular modulation (horizontal) is given by

$$\Delta x' = A\sin(ks_0 + \phi)$$

The longitudinal profile of the electron beam is now encoded onto the horizontal beam angular modulation (Fig. 2). As long as this angular modulation is greater than the intrinsic beam divergence, the concept of temporal beam diagnosis is viable. The angular modulation is resolvable on a distant screen. The beam sweeps out a pattern on the screen with maximum amplitude equal to $2AL$, where L is the distance to the screen.

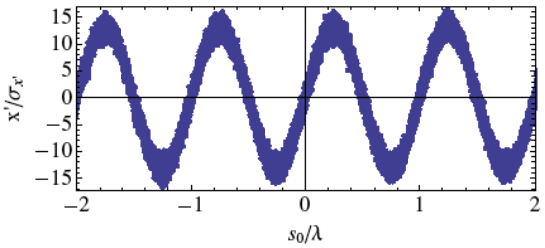

Figure 2: Angular modulation imposed on the electron beam after interaction with the laser in the TEM_{10} mode in the undulator field.

The temporal resolution of this diagnostic is correlated to the angular modulation of the beam in the undulator. However, there is also a strict correlation between the angular modulation and the energy spread. In fact, the energy spread growth inside the undulator for large modulations threatens to wash out the structure for some realistic applications. There are simple solutions, discussed in the following sections, to alleviate this matter such as using a beam collimator upstream of the undulator, or decreasing the number of periods (and thus the R_{56} growth) of the undulator. Finally, the angular modulation scales well for beams of low energy, because the amplitude A is inversely proportional to the square of the energy. The applicability of the diagnostic has been studied in simulations for beams with energies up to 120MeV (see following section).

3.5.2.2 ***Deflector***

The second step of the scheme requires sending the modulated electron beam through an RF deflector (or transverse deflecting cavity), with the deflection orthogonal to the horizontal divergence imposed by the laser modulator. The high frequency time-variation of an RF field deflects the electrons so that a time-dependent transverse kick is imparted. This creates a strong correlation between the longitudinal and transverse position (vertical) of the bunch when viewed upstream on a scintillating screen.

The RF deflector performs an analogous phase space transformation to the laser modulator, but in the vertical dimension, at a wavelength long compared to the longitudinal size of the beam:

$$y_2' = y_1' + A_{RF}k_{RF}s_1;$$

$$\eta_2 = \eta_1 + A_{RF} k_{RF}\, y_1$$

Here A_{RF} is proportional to the deflecting voltage, V_0, and is given by

$$A_{RF} = \frac{eV_0}{\gamma mc^2}$$

The subsequent drift, of length L (see Fig. 1) maps the beam at the deflector exit to the diagnostic screen following the transformation for a simple drift. The bunch resolution on the screen after the drift, now only depends on the initial 6D phase space distribution, and the amplitudes of modulation from the laser modulator and the deflector (Fig. 3). Assuming an initial round, Gaussian beam, the resulting distribution after the full transformation (see Ref. 14 for detailed derivation) at the screen is then,

$$f_0 = \frac{1}{(2\pi)^{3/2}\sigma_{x_D}^2 \sigma_z} \mathrm{Exp}\left[-\frac{(x - AL\sin ks_0)^2}{2\sigma_{x_D}^2} - \frac{(y - A_{RF}k_{RF}Ls_0)^2}{2\sigma_{x_D}^2} - \frac{s_0^2}{2\sigma_z^2}\right]$$

where we have used the expression

$$\sigma_{xD}^2 = \sigma_x^2 + L^2\sigma_x'^2$$

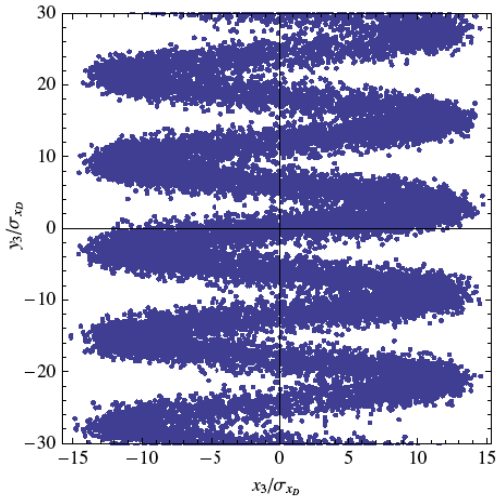

Figure 3: Transverse distribution on the screen after deflection. The longitudinal bunch coordinate is correlated to the trace along the sinusoidal curve.

3.5.2.3 *Longitudinal Diagnostic*

From the results of the previous section, we can now begin to analyze the temporal resolution and its limits. The bunch resolution is set by the amplitude of the angular modulation generated by each component in the scheme. This amplitude must be greater than the intrinsic beam divergence to properly resolve structure. For the RF deflector, this requires, in terms of longitudinal resolution, $\Delta z_{RF} = \sigma_x'/A_{RF}k_{RF}$. This quantity must be less than the wavelength of the laser used in the modulator to distinguish particles in adjacent cycles. The resolution of the laser modulator is analogously given by $\Delta z_{LM} = \sigma_x'/Ak$. The effective temporal resolution of the entire system is then approximately given by the resolution of the laser modulator because

with high power laser systems, Ak can be made much larger than $A_{RF}k_{RF}$. The temporal resolution can be written as,

$$\Delta t \simeq \Delta t_{LM} = \frac{\epsilon_{n,x}}{\gamma c A k \sigma_x}.$$

This is a significant improvement in resolution compared to the deflector alone.

For the scheme to be an effective bunch length monitor, the rms beam size at the screen must be greater than the beam size of the unperturbed beam traveling through the drift. A final constraint is that these sizes must be smaller than the screen dimensions if one wishes to resolve the full beam.

The longitudinal profile of the beam can be mapped to the trace on the screen (transverse distribution). This correlation is given by the equation for the sinusoid of the distribution at the final screen:

$$x(y) = AL \sin(\frac{ky}{k_{RF}A_{RF}L})$$

3.5.3 **Examples**

The bunch length diagnostic scheme has been studied for three cases. The first two cases (UCLA Neptune and BNL ATF) offer the possibility for a proof-of-principle experiment because these facilities utilize a high-power, long wavelength CO_2 laser for experiments on laser-electron beam interaction. The third example (echo-enabled FEL at the SLAC NLCTA) demonstrates the need for a diagnostic with sub-fs resolution. The simulations conducted in this section where performed using Elegant [16].

3.5.3.1 ***UCLA Neptune***

The UCLA Neptune facility has a high brightness beam of 13 MeV, with an emittance of 3mm-mrad and charge of 300pC. The facility also employs a high power CO_2 laser (λ=10.6μm) that reaches TW-scale power. It has hosted other electron-beam-laser interaction experiments [17,18,19]. For this example we consider a 10-period, undulator that is resonant at the laser wavelength (10.6μm). The undulator parameter is K=.0855 (period of 9mm, peak field of 1.02T) [20]. We also consider an RF deflector of length 30cm, operating at a deflecting voltage of 5MV in the X-band frequency ($\lambda_{RF} = 2.6$cm). A 200μm round collimator is used at the beginning of the undulator to reduce the effects of energy spread growth accumulated in the undulator.

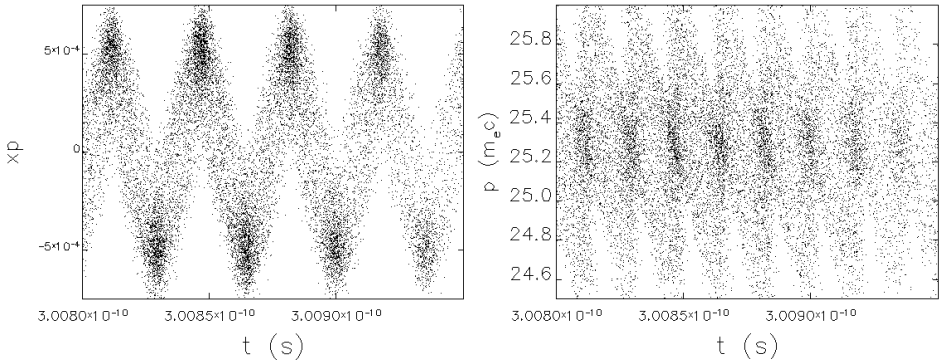

Figure 4: The temporal-transverse angular correlation of the beam immediately after the laser modulator section for the Neptune parameter set (left). The beam phase space after the laser modulator section (right). Simulations performed with Elegant.

The beam is coupled to the TEM_{10} laser mode with a laser power of 300 MW. The angular modulation imposed by the laser modulator is shown in (Fig. 4-left) as well as the microbunched phase space (right). The temporal structure of the beam is encoded into the transverse trace space and propagated to the deflecting cavity. The deflector imparts a vertical kick, when operated at the zero RF crossing, to impose a vertical-temporal correlation on the beam. The beam is then propagated through a 1m long drift to a diagnostic screen. Figure 5 shows the resultant image on the screen (the beam transverse distribution) for two cases. First, with the laser modulation turned off, the beam samples the RF deflector kick and the vertical coordinate after the drift correlates directly to the temporal beam profile (Fig. 5- left). The resolution of such a system is on the order of <10fs for the given parameters. Then the laser modulator is turned on, and the beam distribution has a sinusoidal shape, which improves the resolution to <1fs for the Neptune parameters (Fig. 5- right).

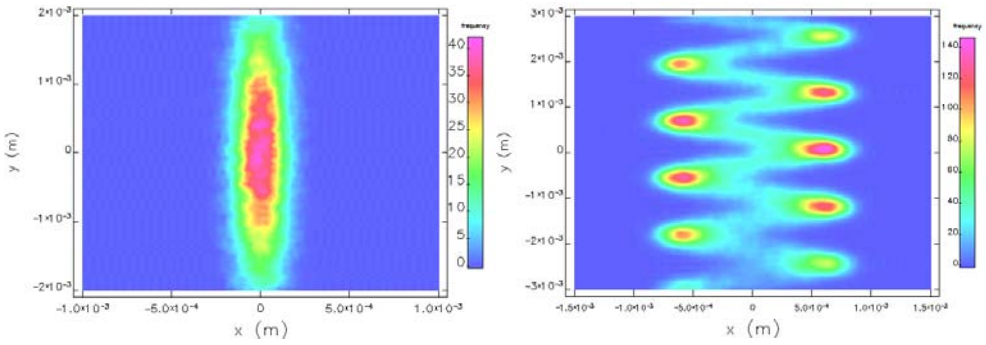

Figure 5: Beam distribution at the final screen for the case with the RF deflector and no laser modulator (left). The final beam distribution on the diagnostic screen when the laser modulator is employed (right). Simulations performed with Elegant.

The relatively low energy beam provides a large angular modulation amplitude while maintaining reasonable emittance. One caveat of operating at low energies is that the beam at Neptune is susceptible to space-charge forces that are not fully accounted in the model. This effect may threaten to wash out structure, especially at short pulse lengths and tight focuses.

3.5.3.2 *BNL ATF*

The Brookhaven National Laboratory Accelerator Test Facility (BNL ATF) delivers high-brightness electron beams for a variety of advanced accelerator applications. The user-facility is also rich in history in e-beam –laser interactions [21,22,23]. The beam can operate at energies between 45-85 MeV with a nominal charge of 0.5 nC, while preserving the emittance at 1mm-mrad. The high power CO_2 laser is able to generate power >100 GW, with an imminent upgrade to TW levels. Also, the ATF has dedicated X-band infrastructure which includes a klystron and, recently, a ~50 cm X-band deflector.

For the BNL ATF scenario, we consider a 10-period undulator, resonant at the laser wavelength of 10.6μm; this is an undulator similar to the existing LCLS undulator [24,25] with a period of 3cm, and field strength of 1.06 T (K=3.0). For the RF deflector, we consider an X-band cavity (λ_{RF}=2.6 cm) with a length of 46cm (currently installed at the BNL ATF). In addition, we use a 200 μm round collimator upstream of the undulator entrance to reduce the beam size and effective emittance.

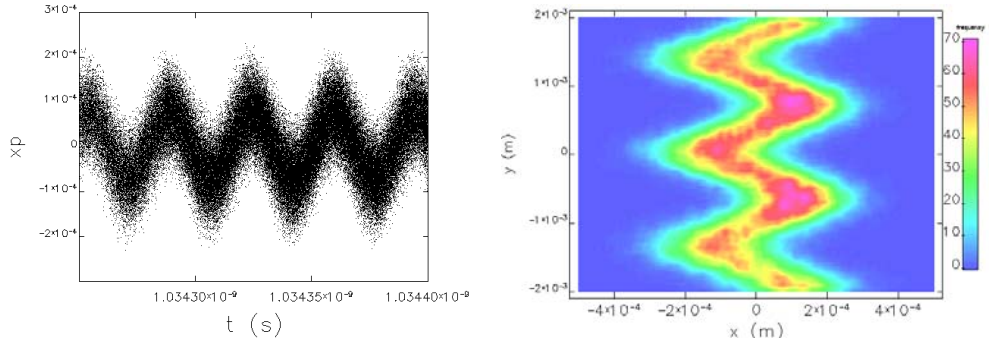

Figure 6: The angular modulation after the laser modulator (left) and the projection on the diagnostic screen after the deflector and 1m drift for the ATF case. Simulations performed with Elegant.

The angular modulation amplitude of the interaction with the laser TEM_{10} mode and power of 3GW is shown in simulation in Fig. 6 –left. The amplitude is on the order of $\Delta x' = 2 \times 10^{-4}$. The beam is propagated through the deflector and a 1m long drift to the final screen shown in false color in Fig. 6–right. The angular modulation results in a sinusoidal pattern with amplitude >200μm. This is readily resolvable using standard optical techniques and an ideal demonstration of the principle. The results for the ATF case are enabled by the high power CO_2 laser program at the facility.

3.5.3.3 *Echo-Enabled FEL at SLAC NLCTA*

As an example of the need of sub-femtosecond resolution in a practical case, we refer to the echo-enabled free electron laser (FEL) experiment at the SLAC NLCTA facility [26]. The echo-enabled free-electron laser requires the energy modulation of an electron beam in an undulator driven by a laser (λ~800nm), followed by compression in a chicane. The beam is then sent through a second modulator with a laser driver operating at double the wavelength (λ~1600nm) and a second chicane to impose density modulations at very short wavelengths. This scheme is an alternative to high harmonic gain FELs to reach x-ray resonant wavelengths. The diagnostic in the experiment is the observation of coherent radiation emitted at the laser harmonics. However, because the

laser driver wavelengths are multiples of each other, the harmonics overlap and it is not trivial to determine if the interaction is driven by the modulation of a single laser, or the interplay of both lasers. A direct measurement in the time-domain would provide direct evidence of the echo-enabled process, however using only an RF deflector with the highest reported resolution, features on the order of 5fs or less are not resolvable. The enhancement to the rf deflector provided by the laser modulator in the proposed diagnostic has the ability to unambiguously confirm the physics underlying the echo enabled FEL case (Fig. 7). The beam parameters for Fig. 7 include energy of 120 MeV, emittance of 1 mm-mrad and a 3-period undulator with K = 6, and period of 6 cm.

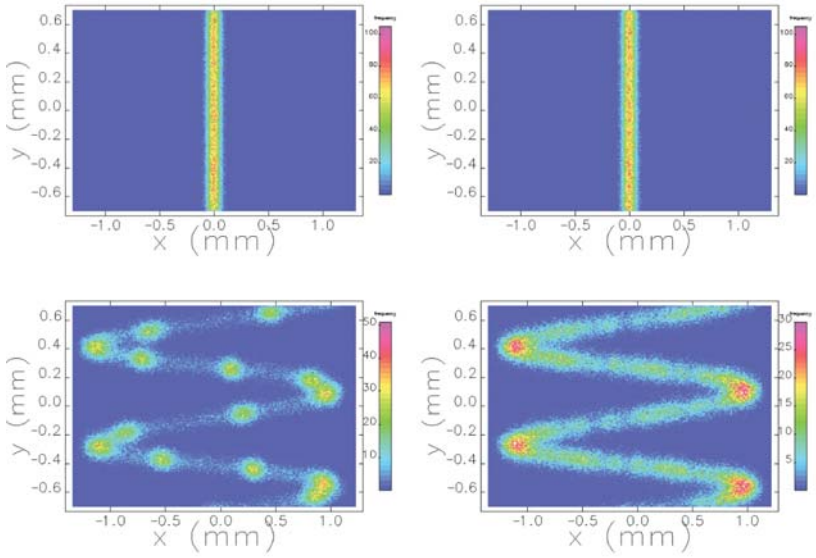

Figure 7: A comparison of the effect of a single laser modulation (left column) and modulation caused by the interplay of two lasers (right column). Top row, the observation screen when only the deflector is powered showing indistinguishable traces. Bottom row, the screen when the laser modulator is also powered, demonstrating enhanced resolution and the ability to differentiate the two effects.

3.5.4 **Alternative Scheme**

The approach proposed above is not the only way to apply a transverse-longitudinal coordinate correlation on the electron beam. One other method currently under study, involves adding another element in the concept to simplify some of the practical issues, specifically related to producing and transporting the TEM_{10} mode in a high power system. In this alternative scheme, a dipole magnet is added just downstream of the modulator (upstream of the deflecting structure in Fig. 8). This system is comparable to other methods that attempt to measure the longitudinal phase space of the beam [27].

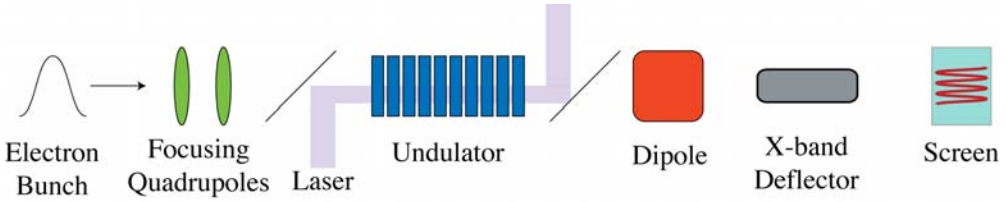

Figure 8: Alternate design for the sub-fs diagnostic includes a dipole magnet.

The advantage of this system is that the laser now operates in the more familiar fundamental TEM_{00} mode to produce an energy modulation on the beam. The subsequent dipole magnet provides a correlation between the transverse coordinate and the energy analogous to the horizontal divergence created by the original laser modulator. In Fig. 8, additional focusing quadrupole magnets are used to optimize the beam prior the interaction. The downstream components (deflector and drift) are identical and a similar temporal resolution can be obtained with the alternative approach.

Figure 9 shows an output of the final transverse distribution using Elegant simulations using a beam with energy 45MeV, normalized emittance of 1 mm-mrad. Such a beam is realizable at the BNL ATF or the SLAC NLCTA facilities. The undulator is 5-periods with a total length of 15cm, resonant at the laser wavelength. The 10.6μm laser operates at the fundamental with a power of 100MW. Indeed, the reduced demands on the laser (power, and operating mode) may make such a scheme more favorable and readily realizable at many facilities.

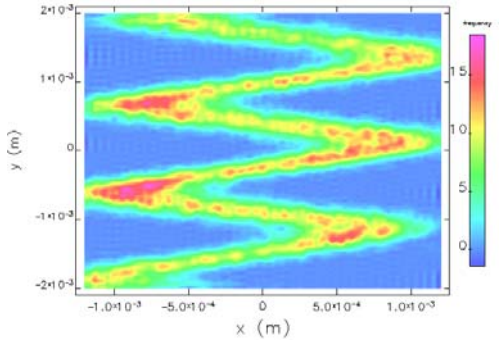

Figure 9: Final transverse distribution on screen after interaction in the undulator, dipole, and deflector.

3.5.5 **Conclusions**

The experimental demonstration of the sub-fs sweeping concept in application to bunch length diagnosis is currently underway. The theoretical and numerical examples show that such a method is viable under certain beam conditions. There are also some limitations to the extent of the scheme. For example, although the resolution is enhanced compared to a deflector alone, the resolution is not linear. In fact, at the turning points of the sinusoidal trace, the resolution is equal to that of the deflector. In a practical measurement, one may circumvent this issue by changing the laser phase (which may also occur due to the inherent jitter in the system) so that different parts of

the beam are sampled on different shots at the "high-resolution" part of the curve (the linear part).

The diagnostic proposed herein provides resolution on the sub-fs scale for high brightness electron beams. The proof-of-principle experiment is underway for testing at the BNL ATF with the possibility to engage the diagnostic at the SLAC NLCTA in the near future, to unambiguously ascertain the beam modulation given by the echo-enabled FEL program.

3.5.6 **References**

1. *Linac Coherent Light Source Design Study Report*, SLAC-R-521 (1990).
2. TESLA FEL, Deutsches Elek. Synch. 2001-05, Tech. Report DESY-01-011, Germany (2001).
3. B.D. Patterson, *et al.,* New J. Phys. **12** 035012, (2010).
4. S.G. Anderson, *et al.*, Phys. Rev. STAB **8**, 014401 (2005).
5. L. Serafini and M. Ferrario, AIP Conf. Proc. **581**, 87 (2001).
6. H. Loos et al., Proceedings of FEL08, Gyeongju, Korea, 2008, JACoW, THBAU01.
7. I. Wilke, *et al.*, Phys. Rev. Lett. **88**, no.12, 124801 (2002).
8. U. Happek, A.J. Sievers, E.B. Blum, Phys. Rev. Lett. **67**, no.21, 2962 (1991).
9. R. Akre, *et al.*, Phys. Rev. STAB **11**, 030703 (2008).
10. G. Andonian, *et al.*, Phys. Rev. STAB **12**, 030701 (2009).
11. D. X. Wang *et al.,* Phys. Rev. E **57** pp. 2283-2286 (1998).
12. E. Saldin *et al.*, Nucl. Instrum. and Meth. A **539**, 449 (2005).
13. D. Xiang and Y. Ding. Phys. Rev. ST Accel. Beams **13,** 094001 (2010).
14. G. Andonian, *et al*., Phys. Rev. ST Accel. Beam **14**, 072802 (2011)
15. A. Zholents and M. Zolotorev, *New Journal of Physics* **10**, 025005 (2008).
16. M. Borland, APS Technical Report Bo. LS-287 (2000).
17. P. Musumeci, *et al.*, Phys. Rev. Lett. **94**, 154801 (2005).
18. S. Tochitsky, *et al.*, Phys. Rev. STAB **12**, 050703 (2009).
19. E. Hemsing, *et al.*, Phys. Rev. Lett. **102**, 174801 (2009).
20. F. O'Shea *et al.*, Phys. Rev. STAB **13**, 070702 (2010).
21. W. Kimura, *et al*., Phys. Rev. Lett. **74**, 546 (1995).
22. E. Kallos*, et al*., Phys. Rev. Lett. **100**, 074802 (2008).
23. I. Pogorelsky, *et al*., Phys. Rev. STAB **1**, 090702 (2000).
24. I. Vasserman, *et al.*, Proc FEL 2004, 367, Trieste, Italy (2004).
25. E. Trakhtenberg, *et al.*, Proc PAC 2007, 1148, Albuquerque, NM, USA (2007).
26. D. Xiang, *et al.*, Phys. Rev. Lett. **105**, 114801 (2010).
27. C. Behrens and Ch. Gerth, Proc DIPAC09, TUPB44, Basel, Switzerland (2009).

3.6 Single-Spike Self-Amplified Spontaneous Emission Free-Electron Laser Experiments at SPARC

Gabriel Marcus
Lawrence Berkeley National Laboratory,
1 Cyclotron Road, Berkeley, CA 94720, USA
Mail to: gmarcus@lbl.gov

3.6.1 Introduction

Single pass x-ray, self-amplified spontaneous emission free-electron lasers (SASE FELs), such as the Linac Coherent Light Source (LCLS) [1], have become an essential tool for the investigation of ultrafast chemical and physical processes as they have the ability to operate at spatial and temporal scales of atomic and molecular motion [2-4]. FELs operate on the principle that tunable, narrow bandwidth light pulses can be emitted and amplified by the strong beam-radiation instability affecting a relativistic electron beam (*e*-beam) traversing a periodic magnetic undulator. SASE FELs are only partially coherent, however, as the emitted light is the result of the amplification of initial incoherent radiation shot noise. Thus, the temporal structure of the light pulse is a collection of phase-uncorrelated coherent spikes randomly distributed over the emitting *e*-beam's longitudinal profile. Complete control of the light's time-frequency distribution (something akin to a longitudinal phase-space), including the development of longitudinal coherence at the Fourier limit, is essential for next generation FELs and will allow investigation into the dynamics of electrons, spins and phonons with unprecedented spatial and temporal resolution. There is, therefore, a strong case for extending the temporal duration of these ultrafast pulses into the sub-femtosecond regime.

Longitudinal coherence may be established in an FEL by seeding it with an external laser [5] at the fundamental frequency given by

$$\omega_r = \frac{2\gamma^2\omega_u}{1+K^2/2+\gamma^2\theta^2}, \tag{1}$$

where $\omega_u = 2\pi c/\lambda_u$, $K = eB_u\lambda_u/2\pi m_0 c$ is the undulator strength parameter, λ_u is the undulator period, γ is the electron beam energy in units of the rest energy m_0c^2, and θ is the emission angle from the nominal *e*-beam propagation direction, z. This principle can be extended to higher harmonics through various processes including high-gain harmonic-generation (HGHG) [6,7], FEL cascades [8], and echo-enabled harmonic generation (EEHG) [9]. These methods, however, are all constrained by the availability of a suitable seed laser source. Alternatively, it is possible to obtain longitudinally coherent single-spike operation from a SASE FEL if the gain region within the *e*-beam is limited to only a few cooperation lengths [10], defined as the slippage distance of the FEL light with respect to the electrons in a power gain length. The cooperation length is given as

$$L_c = \frac{\lambda_r}{4\pi\sqrt{3}\rho}, \tag{2}$$

where ρ is the well known Pierce parameter [11]. This can be accomplished through various mechanisms including compression of low-charge, high-brightness *e*-beams [12] or through transverse or longitudinal phase-space manipulations that preferentially concentrate the gain along a small portion of the *e*-beam [13-18]. The development of longitudinal coherence through phase-space manipulations might suggest measuring the FEL longitudinal time-frequency distribution directly. Additionally, many qualitative longitudinal characteristics of ultrafast pulses can be obtained directly from a time-frequency distribution. This observation, however, is not possible in the x-ray wavelength range because of the lack of appropriate diagnostics. Thus, one must examine, as is often the case in FEL research, the physics of these schemes at longer wavelengths.

This report serves a dual purpose in the context of the application, control, and diagnosis of femtosecond beams. It summarizes recent experimental results that were obtained at the SPARC FEL test facility in Frascati, Italy showing the development of longitudinal coherence from a SASE FEL amplifier under advanced *e*-beam phase-space manipulation techniques in the optical wavelength regime. Additionally, the concept of *phase-space optics* [19] is briefly introduced and is discussed in the context of Frequency-Resolved Optical Gating (FROG) [20]. Time-domain measurements of near single-spike pulses were made at SPARC using an advanced FROG diagnostic based on a Transient-Grating (TG) geometry and are discussed briefly. The results presented in this report indicate a possible pathway for the production of near Fourier-transform limited single-spike radiation in the femtosecond regime at X-ray wavelengths. Furthermore, this report serves as a very brief review/introduction of phase-space optics and the FROG technique for the uninitiated in the field of *e*-beam physics in hopes that it will stimulate discussion on how to advance this diagnostic modality to shorter wavelength operation.

3.6.2 *e*-beam Energy Chirp and Undulator Tapering Experiment

One promising method to increase the longitudinal coherence of SASE FEL radiation relies on electron beam phase space manipulations that preferentially concentrate the gain along a small longitudinal portion of the *e*-beam. The method utilizes an energy-chirped *e*-beam and an appropriately chosen undulator taper (secular variation of the undulator field amplitude or period along the nominal beam propagation direction, z). This method is described in detail elsewhere [13-15], but can be summarized as follows: the resonant frequency of light amplified in a FEL is determined by, among other things, the *e*-beam's mean energy (see equation 1). The amplified light propagates forward with respect to the electrons because its group velocity is larger than the *e*-beam velocity. In an energy-chirped *e*-beam this velocity mismatch brings an amplifying radiation spike out of resonance as it slips forward in the *e*-beam frame, inhibiting the gain, unless an appropriate undulator taper is applied to compensate for the local change in resonance.

3.6.2.1 *The SPARC Facility*

This scenario was recently investigated at the SPARC FEL test facility in Frascati, Italy [14]. High brightness *e*-beams are created at SPARC using an injector that consists of a 1.6 cell RF photocathode gun (one of the most recent iterations of the S-band BNL/UCLA/SLAC type [21]), followed by three traveling wave linac sections, two of

which are embedded in focusing solenoids. Longitudinal *e*-beam compression is obtained by running the first linac section off crest near the zero-crossing phase, where the first solenoid is used to optimize the emittance compensation process [22]. This method, termed velocity bunching [23], gives an increase in the peak current while leaving a residual energy chirp in the electron beam longitudinal phase space [24, 25]. Two quadrupole triplets along with a dipole based magnetic spectrometer and RF deflecting cavity allow the measurement of time-projected and time-resolved (slice) longitudinal and transverse *e*-beam parameters. These same transport optics match the *e*-beam into the undulator, which is comprised of 6 independent, variable gap sections. The undulator sections were discretely tapered through gap adjustment to compensate for the detuning experience by a propagating radiation spike. A more detailed description of the facility can be found in reference [26].

3.6.2.2 ***Results in the Spectral Domain***

The first results using the *e*-beam energy chirp in combination with a compensating undulator taper were obtained in the spectral domain using an in-vacuum spectrometer [27] located downstream of the last undulator section. This spectrometer covers the spectral range from $35-560$ nm and can operate in both the single shot and integrated modes. Most of the FEL light statistics from the chirp/taper experiment were measured with this spectrometer and are reported in [14]. The experiment was optimized to produce radiation at the resonant wavelength $\lambda_r = 540$ nm. Figure 1 shows a typical single-shot spectrum taken for an energy chirped *e*-beam in the absence of an undulator taper.

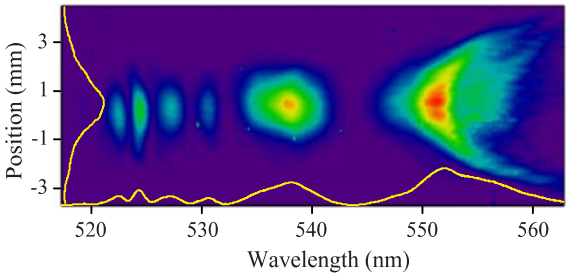

Figure 1: Sing-shot spectrum in the absence of an undulator taper.

The large energy chirp produced a broadband spectrum. In order to compensate for the *e*-beam energy chirp, each undulator was progressively tuned, starting with the first, while minimizing the spectral width on the spectrometer. This process led to an increase in the pulse energy and a narrowing of the spectrum. A representative plot of the spectrum following the undulator tapering can be found in Figure 2 and is compared to results from numerical particle simulations using the FEL code GENESIS.

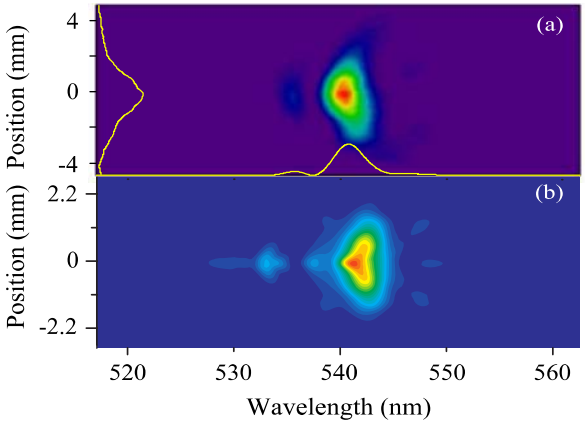

Figure 2: Single-shot spectrum after undulator tapering from the spectrometer (a) and from GENESIS simulations (b) showing roughly one coherence region.

The pulse in Figure 2 had an energy of $300\ \mu J$ and an rms bandwidth of roughly 1.45 nm. A Fourier limited pulse with these characteristics would have an rms duration of $\sim 50\ fs$ and a peak power of 2 GW. The direct measurement of the development of longitudinal coherence in this manner in the time-domain, however, required the implementation of an advanced FROG diagnostic.

3.6.3 Phase-Space Optics – An Introduction

3.6.3.1 *Ultrashort Laser Pulses*

The fundamental quantity of interest that describes an individual pulse of light is the *real* electric field vector $\vec{\varepsilon}(\vec{r},t)$, which is a function of both time (t) and space $(\vec{r})$. The function of any ultrafast diagnostic should be to completely characterize the electric field. This can be somewhat difficult if the field has a complicated spatial dependence. For the time being, the spatial dependence of the field is neglected since the longitudinal (or temporal) structure of the pulse is of greater current interest. The problem is further simplified by making the *scalar approximation*, where the electric field's vector nature is neglected. Simultaneous measurement of two orthogonal polarizations can be combined to yield the full pulse field if necessary. In addition, the *analytic signal* approximation [28, 29] is made, which allows the electric field to be reduced to the following complex form that unambiguously specifies the amplitude and phase:

$$E(t) = \sqrt{I(t)}\exp\left[-i\phi_t(t)\right]. \tag{4}$$

Here, $I(t) = \left|E(t)\right|^2$ and $\phi_t(t)$ are the time-dependent intensity and phase respectively. The field in the frequency domain is found through the application of the Fourier transform:

$$\tilde{E}(\omega) = \sqrt{S(\omega)}\exp\left[i\phi_\omega(\omega)\right] = \frac{1}{\sqrt{2\pi}}\int E(t)\exp\left[-i\omega t\right]dt, \tag{5}$$

where $S(\omega)$ and $\phi_\omega(\omega)$ are the spectral intensity and phase respectively. In order to fully characterize an ultrashort pulse it is sufficient to measure the intensity and phase in either the temporal or spectral domains. However, measurements of the pulse spectrum or the field or intensity autocorrelation fail to obtain the relevant phase information. Thus, full longitudinal pulse reconstruction is not possible using traditional one-dimensional pulse measurement methods.

The complimentary nature of the description of ultrashort laser pulses in both the time and frequency spaces suggests that they can be well described by joint time-frequency distributions in the two-dimensional (t,ω) phase-space. The distributions are central to the characterization of ultrashort pulses because the waveform is not currently directly measurable by today's diagnostics (an optical pulse in the visible spectrum has a period of less than 3 femtoseconds). It turns out that the ultrashort pulse phase information can be recovered from specific phase-space distributions using two-dimensional Fourier transform algorithms [30]. The phase-space description also provides an excellent framework for describing optical pulses that are measured by standard square-law (energy) detectors such as photodiodes.

3.6.3.2 *Phase-Space Descriptions*

There exist many examples of joint phase-space distributions [31], the most common of which is the Wigner distribution:

$$W(t,\omega) = \frac{1}{2\pi}\int E^*\left(t-\frac{\tau}{2}\right)E\left(t+\frac{\tau}{2}\right)\exp[-i\tau\omega]d\tau. \qquad (6)$$

There are many features that make the Wigner distribution attractive for representing short optical pulses. For instance, it is always real, even if the field, $E(t)$, is complex. Also, the projection of the Wigner distribution onto one coordinate axis by integration over the conjugate coordinate, producing what is known as a marginal, yields either the pulse temporal or spectral intensity. However, the Wigner distribution is not positive definite, and thus, cannot necessarily be directly measured by square-law detectors. This concept is illustrated in Figure 3.

It turns out that the Wigner distribution is only one belonging to a class of bilinear distributions that can be obtained from the general *Cohen class*:

$$C(t,\omega) = \frac{1}{4\pi^2}\iiint E^*\left(u-\frac{\tau}{2}\right)E\left(u+\frac{\tau}{2}\right)K(\theta,\tau)\exp\left[-i(\theta t+\tau\omega-\theta u)\right]dud\tau d\theta. \qquad (7)$$

Here, $K(\theta,\tau)$ is a two dimensional function called the kernel. The Wigner distribution is recovered when $K(\theta,\tau)=1$. If, however, the kernel in equation 6 is taken to be the ambiguity function

$$A(\theta,\tau) = \int g^*\left(t-\frac{\tau}{2}\right)g\left(t+\frac{\tau}{2}\right)\exp[i\theta t]dt, \qquad (8)$$

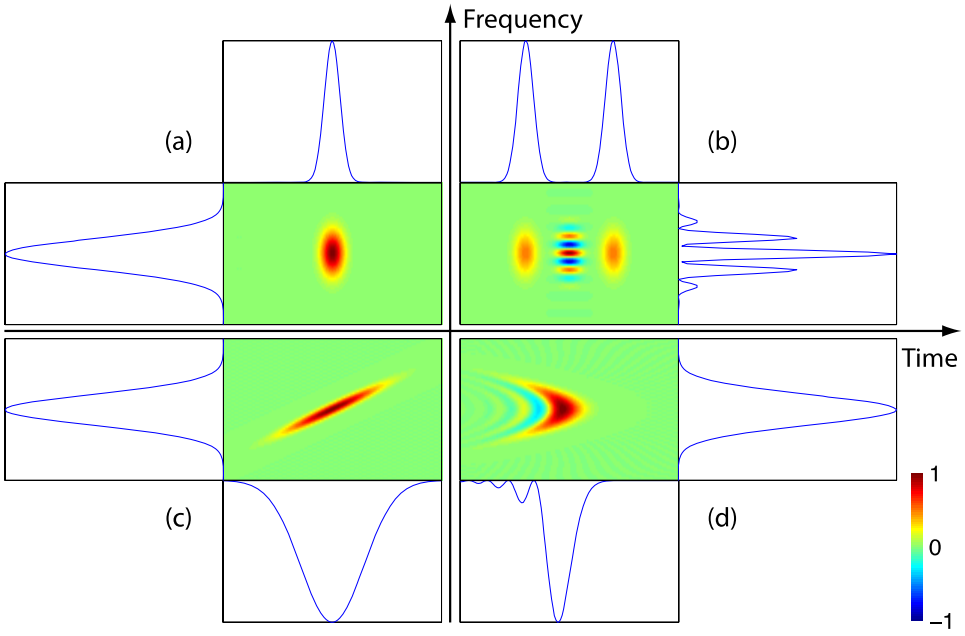

Figure 3: Wigner distribution (normalized) and the marginals of: (a) a Fourier limited Gaussian pulse, (b) two identical Fourier limited Gaussian pulses separated in time, (c) a Gaussian pulse with second order spectral phase, (d) a Gaussian pulse with third order spectral phase.

of an ancillary signal, $g(t)$, with the exception that $K(\theta,\tau) = A(-\theta,\tau)$ the Gabor Spectrogram is obtained:

$$S(\tau,\omega) = \left| \frac{1}{\sqrt{2\pi}} \int E(t) g(t-\tau) \exp[-i\omega t] dt \right|^2 . \tag{9}$$

Examples of spectrograms can be found in Figure 4. It should be noted that the spectrogram is positive definite, and can thus potentially be measured by square-law detectors.

It is clear that the spectrogram is simply the magnitude squared of the Fourier transform of a signal field that takes the form $E_{sig}(t,\tau) = E(t)g(t-\tau)$. For this reason, the spectrogram is often referred to as the short-time Fourier transform, because the gate, $g(t)$, presumably emphasizes the field, $E(t)$, for a short time interval around the time $t = \tau$, and suppresses it at all other times. Determining the spectrum of the signal field is the mathematical equivalent of taking it's Fourier transform. This is the operating principle behind frequency-resolved optical gating [32]. A FROG diagnostic measures the signal *spectrum vs. delay* as opposed to the signal energy vs. delay. Measuring the signal spectrum for all delays, by scanning the gate pulse over the unknown pulse longitudinal profile, results in the two-dimensional spectrogram, referred to now as a FROG trace.

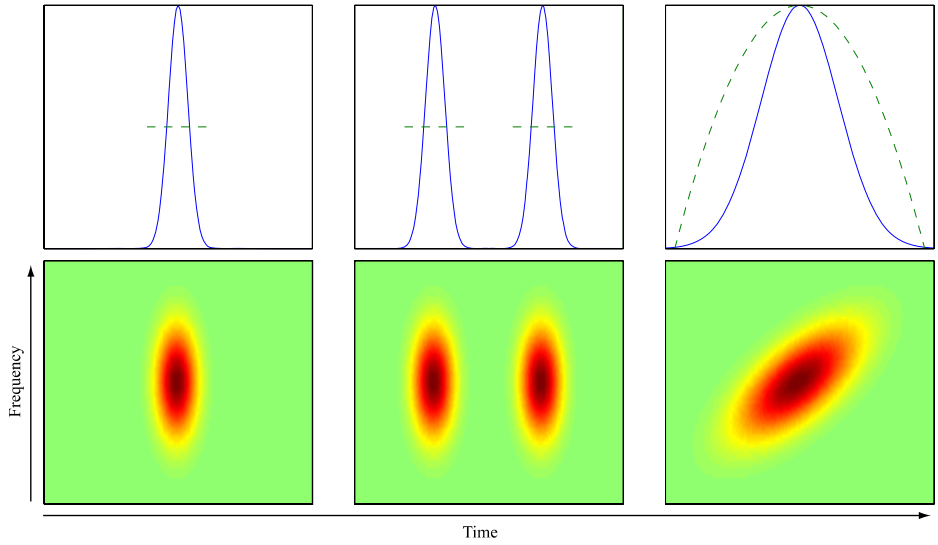

Figure 4: Different Gaussian pulses (top) and their Spectrograms (bottom) for a Gaussian gate pulse. There is a notable difference between the Gaussian pulse with chirp (right) and the Gaussian pulse with a flat spectral phase (left). Notice that the spectrogram does not have the interference region between the two pulses that was seen in the Wigner distribution of a similar pulse (center).

3.6.3.1 *TG FROG*

A FROG diagnostic makes an autocorrelation-type measurement in which the autocorrelation signal field is spectrally resolved. Interfering an unknown pulse with an identical copy inside a nonlinear optical medium generates the autocorrelation signal field. The gate pulse in the expression for the spectrogram in equation 9 is therefore a function of the pulse that is being measured, and depends on which type of nonlinear optical process is used to generate the autocorrelation signal field. Iterative Fourier transform algorithms then extract the phase information and allow for a full longitudinal pulse reconstruction.

The TG FROG diagnostic used to extract the longitudinal profile at the SPARC facility was constructed with the unique capabilities and challenges of measuring FEL output in mind, particularly in its extendibility to short wavelength operation. It was based on a geometry first proposed and demonstrated by Lee [33]. The diagnostic geometry as constructed is shown in Figure 5. The light entering the FROG device is first expanded to a relatively large diameter using a basic telescope, allowing the generation of three identical copies of the input beam after passage through an input mask. The application of the mask is vital as it avoids the use of multiple delay stages and beam splitters, and associated alignment difficulties, to produce the three copies of the beam. More importantly, however, the beam expansion serves to transversely filter the pulse. This mitigates possible sources of corruption in the FROG reconstruction algorithms that may result from non-uniform transverse intensity profiles as well as spatial (transverse) frequency chirp. Spatial chirp is prevalent in FEL light pulses and is a result of the angular dependence of the FEL resonance condition on the emission angle (see equation 1). After their generation, the probe (from the lower hole in the mask) and two gate pulses (from the upper holes in the mask) are passed through a

cylindrical lens, which brings each pulse to a line focus within the third-order nonlinear optical medium.

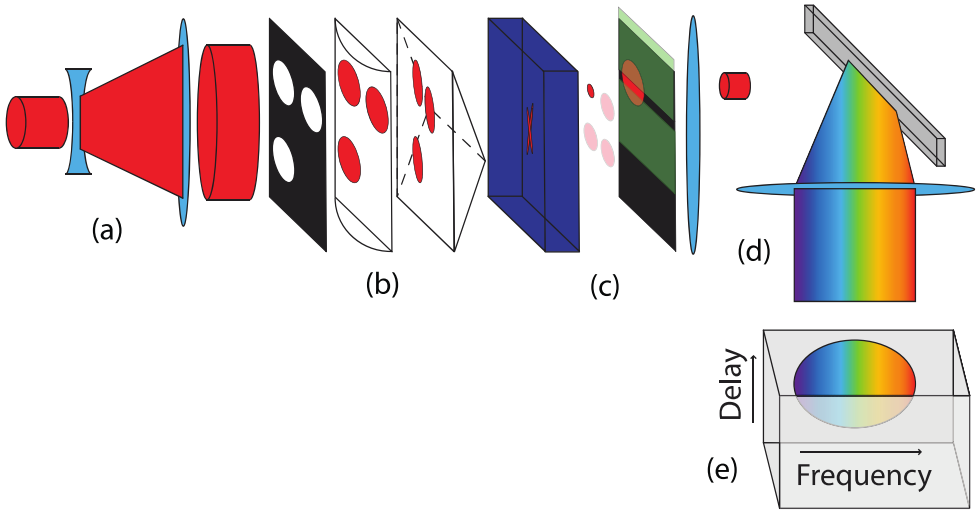

Figure 5: Schematic of the TG FROG diagnostic: (a) beam expander; (B) input mask, cylindrical lens, Fresnel bi-prism; (C) nonlinear optical medium, output mask, knife edge slit; (D) focusing optics, diffraction grating; (E) CCD camera.

Before reaching the nonlinear medium, the pulses are passed through a Fresnel bi-prism, which serves to cross the probe and gate pulses at a large angle. A variable delay is created between the interfering beams that are mapped along the vertical transverse dimension, allowing the diagnostic to make single-shot measurements. The ability to make single-shot measurements is critically important for SASE FEL light pulses, where there is a large shot-to-shot variability due to the stochastic startup nature. A major advantage of the Fresnel bi-prism is that it is automatically aligned in space as well as in time. The interference of the beams within the nonlinear medium generates an autocorrelation signal field, $E_{sig} \propto E(t)\left|E(t-\tau)\right|^2$, by a transient-grating nonlinear interaction termed degenerate four-wave mixing (DFWM) [34]. Here, τ is the relative delay between the gate and probe pulses. This signal is not symmetric with respect to delay, and, as a result, does not have ambiguity in the direction of time. Also, the third-order nonlinear optical process does not suffer from the phase-matching constraints between the signal and pump fields that limit second-order nonlinear processes. This permits phase matching across a broad spectral range, which is ideal for a tunable laser source such as the FEL; it is limited only by the transparency of the nonlinear optic. The signal field is created at the same frequency as the pump and probe pulses, as opposed to the second-harmonic generated in second-order nonlinear optical processes. This makes it challenging to filter scattered or stray light, arising from spontaneous undulator emission, or radiation that diffracts (overcoming the gain guiding) out of the FEL upstream. Once the signal field is optimally isolated, it is passed through a custom fabricated spectrometer consisting of focusing optics and a holographic reflective diffraction grating where it is spectrally resolved along the transverse dimension orthogonal to the delay direction, and imaged into a CCD camera to yield a FROG trace. The line focus in the nonlinear optic serves as the entrance slit to the

spectrometer. The diffraction grating is mounted on a remotely controlled motorized rotation stage. Changing the angle at which the light impinges on the grating changes the wavelength of light that ultimately reaches the CCD camera. This is the only diagnostic realignment that is necessary when tuning the FEL (or any other laser source) to a different resonant wavelength. The expression for the trace in this particular geometry is

$$I_{FROG}^{TG}(\omega,\tau) \propto \left| \int E(t)\left|E(t-\tau)\right|^2 \exp[-i\omega t]dt \right|^2. \tag{10}$$

3.6.4 **Results of the Chirp/Taper Experiment in the Temporal-Domain**

The results of TG FROG measurements of FEL pulses from an energy chirped *e*-beam and a tapered undulator are reported in [16]. A typical experimental FROG trace is shown in Figure 6 (a); note that there is notable noise in the image.

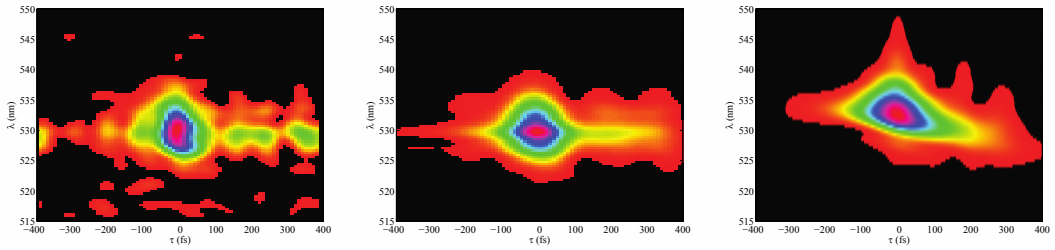

Figure 6: Comparison of (a) experimental, (b) reconstructed, and (c) simulated FROG traces.

One strength of the reconstruction process, however, is the ability of the algorithm to filter out the noise because of the robust over-sampling involved [35]. Both the reconstructed trace in Figure 6 (b) and the trace resulting from detailed numerical particle simulations using the three-dimensional FEL code GENESIS [36] in Figure 6 (c) show good overall agreement with the experimental trace. Figure 7 compares the longitudinal profile from the reconstruction to what was obtained through simulations after post-processing the data to extract the longitudinal profile at the transverse location indicated by the input mask in Figure 5. In addition, the profiles are compared to both the full pulse longitudinal profile and the simulated longitudinal profile for a chirped *e*-beam in the absence of an undulator taper. This underscores the significance of the chirp and taper combination.

One advantage of using the FROG technique to obtain the longitudinal pulse information is that the temporal and spectral content along with the pulse phase information can be obtained simultaneously from the associated trace. This allows for a rigorous determination of the time-bandwidth product (TBP) on a single-shot basis. The $TBP \approx 1.2$ for the FROG trace in Figure 6 (a,b) and for the reconstructed pulse in Figure 7 indicates that single-spike radiation production was nearly achieved while operating in the chirp and taper scenario.

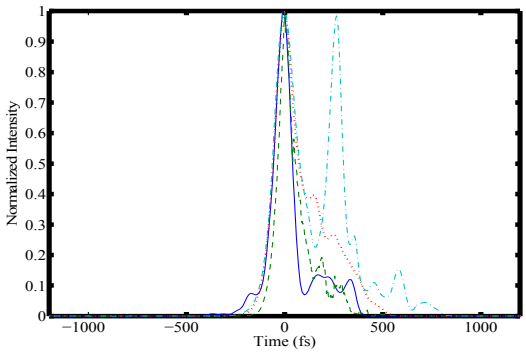

Figure 7: Comparison between the reconstructed intensity (solid blue), simulated power at the output mask (dashed-green), total pulse simulated power (dotted-red), and total pulse simulated power in the absence of an undulator taper (dotted/dashed turquoise).

3.6.5 **Concluding Remarks**

The *e*-beam energy chirp and undulator tapering scheme as presented in [13, 37] is currently being investigated as a promising candidate for a two-color FEL at the proposed NGLS [38, 39]. FROG principles have recently been advanced to shorter wavelength regimes via FROG CRAB [40], where XUV pulses photoionize atoms in the presence of an IR field. This process generates streaked electrons, which can be used for a FROG-like measurement. Pushing true FROG principles, however, where the pulse under consideration is used in an autocorrelation type measurement has proven to be extremely complicated due to the lack of simple components such as beamsplitters and nonlinear media that can operate in the XUV or x-ray wavelength regime [41].

3.6.6 **Acknowledgements**

The work discussed here is based on the efforts of a very large number of individuals. All of the members of the SPARC team are owed due commendation for the long hours spent in the control room making this work possible. The work of G. Marcus would not have been possible without the contributions, advice and guidance of J. B. Rosenzweig, L. Giannessi and S. Reiche.

3.6.7 **References**

1. P. Emma *et al.*, “First lasing and operation of an angstrom-wavelength free-electron laser”, Nature Photon. **4**, 641 (2010).
2. H. N. Chapman *et al.*, “Femtosecond diffractive imaging with a soft-X-ray free-electron laser”, Nature Photon. **2**, 839 (2006).
3. A. Barty *et al.*, “Ultrafast single-shot diffraction imaging of nanoscale dynamics”, Nature Photon. **2**, 415 (2008).
4. G. Gunther *et al.*, “Sequential femtosecond X-ray imaging”, Nature Photon. **5**, 99 (2011).
5. T. Watanabe *et al.*, “Experimental characterization of Superradiance in a single-pass high-gain laser-seeded free-electron laser amplifier”, Phys. Rev. Lett., **98**, 034802 (2007).

6. L. H. Yu *et al*., "High-gain harmonic-generation free-electron laser", Science, **289**, 932 (2000).
7. L. H. Yu *et al*., "First ultraviolet high-gain harmonic-generation free-electron laser", Phys. Rev. Lett., **91**, 074801 (2003).
8. L. Giannessi, P. Musumeci, and S. Spampinati, "Nonlinear pulse evolution in seeded free-electron laser amplifiers and in free-electron laser cascades", J. Appl. Phys., **98**, 043110 (2005).
9. A. Zholents and G. Penn, "Obtaining two attosecond pulses for x-ray stimulated raman spectroscopy", Nucl. Instrum. Meth. Phys. Res., Sect. A, **612**, 254 (2010).
10. Bonifacio *et al*., "Spectrum, temporal structure, and fluctuations in a high-gain free-electron laser starting from noise", Phys. Rev. Lett., **73**, 70 (1994).
11. R. Bonifacio, C. Pellegrini, and L. M. Narducci, "Collective instabilities and high-gain regime in a free electron laser", Opt. Commun., **50**, 373 (1984).
12. J. Rosenzweig *et al*., "Generation of ultra-short, high-brightness electron beams for single-spike sase fel operation", Nucl. Instrum. Meth. Phys. Res., Sect. A, **593**, 39 (2008).
13. E. L. Saldin, E. A. Schneidmiller and M. V. Yurkov, "Self-amplified spontaneous emission fel with energy-chirped electron beam and its application for generation of attosecond x-ray pulses", Phys. Rev. ST Accel. Beams, **9**, 050702 (2006).
14. L. Giannessi *et al*., "Self-amplified spontaneous emission free-electron laser with an energy-chirped electron beam and undulator tapering", Phys. Rev. Lett., **106**, 144801 (2011).
15. G. Dattoli *et al*., "Energy phase correlation and pulse dynamics in short bunch high gain fels", Opt. Commun., **285**, 710 (2012).
16. G. Marcus *et al*., "Time-domain measurement of a self-amplified spontaneous emission free-electron laser with an energy-chirped electron beam and undulator tapering", Appl. Phys. Lett., **101**, 134102 (2012).
17. P. Emma *et al*., "Femtosecond and subfemtosecond x-ray pulses from a self-amplified spontaneous-emission-based free-electron laser", Phys. Rev. Lett., **92**, 074801 (2004).
18. A. Zholents *et al*., "Proposal for intense attosecond radiation from an x-ray free-electron laser", Phys. Rev. Lett., **92**, 224801 (2004).
19. M. Testorf, B. Hennelly and J. Ojeda-Castaneda, "Phas-space optics: fundamentals and applications", McGraw-Hill (2009).
20. R. Trebino and D. J. Kane, "Using phase retrieval to measure the intensity and phase of ultrashort pulses: frequency-resolved optical gating", J. Opt. Soc. Am. A, **10**, 1101 (1993).
21. J. Rosenzweig *et al*., "RF and magnetic measurements on the sparc photoinjector and solenoid at ucla", Proc. of the 2005 part. accel. conf., 2624 (2005).
22. M. Ferrario *et al*., "Experimental demonstration of emittance compensation with velocity bunching", Phys. Rev. Lett., **104**, 054801 (2010).
23. L. Serafini and M. Ferrario, "Velocity bunching in photo-injectors", AIP conference proceedings, **581**, 87 (2001).
24. S. G. Anderson, P. Musumeci and J. B. Rosenzweig, "Velocity bunching of high-brightness electron beams", Phys. Rev. ST Accel. Beams, **8**, 014401 (2005).
25. D. Filippetto *et al*., "Phase space analysis of velocity bunched beams", Phys. Rev. ST Accel. Beams, **14**, 092804 (2011).
26. L. Giannessi *et al*., "Self-amplified spontaneous emission for a single pass free-electron laser", Phys. Rev. ST Accel. Beams, **14**, 060712 (2011).
27. L. Poletto *et al*., "Instrumentation for analysis and utilization of extreme-ultraviolet and soft x-ray high-order harmonics", Review of Scientific Instruments, **75**, 4413 (2004).
28. D. Gabor, "Theory of communication", J. Inst. Elec. Eng., **93**, 429 (1946).
29. D. Vakman, "On the analytic signal, the teager-kaiser energy algorithm, and other methods for defining amplitude and frequency", Signal Processing, IEEE Trans., **44**,

791 (1996).
30. K. W. DeLong and R. Trebino, "Improved ultrashort pulse-retrieval algorithm for frequency-resolved optical gating", J. Opt. Soc. Am. A, **11**, 2429 (1994).
31. L. Cohen, "Time-frequency distributions – a review", Proceedings of the IEEE, **77**, 941 (1989).
32. R. Trebino, "Frequency-resolved optical gating: the measurement of ultrashort laser pulses", Kluwer Academic (2000).
33. D. Lee *et al*., "Experimentally simple, extremely broadband transient-grating frequency-resolved optical gating arrangement", Opt. Express, **15**, 760 (2007).
34. H. Eichler, P. Gunter and D. Pohl, "Laser-induced dynamic gratings", Springer-Verlag (1986).
35. D. N. Fittinghoff *et al*., "Noise sensitivity in frequency-resolved optical-gating measurements of ultrashort pulses", J. Opt. Soc. Am. B, **12**, 1955 (1995).
36. S. Reiche, "GENESIS 1.3: a fully 3D time-dependent fel simulation code", Nucl. Instrum. Meth. Phys. Res., Sect. A, **429**, 243 (1999).
37. W. M. Fawley, "Production of ultrashort fel xuv pulses via a reverse undulator taper", Nucl. Instrum. Meth. Phys. Res., Sect. A, **593**, 111 (2008).
38. J. Corlett *et al.*, "FEL design studies at lbnl: activities and plans", ICFA Newsletter #42 (2007).
39. A. Zholents, "A proposal for a generation of two-color ultra-short x-ray pulses", NGLS Tech. Note No. 25.
40. Y. Mairesse and F. Quere, "Frequency-resolved optical gating for complete reconstruction of attosecond bursts", Phys. Rev. Lett., **71**, 011401 (2005).
41. R. Trebino, "Measuring the seemingly immeasurable", Nature Photonics, **5,** 189 (2011).

3.7 Broad Bandwidth THz Pulse and e-Beam Characterization

J. van Tilborg, D. Bakker, N. H. Matlis, and W. P. Leemans
Lawrence Berkeley National Laboratory
1 Cyclotron road, Berkeley CA 94720, USA
Mail to: JvanTilborg@lbl.gov

3.7.1 Introduction

Control and measurement of terahertz (THz) pulses allow scientists to unravel ultra-fast phenomena in plasmas, semi-, and superconductors. The method of laser-based electro-optic sampling (EOS) [1,2] has proven a powerful technique for characterizing broad-bandwidth THz radiation. EOS also serves as a single-shot temporal diagnostic for femtosecond accelerator-produced electron beams [3,4,5]. Conventional EOS-based techniques rely on a temporal cross-correlation of the THz field profile with an optical probe pulse [3,6,7]. Here the covered spectral bandwidth is intrinsically limited by the probe laser bandwidth. Although few-fs, few-cycle probe pulses have been applied in multi-shot EOS configurations [8], single-shot diagnostics have been limited to longer >30 fs probe beams and <10 THz bandwidth coverage. Furthermore, the multiple probe beams, secondary nonlinear effects and femtoscond laser control make for a challenging single-shot diagnostic.

Here [9] we experimentally demonstrate and discuss an EOS configuration operating directly in the spectral domain, by measuring the spectral sidebands created outside the probe bandwidth (bandwidth coverage now only limited by the EO crystal). This technique has single-shot capabilities and is compatible with fiber integration,

offering strong practical advantages. While Jamison *et al.* [10] recently observed EO-induced spectral broadening of a narrow-bandwidth probe by ultra-short (broad-bandwidth) electron beams, here in this proceedings the sideband generation concept is specifically studied as a stand-alone broad-bandwidth diagnostic for THz pulses or electron beams. By developing a narrow-bandwidth optical probe and a laser-driven broad-bandwidth THz source rich in spectral features (0-8 THz bandwidth coverage), conditions are realized to gain insight into the diagnostic validity, advantages, and potential challenges. These novel results provide a guide to utilizing EO-induced sideband generation as a practical single-shot diagnostic.

3.7.2 **Experimental Setup**

In order to experimentally study EO-induced optical sidebands, a setup was developed (see Fig. 1) consisting of a narrow-bandwidth probe pulse (2.9 ps duration) and a broad-bandwidth THz source rich in spectral features. The EO crystals used were either 200-μm-thick ZnTe (zinc telluride) or GaP (gallium phosphide), which defined the spectral domain of study to 0-3.5 THz or 0-8 THz, respectively.

The laser-based THz generation arm was derived from a 1-kHz titanium-sapphire laser system λ_0=804 nm, f_0=373 THz). The beamsplitter transmitted 92% of the laser light towards the THz arm. The beam diameter in this arm was 3.5 mm (defined by an iris), the pulse duration 45 fs [intensity full-width-at-half-maximum (FWHM)], and the pulse energy after the iris 100 μJ. The laser was propagated through a 100 mm focal length lens (lens 1), where 15 mm before focus a 100-μm-thick frequency doubling BBO crystal (type-I β-barium borate) was placed to produce both fundamental f and frequency-doubled 2f radiation at the focus in air. This configuration has been demonstrated (Refs. [11,12] and citations therein) to yield broad-bandwidth THz radiation due to the creation of directional currents of the electrons in the air-based plasma. The THz radiation was collected by a 50-mm-diameter silicon lens (7 mm thick, focal length of 75 mm), and focused through a thin nitro-cellulose pellicle onto the EO crystal. The entire THz line was in air. It is important to emphasize that this

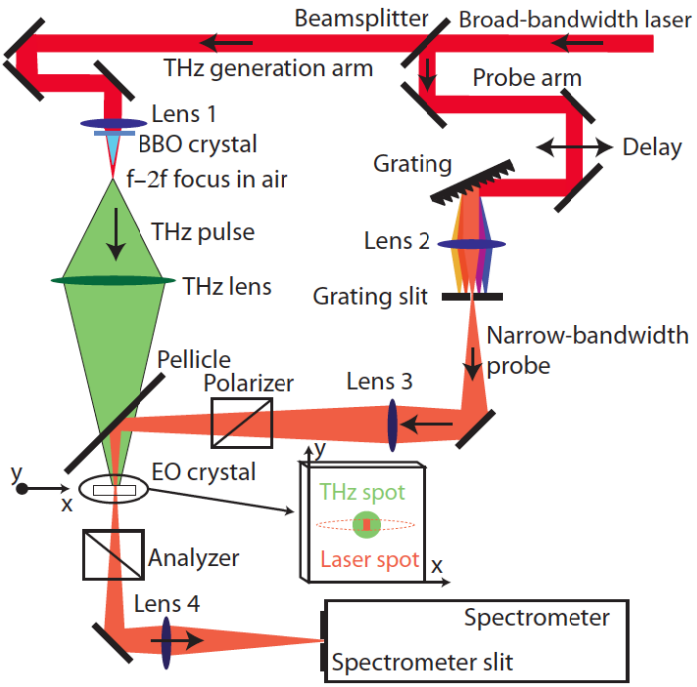

Figure 1: Experimental setup for the THz-induced optical sideband diagnostic. A laser beam is split by a beamsplitter into a pump arm for THz generation and a probe arm for EO detection. The THz pulse is focused by a Silicon lens through a pellicle onto an EO crystal. The probe arm is reflected off a grating-lens-slit combination to produce a 0.11-THz-bandwidth probe pulse onto the EO crystal, after which an imaging spectrometer records the EO-modulated optical spectrum.

study was not geared towards optimization or understanding of the THz source itself, but solely focused on the sideband generation concept. The narrow-bandwidth probe beam was derived from the same laser line as the THz generation arm to guarantee temporal synchronization. The size of the probe beam was 5 mm (FWHM).

As illustrated in Fig. 1 the reflection off the beam splitter (15 μJ/pulse) was sent through a delay stage onto a 600 lines/mm grating to accomplish spectral dispersion. A lens placed after the grating (lens 2, focal length 150 mm) produced a horizontal line focus, with each color focused to a different position (spatial chirp). A slit was placed in the focal plane of the lens, therefore only transmitting a narrow controllable part of the optical bandwidth. Lens 3 (focal length of 100 mm) imaged the line focus onto the EO crystal, with a vertical size of 15 μm (FWHM) and a horizontal size as controlled by the grating slit. The reflection off the pellicle was circa 9%. The polarizer and EO crystal z-axis were rotated such that the EO-generated optical beam was polarized orthogonally to the original optic probe. Due to imperfect extinction and intrinsic crystal birefringence, ~0.15% of the probe energy still made it through the analyzer (~0.017% in the case of GaP). The EO-modulated probe beam (plus remnant original probe leakage) was then imaged at x4.2 demagnification on the entrance slit of an imaging optical spectrometer (300 grooves/mm grating). The CCD camera in the spectrometer was a 1392x1032 pixel 10-bit (effective) camera, with a 0.047 nm/pixel calibration around 800 nm. Since the spectrometer slit was transmitting only a controllable portion

(of order 2%) of the horizontal line focus at the EO crystal, the grating slit (see Fig. 1) served no benefit and was eventually removed from the setup.

3.7.3 **Observation of THz-Induced Sidebands on 2.9-ps Laser Pulses**

An image of the measured optical spectrum [9], measured with the 200-μm-thick ZnTe crystal is shown in Fig. 2(a). For this measurement the spectrometer slit was set at 10 μm, which corresponds to a horizontal acceptance at the EO crystal of 45 μm. While the sideband technique has single-shot capabilities, the weak THz field (~1 kV/cm) and the weak probe beam energy (losses from low beamsplitter reflectivity, low pellicle reflectivity, and strong bandwidth reduction) required the CCD shutter to be opened for 5 seconds (5000 laser shots), after which 8 consecutive images were averaged. Although both sidebands are quantitatively symmetric (as predicted), the small asymmetry in amplitude is most likely attributed to spectrally-dependent optics transmission and reflection. The vertical size of the optical sidebands was measured to be 15 μm (FWHM), consistent with the size of the probe beam at the EO crystal. Note that remnant unmodulated probe radiation frustrated THz retrieval around λ_0 hence the black bar at 804 nm.

In a subsequent experiment, the EO crystal was switched to 200 μm-thick GaP (acquisition time increased to 6 seconds, with 34 consecutive images averaged). Based on the spectrometer images for ZnTe and GaP, the retrieved spectral line-outs are shown in Fig. 2(b), where the wavelength axis was converted to a frequency axis $\nu=c/\lambda-f_0$. One can see that the spectra are consistent with the smaller 0-3.5 THz bandwidth for ZnTe and larger 0-8 THz bandwidth for GaP. The GaP-induced sideband spectrum was a factor of 4 weaker than ZnTe. Note that since the THz source relies on a strong nonlinearity at focus in air, one can expect drifts in THz peak field and spectral content over time. Another observation in Fig. 2(b) is the many sharp spectral features in the spectra (which match for the ZnTe and GaP observations, see dashed lines). Such spectra were also observed with a scanning Michelson interferometer by Kim *et al.* [11], and can be attributed to absorption of the THz radiation in the generation plasma and in air-based water vapor. The black curve in Fig. 2(b) shows the air-based water absorption coefficient, as measured at lower spectral resolution with a Michelson interferometer in an independent study, where the frequencies of strongest absorption indeed line up with several of the minima in the THz spectrum. Spectral features as sharp as 0.15 THz (FWHM) were observed. This observation can be compared to the expected spectral resolution, which is determined by the convolution of the laser probe bandwidth and the intrinsic spectrometer resolution. The data in Fig. 2 demonstrates that THz-induced optical sidebands are measured over a bandwidth many times larger than the optical probe bandwidth. The limitation for bandwidth coverage is no longer set by the probe, but is solely a matter of crystal selection. The spectral resolution is determined by the probe duration, which for >1-ps pulses is on the 0.1 Thz level or lower.

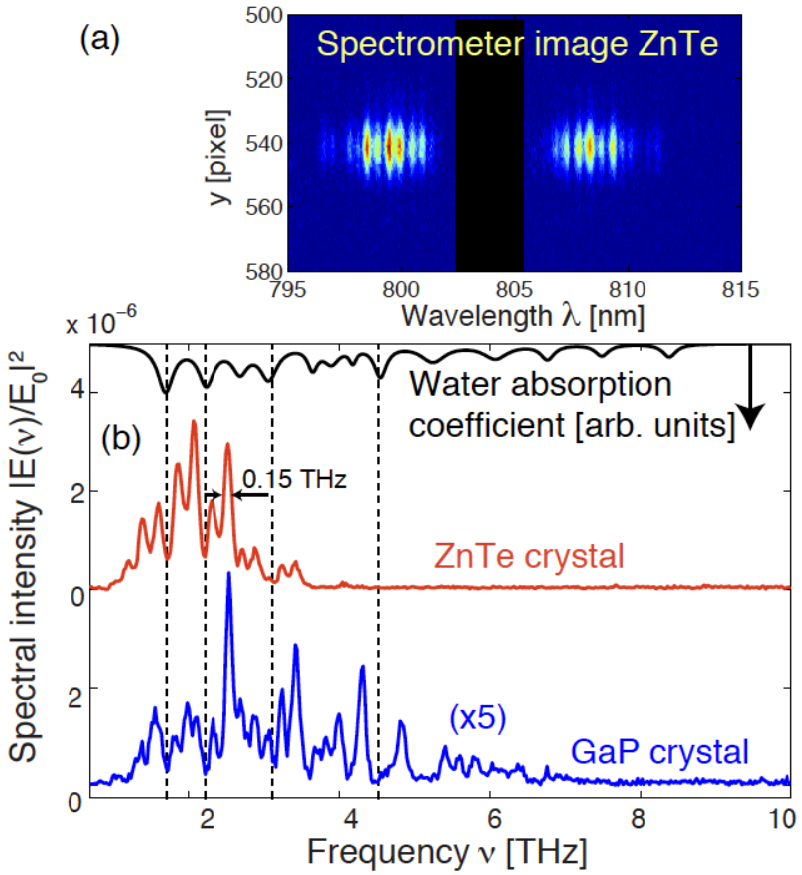

Figure 2: (a) Spectrometer image obtained with 200-μm-thick ZnTe as the EO crystal (spectral range of 0-3.5 THz). (b) Lineouts of the spectral images for ZnTe (red curve) and GaP (blue curve, multiplied by 5). The spectral range of 200-μm-thick GaP is 0-8 THz. The spectral features, a result from absorption in the plasma and in air-based water vapor, line up for both measurements and were found to be as sharp as 0.15 THz (FWHM). The black curve in (b) shows the air-based water absorption coefficient, where the frequencies of strongest absorption line up with the minima in the retrieved THz spectrum.

3.7.4 **Concepts for Few-fs e-Beam Characterization**

With the probe bandwidth no longer a limiting factor in THz retrieval, it is now only the crystal transfer function $T_{crystal}$ which will affect the bandwidth coverage. $T_{crystal}$ can be modeled as a product of several factors, namely the frequency dependent EO parameter $\chi^{(2)}_{eff}$ [13], the effect of Fabry-Perot reflections of the THz pulse inside the crystal [14], and the phase-matching function ζ [2,14] which incorporates THz absorption, dispersion, and velocity walk-off between optical and THz fields. $T_{crystal}$ can either be measured and calibrated, or retrieved from the literature. Extensive crystal research and development (for example, anti-reflective coatings or multi-crystal sandwiching), necessary to find the optimum EO configuration, is beyond the scope of this paper. For simplicity we will approximate the EO parameter $\chi^{(2)}_{eff}$ as a constant. This approximation holds for THz frequencies outside of the phonon resonance bands

[13]. Within these bands, THz pulse reconstruction becomes unreliable due to the strong absorption and varying index of refraction.

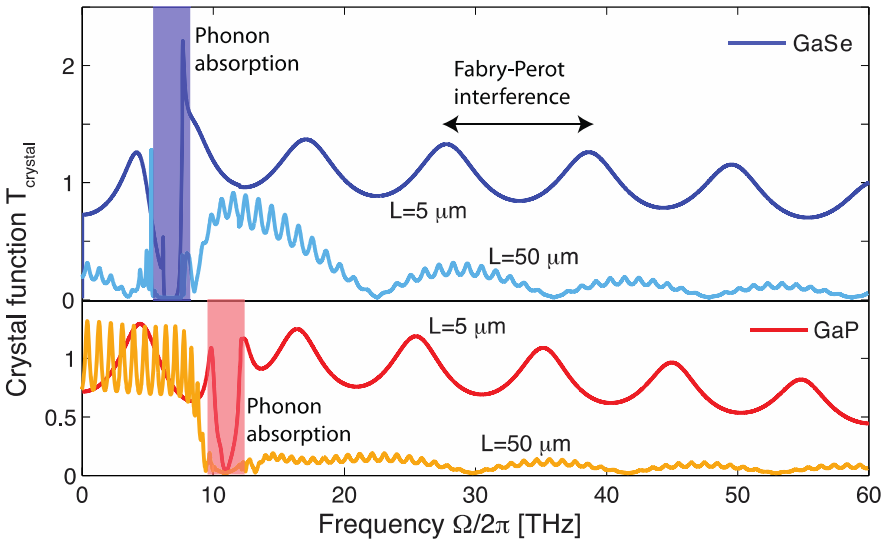

Figure 3: Crystal transfer function in the THz domain. The crystal transfer function $T_{crystal}$ is shown for the crystals GaSe (top) and GaP (bottom) for crystal thicknesses of 5 μm and 50 μm. Thinner crystals cover a larger THz spectrum at the cost of a reduced EO effect. The periodic oscillations on $T_{crystal}$ arise from THz pulse reflections inside the EO crystal (Fabry-Perot effect). The phonon absorption bands indicate the spectral region where EOS-based THz pulse retrieval becomes unreliable.

As an illustration of the effects of the crystal transfer function, the function $T_{crystal}$ is plotted in Fig. 3 for GaSe (type II, 10 deg tilt) and GaP crystals of thicknesses 5 μm and 50 μm respectively. Data on the indices of refraction for GaP [13] and GaSe [15] were obtained from the literature. For 5-μm-thick crystals, the crystal transfer function appears as a non-zero smoothly-varying function over a large spectral extent (>60 THz).

4.6.5 Conclusion

In conclusion, we have presented the concept of THz-induced optical sideband generation as a single-shot THz pulse diagnostic. The technique can be applied to electro-magnetic THz radiation as well as to the self-fields of femtosecond electron bunches. The novel approach does not suffer from laser bandwidth limitations, enabling large spectral coverage (>60 THz) and high temporal resolution (few femtoseconds, or less). Its spectral resolution is set by the laser pulse duration. It is shown that proper selection of the EO crystal (such as 5μm-thick GaSe) can support this bandwidth. We have experimentally demonstrated the diagnostic by observing optical sidebands from a laser-based THz source.

3.7.5 Acknowledgments

This work was supported by the Director, Office of Science, Office of High Energy Physics, of the U.S. Department of Energy under Contract No. DE-AC02-05CH11231.

3.7.6 References

1. G. Gallot and D. Grischkowsky, "Electro-optic detection of terahert radiation", J. Opt. Soc. Am. B **16**, 1204-1212 (1999).
2. S. P. Jamison, A. M. MacLeod, G. Berden, D. A. Jaroszynski, and W. A. Gillespie, "Temporally resolved electro-optic effect", Opt. Lett. **31**, 1753-1755 (2006).
3. G. Berden, S. P. Jamison, A. M. MacLeod, W. A. Gillespie, B. Redlich, and A. F. G. van der Meer, "Electro-optic technique with improved time resolution for real-time, nondestructive, single-shot measurements of femtosecond electron bunch profiles", Phys. Rev. Lett. **93**, 114802 (2004).
4. J. van Tilborg, C. B. Schroeder, C. Toth, C. G. R. Geddes, E. Esarey, and W. P. Leemans, "Single-shot spatiotemporal measurements of high-field terahertz pulses", Opt. Lett. **32**, 313-315 (2007).
5. A. D. Debus, M. Bussmann, U. Schramm, R. Sauerbrey, C. D. Murphy, Zs. Major, R. Horlein, L. Veisz, K. Schmid, J. Schreiber, K. Witte, S. P. Jamison, J. G. Gallacher, D. A. Jaroszynski, M. C. Kaluza, B. Hidding, S. Kiselev, R. Heathcote, P. S. Foster, D. Neely, E. J. Divall, C. J. Hooker, J. M. Smith, K. Ertel, A. J. Langley, P. Norreys, J. L. Collier, and S. Karsch, "Electron bunch length measurements from laser-accelerated electrons using single-shot THz time-domain interferometry", Phys. Rev. Lett. **104**, 084802 (2010).
6. J. Shan, A. S. Weling, E. Knoesel, L. Bartels, M. Bonn, A. Nahata, G. A. Reider, and T. F. Heinz, "Single-shot measurement of terahertz electromagnetic pulses by use of electro-optic sampling", Opt. Lett. **25**, 426-428 (2000).
7. N. H. Matlis, G. R. Plateau, J. van Tilborg, and W. P. Leemans, "Single-shot spatio-temporal measurements of ultrashort THz waveforms using temporal electric-field cross correlation", J. Opt. Soc. Am. B **28**, 23-27 (2011).
8. A. Sell, R. Scheu, A. Leitenstorfer, and R. Huber, "Field-resolved detection of phase-locked infrared transients from a compact Er:fiber system tunable between 55 and 107 THz", Appl. Phys. Lett. **93**, 251107 (2008).
9. J. van Tilborg, D. J. Bakker, N. H. Matlis, and W. P. Leemans, "Spectral sidebands on a narrow-bandwidth optical probe as a broad-bandwidth THz pulse diagnostic", Opt. Express **19**, 26633 (2011)
10. S. P. Jamison, G. Berden, P. J. Phillips, W. A. Gillespie, and A. M. MacLeod, "Upconversion of a relativistic Coulomb field terahertz pulse to the near infrared", Appl. Phys. Lett. **96**, 231114 (2010).
11. K. Y. Kim, A. J. Taylor, J. H. Glownia, and G. Rodriguez, "Coherent control of terahertz supercontinuum generation in ultrafast laser-gas interactions", Nat. Phot. **2**, 605-609 (2008).
12. H. Wen and A. M. Lindenberg, "Coherent terahertz polarization control through manipulation of electron trajectories", Phys. Rev. Lett. **103**, 023902 (2009).
13. A. Leitenstorfer, S. Hunsche, J. Shah, M. C. Nuss, and W. H. Knox, "Detectors and sources for ultrabroadband electro-optic sampling: experiment and theory", Appl. Phys. Lett. **74**, 1516-1518 (1999).
14. J. Faure, J. van Tilborg, R. A. Kaindl, and W. P. Leemans, "Modelling laser-based table-top THz sources: Optical rectification, propagation and electro-optic sampling", Opt. Quantum Electron. **36**, 681-697 (2004).
15. K. L. Vodopyanov and L. A. Kulevskii, "New dispersion relationship for GaSe in the 0.65-18 μm spectral region", Opt. Comm. **118**, 375-378 (1995).

3.8 Femtosecond Electron and X-ray Beams at the Linac Coherent Light Source

Yuantao Ding, for the LCLS team
SLAC, 2575 Sand Hill road, Menlo Park, CA 94025, USA
Mail to: ding@slac.stanford.edu

3.8.1 Introduction

Free-electron lasers (FELs) hold great promise as tunable, high-power, ultrashort, coherent sources for short-wavelength radiation. In the x-ray wavelength, a high-gain FEL can generate multi-gigawatt (GW) and femtosecond (fs) coherent x-ray pulses. Since the operation of the first hard x-ray FEL facility at the Linac Coherent Light Source (LCLS) in October 2009 [1], SACLA has also began delivering hard x-rays to users in 2012 [2]. At soft x-ray wavelengths, FLASH [3] was the first user facility operating since 2005. More recently, Fermi FEL [4] – using a coherent seed to provide fully coherent x-ray pulses – has also been available to users.

At LCLS, the typical operating charge is 150-250 pC, and the corresponding pulse duration is about 50 fs to a few hundred fs. More beam parameters can be found in [1]. Recently a hard x-ray self-seeding mode has been developed [5] and the photon energy in the soft x-ray side has been extended to 280 eV. These additions make LCLS more flexible to support users for scientific research.

Generation of even shorter x-ray pulses (femtoseconds to attoseconds) is attracting much attention within the x-ray FEL user community. Many efforts have been made to generate and measure the femtosecond and attosecond electron and x-ray beams. In this section, we will discuss the present operation modes at LCLS to produce x-ray pulses with a few fs duration. Characterization of the fs electron and x-ray beams, which is even more challenging, will also be discussed.

3.8.2 Generation of Femtosecond Electron and X-ray Beams

In an x-ray FEL operating in the self-amplified spontaneous emission (SASE) mode, the x-ray pulse evolves with many spikes due to its noisy start-up. Within each spike, it is temporally coherent. The spike length (coherence length) is about 1 fs for soft x-rays and 0.2-0.3 fs for hard x-rays. Typically the electron bunch length is longer than the coherent length, which means the x-ray pulse consists of a series of spikes. For example, there are a few hundred spikes for the LCLS 100-fs x-ray pulse at 1.5 Å wavelengths. Several methods to reduce the bunch length down to or below the 1-fs regime have been proposed. One direct method is to reduce the electron bunch charge - hence to reduce the bunch length - to get a short x-ray pulse [6, 7]. We call this scheme the low-charge mode. The other way is to keep the same electron bunch, but to manipulate the electron bunch with a slotted foil [8] or with ultrashort optical lasers [e.g., 9-13]. After this manipulation, only a small fraction of the electron bunch will lase while the lasing in other parts is suppressed, so a short x-ray pulse can be obtained.

In the following sections, we focus on two schemes developed at LCLS: low charge (~20 pC) mode and emittance-spoiling foil scheme. We will report the performance of these two methods at LCLS.

3.8.2.1 *Low Charge (20 pC) Operation Mode*

Reducing the bunch charge from nC to pC, the strong interaction of the bunch self-field throughout the accelerator will be much weaker, allowing stronger compression longitudinally. In this way, we can still achieve ~kA peak current to support FELs.

At LCLS, based on the resolution of the present diagnostic devices, we ran the low charge mode at 20pC. Experiments and simulations show such a bunch is capable of generating intense x-rays in the LCLS undulator with a few femtosecond pulse duration [7], and it has been developed to a regular operating mode for user experiments.

We showed the measured slice emittance at the LCLS injector (135 MeV) in Fig. 1, with a bunch charge of 20 pC and laser spot diameter on the cathode of 0.6 mm. This measurement was made in the LCLS injector area (beam energy of 135 MeV), using a "quad-scan" method combined with an S-band (2856 MHz) rf deflector. In the middle of the bunch, the slice emittance is about 0.14 μm, which is mainly dominated by the cathode thermal emittance. This is more than a factor of 2 lower than the typical emittance measured with a bunch charge of 150-250 pC.

The low-charge electron bunch of 20 pC has been accelerated in the SLAC linac to 13.6 GeV and longitudinally compressed through two bunch compressors. The pulse duration is too short to be measured directly using the present LCLS beam diagnostic devices. Some ongoing developments to improve the diagnostic resolution will be discussed in the following sections. In the present machine beamline, a photodiode, with bandwidth 1.0-2.5 μm, is used to collect the coherent optical transition radiation (OTR) generated on an aluminum screen located just downstream of the second bunch compressor. This signal provides a relative bunch length measurement. In Fig.2, we showed the OTR signals vs linac rf phase. The signal peaks at a full compression point. Based on simulations, the bunch duration can be as short as a few microns.

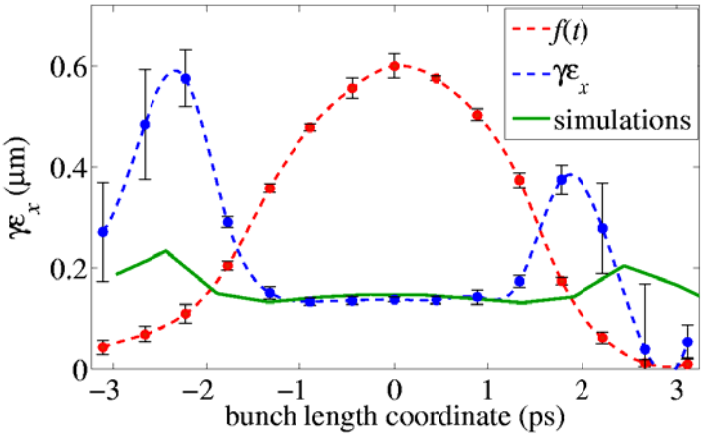

Figure 4: Measured and simulated slice emittance at the LCLS injector with a bunch charge of 20pC [7].

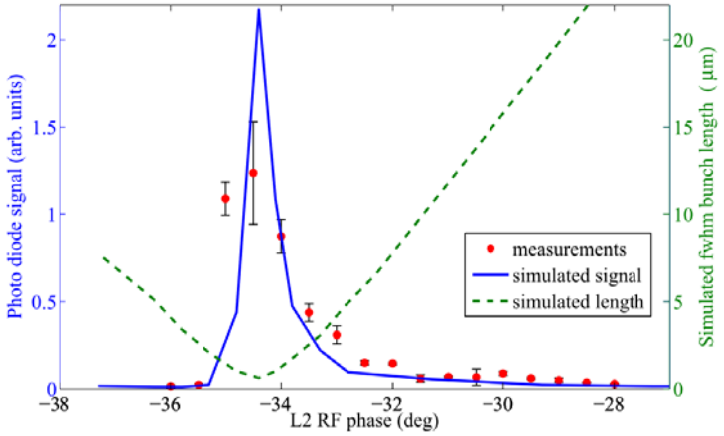

Figure 5: Measured and simulated photodiode OTR signals vs. linac rf phase at the LCLS second bunch compressor, with a bunch charge of 20pC. The green dashed curve shows the simulated fwhm bunch length [7].

Start-to-end simulations showed the radiation x-ray pulses from a 20-pC bunch can reach a power level over giga-watts (GW) with a pulse duration of less than 10 fs [7]. At present, measurement of x-ray pulse duration is still not available at LCLS. The pulse energy, measured from a gas detector shot by shot, is a typical parameter to record during the commissioning and operation. Similarly to Fig.2, we scanned the linac rf phase to change the compression factor, and at the same time recorded the x-ray pulse energy and bunch length signal (from photodiode OTR). We show one result in Fig.3, which is a hard x-ray case, and the maximum pulse energy is about 150 μJ. At full compression, we still got a few tens of μJ pulse energy, while the pulse duration is expected to be only a few fs. Compared with Fig.2, the rf phase at full compression is shifted a few degrees. This can be due to different initial beam conditions in the injector and/or rf phase drifting.

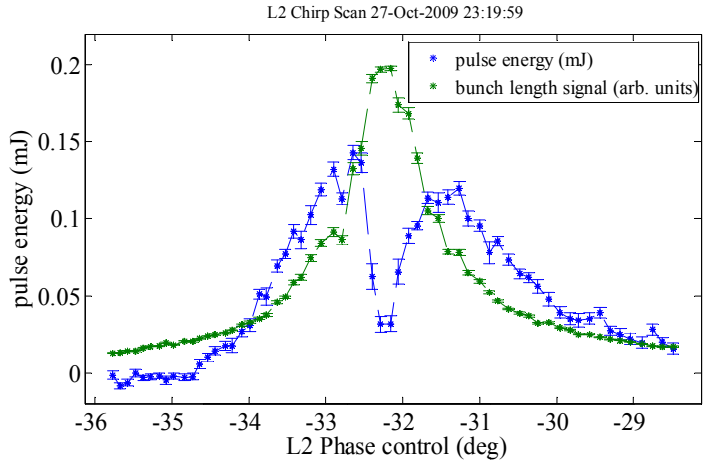

Figure 6: Measured x-ray pulse energy and bunch length signal at the LCLS, with 20 pC charge, e-beam energy 13.6 GeV**.**

For soft x-ray generation, however, the measured pulse energy at full-compression is almost zero. One of the reasons is the slippage effect is stronger at soft x-ray wavelengths. When the bunch is fully compressed, it is too short to sustain a sufficient

FEL gain before the radiation slips out of the e-beam bunch. Another reason could be the larger relative energy spread for a low-energy beam which can suppress the microbunching.

Further optimization of low charge operation has been accomplished, mainly based on start-to-end simulations. With a 20-pC bunch charge, it is possible to combine with the slotted foil technique, a scheme to be discussed in the next section, to produce single-spike soft x-rays [14]. By going to 1-pC bunch charge, a recent study shows we can even achieve single-spike hard x-rays [15].

3.8.2.2 *Emittance-Spoiling Foil Method*

The emittance-spoiling foil technique, which was first proposed in 2004, is another method used at the LCLS for generating ultrashort x-ray pulses [8]. It has been on-line since 2010. The ease of operation for this technique has been beneficial for many scientific experiments, and more importantly, the two-pulse mode from double-slot setup enables x-ray pump/x-ray probe experiments without relative timing jitter issues.

The method relies upon the fact that in a magnetic bunch-compressor chicane the beam is tilted at a large angle relative to the longitudinal axis (see Fig. 4). At the point of maximum tilt (center of the chicane) a thin foil is placed in the path of the beam. The foil has a vertically (y) oriented narrow slot at its center. The Coulomb scattering of the electrons passing through the foil increases the horizontal and vertical emittances of most of the beam, but leaves a very thin unspoiled slice where the beam passes through the slit. Details about the method and simulation results can be found in [8, 16].

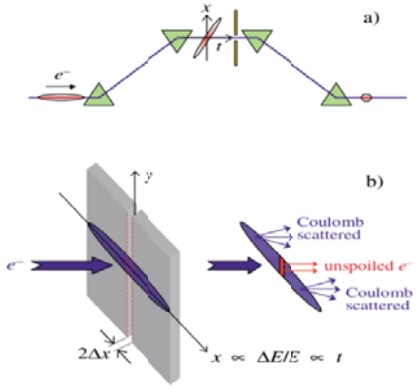

Figure 7: Sketch of the slotted foil setup [emma2004].

To achieve a variable pulse duration and separation, an aluminum foil (3-μm thickness) with different slot arrays was designed. The present version includes a vertical V-shaped single slot with a variable slot width (220-1580 μm), and two V-shaped double slots with different slot separation at two fixed slot widths (300 and 430 μm), as shown in the bottom of Fig. 5.

After the electron beam passes through the emittance-spoiling foil, one or two unspoiled time slices with good emittance will contribute to FEL lasing. We show one example of the measured FEL pulse energy versus the foil vertical position in Fig.5, as reported in [17]. In this example the photon energy was 1.5 keV, and the electron beam energy was 5.8 GeV with peak current of 1.5 kA. When the electron beam emittance is totally spoiled, for example, at the far right part of this figure, the FEL beam is fully suppressed. While moving the foil vertically to let the beam pass through the narrower part of the single slot, the FEL beam intensity starts to grow. With a very narrow slit,

the uncorrelated energy spread and betatron beam size dominate the output pulse length [16], and we get a nonlinear growth of the pulse energy versus the slot width. When the slot gets larger, the growth becomes linear and the pulse length is mainly determined by the slot width. It is also shown that in the two double-slot areas, the measured pulse energy from each area is almost constant, while the pulse separation actually varies during the scan.

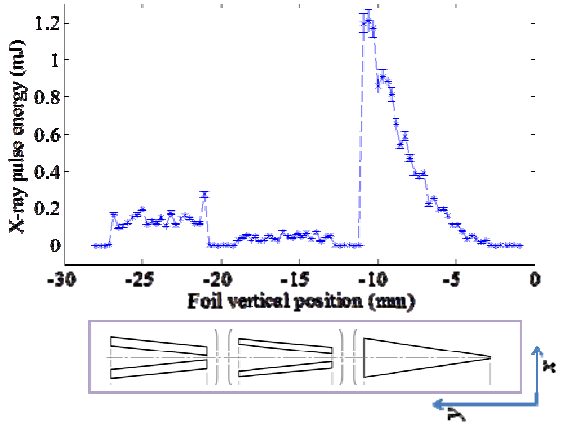

Figure 8: Measured FEL pulse energy vs. foil vertical position. The slot arrays are shown in the bottom [17].

During operation, the pulse duration can be controlled by choosing the slot width and/or the beam current (by changing the compression factor). Based on calculations (see equations in [16, 17]), for the double-pulse mode, the minimum pulse separation is about 10 fs, and the maximum can be about 80 fs (at 1-kA peak current); for the single-pulse mode, the minimum pulse duration is about 10 fs (at 3-kA peak current). Measurement at this time-scale is very challenging, and we will discuss it in the following sections.

3.8.3 **Characterization of Femtosecond Electron and X-ray Beams**

Measuring the length of ultrashort electron bunches is an important but challenging topic. Techniques exist for measuring the coherent radiation spectrum of a short bunch in order to reconstruct its temporal profile (see Ref. [18] for a recent excellent example). Information about the bunch length can also be obtained from the statistical fluctuation of the incoherent radiation intensity [19, 20]. The more direct measurement methods include rf zero phasing that introduces an energy-to-time correlation [21] and the use of a transverse deflecting cavity that introduces a transverse-to-time correlation [22]. Measurement of the correlated coordinates yields information about the bunch length. The resolution of these different techniques is machine specific, but typically limited to the 100-fs to 10-fs levels (see, e.g., Refs. [21, 23, 24]). In particular, the compressed low-charge bunches in the LCLS, which are expected to be less than 10 fs in duration, are too short to be measured currently by these standard techniques. In principle, the resolution of the transverse deflecting method can be improved by increasing the defecting voltage and rf frequency of the transverse cavity, as planned at the LCLS [25]. Recently, a novel longitudinal-to-transverse mapping

method using an x-band deflector has been proposed to further improve the temporal resolution to below the 1-fs level [26].

Measurement of the electron bunch length is helpful in estimating the FEL x-ray pulse duration. However, for a realistic beam, such as that with a Gaussian shape or a spiky profile, the FEL amplification varies along the bunch due to peak current or emittance variation. This will result in differences between the temporal shape or duration of the electron bunch and the x-ray pulse. Initial experiments at LCLS have revealed that characterization of the x-ray pulse duration on a shot-by-shot basis is critical for the interpretation of the data. However, measuring femtosecond x-ray pulses is an extremely challenging topic. Conventional photodetectors and streak cameras do not have a fast enough response time for characterizing the ultrashort x-ray pulses. In addition, because of the vanishing small cross sections in nonlinear processes and the lack of mirrors, temporal correlation techniques that are widely used in the optical frequencies are very difficult to realize. To overcome these difficulties, a few new concepts of ultrafast x-ray diagnostics have been developed recently. One of them is the terahertz-field streaking method, where a terahertz field generated from a specific undulator [27] or from a laser [28] has been used to modulate the photoelectron energy. Another new method is proposed to use a transverse deflecting cavity to measure the FEL induced time-correlated electron energy spread, from which the x-ray temporal profile can be retrieved [25].

In the following sections, we will focus on discussing three schemes developed or under developing at the LCLS: longitudinal mapping [29], X-band transverse deflector [25] and cross-correlation technique [17]. Two frequency domain methods - one is a wide-band spectrometer for e-beam temporal reconstruction [30], and the other one is statistical analysis based on x-ray spectral correlation function [31] - have also been developed recently at LCLS.

3.8.3.1 *Longitudinal Mapping of Electron Beams Using a Spectrometer*

The longitudinal mapping technique, which was first suggested in Ref. [32] and developed in Ref. [33, 34], was used to observe the longitudinal profile of an FEL microbunched electron bunch at a low-energy superconducting linac. Recently it has been further investigated and applied at the LCLS [29, 35]. This technique involves adjusting the LCLS second bunch compressor followed by running the bunch on an rf zero-crossing phase of the final 550-m linac. As a result, the time coordinate of the bunch is directly mapped onto the energy coordinate at the end of the linac. A high-resolution energy spectrometer located at an existing transport line (A-line) is then commissioned to image the energy profile.

To describe this method, we add a diagnostic chicane right after BC2 and run the beam in the L3 linac on an rf zero-crossing phase (where there is no net acceleration). We sketch the setup in Fig. 6. Nominal setup parameters are given in black type; those changed for measurement mode are in red and have an over-bar. The head of the bunch is assumed at z<0 ($z = ct$). A simple chicane has $R_{56} < 0$ with this convention.

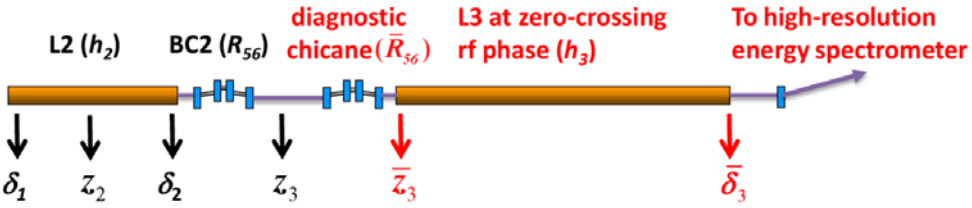

Figure 9: Schematic setup for short bunch measurement using a chicane and an rf linac. In red are parameters that changed for the bunch length measurement [29].

Suppose a diagnostic chicane strength is $\bar{R}_{56}$, and the rf-induced linear energy chirp in L3 is

$$h_3 = \pm\frac{2\pi}{\lambda_{rf}}\frac{eV_3}{E_2},$$

where the rf wavelength λ_{rf}=10.5cm for S-band linac, V_3 is the maximum accelerating voltage of L3, and $\pm$ refers to the two rf zero-crossing phases. Then longitudinal phase space is transformed between BC2 end and L3 end according to

$$\begin{pmatrix}\bar{z}_3\\ \bar{\delta}_3\end{pmatrix} = \begin{pmatrix}1 & 0\\ h_3 & 1\end{pmatrix}\begin{pmatrix}1 & \bar{R}_{56}\\ 0 & 1\end{pmatrix}\begin{pmatrix}z_3\\ \delta_2\end{pmatrix} = \begin{pmatrix}1 & \bar{R}_{56}\\ h_3 & 1+h_3\bar{R}_{56}\end{pmatrix}\begin{pmatrix}z_3\\ \delta_2\end{pmatrix},$$

where z_3 and $\bar{z}_3$ are the longitudinal bunch coordinates after BC2 and the diagnostic chicane, δ_2 and $\bar{\delta}_3$ are the relative energy coordinates at the end of L2 and L3, respectively (see Fig. 6). To have a one-to-one correspondence between z_3 and the final energy coordinate $\bar{\delta}_3 = h_3 z_3 + (1 + \mathrm{h}_3\bar{R}_{56})\delta_2$, it requires that [33]

$$(1 + \mathrm{h}_3\bar{R}_{56}) = 0.$$

Hence, to first order, the final energy coordinate is independent of the initial energy coordinate, and we have

$$z_3 = \frac{\bar{\delta}_3}{h_3}, \text{ and } \sigma_{z3} = \frac{\bar{\sigma}_{\delta 3}}{|h_3|}.$$

Here $\bar{\sigma}_{\delta 3}$ is the final rms energy spread at the L3 end, and σ_{z3} is the rms bunch length after BC2. Thus the final energy profile of the beam is a scaled image of its temporal profile after BC2, and an energy spectrum measurement yields the bunch profile. In the actual measurements, the diagnostic chicane is actually part of BC2, with its total strength changed to $R_{56} + \bar{R}_{56}$.

The longitudinal wake fields in the long linac can change the rf-induced energy spread. We can compensate this effect by shifting linac rf phase or adjusting chicane $\bar{R}_{56}$ [29]. The energy spread generated by a very short bunch (with σ_{z3}~1 μm) through this technique is about $\sigma_{\delta 3} = |h_3|\sigma_{z3}$~$10^{-4}$. To measure such a small energy spread, a high-resolution spectrometer is needed. The A-Line, one of the two original beam transport systems at SLAC, has a high dispersion point in the middle of a 24-degree bending section. A phosphor screen profile monitor (PR18) was installed at the high dispersion point (dispersion about 6m) to record the beam images.

To validate this technique, we compare the measurement results using the standard transverse deflector method with a bunch charge of 40 pC. At the nominal BC2 setting (with R_{56}= -24.7 mm), we first measure the bunch length using an rf deflector

(TCAV3), located after BC2, as a function of the L2 phase. We then set BC2 R_{56}= -34 mm to provide the strength for the diagnostic chicane as well as to compensate for the L3 wakefield. An energy feedback based on a BPM near PR18 is used to hold the L3 phase (near zero-crossing). Averaged PR18 rms beam size (over a few shots) yields the post-BC2 bunch length for the nominal BC2 setting as a function of the L2 phase. A comparison of the rms bunch length is shown in Fig. 7. When the bunch is either under or over-compressed with the rms bunch length longer than 3 μm, the two methods are in reasonable agreement. Near the full compression phase, TCAV3 reaches its resolution limit and yields scattered results, while the PR18 measurements shows a smooth curve with the minimum rms bunch length slightly above 1 μm. This minimum is believed to be limited by the resolution of the very old PR18 screen.

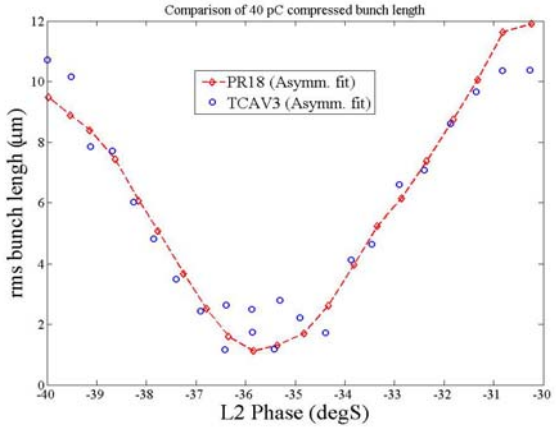

Figure 10: Comparison of 40 pC bunch length vs. linac phase measured from longitudinal mapping (PR18) and from deflector (TCAV3) [35].

A new phospher screen (ZnS) of 0.1 mm thickness was installed to replace the old screen in order to improve the PR18 resolution. The target inscribed on the new screen suggests that the resolution is about 125 μm in y and about 250 μm in x (a factor of 2 due to the 60-degree viewing angle). The smallest horizontal beam size measured on the screen is about 330 μm with 10-pC charge. After subtracting the screen resolution of 250 μm, we get a minimum rms bunch length of ~0.27μm or 0.9 fs [35].

3.8.3.2 *Electron and X-ray Pulse Temporal Characterization Using an X-band Transverse Deflector*

In another section of this newsletter [36], electron beam longitudinal phase space measurement using a transverse deflecting structure together with an energy spectrometer is discussed. More details and references can be found there. In this section, we will discuss the use of an X-band deflector to further improve the temporal resolution down to femtoseonds, and also to reconstruct the x-ray temporal profile based on the measured e-beam phase space [25].

The idea of using an rf deflecting structure (operating in the TM11mode) to kick the electron beam was first proposed in the 1960s [37] and has been recently used for e-beam bunch length and temporal profile measurements in FELs and other accelerator facilities [22]. Here we propose to install the deflector after the FEL undulator. To obtain the x-ray temporal profile, we first suppress the FEL process (e.g., by kicking the e-beam to make a local oscillating orbit inside the undulator) and measure the e-beam

time-energy phase space, from which we can get the e-beam temporal profile and also achieve a baseline on the e-beam energy loss. Next, the FEL is restored and we measure the time-energy phase space again for each bunch. By subtracting the baseline measured with FEL-off, we can obtain the time-resolved energy loss or energy spread due to FEL radiation, shot by shot. The x-ray temporal power profile is then determined by combining the e-beam current profile and the time-resolved energy loss.

Figure 8 shows a layout of this diagnostic system planned at the LCLS. We used two 1-meter long X-band (11.424 GHz) rf deflecting structures to provide a maximum horizontal kick of 48 MeV/c. Note that an X-band rf deflector has been chosen over an S-band one – like the original transverse deflector [37] - in order to impart a stronger sweep to the beam and thus improve the temporal resolution. At X-band the rf wavelength, λ_{rf}, is smaller, giving a factor 4 improvement compared to S-band. Furthermore, higher rf gradients can be achieved at X-band, allowing deflecting voltage to be increased and further improving the kicking strength.

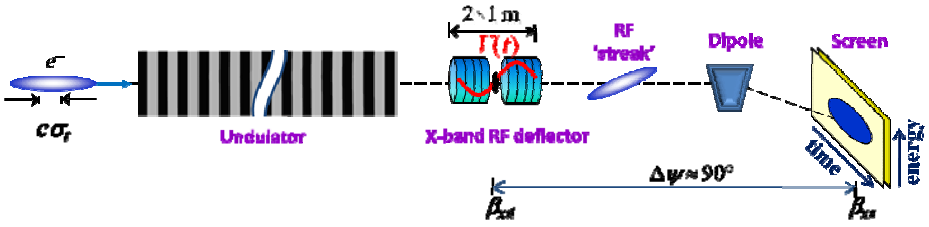

Figure 11: A layout of deflector setup at LCLS undulator dump line [25].

As discussed in [36], once the deflecting structure is fixed (rf wavelength and maximum deflecting voltage), the resolution is then determined by the beam optics design. For temporal resolution, a larger beta function and a 90-degree phase advance between the deflector and the observation screen at the deflecting plane are preferred. The energy resolution is determined by the spectrometer, where a smaller beta function and a larger dispersion at the screen in the bending plane should be considered. Based on the present LCLS design, the expected temporal resolution is about 2 fs rms.

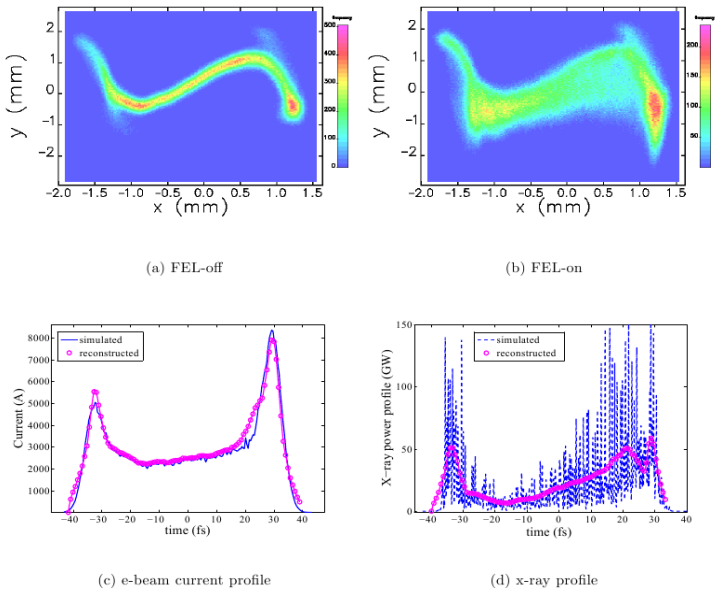

Figure 12: Simulations of the images on the screen ((a) and (b)) based on LCLS beam parameters with bunch charge 250pC, energy 13.6 GeV. The reconstructed e-beam and x-ray profiles are shown in (c) and (d) [25].

We show a simulation example in Fig. 9 for a hard x-ray case with a bunch charge of 250 pC. We can see a clear difference in the phase space between FEL-on and FEL-off. Both e-beam and x-ray pulse temporal profiles are obtained. Limited by the resolution, we cannot measure the x-ray single-spikes (about 200-as level). Note the coherent synchrotron radiation (CSR) from the bunch compressors in the upstream beam line will introduce a transverse kick to the electrons which is correlated to their longitudinal position in the bunch. This correlation between the horizontal and longitudinal planes can affect the phase space reconstruction technique. This effect in principle can be corrected by performing a second measurement at the other rf zero-crossing phase, 180° from the first measurement [38]. It would also be helpful for future designs to set the deflecting cavity and bunch compressor in different planes.

The two 1-meter structures were installed in the LCLS dump beamline in the summer 2012. The power source and other related elements are scheduled to be ready in March 2013 [39]. A picture of the installed structures in the LCLS undulator tunnel is shown in Fig.10.

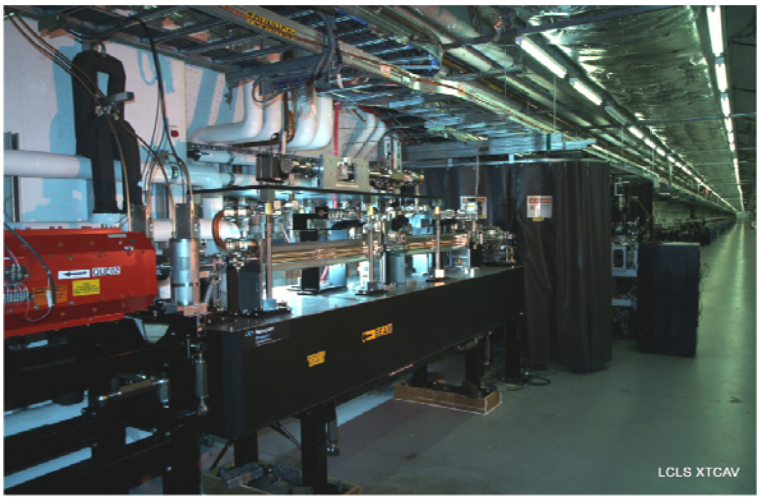

Figure 13: Photo of installed X-band deflecting structures at LCLS [39].

3.8.3.3 *X-ray Pulse Temporal Characterization Using a Cross-Correlation Technique*

Another technique based on a cross-correlation method has been demonstrated at the LCLS to measure femtosecond x-ray pulses [17]. This concept was first proposed by Geloni et al. [18]. In this scheme, to overcome the difficulties of splitting the x-ray pulses, a magnetic chicane is added in the middle of the FEL undulator. This chicane is to wash out the microbunching of electrons generated in the first part of the undulator, and also to make an offset for an x-ray optical delay line. After the chicane, the x-ray pulse overlaps with the "fresh" electron bunch, and their relative delay is controlled by the x-ray delay line. Since the "fresh" bunch idea [41] is involved, the system has to work in the exponential gain regime (before saturation).

The configuration can be further simplified by only using a chicane [40]. In this setup, the chicane has to play two roles: delay the electrons and smear the microbunching. As a result, the delay cannot reach zero otherwise the microbunching is preserved. In the following example, we show at hard x-ray wavelengths a minimum delay of 2-fs is required to provide enough R_{56} to smear microbunching. Hence for single bunch measurement only a partial correlation trace will be obtained. However, for the two-pulse mode, as produced in the emittance-spoiling foil scheme with double slots, we are able to obtain a full correlation trace with only using a chicane. In this mode, by variably delaying the electron beam with a chicane, the first electron bunch crosses over the second x-ray pulse and a full correlation trace is measured, from which both the pulse separation and duration can be retrieved [17].

At the LCLS undulator beamline, one LCLS undulator segment U16 (of 33 four-meter long undulator sections) has been replaced with a 3.2-m long magnetic chicane for the hard x-ray self-seeding program [5]. This chicane enables the cross-correlation measurements by operating the FEL in SASE mode. The present design of the chicane and chamber allows a maximum delay of about 40 fs.

We show a schematic layout of this diagnostic in Fig. 11. We focused our study at LCLS on using the emittance-foil configuration. The foil contains a single slot with variable widths, and double slots with variable separations. This slotted-foil enables us

to change the output x-ray pulse duration and to control the separation of two pulses in a simple way.

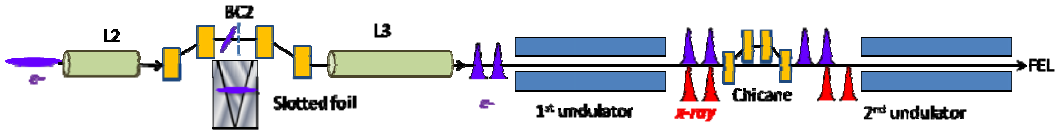

Figure 14: A schematic layout of the cross-correlation configuration at the LCS. A double-slotted foil setup is used for the illustration [17].

Clearly, this is a multi-shot based method. From the correlation trace measured by scanning the chicane delay, we can analyze the trace to get the pulse duration. A gas detector or a YAG screen was used to record the final x-ray pulse energy at each delay point. We show an example of the measured single pulse correlation trace in Fig. 12 [17]. The electron beam charge was 150 pC, the peak current was 3 kA, and the energy was 13.6 GeV. The x-ray photon energy was 8.3 keV. We used 13 undulator sections for each part in this measurement. Each data point is based on an average of 60 recorded shots. For this single bunch mode, the intensity correlation function should reach its maximum value at a relative delay $\tau = 0$ (overlapped), then it should go down with a larger delay until the x-ray pulse and the electron bunch totally miss. Therefore, during the Gaussian fitting, we chose a zero offset. To estimate the full width at half maximum (fwhm) of a pulse, the fwhm of the intensity correlation curve obtained from this fitting has to be divided by a deconvolution factor, which is related to a specific pulse shape. For example, for a Gaussian-shaped bunch, this deconvolution factor is $\sqrt{2}$. As shown in Fig.12, the fitting was from a minimum delay of 2 fs. For the no-foil case, the measured fwhm pulse duration (after dividing a factor 1.5) is 14.1 fs, and for slot widths 1.53 mm and 0.93 mm, the pulse fwhm durations are 7.3 fs and 3.8 fs, respectively.

Figure 13 shows examples of measured correlation curves for the two-pulse mode [17]. The photon energy was at 2 keV. We see a clear peak of the pulse energy while scanning the delay of the electrons. This peak means that the first electron slice overlaps with the second x-ray pulse and the FEL is enhanced, which determines the pulse separation. Also the width of the peak, as in the single bunch mode, gives information about the pulse duration. A Gaussian fit has been made to get the offset (pulse separation) and the width. In these two examples, the slot separations were 840 μm and 1400 μm, and the measured pulse separations were 14.7 fs and 22.7 fs. The measured pulse durations were 6.1 fs and 6.5fs, which are very similar since the slot width was fixed while changing the separation.

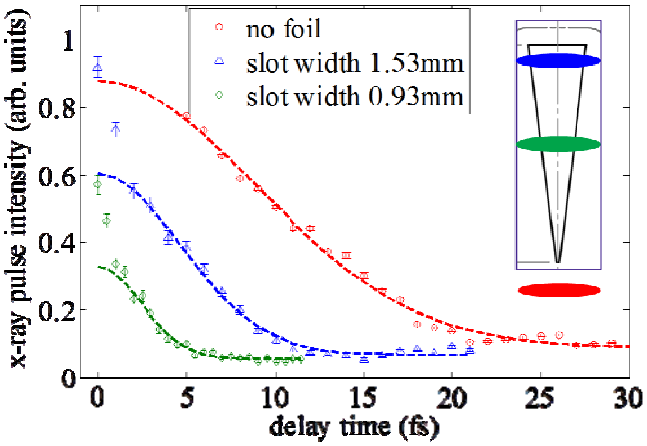

Figure 15: Cross-correlation measurements for a single bunch. Photon energy was 8.3keV, e-beam bunch charge 150pC and current 3 kA [17].

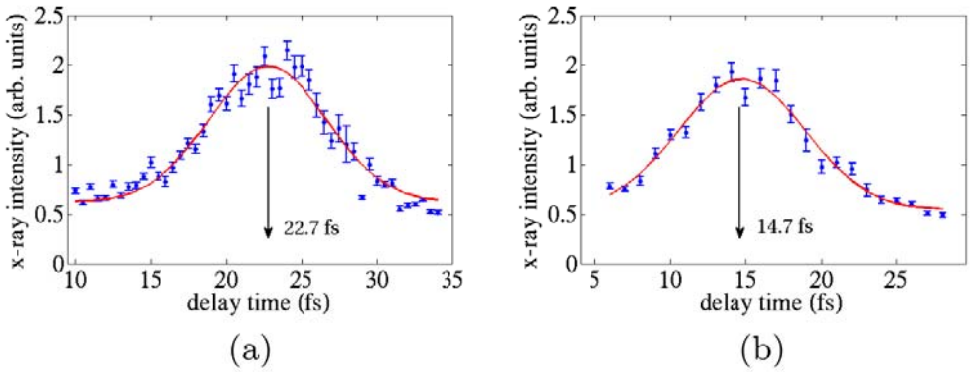

Figure 16: Cross-correlation measurements for double-pulse mode for different slot separations. The peaks show the separation (22.7 fs and 14.7 fs), and the widths give the pulse duration (6.5 fs and 6.1 fs) [17].

3.8.4 **Summary and Outlook**

Femtosecond x-ray FELs provide a unique tool for ultrafast scientific research. The low-charge bunch and emittance-spoiling foil scheme at LCLS are two widely used operation modes to deliver users ultrashort x-ray pulses of less than 10 fs. The double-slotted foil can also generate 2-color FELs with a variable delay [42], which is currently under experimental investigations [43]. If we combine the low-charge mode with slotted-foil, a single-spike x-ray pulse can also be generated at soft x-ray wavelengths. With even lower electron bunch charges or using very short laser pulses to manipulate the electron bunch, a single attosecond x-ray pulse may be obtained in the hard x-ray wavelength region.

Measurements of these femtosecond-scale electron and x-ray beams are still a challenging topic, and two more schemes at the LCLS are expected to be ready soon - the transverse deflector [25] and the wide-band spectrometer [30]. New diagnostic concepts with a femtosecond or even attosecond resolution are still highly desired.

3.8.5 References

1. P. Emma et al., “First lasing and operation of an angstrom-wavelength free-electron laser”, Nature Photon. 4, 641 (2010).
2. Ishikawa T. et al. “A compact X-ray free-electron laser emitting in the sub-angstrom region”, Nature Photon. 6, 540–544 (2012).
3. W. Ackermann et al., “Operation of a free-electron laser from the extreme ultraviolet to the water window”, Nature Photon. 1, 336 (2007).
4. E. Allaria et al., “Highly coherent and stable pulses from the FERMI seeded free-electron laser in the extreme ultraviolet”, Nature Photonics 6, 699, (2012)
5. J. Amann et al., “Demonstration of self-seeding in a hard X-ray free-electron laser”, Nature Photon. 6, 693 (2012).
6. For example, J. B. Rosenzweig et al., “Generation of ultra-short, high brightness electron beams for single-spike SASE FEL operation”, Nucl. Instrum. Methods Phys. Res., Sect. A 593, 39 (2008); X. J. Wang and X. Y. Chang, “Femto-seconds kilo-ampere electron beam generation”, Nucl. Instrum. Methods Phys. Res., Sect. A 507, 310 (2003);
7. Y. Ding, A. Brachmann, F.-J. Decker, D. Dowell, P. Emma, J. Frisch, S. Gilevich, G. Hays, Ph. Hering, Z. Huang, R. Iverson, H. Loos, A. Miahnahri, H.-D. Nuhn, D. Ratner, J. Turner, J. Welch, W. White, and J. Wu, “Measurements and Simulations of Ultralow Emittance and Ultrashort Electron Beams in the Linac Coherent Light Source”, Phys. Rev. Lett. 102, 254801 (2009).
8. P. Emma, K. Bane, M. Cornacchia, Z. Huang, H. Schlarb, G. Stupakov, and D. Walz, “Femtosecond and Subfemtosecond X-Ray Pulses from a Self-Amplified Spontaneous-Emission–Based Free-Electron Laser”, Phys. Rev. Lett. 92, 074801 (2004).
9. A. A. Zholents and G. Penn, “Obtaining attosecond x-ray pulses using a self-amplified spontaneous emission free electron laser”, Phys. Rev. ST Accel. Beams 8, 050704 (2005)
10. E. L. Saldin, E. A. Schneidmiller, and M. V. Yurkov, “Self-amplified spontaneous emission FEL with energy-chirped electron beam and its application for generation of attosecond x-ray pulses”**,** Phys. Rev. ST Accel. Beams 9, 050702 (2006).
11. Y. Ding, Z. Huang, D. Ratner, P. Bucksbaum, and H. Merdji, “Generation of attosecond x-ray pulses with a multicycle two-color enhanced self-amplified spontaneous emission scheme”, Phys. Rev. ST Accel. Beams, 12, 060703 (2009);
12. D. Xiang, Z. Huang, and G. Stupakov, “Generation of intense attosecond x-ray pulses using ultraviolet laser induced microbunching in electron beams”, Phys. Rev. ST Accel. Beams 12, 060701 (2009)
13. A. Zholents and G. Penn, “Obtaining two attosecond pulses for X-ray stimulated Raman spectroscopy”, Nucl. Instrum. Methods A 612, 254 (2010).
14. L. Wang, Y. Ding and Z. Huang, “Optimization for single-spike FELs at the LCLS with a low charge beam”, IPAC11, San Sebastian, Spain (2011).
15. V. Wacker, Y. Ding, J. Frisch, Z. Huang, C. Pellegrini and F. Zhou, “Sub-femtosecond hard x-ray pulse from very low charge beam at LCLS”, FEL12, Nara, Japan (2012).
16. P. Emma, Z. Huang, and M. Borland, “Attosecond X-ray Pulses in the LCLS using the Slotted Foil Method”, FEL2004, Trieste, Italy (2004).
17. Y. Ding, F.-J. Decker, P. Emma, C. Feng, C. Field, J. Frisch, Z. Huang, J. Krzywinski, H. Loos, J. Welch, J. Wu , F. Zhou, PRL in press (2012).
18. B. Schmidt et al., in Proceedings of the 11th European Particle Accelerator Conference, Genoa, 2008 (EPS-AG, Genoa, Italy, 2008), p. 130.
19. M. Zolotorev and G. Stupakov, “Spectral Fluctuations of Incoherent Radiation and Measurement of Longitudinal Bunch Profile”, PAC97, Vancouver, BC, Canada (1997). p. 2180.
20. J. Krzywinski, E.L Saldin, E.A Schneidmiller, M.V Yurkov, “A new method for

ultrashort electron pulse-shape measurement using synchrotron radiation from a bending magnet", Nucl. Instrum. Methods Phys. Res., Sect. A 401, 429 (1997).
21. D. X. Wang, G. A. Krafft, and C. K. Sinclair, "Measurement of femtosecond electron bunches using a rf zero-phasing method", Phys. Rev. E 57, 2283 (1998).
22. For example, R. Akre, L. Bentson, P. Emma, P. Krejcik, "A transverse RF deflecting structure for bunch length and phase space diagnostics", in Proceedings of the Particle Accelerator Conference, Chicago, IL, 2001, p. 2353; X.-J Wang, "Producing and measuring small electron bunches", PAC99, New York (1999).
23. K. Bane et al., "Measurements and modeling of coherent synchrotron radiation and its impact on the Linac Coherent Light Source electron beam", Phys. Rev. ST Accel. Beams 12, 030704 (2009).
24. Michael Röhrs, Christopher Gerth, Holger Schlarb, Bernhard Schmidt, and Peter Schmüser, "Time-resolved electron beam phase space tomography at a soft x-ray free-electron laser", Phys. Rev. ST Accel. Beams 12, 050704 (2009).
25. Y. Ding, C. Behrens, P. Emma, J. Frisch, Z. Huang, H. Loos, P. Krejcik, and M-H. Wang, "Femtosecond x-ray pulse temporal characterization in free-electron lasers using a transverse deflector", Phys. Rev. ST Accel. Beams 14, 120701 (2011).
26. D. Xiang and Y. Ding, "Longitudinal-to-transverse mapping for femtosecond electron bunch length measurement", Phys. Rev. ST Accel. Beams 13, 094001 (2010).
27. U. Frühling et al., "Single-shot terahertz-field-driven X-ray streak camera", Nat. Photon. 3, 523 (2011).
28. A. Cavalieri et al., Nat. Photon.
29. Z. Huang, K. Bane, Y. Ding, P. Emma, "Single-shot method for measuring femtosecond bunch length in linac-based free-electron lasers", Phys. Rev. ST Accel. Beams 13, 092801 (2010).
30. T. Maxwell, , C. Behrens, Y. Ding, A. Fisher, J. Frisch, and H. Loos, "Middle-infrared prism spectrometer for single-shot bunch length diagnostics at the LCLS", IBIC12, Tsukuba, Japan (2012).
31. A. A. Lutman, Y. Ding, Y. Feng, Z. Huang, M. Messerschmidt, J. Wu, and J. Krzywinski, "Femtosecond x-ray free electron laser pulse duration measurement from spectral correlation function", Phys. Rev. ST Accel. Beams 15, 030705 (2012).
32. E. R. Crosson et al., in Micro Bunches Workshop, edited by M. Blum et al., AIP Conf. Proc. No. 367 and No. 397 (AIP, New York, 1996).
33. K. Ricci and T. Smith, "Longitudinal electron beam and free electron laser microbunch measurements using off-phase rf acceleration", Phys. Rev. ST Accel. Beams 3, 032801 (2000).
34. K. Ricci, E. R. Crosson, and T. Smith, "Direct measurement of electron bunch shapes and coherent undulator radiation produced by 100 femtosecond structure", Nucl. Instrum. Methods Phys. Res., Sect. A 445, 333 (2000).
35. Z. Huang et al., "Measurement of Femtosecond LCLS Bunches Using the SLAC A-line Spectrometer", PAC11, THP183, New York (2011).
36. C. Behrens et al., "Recent applications of longitudinal phase space diagnostics", in this newsletter.
37. G. A. Loew and O. H. Altenmueller, "Design and applications of rf separator structures at SLAC", SLAC Report No. SLAC-PUB-135, 1965.
38. H. Loos et al., "Experimental Studies of Temporal Electron Beam Shaping at the DUV-FEL Accelerator", Proceedings of FEL05, p 632, Stanford, CA (2005).
39. P. Krejcik et al., "Ultra-short electron bunch and x-ray temporal diagnostics with an X-band transverse deflecting cavity", IBIC12, Tsukuba, Japan (2012).
40. G. Geloni, V. Kocharyan, and E. Saldin, "ultrafast x-ray pulse measurement method", DESY 10-008.
41. I. Ben-Zvi, K. M. Yang, L. H. Yu, "The "fresh-bunch" technique in FELS", Nucl. Instrum. Methods A 318, 726 (1992)

42. C. Feng, Y. Ding, Z.Huang, A. Lutman and J. Krzywinski, “Two-color FEL schemes based on emittance spoiler technique”, FEL12, Nara, Japan (2012).
43. A. A. Lutman, private communication.

3.9 A Review of Microbunching Instabilities in High Brightness Beam Transport

Daniel Ratner
SLAC, P.O. Box 4349, MS 20, Stanford, CA 94309, U.S.A.
Mail to: dratner@SLAC.Stanford.EDU

3.9.1 Introduction

The development of ultra-bright election beams has lead both to new accelerator applications as well as new problematic instabilities. One such example is the microbunching instability (MBI), which was first studied a decade ago during the development of X-ray Free Electron Lasers (FELs) [1, 2]. MBI was immediately acknowledged as a serious issue for FELs, and indeed there has already been one review in ICFA on the topic [3]. This review will focus on recent advances of one particular variant of MBI, in which Longitudinal Space Charge (LSC) forces produce strong microbunching at wavelengths shorter than the electron bunch [4, 5, 6, 7]. (Coherent synchrotron radiation, CSR, can also drive a similar instability [8, 9]. An earlier ICFA article focused on related instabilities in storage rings [10].)

MBI requires an initial level of density modulation to start the instability; possible sources have been suggested including density modulations due to the laser in photocathode beams, and the random density fluctuations of shot noise [3]. Evidence of optical wavelength microbunching was first seen during commissioning of the Linac Coherent Light Source (LCLS), where optical transition radiation (OTR) screens downstream from the injector recorded coherent OTR (COTR) from an uncompressed electron bunch [11]. Later measurements confirmed that the MBI not only impeded diagnostics, but also interferes with the FEL lasing process [12]. Given the large bandwidths and short wavelengths $(\lambda < 1\mu m)$ of the observations, electron shot noise amplified by LSC was seen as the most probable explanation.

Prior studies of shot-noise LSC MBI used one-dimensional (1D) models to predict the instability gain. Venturini noted [13] that 1D models of LSC impedance may fail at short wavelengths due to transverse non-uniformity. The need for detailed comparisons of theory and experiments motivated the development of three-dimensional (3D) MBI models [14, 15, 16, 17]. The emergence of MBI at linacs around the world spurred efforts at mitigating the instability's effects. The first laser heater, designed to damp the instability, was commissioned at LCLS [12, 4, 5]. Schemes for operating diagnostics in the presence of MBI have also proliferated in recent years [18, 19, 20, 21]. In this review we start by describing a 3D model of MBI, and as an example provide a comparison of the theory to the initial LCLS observations. We then review experimental schemes for both damping and avoiding MBI effects. Finally, we describe dispersive shot noise suppression [22], a version of the recently identified noise suppression phenomenon [23, 24] that is closely related to MBI.

3.9.2 **3D Model of MBI**

The goal of this section is to calculate the final microbunching of an initially randomly distributed electron beam. For this calculation we assume the accelerator is divided into two regions; in the first section the electrons can change energy but do not move longitudinally, while in the second section the electrons move longitudinally but do not change energy (Fig. 1). In both sections, the electrons can move in the transverse dimensions. This approximation is designed for the case of relativistic electrons moving through an accelerator region followed by a dispersive region, such as a bunch compressor chicane.

To derive the final electron density, we start with a random distribution of electrons in full six-dimensional (6D) phase space. The unevenly distributed electrons produce LSC fields, which in turn modulate the electron energies as they travel along the accelerator. A dispersive element with nonzero momentum compaction can then convert the energy modulation to a change in longitudinal position. As a result, the longitudinal density distribution is modified from the initial random distribution and may show enhancement at some frequency range, i.e., the beam is microbunched at these frequencies.

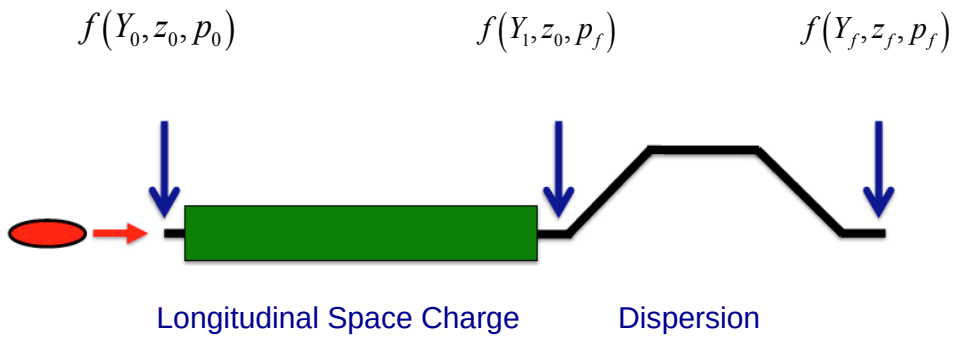

Figure 1: Schematic of the interaction-dispersion model system, with transverse coordinates Y and longitudinal coordinates *z, p*. Longitudinal space charge causes an energy modulation, $p_0 \to p_f$, which then produces a density modulation, $z_0 \to z_f$ following a dispersive region. We allow for transverse motion, $Y_0 \to Y_1 \to Y_f$ everywhere. The dispersion may be positive or negative.

In practice, microbunching most often appears as COTR emitted from thin foils in the beam path. The COTR from *N* electrons radiated at wave vector *k* into solid angle Ω has intensity

$$\left(\frac{d^2I}{dkd\Omega}\right)_{tot} = \left(\frac{d^2I}{dkd\Omega}\right)_1 N\left|b(K)\right|^2,$$

with the single-electron angular spectrum at angles θ_x and θ_y and relativistic factor γ,

$$\left(\frac{d^2I}{dkd\Omega}\right)_1 \propto \frac{\gamma^4\left(\theta_x^2+\theta_y^2\right)}{\left[1+\left|\gamma^2\left(\theta_x^2+\theta_y^2\right)\right]^2} \qquad (1)$$

and bunching factor at the screen,

$$b(K) = \frac{1}{\sqrt{N}} \sum_j \exp\left[-i\tilde{K}\tilde{X}_j\right] \exp\left[-ik\delta z_j\right]. \tag{2}$$

The essence of this approach to solving for the bunching factor is that we have separated out the 'single electron' portion due to the wave vector and electron coordinates at the screen

$$\tilde{K} \equiv \left[k\theta_x\, 0\, k\theta_y\, 0\, k0\right]$$
$$\tilde{X}_j \equiv \left[x_j, x'_j, y_j, y'_j, z_j, p_j\right] \tag{3}$$

from the 'collective' portion due to space charge effects

$$\delta zj \equiv \sum_{i\neq j}^{N} dz_{j,i} \equiv \sum_{i\neq j}^{N} \frac{e^2}{4\pi\varepsilon_0} \int_0^L ds \frac{R_{8\to L}^{(56)}}{\lambda_8 mc^2} \frac{\partial}{\partial z_i} \frac{1}{\left|X_j(s) - X_i(s)\right|} \tag{4}$$

where tilde denotes transpose, vertical bars denote vector amplitude, $R_{8\to L}$ is the transfer element from position s in the accelerator to the end of the LSC region *L*, $\lambda_8 mc^2$ is the energy of the *j*th electron at position *s*, and the sum is over all electrons in the bunch. The additional phase accumulated due to the collective interaction of the electron space charge forces, $k\delta z$, is what drives the microbunching. By assuming the additional phase is small we can linearize this term and solve for the bunching factor analytically.

To quantify MBI, our goal then is to find the expectation value (following [25])

$$\left\langle \left|b(K)\right|^2 \right\rangle = \frac{1}{N} \left\langle \sum_j^N \sum_l^N e^{-i\tilde{K}(X_j - X_l)} e^{-ik\left(\sum_{i\neq j} \partial z_{ji} - \sum_{i\neq l} \partial z_{li}\right)} \right\rangle \tag{5}$$

Conceptually, it is instructive to separate the sum into an 'incoherent' portion with $j = l$ and a 'coherent' portion with $j \neq l$. In the case of randomly distributed electrons (i.e. a shot noise beam), the $j \neq l$ phases are randomly distributed across 2π and average to zero. For this special case we then find $\left\langle \left|b(K)\right|^2 \right\rangle = 1$. The more interesting case occurs when the coherent terms, with $j \neq l$, have a non-zero expectation value.

To find the bunching factor of an arbitrary electron beam we integrate over the final particle distribution function, $\Psi_N(X_1,...,X_N)$. Because the final Ψ_N may be a complicated function of the coordinates of all *N* particles and the 6D beam transfer matrices, R, we will rewrite our bunching factor in terms of the initial coordinates through $X(s) = R_{0\to 8} X_0$ and then integrate over the simpler initial distribution of all particles, $\Psi_N(X_1,...,X_N)$. For an initially uncorrelated beam we can decompose

$$\Psi_N(X_{01},...,X_{0N} = \prod_i^N \Psi(X_{0i}), \tag{6}$$

written as a product of the single particle distribution functions, $\Psi(X)$. We can

then integrate over the single particle distributions to find

$$\left\langle \left| b(K) \right|^2 \right\rangle = 1 + N \int dX_{01} \int dX_{02} \Psi(X_{01}) \Psi(X_{02}) \times e^{-iK(R_{0\to L}X_{01} - R_{0\to L}X_{02})} \left[\Gamma_1 + \Gamma_2 \right] . \quad (7)$$

with definitions expanded in powers of $k\partial << 1$

$$\Gamma_1 \approx -ik(\partial z_{1,2} - \partial z_{2,1})$$
$$\Gamma_2 \approx Nk^2 \int dX_{0i} \left| \Psi(X_{0i}) \partial z_{\mathbf{1},i} \, dz_{2i} \right. . \quad (8)$$

To derive the last result we also assumed $\Gamma_2 << 1$ and that all microbunching occurs at wavelengths much shorter than the bunch length. A full derivation of Eq. 7 can be found in [26].

The First term Γ_1 is linear in $k\partial z$, while the second term $(\Gamma_2)$is quadratic in $k\partial z$. Even though $k\partial z$ is presumed to be small, we cannot ignore the quadratic term because it also contains a factor of *N*, which in the case of LCLS can be as large as 1 billion. MBI occurs when the second term dominates. In principle it is possible to evaluate Eq. 7 for nearly arbitrary 6D transport matrices and initial distributions. For Gaussian distributions most of the integrals in Eq. 7 have analytical solutions even for arbitrary transport matrices. (See Eqs. 3.39 and 3.46 in [15].) In practice, it may be sufficient to analyze simpler cases; in the next section we will work through an example for the LCLS COTR observations.

There may be situations for which it is not possible to break the instability into discrete regions with LSC and dispersion. If the particles move longitudinally during the LSC interaction, a plasma approach is better suited to the analysis [16, 17]. Rather than tracking discrete particles according to transfer matrices, Refs. [16, 17] start from the coupled Vlasov-Poisson equations to describe the beam evolution in 6D phase space. While the Vlasov approach has its own constraints (for example fixed beam density), it allows for self-consistent treatment of longitudinal motion during the interaction. In addition, transverse motion during the interaction is simpler to analyze using the Vlasov formalism than with the transfer matrix model described above.

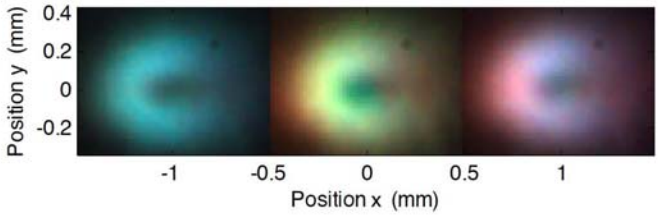

Figure 2: Strong COTR measured after the second bunch compressor chicane at LCLS. Real-color images show the shot-to-shot fluctuation in wavelength. Figure taken from Ref. [28].

3.9.3 **COTR Observations**

During commissioning of LCLS, dramatic enhancement of the radiation from OTR screens was the First conclusive evidence of MBI [11]. Subsequently a number of other linacs have reported similar observations [18, 19, 20, 27]. The multiple compression stages at LCLS leads to particularly strong MBI, as seen in Fig. 2. The resulting coherent radiation inhibits the use of OTR diagnostics and even damaged a camera. Most of the MBI reports are consistent with shot noise origins; the LSC observations are largely too broad bandwidth to start from laser modulations, and in one case has been observed at a facility with thermionic cathodes that do not employ lasers [19].

As an example of applying the results of Eq. 7, we take the case of the initial COTR observations downstream from the LCLS injector [28]. To compare the measurements to the theory described above, we plug Eq. 7 in for the bunching factor and integrate over the camera collection angle Θ_m

$$\frac{dW}{dw} = \int_{-\theta/2}^{\theta m/2} d\theta \int_{\theta m/2}^{\theta m/2} d\theta_y \left(\frac{d^2 W}{dw d\Omega} \right)_1 \left[N + N^2 \left| b(k) \right|^2 \right] \tag{9}$$

We assume an initial distribution, Ψ (X_0), that is a transverse Gaussian in both position (x,y) and angle (x', y'), and flat-top longitudinally. The quadratic term, Γ_2, dominates for $k^2 \left| dz \right|^2 >> 1/N,$ so we drop the other terms. Assuming a short impedance section of total length L $>>\beta$, the transfer matrices are nontrivial only downstream of the impedance section. Keeping just the dominant transfer elements for the beam line (see Fig. 3) we find the longitudinal phase of the single electron component in Eq. 7

$$\begin{aligned} KRX = k\big[& z_0 + R_{56}\tilde{p}_0 + R_1 x_0 \\ & + R_2 x_0' + \ \theta_y R_{33} y_0 + \theta_y R_{34} y_0' \ \big], \end{aligned} \tag{10}$$

with definitions $R_1 \equiv R_{51} + \theta_x R_{11}$ and $R_2 \equiv R_{52} + \theta_x R_{12}$.. The asymmetry between x and y coordinates is due to the dogleg in the x-dimension. Defining $R_q \equiv \sqrt{R_1^2 + \theta_y^2 R_{33}^2}$ and tan $\nu \equiv \theta_y R_{33} / R_1$ so that $R_1 \cos\phi + \theta_y R_{33} \phi = R_q \cos(\phi + \nu)$ and assuming a circular beam σ with $k\sigma/\gamma >> 1$ we find

$$\left\langle \left| b(K) \right|^2 \right\rangle \approx \frac{4}{3} \left[\frac{I}{I_{A\gamma}} \frac{R_{56} L}{\sigma^2} \right]^2 \frac{e^{\left[-\sigma'^2 k^2 (R_2^2 + \theta_y^2 R_{34}^2) - K^2 R_{56}^2 \sigma_p^2 \right]}}{\left[\gamma^2 R_q^2 + 1 \right]^2}, \tag{11}$$

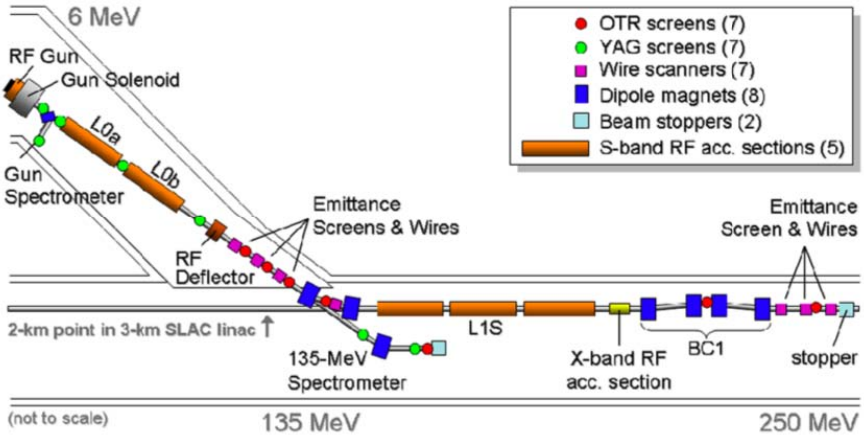

Figure 3: Schematic of the LCLS beamline through the first bunch compressor at the time of measurements. The current beam line is nearly identical except for the addition of a laser heater in the dogleg following L0b. Figure taken from Ref. [11].

with peak current $I_0 = ecn_0$, Alfvén current $I_A = ec/r_e = 4\pi\varepsilon_0 mc^3/e$ kA, and slice energy spread σ_p. To find the maximum gain, we set $R_{51} = R_{52} = 0$ (the nominal running condition) and use R_{11}, R_{12}, R_{33}, R_{34} from the LCLS design lattice. Because the gain depends sensitively on the slice energy spread, we can use Eq. 11 to estimate $\sigma_p \approx 3\ keV\ rms$ (Fig. 4), consistent with the typical slice energy spread measured from a photocathode rf gun [29]. The discrepancy at short wavelengths may be due to regions of smaller energy spread where the short wavelength microbunching survives.

The first evidence for MBI came from setting the 'QB' quadrupole (inside the dogleg) off achromat. While this would have little effect on an incoherent beam the non-zero R_{50} and R_{51} terms strongly suppress MBI (Fig. 5). Setting R_{51} and R_{52} nonzero in Eq. 11 should give the microbunching gain at different QB settings, but predicts a width about a factor of 2 narrower than in the measured QB curve. The MBI may be less sensitive than a Gaussian distribution predicts, especially if the cathode or drive laser produce a transversely non-uniform beam.

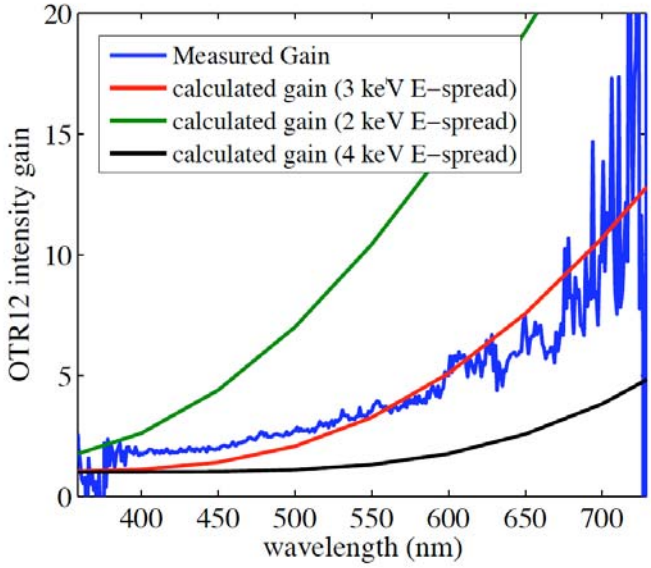

Figure 4: OTR intensity gain for 250 pC charge at OTR12 as a function of the optical wavelength. Figure taken from Ref. [14].

3.9.4 **Mitigating MBI**

3.9.4.1 ***Laser Heaters***

Shortly after MBI was identified as a problem for X-ray FELs, the energy spread damping mechanism was seen as a possible solution. By increasing the slice energy spread, the final exponential term in Eq. 11 damps the microbunching gain. Typically linac electron beams have smaller longitudinal phase space than is needed for an FEL, so it is acceptable to intentionally increase the energy spread of the beam (being careful to leave the relative spread well below the Pierce parameter ρ, which governs FEL performance.) To increase the slice energy spread, a laser 'heater' was proposed [4, 5]. In a heater, the electron beam interacts with a laser beam in an undulator, producing a periodic energy modulation. The interaction is placed in the middle of a chicane both to allow easy access for the laser as well as to produce more uniform heating by mixing phase space.

The laser heater was implemented during commissioning of LCLS [12]. An IR laser (split from the photocathode laser) modulates the electron beam energy shortly after the injector. Fig. 6 shows the increase in the slice energy spread as a function of laser power. While the heater does not fully suppress the MBI, Fig. 7 shows the damping is sufficient to improve the gain length by 30%. Unexpectedly, the LCLS laser heater creates substantial energy spread even with only ~1μJ laser power (see Fig. 11 of Ref. [12]). This so called 'trickle heating' is explained by LSC-induced microbunching seeded by the laser heater modulation, i.e. starting from a periodic distribution function $\psi(X)$ in Eq. 7.

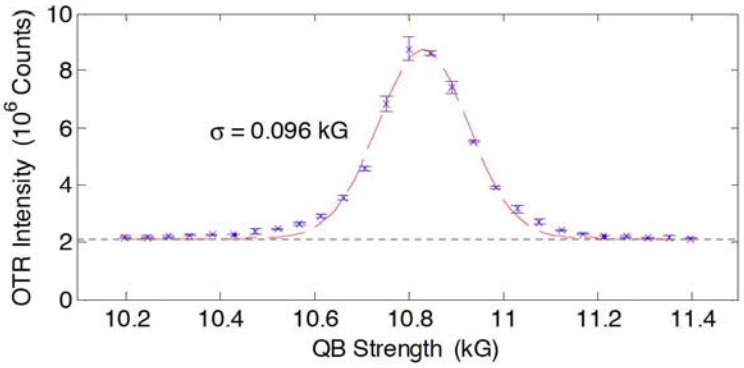

Figure 5: The integrated OTR signal as a function of the dogleg 'QB' quadrupole strength. MBI dominates at the peak when the bend is achromatic. When the QB quadrupole shifts, the MBI disappears and the camera measures the incoherent OTR level. Fig. taken from [28].

Laser heaters by their nature decrease the brightness of the electron beam. The larger phase volume lowers the instability gain, but can lower the FEL gain as well (as seen in Fig. 7). Ideally, the heating would be reversible; during the acceleration and compression stages, a large pseudo energy spread could wash out MBI, but the beam would return to its small initial energy spread for optimal FEL performance. By the Panofsky-Wenzel theorem, a transverse detecting cavity necessarily also changes the particle energies [30]. A recent proposal for a reversible heater makes use of two transverse cavities to impose, and then later remove, an energy modulation [31]. Between the two cavities, the pseudo-energy spread suppresses MBI. Seeding FELs prior to bunch compression also has the same effect [32].

3.9.4.2 *COTR-Free Diagnostics*

Even though a laser heater improves FEL performance, sufficient MBI remains to render OTR diagnostics unusable; the bright radiation is not proportional to the electron beam density, distorting measurements of transverse beam properties such as emittance. LCLS largely abandoned OTR screens in favor of traditional diagnostics (e.g. wire scanners) that are not susceptible to microbunching. However, wire scanners are slow and give averaged profile information. OTR screens, on the other hand, can provide single shot profiles simultaneously in both transverse dimensions. As a result, there have been efforts to develop new imaging techniques that function even in the presence of MBI. Iterative phasing (a common technique in crystallography) can reconstruct the electron profile from the COTR itself [21]. An experimental demonstration at the Next Linear Collider Test Accelerator (NLCTA) showed that the reconstructed profile is an accurate reproduction of the incoherent OTR profile. It may also be possible to avoid the coherent portion of the radiation from OTR screens. For example, from Eq. (11) it is

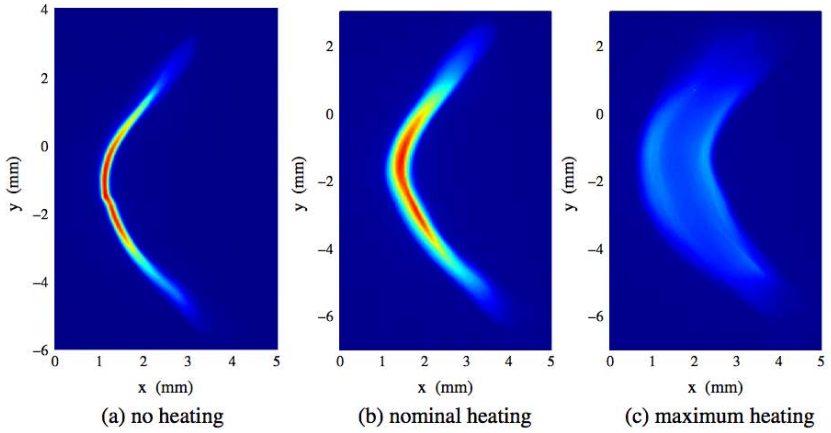

Figure 6: YAG screen images of the electron beam in a dispersive region downstream from a transverse cavity. The 'y' coordinate represents time and the 'x' coordinate represents energy. Images show a) laser heater off, b) nominal heating from 10μJ, and c) maximum heating from 220μJ. The faint double line visible in the plot at right is evidence of the laser beam radius exceeding thatof the electron beam. Figure taken from Ref. [12].

evident that at sufficiently large angles, the MBI gain vanishes; as a result, spatially filtering out small angles will preferentially remove COTR. Similarly, energy spread damps COTR at high frequencies, so a high pass filter will also preferentially block COTR.

A number of groups around the world have turned to scintillation screens to avoid COTR problems. As with an OTR screen, microbunched electrons radiate coherently as they pass through a scintillator. However, by separating out the additional (incoherent) scintillation light it is possible to obtain an image of the beam despite MBI-driven COTR. The scintillation can be separated by temporal [20], frequency [18], or spatial [19] filtering. For temporal filtering, the camera triggers after the COTR passes, but before the slow (nanosecond) scintillation process ends [20]. More detailed discussion of this method can be found in 'Recent applications of longitudinal phase space diagnostics' by C. Behrens and C. Gerth in this newsletter. For frequency filtering, a bandpass filter at the fluorescence peak avoids the majority of the broadband COTR, so that the scintillation signal dominates [18]. Finally, because scintillation is emitted at wide angle compared to the COTR, a spatial mask can also reduce the effect of COTR [19]. It should be noted that COTR in the UV potentially could itself drive fluorescence, which would distort the scintillation signal in all three cases [33].

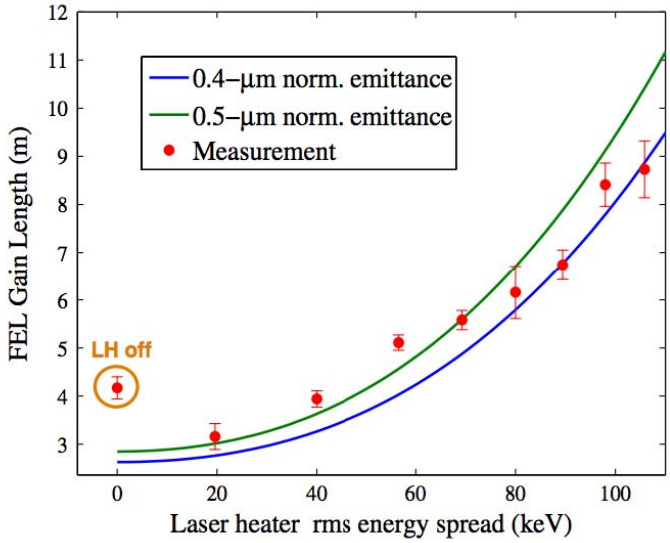

Figure 7: FEL gain length as a function of laser heater power. Producing a 20 keV energy spread lowers the gain length by 30%, but as the energy spread increases towards ρ, the gain length starts to grow as well. Figure taken from Ref. [12].

3.9.4.3 *Noise Suppression*

We conclude with a short discussion of shot noise suppression. To this point we have concentrated on the quadratic term, Γ_2, in Eq. 8. While Γ_2 dominates when MBI gain is large, in other regimes the linear term Γ_1 also contributes to the total bunching. While Γ_2 is always non-negative, Γ_1 can be negative, and in certain regimes can push $b(\mathrm{K}) < 1$ [22]. This phenomenon is called 'shot noise suppression,' because the bunching factor is smaller than that expected for a random distribution of electrons, i.e. shot noise. In the 1D limit (no transverse motion) and with negligible slice energy spread, the bunching factor is quadratic in

$$\left\langle \left| b(k) \right|^2 \right\rangle \approx (1-\Upsilon)^2 \tag{12}$$

with definitions

$$\begin{aligned} \Upsilon &\equiv n_0 R_{56} A \left[1 - 2 I_1(k\sigma/\gamma) K_1(k\sigma/\gamma) \right] \\ A &\equiv \frac{4\pi r_e L}{\pi \sigma^2 \gamma}, \end{aligned} \tag{13}$$

longitudinal charge density n_0, classical electron radius r_e, beam radius σ, and modified Bessel functions I_1 and K_1. Note in the high frequency limit Υ has no k dependence;

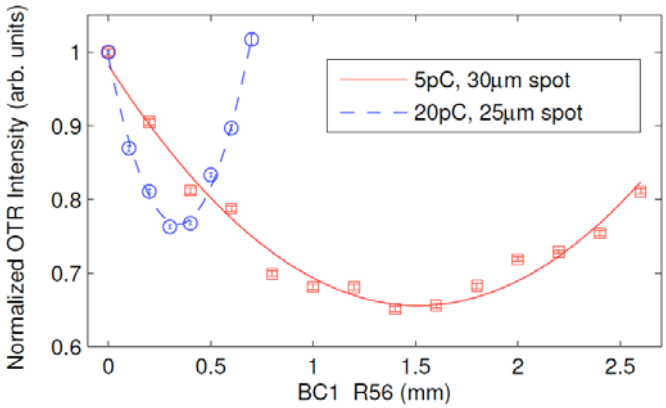

Figure 8: Observations of dispersive shot noise suppression at LCLS. The OTR intensity varies quadratically as a function of R_{56}. The lower charge (smaller n_0) requires stronger R_{56} to reach optimal suppression (Eq. 13). As the R_{56} increases past $\Upsilon = 1$, the beam enters the MBI regime and the COTR continues to grow quadratically (data not shown). Figure taken from Ref. [22].

by setting $n_0 R_{56} A = 1$, we force $|b(k)|^2 \to 0$ for all $k >> \gamma/\sigma$. (Full derivation can be found in [22].) As a result we conclude that it is possible to suppress density fluctuations (and all related radiation mechanisms) across a wide bandwidth range. Fig. 8 shows experimental evidence of dispersive noise suppression [34]. As the chicane R_{56} increases, the OTR signal decreases quadratically, and then begins growing again, eventually entering the MBI regime for $\Upsilon > 2$. The dispersive suppression phenomenon described here is closely related to other noise suppression schemes (e.g. from plasma oscillations) that have been proposed in recent years [23, 24, 35, 36].

One obvious application for noise suppression is in slowing the MBI; by reducing the initial shot noise fluctuations, the gain of the instability decreases. However, because plasma oscillations and dispersive regions will return the beam to its initial shot noise state, practical MBI damping may be difficult to achieve. A more promising application is seeded FELs; the power requirement for the seed laser is set by the spontaneous radiation of the beam, so suppressing shot noise fluctuations will lower the seed laser power requirement. Short wavelength seeding schemes are limited by seed laser power, so noise suppression could help push seeded FELs towards the X-ray limit.

3.9.5 Acknowledgements

The author would like to thank A. Marinelli and Z. Huang for helpful comments. Work supported by Department of Energy contract DE-AC02-76SF00515.

3.9.6 References

1. M. Borland et al. *Nucl. Instrum. Meth.* A, 483:268, 2002.
2. E. L. Saldin, E. A. Schneidmiller, and M. V. Yurkov. *Nucl. Instrum. Meth. A,* 490:1, 2002.
3. Z. Huang, J. Wu, and T. Shaftan. Microbunching instability due to bunch compression. *ICFA Beam Dynamics Newsletter*, 38, 2007.
4. E. Schneidmiller E. Saldin and M. Yurkov. *Nucl. Instrum. Meth. A,* 528:355, 2004.

5. Z. Huang, M. Borland, P. Emma, J. Wu, C. Limborg, G. Stupakov, and J. Welch. Suppression of microbunching instability in the linac coherent light source. *Phys. Rev. ST-AB*, 7:074401, 2004.
6. T. Shaftan and Z. Huang. *Phys. Rev. ST-AB*, 7:080702, 2004.
7. R. Warnock M. Venturini and A. Zholents. *Phys. Rev. ST Accel. Beams*, 10:054403, 2007.
8. Z. Huang and K.J. Kim. Formulas for coherent synchrotron radiation microbunching in a bunch compressor chicane. *Phys. Rev. ST Accel. Beams*, 5:074401, 2002.
9. G. Stupakov S. Heifets and S. Krinsky. *Phys. Rev. ST-AB*, 5:064401, 2002.
10. G. Stupakov and R. Warnock. Microbunch instability theory and simulations. *ICFA Beam Dynamics Newsletter*, 35, 2004.
11. R. Akre et al. *Phys. Rev. ST Accel. Beams*, 11:030703, 2008.
12. Z. Huang et al. Measurements of the linac coherent light source laser heater and its impact on the x-ray free-electron laser performance. *Phys. Rev. ST Accel. Beams*, 13:110703, 2010.
13. M. Venturini. Models of longitudinal space-charge impedance for microbunching instability. *Phys. Rev. ST Accel. Beams*, 11:034401, 2008.
14. D. Ratner, A. Chao, and Z. Huang. Three-dimensional analysis of longitudinal space charge microbunching starting from shot noise. *In Proceedings of the 2008 Free Electron Laser Conference, 2008*.
15. D. Ratner. Much Ado About Microbunching: Coherent Bunching in High Brightness Electron Beams. PhD thesis, Department of Applied Physics, Stanford University, 2011.
16. A. Marinelli and J.B. Rosenzweig. Microscopic kinetic analysis of spacecharge induced optical microbunching in a relativistic electron beam. *Phys. Rev. ST Accel. Beams*, 13:110703, 2010.
17. A. Marinelli, E. Hemsing, and J.B. Rosenzweig. Three dimensional analysis of longitudinal plasma oscillations in a thermal relativistic electron beam. *Physics of Plasmas*, 18:103105, 2011.
18. A. Lumpkin, N.S. Sereno, W.J. Berg, M. Borland, Y. Li, and S.J. Pasky. Characterization and mitigation of coherent-optical-transition-radiation signals from a compressed electron beam. *Phys. Rev. ST Accel. Beams*, 12:080702, 2009.
19. H. Tanaka. Status report on the commissioning of the japanese XFEL at SPring-8. *In Proceedings of IPAC2011, San Sebastian, Spain, 2011*.
20. C. Behrens, C. Gerth, G. Kube, B. Schmidt, S. Wesch, and M. Yan. Electron beam profile imaging in the presence of coherent optical radiation effects. *Phys. Rev. ST Accel. Beams,* 15:062801, 2012.
21. A. Marinelli et al. Single-shot coherent diffraction imaging of microbunched relativistic electron beams for free-electron laser applications. *Phys. Rev. Lett,* To be published, 2012.
22. D. Ratner, Z. Huang, and G. Stupakov. Analysis of shot noise suppression for electron beams. *Phys. Rev. ST Accel. Beams,* 14:060710, 2011.
23. A. Gover and E. Dyunin. Collective-interaction control and reduction of optical frequency shot noise in charged-particle beams. *Phys. Rev. Lett.,* 102:154801, 2009.
24. V. Litvinenko. Suppression of shot noise and spontaneous radiation in electron beams. *In Proceedings of the 2009 FEL Conference, 2009.*
25. G. Stupakov. Effect of finite pulse length and laser frequency chirp on HGHG and EEHG seeding. *Report SLAC-PUB-14639, SLAC, 2011.*
26. D. Ratner. *Report SLAC-R-992, SLAC, 2012*.
27. A. Lumpkin, R.J. Dejus, and N.S. Sereno. Coherent optical transition radiation and self-amplified spontaneous emission generated by chicanecompressed electron beams. *Phys. Rev. ST Accel. Beams*, 12:040704, 2009.
28. H. Loos et al. In Proceedings of the 2008 Free Electron Laser Conference, 2008.
29. M. Hüning and H. Schlarb. *In Proceedings of the 2003 Particle Accelerator*

Conference, 2003.
30. W. Panofsky and W. Wenzel. Some considerations concerning the transverse detection of charged particles in radio frequency fields. *Rev. Sci. Instrum..,* 27:967, 1953.
31. C. Behrens, Z. Huang, and D. Xiang. Reversible electron beam heating for suppression of microbunching instabilities at free-electron lasers. *Phys. Rev. ST Accel. Beams,* 15:022802, 2012.
32. D. Ratner, A. Chao, and Z. Huang. Two-chicane compressed harmonic generation of soft x-rays. *Phys. Rev. ST Accel. Beams,* 14:020701, 2011.
33. Personal correspondence with Jo Frisch.
34. D. Ratner and G. Stupakov. Observation of shot noise suppression at optical wavelengths in a relativistic electron beam. *Phys. Rev. Lett.,* 109:034801, 2012.
35. A. Nause, E. Dyunin, and A. Gover. Optical frequency shot-noise suppression in electron beams. *J. of Applied Physics,* 107:103101, 2010.
36. A. Gover, A. Nause, E. Dyunin, and M. Fedurin. Beating the shot-noise limit. *Nature Physics, 2012.*

3.10 Single-Shot Spatiotemporal Measurements of Ultrashort THz Waveforms Using Temporal Electric Field Cross-Correlation

N. H. Matlis, G. R. Plateau, J. van Tilborg, W. P. Leemans
Lawrence Berkeley National Laboratory, 1 Cyclotron Rd., Berkeley, CA 94720
Mail to: nhmatlis@lbl.gov

Abstract:

A new single-shot technique based on linear spectral interferometry between a temporally-short reader pulse and a temporally-long probe pulse is demonstrated for measuring the spatiotemporal phase and amplitude of an optical probe, for use as an ultrafast diagnostic. The probe spatiotemporal field information is recovered, with a resolution set by the duration of the reader pulse, by applying a single Fourier-transform operation to the interferogram image, without need of any reference data. The technique was used in conjunction with electro-optic sampling to measure waveforms of coherent, ultrashort THz pulses emitted by electron bunches from a laser-plasma accelerator with sub-50 fs resolution. The presence of strong spatiotemporal coupling in the THz waveforms and of complex temporal electron bunch structure was determined.

3.10.1 **Introduction**

Optical probing has long been an important tool for the characterization of ultrafast phenomena, because of its versatility, its sensitivity and its ability to resolve both spatial and temporal features with high resolution. Because of its simplicity, the configuration most commonly used to probe temporal dynamics is a multi-shot one in which the delay of a probe pulse shorter than the features to be resolved is scanned. This approach, however, is impractical for experiments done at low rep-rates or in which the signal varies significantly from shot to shot, motivating the development of techniques capable of recording temporal variations in a single shot. Such is the case for the field of terahertz time-domain spectroscopy (THz-TDS), which relies on optical mapping of the electric-field temporal waveforms of pulses of terahertz radiation (THz) via a technique known as electro-optic sampling (EOS) [1-4]. In EOS, the THz pulse induces a transient birefringence in an electro-optically active crystal which results in a polarization

rotation of a co-propagating optical probe pulse. The rotation is then converted to a temporal amplitude modulation by a polarizer.

THz-TDS has seen a dramatic surge in recent years because of the utility of ultrashort THz pulses as probes in an increasingly wide range of applications. For some applications, such as the characterization of current dynamics in semi- and superconductors (e.g. [5-7]) a scanning configuration can be implemented successfully because of the use of high rep-rate (kHz) lasers and the stability of the material response function. For many other applications, such as the diagnosis of electron bunch durations in laser-plasma accelerators (LPAs) [8], single-shot detection is critical, due to the large shot-to-shot variability and the low rep-rates of high-intensity laser systems. As a result, a large body of work has been done to develop single-shot, EOS-based optical techniques which satisfy the needs of these applications [2-4, 9-18]. Each, however, has had significant limitations.

Single-shot EOS was first achieved by a technique named \spectral encoding," in which a chirped pulse was used to provide a mapping between time and wavelength [10]. Spectral encoding, however, was plagued by a loss of temporal resolution due to the modification of the time-wavelength mapping caused by the encoding process which produced distortions in the measurement [12,13,19]. This shortcoming was later addressed by combining the chirped probe with a temporally-short pulse in a second-harmonic cross-correlation geometry [14, 15], providing high temporal resolution in the 10s of fs. This technique, however, has the disadvantage that it requires high probe intensities and thus expensive amplified lasers in order to get adequate signal. In addition, because the temporal signal is encoded spatially and the probe laser is focused at the interaction, spatial information about the THz pulses is lost. As the THz pulses in many of these applications are few- to single-cycle, implying relative bandwidths of order unity, the focused THz waveforms can exhibit strong spatiotemporal coupling due to a large variation of the Gaussian beam parameters over the spectrum [20]. Failure to resolve the spatial variations can therefore result in a loss of critical information.

In this article, a new technique named Temporal Electric-field Cross-correlation (TEX) is presented which overcomes the above limitations, allowing measurement of THz waveforms with high temporal resolution and simultaneously providing one dimension of spatial information. TEX is based upon measurement of the linear cross-correlation of a chirped probe with a compressed reader pulse using spectral interferometry. The full electric-field information of the optical probe, convolved with that of the short reader, is retrieved, allowing signals to be encoded onto either the phase or the amplitude of the probe or both. This dual capability is not present in previous EO methods, and makes TEX applicable to the measurement of a wide range of phenomena beyond EO sampling. Because the detection is linear, TEX can be implemented with low-cost, unamplified laser systems, and because it does not require focusing of the optical probe, spatial information can be recorded and retrieved. The temporal detection window is easily tunable in the several ps range by adjusting the chirp of the probe pulse, and the temporal resolution of the phase and amplitude retrieval is set by the duration of the short reader pulse pulse, which convolves the signal. Implementation of TEX to measure waveforms of intense THz pulses from an LPA is also demonstrated. Electrons experiencing a dielectric transition (such as a metallic foil or a plasma-vacuum boundary [21, 22]) emit coherent transition radiation in the THz regime. The temporal and spectral properties of the THz radiation are

strongly correlated to the electron-bunch temporal structure, making it an ideal diagnostic for ultrashort electron bunches.

It should be noted that the ability to retrieve the full electric field of an optical probe is not unique to TEX, but is shared by other techniques such as Frequency Domain Holography (FDH) and Single-shot Supercontinuum Spectral Interferometry (SSSI) [23-25]. The key advantage of TEX over FDH and SSSI is that recovery of the probe amplitude and phase does not require any reference data, and is obtained from the TEX interferograms by a single Fourier transform operation, making it significantly easier to use than the others. FDH and SSSI by contrast, provide the pure electric-field retrieval of the probe without convolution.

3.10.2 **Experimental Setup**

Figure 1 shows the setup for TEX, implemented on an LPA-based THz source [1, 21, 26]. Using ~ 400 mJ, 800 nm, 45 fs pulses focused into a 2 mm gas jet of Helium, electron bunches with large energy spreads and sub-ps bunch durations were produced, resulting in generation of coherent transition radiation (CTR) in the range of 0-4 THz. A portion of the radially-polarized cone of THz emission was asymmetrically sampled by collection with an off-axis parabola (OAP). The resulting collimated beam of THz was primarily linearly polarized, with a residual transversely-polarized component analytically estimated to be at the 10% level. The THz beam was then refocused with a second OAP onto a 200 μm thick gallium phosphide (GaP) crystal cut along <1; 1; 0>. An optical pulse split from the pump beam that generated the electrons was over-compressed, resulting in a temporally chirped pulse ("probe") with a full-width half-maximum (FWHM) duration of 2 ps. A second fully-compressed optical pulse ("reader"), measured to have a FWHM duration of 45 fs, was also split from the pump beam. The probe and the THz pulses were overlapped colinearly in the GaP crystal, resulting in the EO interaction. A polarizer was used to purify the polarization state of the incident *probe*, and a second polarizer (referred to as an "analyzer") was used to convert polarization rotations into amplitude modulations. A quarter wave plate (QWP) was used to offset the transmission to the 50% level, allowing both positive and negative THz fields to be resolved. The transmitted *probe* pulse was then combined colinearly with, but temporally offset from the *reader* and sent into a 0.27 m imaging spectrometer with a 14-bit, 1 Mpix cooled CCD detector, producing a spectral interferogram image ("TEXogram"). A pair of achromatic lenses was used to image the interaction plane to the input plane of the spectrometer, where the spectrometer slit is used to select a spatiotemporal slice of the *probe*.

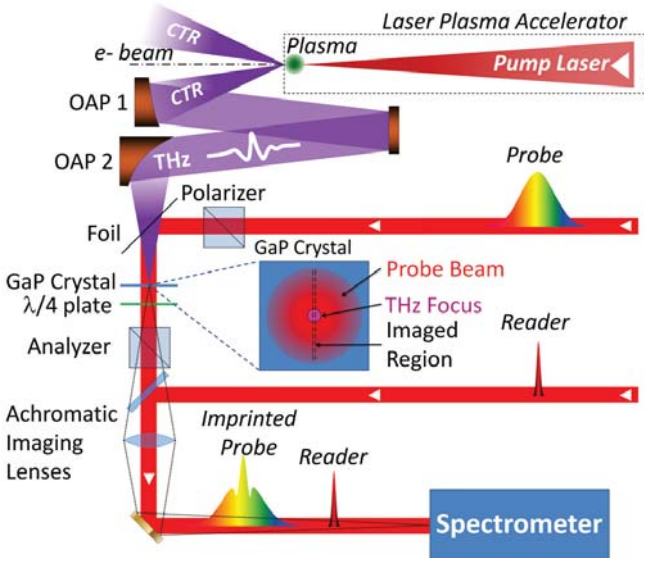

Figure 1: Schematic of the TEX detection scheme.

The choice to encode the THz signal onto either the amplitude or the phase of the *probe* field is made by appropriately choosing the polarization state of the incident *probe* (Fig. 2). If the polarization is aligned at 45° to the principal axes of the THz-induced index ellipsoid, the probe polarization will be rotated in proportion to the THz field strength [27, 28], but the phase-shift contribution from each of the axes will cancel, resulting in pure amplitude modulation (Fig. 2a). However, if the *probe* polarization is aligned along one of the principal axes, the probe will experience a temporally-varying phase-shift, but no polarization rotation, resulting in pure phase modulation (Fig. 2b). For other polarization states, the THz imprint is mixed between phase and amplitude with a strongly nonlinear dependence on the field strength, making waveform retrieval unreliable.

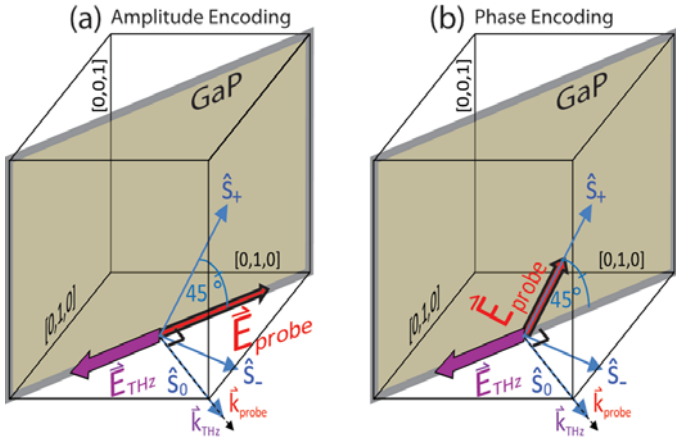

Figure 2: (a) Amplitude-encoding geometry. The probe polarization is aligned between the principal axes (S+,S-) of the THz-induced birefringence, resulting in polarization-rotation only. (b) Phase-encoding geometry. The probe polarization is parallel with one of the principal axes, resulting in phase-shifting only.

3.10.3 **Analysis**

The recovery of THz waveform occurs in two distinct steps. The first is the recovery, post-interaction, of the spatiotemporal electric field of the *probe*, which can be written $E_p(y,t) \equiv \mathsf{E}(y,t)\exp\{i\Phi(y,t)\}$, where t is time, y is the spatial coordinate, and $\mathsf{E}(y,t)$ and $\Phi(y,t)$ are the *probe's* temporal amplitude and phase, respectively. The second is the determination of the THz waveform spatiotemporal profile, $E_{THz}(y,t)$, from the THz-induced modulations of either the *probe* amplitude or the *probe* phase, depending on the method of encoding.

In the first step, $E_p(y,t)$ is obtained from the TEXogram by applying a single 1D Fourier Transform (FT) operation independently to each row of the spectral image. The TEXogram is described by $T_{EX}(y,\omega) = |E_p(y,\omega)|^2 + |E_r(y,\omega)|^2 + E_p(y,\omega)E^*_r(y,\omega) + c.c.$ where ω is the optical angular frequency, and $E_p(y,\omega)$ and $E_r(y,\omega)$ are the electric-fields of the *probe* and *reader* pulses respectively in the spectral domain. The FT results in a time-domain signal containing four components corresponding to the four terms of the TEXogram. The first two terms of $T_{EX}(y,\omega)$ produce overlapping peaks known as "coherence spikes" at t = 0, while the third and fourth terms (i.e. "cross-terms"), which are responsible for the fringes in the *TEXogram*, produce side-peaks at $t = \pm\Delta t$, where Δt is the delay of the probe behind the reader (Fig. 3). The "convolution theorem" of FTs identifies the FT of the cross-terms with the complex cross-correlation of the electric-fields of the probe and the reader in the time-domain; i.e., if the FT is expressed as: $FT[T_{EX}(y,\omega)]\,(t) = A(y,t) + C(y,t) + C^*(y,-t)$, where A(y,t) is the FT of the first two terms of $T_{EX}(y,\omega)$, and $C(y,t) \equiv FT[E_p(y,\omega)E^*_r(y,\omega)](t)$ is the FT of the first cross-term, then $C(y,t) = \int_{-\infty}^{\infty} E_p(y,\tau)E_r^*(y,\tau - t)d\tau$ is the cross-correlation of the *probe* temporal field given by $E_p(y,t) = FT[E_p(y,\omega)](t)$ with the *reader* temporal field given by $E_r(y,t) = FT[E_r(y,\omega)](t)$. For a *reader* with a suitably short duration and negligible spectral phase, the side peak in the FT of $T_{EX}(y,\omega)$ approximates the chirped probe pulse in both amplitude and phase: $C(y,t) \approx E_p(y,t)$.

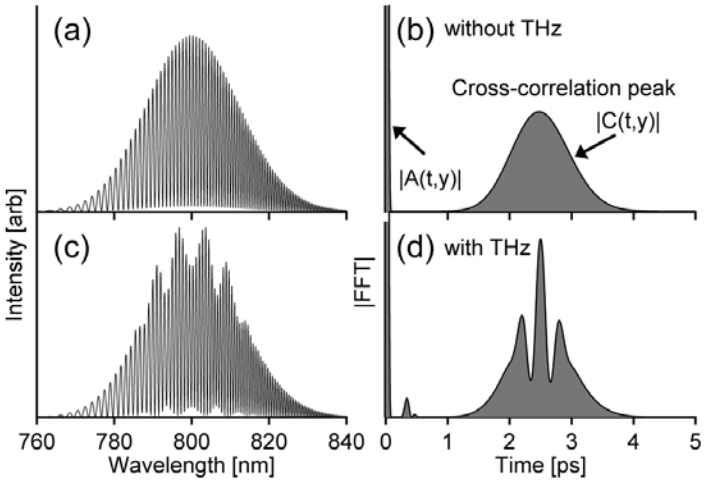

Figure 3: (a) Simulated TEX interferogram in the absence of THz showing interference in the spectrometer between copropagating probe and reader pulses separated in time by 2.5 ps. (b) Modulus of the Fourier transform of the interferogram in (a) showing a broad side peak at 2.5 ps which represents the amplitude of the cross-correlation between the probe and reader electric-fields. (c) Simulated TEX interferogram with THz present. (d) Modulus of the complex Fourier transform of the interferogram in (c), showing a THz-induced modulation in the side peak amplitude.

In the second step, the THz waveform is recovered by determining the modulation to either $E(y,t)$ or $\Phi(y,t)$. In the amplitude-encoding method, the transmitted probe amplitude is given by $E_T^2(y,t) = \frac{1}{2} E_0^2(y,t)[1 + \sin(\alpha E_{THz}(y,t))]$, where $\alpha \equiv 2\pi L/\lambda\, n_0^3\, r_{41}$, L is the crystal thickness, λ is the optical wavelength, n_0 is the linear index in the absence of THz, r_{41} is the linear electro-optic coefficient, and the 0 and T subscripts denote field quantities before and after the interaction, respectively. In the phase-encoding method, the transmitted phase is given by $\Phi(y,t) = \Phi_0(y,t) \pm \frac{1}{2} E_{THz}(y,t)$, where the sign depends on the choice of principal axis. As $E_0(y,t)$ and $\Phi_0(y,t)$ are not simultaneously acquired in TEX, a separate ("null") shot in the absence of THz is required. The reconstructed waveform is thus given by: $E_{THz}(y,t) = \alpha^{-1}\arcsin[E_T^2(y,t) / E_{null}^2(y,t) - 1]$ for amplitude encoding and by $E_{THz}(y,t) = 2\,\alpha^{-1}[\Phi_T(y,t) - \Phi_{null}(y,t)]$ for phase encoding.

The temporal resolution of the THz waveform retrieval is determined by two independent factors: the duration of the reader, which determines the temporal resolution of the probe electric-field recovery, and the thickness of the EO crystal, which determines the EOS phase-matching bandwidth. Calculations simulating the probe field retrieval process in both phase- and amplitude-encoding configurations for a 45 fs reader confirm accurate reconstruction of the encoded signal for frequencies beyond ~8 THz, which is the resolution limit set by the 200 μm GaP crystal. The limitation to the temporal range of the detection is set by the bandwidth and spectral resolution of the imaging spectrometer, which must be capable of resolving the spectral fringes over the full bandwidth of the probe.

3.10.4 **Results**

Figure 4 shows a sample THz spatiotemporal waveform image acquired using TEX in the amplitude-encoding configuration. The measured waveform is nearly single cycle, and displays sharp temporal features of order 100 fs, illustrating the need for high temporal resolution. The waveform also exhibits strong spatiotemporal coupling, in the shape of an X, as was described by Jiang et al. [20], which can be understood in terms of a variation of the Gouy phase shift and focused-waist size with wavelength. To diagnose the structure of the electron bunch, the spectrum of the THz waveform shown in figure 4 was calculated and compared with theory. The spatial and temporal features of the spectral image were modeled (Fig. 5) by using CTR emission theory [26] with the inclusion of collection and propagation effects. To accurately model both the low- and high-frequency parts of the spectral image, two bunches of different duration and charge (90% of the charge in a 140 μm-rms bunch and 10% in a 50 μm bunch) were required. Comparison of a one-bunch model (containing only the longer bunch) with the two-bunch model shows that the contribution to the THz emission above ~0.75 THz comes entirely from the shorter bunch, in spite of its small relative charge (Fig. 5c).

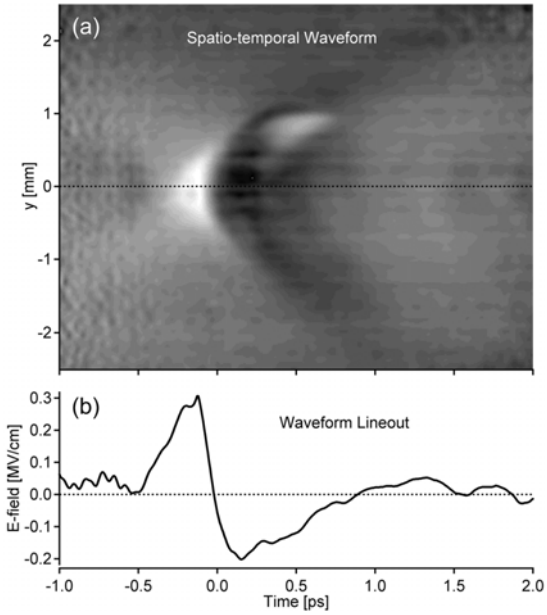

Figure 4: Data showing (a) THz spatiotemporal waveform extracted from the raw interferogram and (b) lineout of waveform at y = 0 mm.

This high sensitivity to the presence of the shorter electron bunch is an important confirmation of the practicality of the THz-based diagnostic for characterizing LPAs, since the high-energy, low-charge electron bunch component of interest is often accompanied by a lower energy component containing the bulk of the charge. The electron energy spectrum, measured simultaneously, does in fact show a two-component distribution with a large thermal- and a smaller "quasi mono-energetic" component. The importance of recovering the spatial variations in the THz waveform is illustrated by the strong spatial dependence of the spectrum of the focused THz pulse: the higher-frequency component from the short bunch is more localized to the axis. A spatially-integrated technique would under-represent this component, thus diminishing

sensitivity to the presence of the short bunch. In addition, because the transverse focal size of a given spectral component is strongly dependent on not only the wavelength but also the spectrally-varying far-field intensity distribution, the nice correspondence between data and model of the shape of the spectral image provides a confirmation of the THz emission patterns predicted by CTR theory.

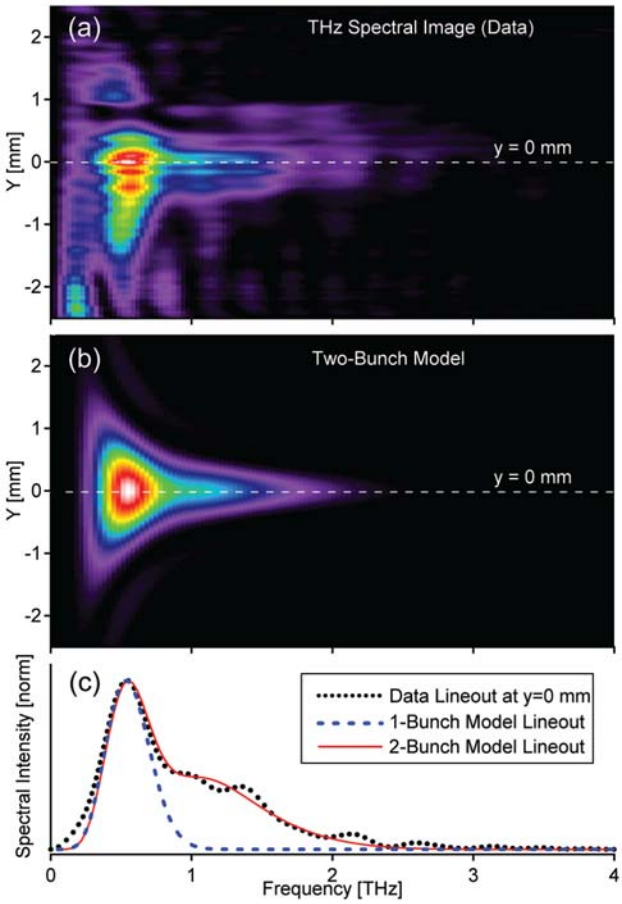

Figure 5: (a) Power spectrum of THz waveform in figure 4. (b) Spectral image calculated using a 2-bunch model (c) lineouts of spectral images for data (black-dotted line), 1-bunch model (blue-dashed line) and 2-bunch model (red-solid line). Comparison shows that a 2-bunch model yields a significantly better fit than a 1-bunch model.

3.10.5 **Conclusions**

A new single-shot technique (TEX) is demonstrated for measurement of ultrafast phenomena resulting in temporal phase or amplitude modulations. TEX provides high temporal resolution and one dimension of imaging simultaneously for the first time in EO sampling, enabling analysis of spatio-temporal and spatio-spectral coupling in the THz waveforms. TEX is significantly easier to setup than previous high-resolution EO techniques because it does not require the use of nonlinear processes other than the linear Pockels effect used for EO sampling. Because TEX is linear in the probe field strength, low-power, low-cost, unamplified laser systems may be used, making it highly accessible. In addition, the dual phase- and amplitude-encoding capability makes it

applicable to a wide range of phenomena. The temporal resolution is set by the duration of the reader pulse, and can be made smaller than the intrinsic limitation set by phase-matching in the EO sampling process. The single-shot temporal detection window is tunable in the range of several to 10s of ps, and is limited by the bandwidth and spectral resolution of the spectrometer. Numerical analysis confirms the capability of TEX to reproduce THz waveforms in both temporal and spectral domains without significant distortion in both phase- and amplitude-encoding configurations. Waveforms of THz pulses generated as CTR from an LPA were measured using the amplitude-encoding configuration and were analyzed. The resultant THz spectral images were used to demonstrate the presence of heterogeneous electron bunch structure from the LPA. The dependence of the THz spectrum on the electron-bunch duration makes it possible to detect the presence of short electron-bunch substructure with high sensitivity. The authors acknowledge Carl B. Schroeder, Kei Nakamura, Cameron G.R. Geddes, Anthony J. Gonsalves, Csaba Tóth and Eric H. Esarey for their valuable contributions.

This work was supported by DARPA and by the Director, Office of Science, Office of High Energy Physics, of the U.S.Department of Energy under Contract No. DE-AC02-05CH11231.

3.10.6 **References**

1. J. van Tilborg, "Coherent terahertz radiation from laser-wakefield-accelerated electron beams," Ph.D. thesis, Technische Universiteit Eindhoven (2006).
2. Q. Wu and X.-C. Zhang, "Free-space electro-optic sampling of terahertz beams," Appl. Phys. Lett. **67**, 3523-3525 (1995).
3. Q. Wu, T. Hewitt, and X.-C. Zhang, "Two-dimensional electro-optic imaging of thz beams," Appl. Phys. Lett. **69**, 1026-1028 (1996).
4. A. Nahata, D. H. Auston, and T. F. Heinz, "Coherent detection of freely propagating terahertz radiation by electro-optic sampling," Appl. Phys. Lett. **68**, 150-152 (1996).
5. R. A. Kaindl, R. Huber, B. A. Schmid, M. A. Carnahan, D. Hägele, and D. S. Chemla, "Ultrafast thz spectroscopy of correlated electron: from excitons to cooper pairs," Phys. Stat. Sol. (b) **243**, 2414-2422 (2006).
6. M. C. Beard, G. M. Turner, and C. A. Schmuttenmaer, "Transient photconductivity in gaas as measured by time-resolved terahertz spectroscopy," Phys. Rev. B **62**, 15764-15777 (2000).
7. M. C. Hoffmann, J. Hebling, H. Y. Hwang, K.-L. Yeh, and K. A. Nelson, "Thz-pump/thz-probe spectroscopy of semiconductors at high field strengths," J. Opt. Soc. Am. B **26**, A29-A34 (2009).
8. J. van Tilborg, C. B. Schroeder, C. V. Filip, C. Tóth, C. G. R. Geddes, G. Fubiani, R. Huber, R. A. Kaindl, E. Esarey, and W. P. Leemans, "Temporal characterization of femtosecond laser-plasma-accelerated electron bunches using terahertz radiation," Phys. Rev. Lett. **96**, 014801 (2006).
9. Q. Wu and X.-C. Zhang, "Ultrafast electro-optic field sensors," Appl. Phys. Lett. **68**, 1604-1606 (1996).
10. Z. Jiang and X.-C. Zhang, "Electro-optic measurement of thz field pulses with a chirped optical beam," Appl. Phys. Lett. **72**, 1945-1947 (1998).
11. Z. Jiang and X.-C. Zhang, "Single-shot spatiotemporal terahertz field imaging," Opt. Lett. **23**, 1114-1116 (1998).
12. F. G. Sun, Z. Jiang, and X.-C. Zhang, "Analysis of terahertz pulse measurement with a chirped probe beam," Appl. Phys. Lett. 73, 2233-2235 (1998).
13. J. R. Fletcher, "Distortion and uncertainty in chirped pulse thz spectrometers," Opt. Express **10**, 1425-1430 (2002).

14. S. Jamison, J. Shen, A. M. MacLeod, W. A. Gillespie, and D. A. Jaroszynski, "High-temporal-resolution, single-shot characterization of terahertz pulses," Opt. Lett. **28**, 1710-1712 (2003).
15. J. van Tilborg, C. B. Schroeder, C. Tóth, C. G. R. Geddes, E. Esarey, and W. P. Leemans, "Single-shot spatiotemporal measurements of high-field terahertz pulses," Opt. Lett. **32**, 313-315 (2007).
16. U. Schmidhammer, V. DeWaele, J.-R. Marqus, N. Bourgeois, and M. Mostafavi, "Single shot linear detection of 0.0110 thz electromagnetic fields: Electro-optic sampling with a supercontinuum in balanced detection," Appl. Phys. B **94**, 95-101 (2009).
17. I. Wilke, A. MacLeod, W. Gillespie, G. Berden, G. Knipples, and A. van der Meer, "Single-shot electron-beam bunch length measurements," Phys. Rev. Lett. **88**, 124801 (2002).
18. X. Yan, A. MacLeod, W. Gillespie, G. Knippels, D. Oepts, A. van der Meer, and W. Seidel, "Subpicosecond electro-optic measurement of relativistic electron pulses," Phys. Rev. Lett. **85**, 3404-3407 (2000).
19. X.-Y. Peng, O. Wiili, M. Chen, and A. Pukhov, "Optimal chirped probe pulse length for terahertz pulse measurement," Opt. Express **16**, 12342-12349 (2008).
20. Z. Jiang and X.-C. Zhang, "2d measurement and spatio-temporal coupling of few-cycle thz pulses," Opt. Express **5**, 243-248 (1999).
21. W. P. Leemans, C. G. R. Geddes, J. Faure, C. Tóth, J. van Tilborg, C. B. Schroeder, E. Esarey, G. Fubiani, D. Auerbrach, B. Marcelis, M. A. Carnahan, R. A. Kaindl, J. Byrd, and M. C. Martin, "Observation of terahertz emission from a laser-plasma-accelerated electron bunch crossing a plasma-vacuum boundary," Phys. Rev. Lett. **91**, 074802 (2003).
22. W. P. Leemans, J. van Tilborg, J. Faure, C. G. R. Geddes, C. Tóth, C. B. Schroeder, E. Esarey, G. Fubiani, and G. Dugan, "Terahertz radiation from laser accelerated electron bunches," Phys. Plasmas **11**, 2899-2906 (2004).
23. S. P. LeBlanc, E. Gaul, N. H. Matlis, A. Rundquist, and M. C. Downer, "Singleshot ultrafast phase measurement by frequency domain holography," Opt. Lett. **25**, 764-766 (2000).
24. N. H. Matlis, S. Reed, S. S. Bulanov, V. Chvykov, G. Kalintchenko, T. Matsuoka, P. Rousseau, V. Yanovsky, A. Maksimchuk, S. Kalmykov, G. Shvets, and M. C. Downer, "Snapshots of laser wakefields," Nature Phys. **2**, 749-753 (2006).
25. K. Kim, I. Alexeev, and H. Milchberg, "Single-shot supercontinuum spectral interferometry," Appl. Phys. Lett. **81**, 4124-4126 (2002).
26. C. B. Schroeder, E. Esarey, J. van Tilborg, and W. P. Leemans, "Theory of coherent transition radiation generated at a plasma-vacuum interface," Phys. Rev. E **69**, 016501 (2004).
27. R. Boyd, Nonlinear Optics (Academic Press, 1992).
28. G. Gallot and D. Grischkowsky, "Electro-optic detection of terahertz radiation," J. Opt. Soc. Am. B **16**, 1204-1212 (1999).

3.11 Femtosecond synchronization for ultrafast light sources

J. M. Byrd, L. Doolittle, G. Huang, R. W. Wilcox
Mail to: JMByrd@lbl.gov
Lawrence Berkeley National Laboratory, One Cyclotron Road, Berkeley, California 94720, USA

3.11.1 Introduction

The next generation of accelerator-driven light sources will produce sub-100 fsec high brightness x-ray pulses. In particular, pump-probe experiments at these facilities require synchronization of pulsed lasers and x-rays from electron beam on sub-100 fsec time scales over distances of a few hundred meters to several kilometers. Pump-probe experiments at these facilities plan to use an x-ray "probe" to produce snapshots of a the atomic positions within a sample some time following the excitation with a laser "pump". For experiments that require minutes to hours to collect data, the relative drift of the pump and probe must be a fraction of the x-ray pulse length. The recent demonstration of sub-10 fsec pulses motivates the need for femtosecond level synchronization.

In the ideal case, the relative timing of the pump laser and x-ray probe can be adjusted once the x-ray pulse and pump laser are perfectly synchronized to the master clock. However, both the pump and probe pulses can exhibit substantial jitter with respect to the master clock. For example, phase variations of difference accelerating sections of the linac create energy jitter which result in timing jitter after passing through electron bunch compressors. Furthermore, additional jitter of the x-ray pulse with respect to the electron pulse arises from the SASE lasing process. In the case of the laser oscillator, jitter with respect to the master clock can arise from a number of sources such as noise in the pump laser or acoustic vibrations of the laser cavity. In order to compensate for this additional time jitter, one can measure the relative jitter of x-ray, electron, and laser pump beams with respect to the master clock and use this to correct the timing for each pulse and allow the proper ordering of the "frames" of the movie. This configuration is illustrated in Fig. 1b.

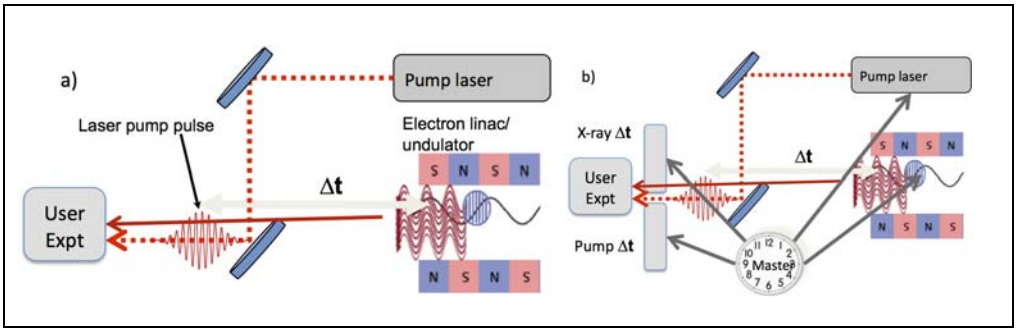

Figure 1. The relative time of the laser pump and x-ray probe must be controlled to a fraction of the x-ray pulse length. b) Jitter between the pump laser and x-ray pulse with respect to a master clock can be corrected by measuring the shot-to-shot jitter with synchronized diagnostics.

Many of the experiments intended for future light sources will have some specified pulse widths for the X-ray and optical pulses incident on the specimen, and there will be

a range over which the relative timing is varied during the experiment. Therefore, the impact of timing uncertainty can be evaluated relative to these pulse widths and scan ranges. If the relative timing uncertainty is less than or equal to the smallest pulse width, timing is fully controllable and this is the best case. If timing uncertainty is greater than the shortest pulse but smaller than the scan range, the pulse width is effectively lengthened by statistical fluctuations, although its bandwidth remains the same. If the uncertainty is equal to the scan range, and if the timing can be measured on each shot with enough precision, then the experimental time range is scanned in a statistical manner. Data must be post-processed to assign the "time-stamped" or "binned" data to successive intervals of time. If the uncertainty is larger than the scan range, then shots are wasted and the effective repetition rate is reduced. Data can still be acquired if it is time-stamped, but the experiment will take longer.

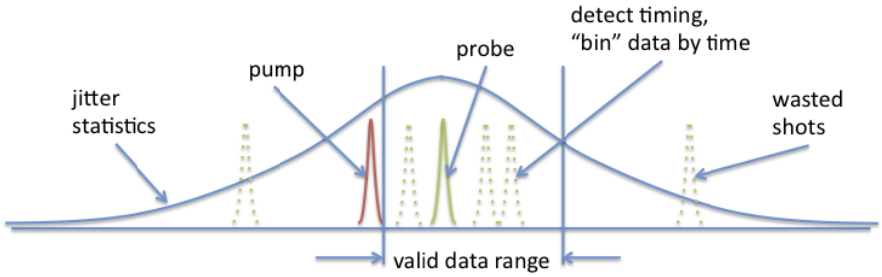

Figure 2. Effect of jitter statistics on pump/probe correlation.

There are three challenges in reaching the level of synchronization required for pump-probe experiments. The first is transmission of a stable timing signal to multiple remote clients over a relatively large facility. For example, in a facility of a several hundred meters in length, diurnal temperature variation results in cable length variation of several hundred picoseconds. The second challenge is to synchronize remote clients such as laser and RF systems to the stable timing signal at the femtosecond level. The third challenge is measure the x-ray, laser, and electron arrival times with respect to the master clock, or each other, at the femtosecond level.

One of the key developments in femtosecond timing distribution over the past few years has been the development of stabilized optical fiber links to sense and compensate for variations in the propagation delay in an individual link at the femtosecond level. Two approaches have been developed for link stabilization. In the first approach, pulses from an ultrastable mode-locked laser are transmitted over the length of the fiber. The repetition rate of pulses reflected from the end of the fiber is compared with transmitted pulses. Because of the stability of the pulse repetition rate, variations in the fiber length can be detected and corrected. In the second approach, a single optical frequency is transmitted over the fiber and reflected from the end. The relative optical phase of the reflected and forward signals is used as a measure of the variation of the fiber length. The sensitivity arises from the ability to stabilize the optical wavelength. Both approaches take advantage of the remarkable progress in optical metrology by using either a highly stable mode-locked oscillator or a single wavelength source as a reference for stabilizing the optical link.

This article presents an informal review of the elements in a femtosecond synchronization system and describes the status and potential for improvement in several areas with the goal of reaching synchronization at the few fsec level and beyond.

3.11.2 **Femtosecond Timing Distribution**

One of the key features in any synchronization scheme is the ability to stably transmit a master clock signal to the remote clients with negligible uncontrolled relative timing drift between the clients. A schematic view of this distribution is shown in Fig. 2. The master clock signal is distributed over the accelerator to remote clients in a star configuration. The phase of the master clock signal is corrected at the end of each fiber link for the variation in the propagation delay of that link. Thus the relative timing drift of clients locked to the master signal on independent fiber links is minimized over many hours and even days.

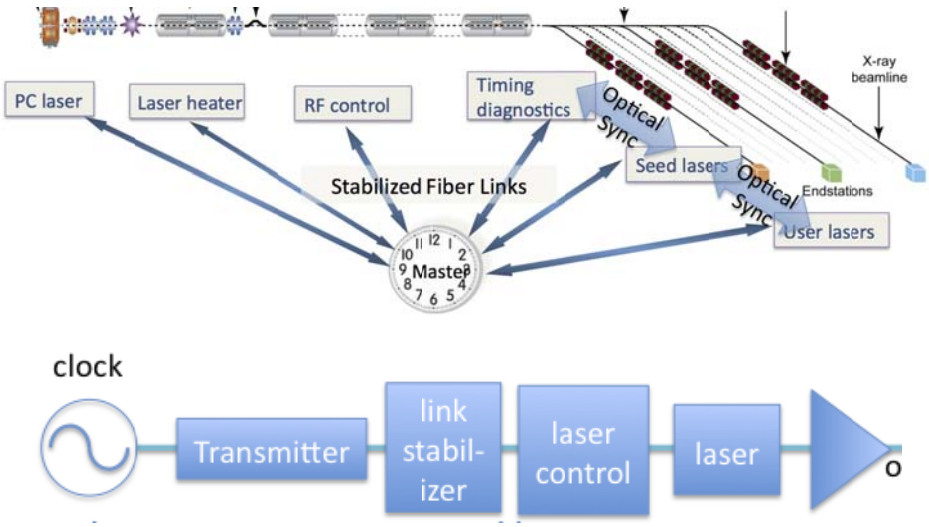

Figure 3: Top: Star configuration for timing distribution over the accelerator complex. Bottom: Common elements in any femtosecond synchronization system.

The common elements in any femtosecond synchronization system include a stable clock, transmitter, link stabilizer, remote client controller, and the remote client as shown for the example of a laser system in Fig. 2. The following sections describe some of the advances in these elements that will eventually allow synchronization at an FEL facility at the few fsec level and beyond.

3.11.3 **Master Clock Stability**

A timing distribution system sends information about the state of the clock to distant locations. It is important that the clock is stable, but the required stability is determined by the specification for temporal uncertainty and the path length difference between any two timing information paths to a common point. One can choose the pump/probe experiment as this common point, and measure the maximum propagation time difference between two paths $t_D = t_A - t_B$ from the clock to the experiment, as shown in Fig. 4.

Figure 4. Two timing signal paths with different delays to the experiment.

The clock has to be stable enough to preserve the synchronicity between timing signals traveling the two paths, to within the uncertainty spec. There will be two frequency regimes of timing variation to examine, which we can name "jitter" (for higher frequencies) and "drift" (for lower frequencies). If the jitter of the clock frequency is large, there can be a differential timing change between the two paths with delays t_A and t_B, because the clock phase has changed during the delay difference, $t_D = t_A - t_B$. The "high frequency" perturbation lower limit f_H should be the frequency for which there is pi phase shift in the differential delay time, or $f_H = 1/2t_D$. We can express the result as

$$\Delta t = \frac{1}{2\pi f_o}\sqrt{\int_{f_H}^{f_N} S(f)df}$$

where S(f) is the single sideband phase noise power spectral density, f_N is half the sample rate (the "Nyquist frequency"), or in this case the repetition rate of the pulsed laser clock, and f_0 is the clock frequency being measured. Thus, if the path delay difference is one microsecond (in 200m of fiber), the jitter integrated from 500kHz up to half the sample frequency will have to be less than the specification of 1fs RMS.

A separate calculation can be done for drift. If the clock frequency changes slowly, the phase delay through each path will be different, and since the receivers are detecting phase, there will be a temporal change. One can calculate the time error as the path delay difference times the frequency stability of the clock.

As an example, we can take the specified values of 200m of fiber (1 microsecond delay), and 1fs allowable error to find the low frequency clock stability spec to be 1 part in 10^9. The values assumed are approximately those expected for NGLS (without knowing the exact length of fiber runs and position of the timing transmitter), so these derived values will be close to the final clock specification.

A clock technology capable of meeting these specifications and producing both RF and optical frequencies is the CEP-stabilized mode-locked laser or "comb," which is a candidate for the next primary time standard. This laser stabilizes the optical offset frequency of the emitted frequency comb, such that the optical frequencies are exact integer multiples of the repetition rate. Then, if the repetition rate or one of its harmonics is locked to an absolute standard (such as an atomic line or a transmitted GPS signal), the optical frequencies are locked to that standard as well. This type of laser is also very stable in the high frequency range, such that the stringent jitter spec is met. The principle of the optical comb is illustrated in Fig. 5.

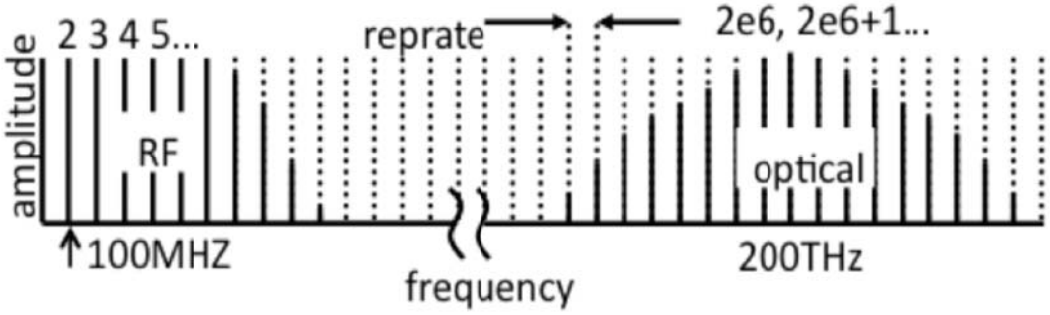

Figure 5: The RF and optical frequencies produced by a modelocked laser. The optical output is a comb of frequencies separated by f_{rep}, and offset from integer multiples by f_{offset}.

Any optical frequency will be an integer multiple of the pulse repetition rate plus an offset frequency which is usually uncontrolled, and which drifts with temperature and jitters with pump power. If this offset was zero, the optical frequencies would be integer multiples of the reprate. To detect this frequency, nonlinear processes are used to generate two higher frequencies from the comb; one is related to the carrier (its second harmonic) and the other is related to the envelope (self-phase modulation producing a broad continuum). When these two frequencies are interfered, their difference frequency will be twice the offset frequency. Since it is not easily possible to make the offset zero, it is made a sub-multiple of the reprate (4 or 5, usually), so that every nth pulse is identical, and the comb produced by picking out the nth pulse is then an ideal one.

This type of comb laser can be used for the clock in order to establish a correspondence between optical and RF frequencies, but also can be used for high stability seed and experiment lasers due to the temporal lock between the carrier and the envelope.

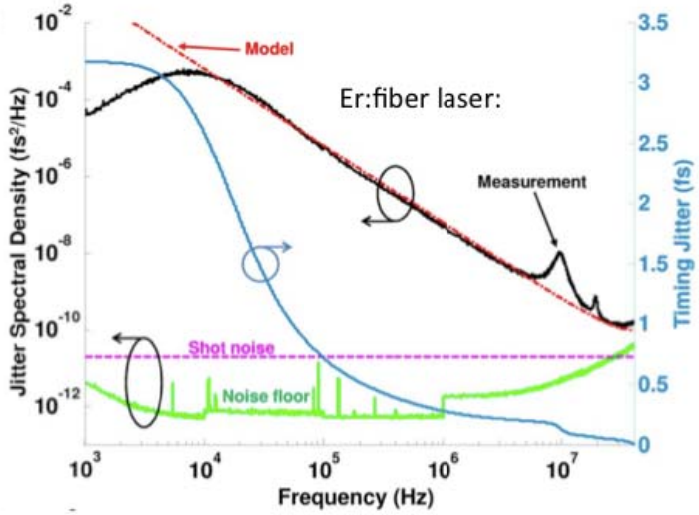

Figure 6. Measured temporal jitter spectrum of modelocked fiber laser.

High frequency jitter of modelocked lasers has been both theoretically and experimentally shown to be very low, in the <1fs range above 100kHz. These lasers are available commercially, typically based on erbium-doped fibers, although titanium

sapphire lasers are also used, as can any ultra short pulse laser. The erbium-doped fiber laser version produces optical wavelengths (~1550nm) that are easily transmitted over standard telecommunications fiber, making it attractive for a distribution system.

3.11.4 **Stabilized Fiber Links**

Several approaches have been developed to synchronize lasers to clocks over stabilized links. The two methods commonly used at FEL facilities are illustrated in Fig. 7 and are known as the pulsed and CW methods, respectively. In the pulsed method, the pulsed laser transmits a highly stabilized pulse frequency. A cross-correlator measurement is used to maintain a constant frequency by modulating the length of the fiber. The remote pulsed laser client locks to the link pulse train via another cross-correlator at the pulse frequency or a harmonic.

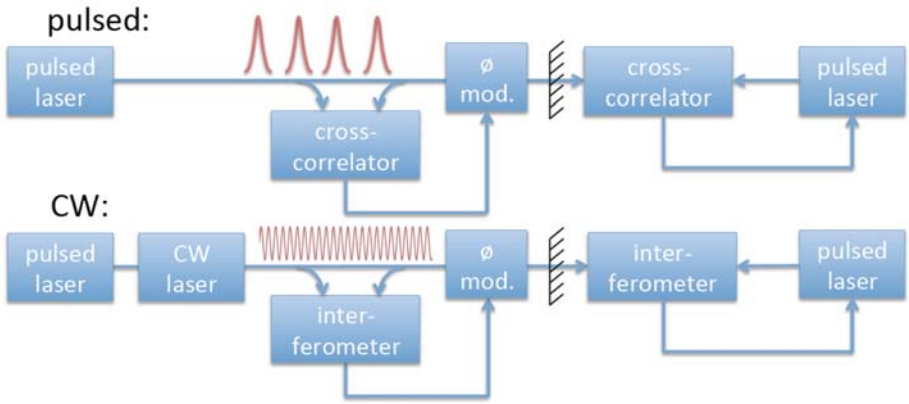

Figure 7. Schematic diagram of locking a remote laser client a master clock via a pulsed or CW stabilized fiber link. The pulsed technique takes advantage of the repetition rate stability of the mode-locked fiber laser transmitted on the fiber. The CW technique takes advantage of the wavelength stability of the transmitted optical carrier.

3.11.5 **Interferometrically Stabilized Fiber Link**

In the approach to the stabilized link developed at Berkeley Lab, each fiber link is an optical interferometer that precisely senses the delay variations in the link due to thermal variations of the fiber. A schematic diagram of one of the stabilized RF transmission links is shown in Fig. 8. The fiber used for transmission is one arm of an interferometer, which tracks changes in the optical phase delay through the fiber. Variations in optical phase are observed at the receiver, along with the amplitude-modulated RF signals to be stabilized. The measured optical phase shift is used to correct the detected RF phase. To compensate for the difference between phase and group delay in the fiber, an additional correction is applied.

Each fiber link is one arm of a heterodyne Michelson interferometer. The reference arm is a short fiber (about 1m) with its temperature stabilized to ±0.01 C. An acousto-optic frequency shifter at the receiver end of the long arm shifts the optical frequency by 100MHz in two passes, adding its input 50MHz RF phase to the optical phase. The beat between the reference and reflected optical carrier is detected as a 100 MHz RF signal whose phase is compared with twice the frequency-shifting signal. The RF phase shift

of this 100MHz signal is equal to the optical phase shift in the long arm, providing an increase in temporal sensitivity of $2x10^6$, the ratio of the optical to the beat frequency. Thus the 100 MHz beat signal can be sent back to the receiver over an unstabilized fiber, a novel feature of this scheme. The receiver then adjusts the frequency shifter RF phase to correct the optical phase, a function typically implemented in the transmitter. This provides the ability to deliver stable optical frequency over fiber.

The stability of our optical phase controller was verified by constructing a Mach-Zehnder interferometer out of two such heterodyne interferometers. One 2km fiber was exposed to ambient temperature variation and a short 2m fiber was in a temperature controlled environment. Diurnal temperature variations caused up to 2ns delay changes in the 2km fiber. After correction, the overall differential phase error between two stabilized links was six optical waves peak-to-peak over ten days.

For stable RF transmission, the CW laser used in the interferometer must have a wavelength stability less than the desired fractional temporal stability of the transmission delay. For a 2 km link with 10 fs stability, this corresponds to a wavelength stability of 10^{-9}. The CW laser frequency is locked to a hyperfine absorption line in Rb vapor, achieving $5x10^{-10}$.

A 2850 MHz RF signal is amplitude modulated onto the optical carrier by a lithium niobate modulator. The bias point is stabilized by detecting the second harmonic of the 2850 MHz modulation in a phase-locked loop. Amplitude modulation depth is typically 70%, detected by a photodiode. One issue with photodiode detection is AM-to-PM conversion, where changes in the average optical power modulate the phase of the detected RF signal. The optical power level is set to a local maximum in the AM-to-PM photodiode response, where there is zero slope and minimal sensitivity to fluctuations in optical power. At this peak, a ±10% variation in average photocurrent causes less than 10 fsec delay variation in the detected RF signal.

The receiver is a digital RF phase comparator used to compare the transmitted RF signal with a local signal to be controlled. Since the delay through coax cables and other RF components is temperature dependent, variations are corrected by subtracting a local calibration signal sent through both comparison paths. All processing of RF signals is done at an intermediate frequency of 50MHz, after mixing down with a 2800MHz local oscillator.

Due to the continuous nature of the signal, retroreflections anywhere in the fiber optic signal path can cause random fluctuations of the received RF signal phase. The measured RF signal is the vector sum of the desired signal and an interference vector whose relative angle is determined by the physical spacing of the reflections, and whose amplitude is determined by the relative optical phase of the signal and retroreflection. This relative optical phase varies rapidly with temperature, in the case of widely spaced reflections. As the amplitude of the interference vector changes, the received RF phase and amplitude varies. To suppress these effects to the less than 10 fs, all optical reflection losses need to be greater than 40 dB, so APC connectors and high return loss components are used.

We initially characterized the performance of this system in our lab by measuring relative time difference between long and short stabilized links. These results described in detail elsewhere. In summary, we measured an RMS deviation of <10 fsec on a 200 m fiber for over 20 hours and <20 fsec on a 2.2 km fiber over 60 hours.

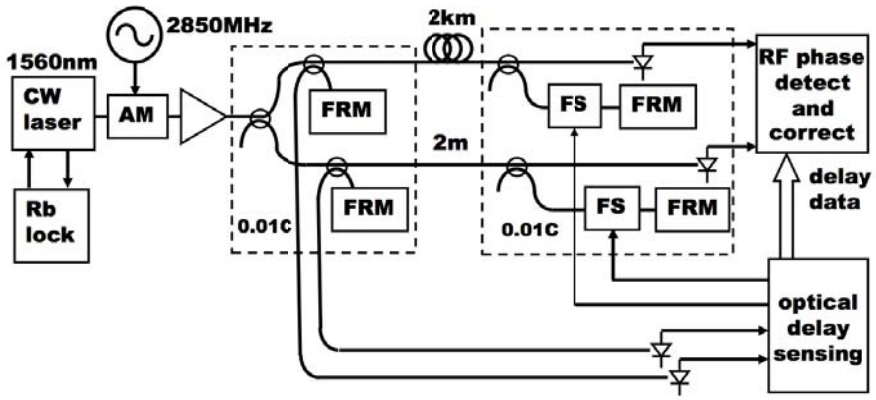

Figure 8: Schematic layout of a single channel RF transmission over an optical link. RF frequency is 2850MHz. AM: Amplitude modulator; FRM: Faraday rotator mirror; FS: optical frequency shifter. Dotted rectangles indicate components temperature controlled to ±0.01 C.

3.11.6 **Fiber Signal Distortion and Perturbations**

There are several optical effects in fiber which can negatively affect performance of the stabilized link. They are listed below, and their mitigation is explained.

Thermo-optic coefficient: This is the main perturbation of the fiber, around 10^{-5} per degree (check with CTE), and is controlled out by interferometer measurement and RF or optical phase control.

Thermal expansion: This is about 25% of the thermo-optic effect, and can be compensated in the same way as the overall thermal delay coefficient.

Dispersion: While the effect on the amplitude modulation is negligible due to narrow bandwidth, dispersion makes the phase and group delays different. We sense phase delay and correct group delay, so an extra factor has to be fed forward to compensate, as explained in the RF control section below. This factor is more important for pulsed timing systems.

Polarization mode dispersion: One limit to the long term stability of optical fiber transmission is polarization mode dispersion (PMD). This effect is due to different indices of refraction for the two different polarization modes in the fiber, a difference which can be minimized by careful manufacturing or by twisting the fiber during pulling in order to scramble the birefringence. For a typical long telecommunications fiber, there will be many zones of rotated birefringence (due to both manufacturing and installation parameters) which add statistically. The differential phase delay is close to the differential group delay (DGD), with two values along orthogonal principal polarization axes. Measurements of the DGD in stable links vary, but if we consider a measured example of 0.02 ps km^1/2 using installed telecom fiber, the expected DGD value for a 200 m long link is 9 fs. This is a factor of 10 below the typical specification for single mode fiber. Thus, DGD becomes a problem only for systems operating in the sub-10 fs regime, and it can be ignored for the <100fs channels.

Most fiber interferometers use Faraday rotator mirrors to cancel fiber birefringence effects by sending the incoming wave back along the orthogonal polarization axis. This results in a constant polarization at the interferometer, so there is no fading of the fringes. In this case, PMD is averaged out and any changes in birefringence will be ignored. Thus, if a signal propagates at one time through the fast axis and at another time through the slow axis, there will be an undetected time shift. The solution to this problem is to replace the Faraday mirror with an active polarization controller and a mirror. The polarization controller outputs a linear polarization to the mirror, which is reflected back through the fiber along the same polarization axes. The signal thus samples the same path twice, and any changes in delay due to birefringence are detected and compensated. A polarization controller is needed in any case, since it enables the transmitted signal to be interfered with the local signal from a controlled laser. Where PMD effects are not important, a Faraday rotator mirror can be used, but then the polarization has to be rotated 90 degrees at the transmitter end.

Stimulated Raman Scattering: This effect only occurs at much higher powers than will be needed in these systems (which will be around 10mW average). SRS scatters signal light into longer wavelengths, starting from noise, so the scattered signal is noisy.

Self phase modulation: At the required powers of a few mW and long modulation periods of hundreds of picoseconds, there will be negligible effects. This is a problem for pulsed systems only.

Stimulated Brillouin Scattering: SBS limits the CW power that can be transmitted through a long fiber, with a gain coefficient that is proportional to the fiber length and the intensity. For a 2km fiber, the threshold is about 70mW, and for 200m it is 700mW. The transmitted power in this system is far below threshold. When threshold is reached, all power is retroreflected, with a small frequency shift of a few MHz. The reflection is noisy, since it is started from noise.

Thermal noise: This may be an issue for extremely fine sensitivity interferometric fiber sensors, but in our case the contribution to time delay is a few attoseconds. This noise is due to rapid thermal variations in the index of refraction.

3.11.7 **Locking Mode-locked Lasers to a Reference**

Control of mode-locked laser timing requires several inputs, of various bandwidths and ranges. The oscillator can for control purposes be considered a voltage-controlled oscillator (VCO) analogous to those in RF. A voltage or motor position input changes frequency. Control of cavity length and thus repetition rate is achieved by moving one or more of the cavity mirrors. The slowest and longest range control is achieved with a stepping motor actuated translator, to compensate for slow thermal drifts. Higher bandwidth control is done with a piezoelectric actuator on a mirror. To enable fast response and minimize acoustic resonance, good actuator designs minimize mirror mass and isolate the actuator from the frame by mounting it in a massive block, decoupling high frequency acoustics. High bandwidth, low source impedance, low noise, high voltage amplifiers must be used to utilize the potential bandwidth of the piezo actuator. Together, these elements can have tens of kHz bandwidth. For example, a commercial

tisaf oscillator with a high speed piezo actuator and amplifier exhibits a first acoustic resonance at 39kHz, with flat response up to that point, as shown in Fig. 9, which plots both amplitude and phase. This provides a wide band transfer function that allows jitter reduction down to 25fs RMS from 10Hz to 10MHz, when the gain and phase delay of the loop are optimized. Figure 10 shows the jitter spectrum and integrated noise measured for this laser, being controlled with respect to a 2856MHz RF reference. This is adequate for many of the NGLS laser applications, although not for FEL seeds and experiment lasers.

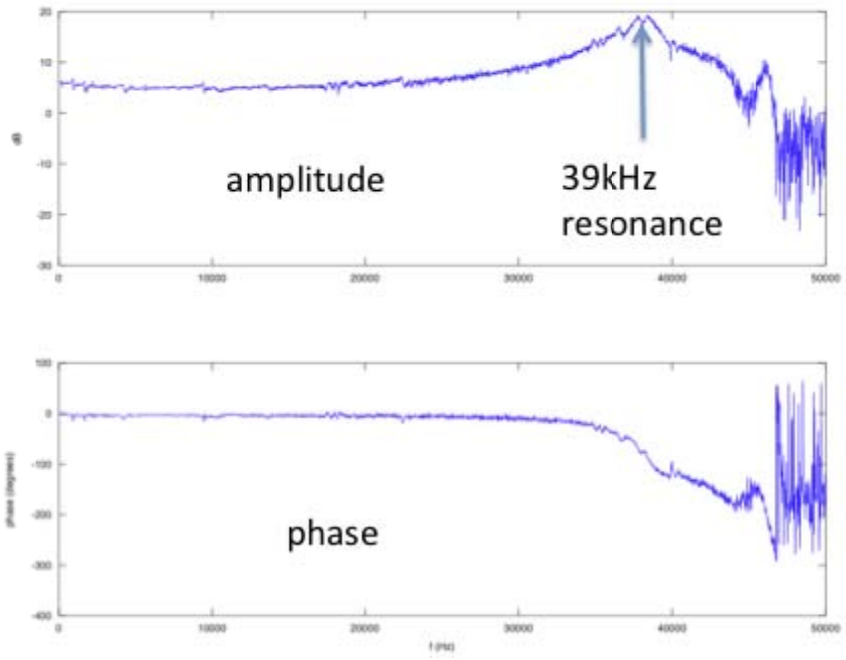

Figure 9. Amplitude and phase of complex transfer function of a commercial Ti-Saph laser driven by a high speed piezo amplifier.

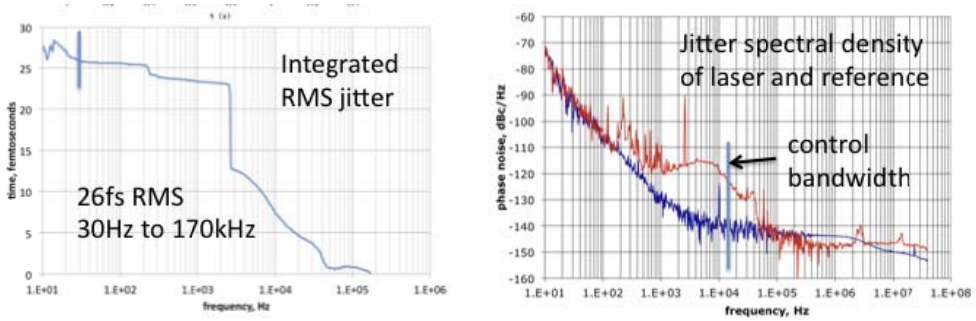

Figure 10. Integrated jitter and spectrum of commercial laser controlled by S-band RF.

Further reduction of the jitter can be accomplished using electro-optic modulators. Typically such modulators are capable of only a few tens of femtoseconds delay range, although this is sufficient once the jitter has been reduced by other means. Intracavity EO modulators have been used in fiber lasers to reduce jitter, with good results. One can also put modulators into free space cavities, although for ultrashort pulse lasers this

is undesirable due to the increased dispersion and nonlinearity. It is possible to increase the bandwidth of a laser control loop by placing an EO modulator outside the cavity and driving it with a separate PI amplifier, taking into account the linear relation between drive voltage and phase (as opposed to the phase integration function of the VCO). Figure 11 shows results of locking a fiber laser to a CW reference, using both piezo mirror control intracavty and an external EO modulator. The modulator allows further reduction of noise, although in this case the noise without EO modulation was small to begin with. External EO modulators may be necessary to achieve 1fs timing jitter with ultrashort pulse lasers for seeds and experiments. To our knowledge, this has not yet been demonstrated experimentally. Some experiments have shown ~1fs jitter from such lasers, but these have been specially stabilized experimental devices, and their jitter has been measured over limited frequency ranges.

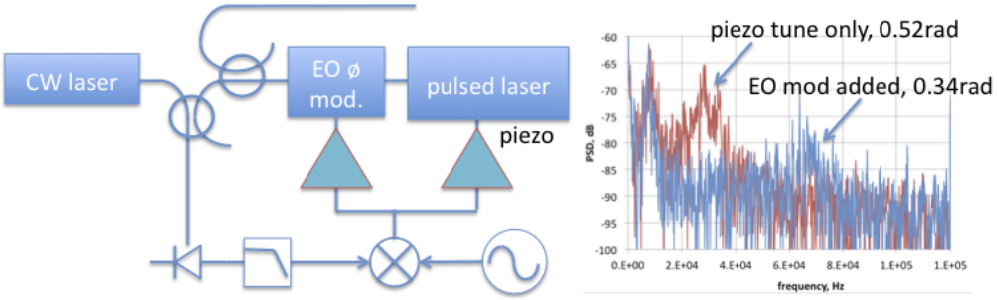

Figure 11. Block diagram of modelocked laser phase controlled by CW laser, with extracavity EO modulator. Power spectrum of jitter with and without EO modulator.

3.11.8 **All Optical Synchronization of Laser Oscillators**

For lasers to be locked at <10fs, they will be first locked to transmitted RF signals, then to the beat note between carriers. The scheme is similar to the "line picker" in the transmitter but in reverse. While photodiode detection senses the envelope directly, carrier beating senses the carrier phase, and since for a CEP-stabilized laser the carrier is locked to the envelope, the envelope timing is implicitly detected. Typical CEP-stabilized lasers have about 0.1 optical radian stability, or 42as uncertainty between carrier and envelope.

We can say that the timing of a controlled laser is compared with the transmitted clock frequency and phase, so that two controlled lasers will be synchronous. When two lasers are CEP-stabilized, they already have one parameter of their frequency comb fixed; the carrier-envelope offset frequency. There is thus only one more parameter that needs to be specified to completely control the frequency spectrum and thus the laser timing. This is the repetition rate, which can be varied by adjusting voltage to a piezoelectric transducer in the laser cavity. Changing the repetition rate amounts to modulating the frequency of each comb line, so that a phase-locked-loop can be established with the laser acting as an optical voltage controlled oscillator (VCO).

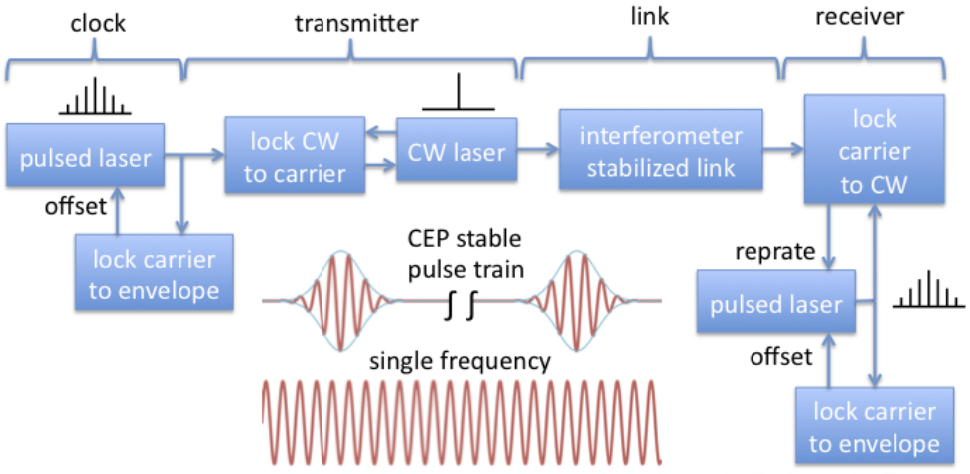

Figure 12. Laser synchronization by optical phase comparison.

It is also possible to explain this synchronization scheme using a time domain analogy. If the phase of the optical carrier is fixed with respect to the envelope of the pulse, one can control the timing of the pulse by comparing optical carrier phase with a CW reference. An analogy would be chains and sprockets controlling the motion of a machine (e.g. a tandem bicycle), where the reference frequency is a moving chain and two sprockets (representing two lasers) have their rotation synchronized by being engaged with the chain. A non- stabilized laser would be a sprocket allowed to slip on its shaft.

There have been demonstrations of locking two CEP-stabilized lasers with one optical frequency. Two Ti:sapphire lasers have been locked to a single frequency laser diode, with temporal synchronization measured by a cross-correlator. A block diagram of this scheme is shown in Figure 13. The CW laser is a frequency-stabilized diode laser, and provides a reference frequency and phase for both lasers, which in each case is optically beat with a nearby comb line on a wide bandwidth photodiode (in the box labeled 'hetero- dyne'). Phase errors are fed back to the lasers' repetition rates. In this experiment, the lasers were not in the same acoustic or thermal environment, and acoustic noise was not minimized. The temporal jitter measured on the cross-correlator from 1 Hz to 100 kHz was 1.5 fs RMS. This included a large clump of noise from 100 Hz to several kHz – probably acoustic – that may have contributed half the total integrated jitter.

Another experiment locked two CEP-stabilized erbium fiber lasers to a common CW source, and indirectly measured the temporal jitter by measuring heterodyne RF beats between the two lasers. The calculated temporal jitter from 0.06 Hz to 500 kHz was 0.9 fs. Since the goal of this experiment was to create a stable frequency reference, there was no direct measurement of the temporal jitter.

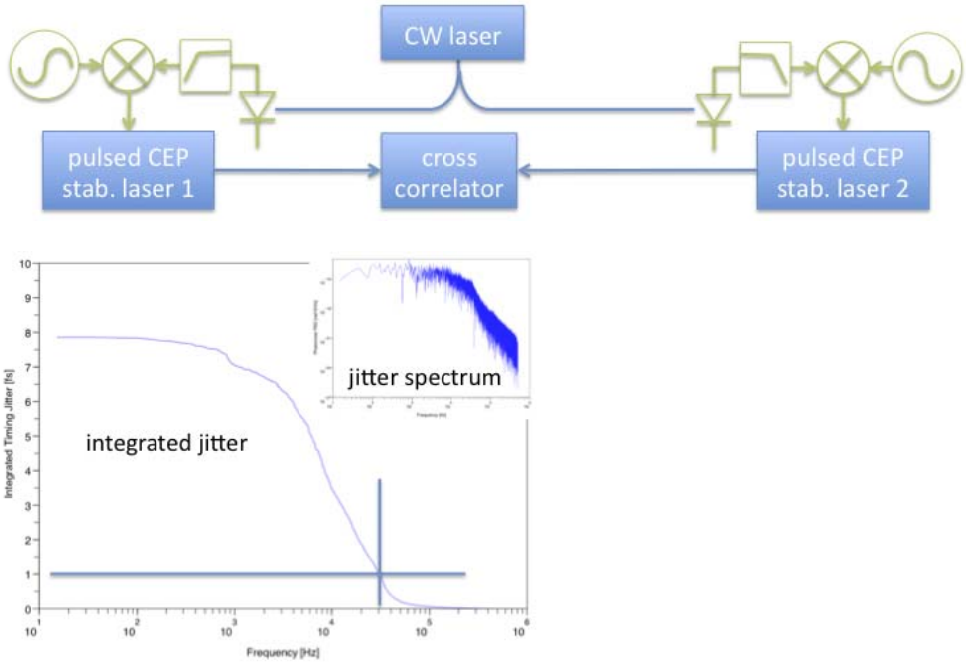

Figure 13. A: cross-correlation measurement of two lasers locked to CW reference.

3.11.9 **Implementation at an FEL Facility**

Including many of the elements described above, we foresee the overall synchronization system for an FEL facility to resemble the schematic illustrated in Fig. 14. An optical clock is distributed over stabilized fiber links to individual RF and laser clients. The remote client is locked to the reference using either an RF or optical scheme as described above depending of the required resolution. For example, control of superconducting cavities at 1.3 GHz is limited to ~0.01 degrees using modern digital controllers corresponding to about 20 fsec. Therefore, there is little need to provide a master reference clock with stability much better than 20 fsec. However, for laser clients the requirement for the relative stability could be a few fsec or better.

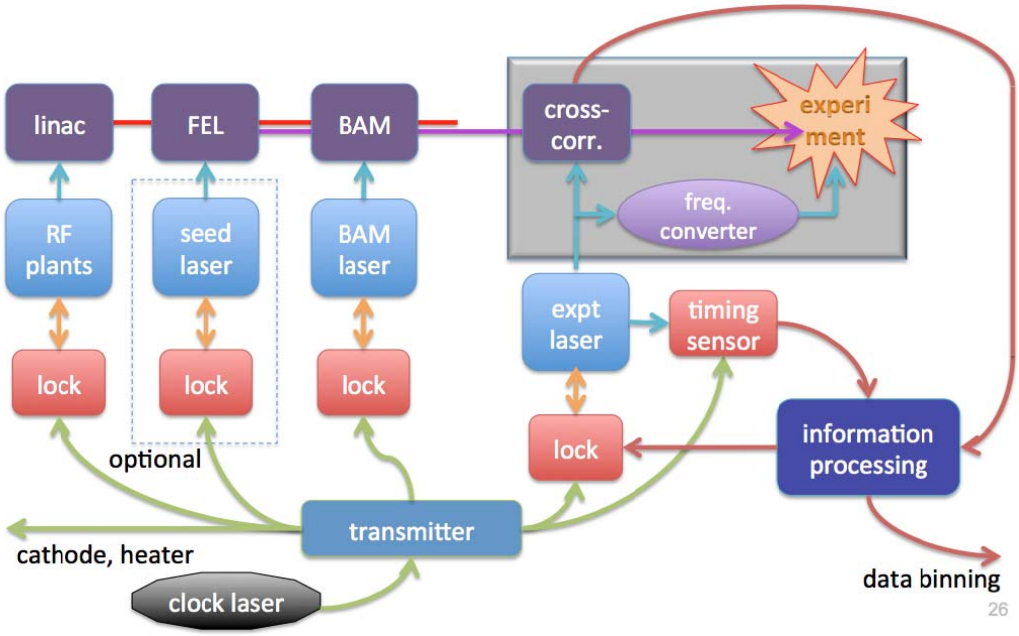

Figure 14. Schematic of the overall synchronization system at an FEL facility.

3.11.10 References

1. P. Emma, et al., "First lasing and operation of an ångstrom-wavelength free-electron laser," Nature Photonics 4, 641 - 647 (2010)
   D. M. Fritz, *et al*. "Ultrafast bond softening in bismuth: mapping a solid's interatomic potential with X-rays." Science 315, 633–636 (2007). A. M. Lindenberg, et al. "Atomic-scale visualization of inertial dynamics," Science 308, 392 (2005).
2. A. L. Cavalieri, et al. "Clocking Femtosecond X Rays," Phys. Rev. Lett. 94, 114801 (2005).
3. O. Lopez, A. Amy-Klein, C. Daussy, Ch. Chardonnet, F. Narbonneau, M. Lours, and G. Santarelli, "86-km optical link with a resolution of $2x10^{-18}$ for RF frequency transfer," Euro. Phys. J. D 48, 35 (2008).
4. P. A. Williams, W. C. Swann, N. R. Newbury, "High-stability transfer of an optical frequency over long fiber-optic links," J. Opt. Soc. Am. B 25 1284 (2008).
5. H. Kiuchi, "Highly Stable Millimeter-Wave Signal Distribution with an Optical Round-Trip Phase Stabilizer" IEEE Trans. Microwave Theory and Tech., 56, 1493 (2008).
6. D. D. Hudson, S. M. Foreman, S. T. Cundiff and J. Ye, Opt. Lett. 31, 1951 (2006).
7. J. Kim, et al., "Drift-free femtosecond timing synchronization of remote optical and microwave sources," Nature Photonics 2, 733 (2008).
8. R. Wilcox, et al, "Stable transmission of radio frequency signals on fiber links using interferometric delay sensing", Opt. Lett. 34, 3050 (2009).
9. J. Ye, J.-L. Peng, R. Jason-Jones, K. W. Holman, J. L. Hall, D. J. Jones, S. A. Diddams, J. Kitching, S. Bize, J. C. Bergquist, L. W. Holberg, L. Robertsson, and L.-S. Ma, "Delivery of high-stability optical and microwave frequency standards over an optical fiber network" J. Opt. Soc. Am. B 20, 1459 (2003).
10. J. W. Staples, J. M. Byrd, L. Doolittle, G. Huang, and R. Wilcox, "A Femtosecond-Level Fiber-Optics Timing Distribution System Using Frequency-Offset Interferometry," Proceedings of the 2008 Linear Accelerator Conference, M. Comryn, ed. (IEEE, 2008).
11. A. Bruner, V. Mahal, I. Kiryuschev, A. Arie, M. A. Arbore, M. M. Fejer, "Frequency

stability at the kilohertz level of a rubidium-locked diode laser at 192.114 THz" Appl. Opt. 37, 6410 (1998).
12. S. Masuda, A. Seki, S. Niki, "Optical frequency standard by using a 1560 nm diode laser locked to saturated absorption lines of rubidium vapor," Appl. Opt. 46, 4780 (2007).
13. F. X. Kartner, H. Byun, J. Chen, F. J. Grawert, F. O. Ilday, J. Kim, and A. Winter, "Progress in Large-Scale Femtosecond Timing Distribution and RF-Synchronization," in Proceedings of the 2005 Particle Accelerator Conference, C. Horak, ed. (IEEE, 2005).
14. J. M. Byrd, et al., "Femtosecond Synchronization of Laser Systems for the LCLS," in Proceedings of the 2010 International Particle Accelerator Conference, Kyoto, Japan.
15. M. Ferianis, et al. "All-optical Femtosecond Timing System for the Fermi@Elettra FEL", in Proceedings of the 2011 Free Electron Laser Conference, Shanghai, China.

4 Workshop and Conference Reports

4.1 HB2012 – the 52nd ICFA Advanced Beam Dynamics Workshop on High-Intensity and High-Brightness Hadron Beams

Jingyu Tang and Jiuqing Wang
Institute of High Energy Physics, CAS, Beijing, China
Mail to: tangjy@ihep.ac.cn

4.1.1 Workshop Theme and Organization

The 52nd ICFA Advanced Beam Dynamics Workshop on High-Intensity and High-Brightness Hadron Beams (HB2012) took place from September 17 to 21, 2012, in Beijing, China. The workshop was hosted by Institute of High Energy Physics (IHEP), CAS, and is a continuation of the successful biennial HB workshop series started about ten years ago (2002 at Fermilab, 2004 at GSI, 2006 at KEK, 2008 at ORNL and 2010 at PSI).

HB2012 keeps the traditions in the workshop series to provide a platform for presenting and discussing new progresses, status and future developments of high intensity and high brightness hadron beams, including beam physics in circular and linear hadron machines, technical systems and accelerator projects (under construction or in design) around the world. The workshop venue was in Park Plaza Beijing West Hotel, and a tour to IHEP accelerator facilities and development laboratories was arranged in the afternoon of the last day, which include Beijing Electron Positron Collider (BEPC), prototypes for China Spallation Neutron Sources, the R&D RFQ for ADS and the IHEP workshop.

Following the recommendation of the HB2010 International Advisory Committee (IAC), the International Organizing Committee (IOC) for HB2012 was established to play the role of both the IAC and the Scientific Program Committee in the previous workshops. The IOC has twenty-eight members from major accelerator laboratories and institutions all over the world. During the HB2012 organization, the IOC members contributed to define the workshop goals and scope, selecting plenary talks and speakers, defining working groups (WG) and selecting WG conveners, balancing the

invited talks, reviewing and finalizing the scientific program. HB2012 formed five working groups, less than in the previous HB workshops. Each WG had three conveners, representing the three regions in most cases.

The five-day workshop began with a plenary session comprising eight invited talks and followed by a poster session in the second half of the afternoon. The following three days were dedicated to two parallel sessions organized by five working groups, which include ninety talks and working group discussions. The most of the oral presentations were invited by the working group conveners, and the contributed ones were selected from the submitted abstracts. On the last day, summary talks were presented by the working group conveners.

There were 175 registered participants, comparable to HB2010 but more than previous HB workshops. The number of participants (62) from China increased significantly from previous HB workshops, with the majority from the host institute (44) and IMP-Lanzhou (11). This was attributed to two factors: (1) there are two ongoing major proton accelerator projects in China – China Spallation Neutron Source (CSNS) and the Accelerator Driver System (China-ADS); (2) the registration fee for Chinese participants was reduced with a NSFC fund. Among 113 foreign participants, the main contributions were made from CERN (24), FNAL(12), GSI(10), STFC/RAL(9), KEK(7) and JAEA/J-PARC(5).

4.1.2 **Scientific Program**

The plenary program focused on the new results obtained from the facilities that have improved their performance in the last years, the projects currently in the construction phase or in the research phase, the widely-concerned physics phenomena and the technological advancement or challenges in high-intensity hadron accelerators. R. Schmidt from CERN presented the new development in accelerating beams more than 100 MJ in LHC. K. Yamamoto presented the recovery status of J-PARC accelerator facilities after the catastrophic earthquake in March 2011. S.N. Fu presented high-intensity issues in the major proton accelerator facilities at IHEP: China Spallation Neutron Source currently under construction and China-ADS driver linac in the R&D phase. O. Kester from GSI also presented high-intensity issues in the FAIR project which is foreseen to start the construction soon. I. Hofmann (GSI) presented the simulation tools for high-intensity beam studies and the benchmarking against real machines. Two technological development talks by Y. Yamazaki (MSU) and V. Lebedev (FNAL) were about high beam power circular accelerators and linacs, respectively. The opening day concluded with a stimulating poster session containing contributions from all working groups.

The parallel sessions were organized by five working groups, as shown in Table 1, dedicating to wide topics mainly in beam dynamics but also in accelerator components and operations. A few parallel sessions were jointly arranged by two working groups. For beam dynamics in circular machines, the talks were spread over beam collective effects, simulation methods, space charge effects, non-linear field induced resonances, beam-beam effect in hadron colliders and other high-intensity aspects in machine upgrading. For beam dynamics in linacs, the talks were focused on beam dynamics studies for specific machines, dynamics design methods for RFQs and other specific linac sections, and general beam dynamics aspects among which two were discussion-oriented talks about the halo definition and equipartition, specially arranged by the WG-

B conveners. For the sessions on accelerator system design, injection, extraction and beam-material interaction, the talks covered the topics such as superconducting RF cavity developments and the test facilities, ion source, injection/extraction design, collimation and beam loss control, electron cooling, beam chopping, and material damage by beams. For machine operations and commissioning, the talks were presented about the operation experience with high-intensity beams for the operating machines and the commissioning plans for the machines under construction. For beam diagnostics and instrumentation for high-intensity beams, the talks were about design and performance of the diagnostic devices in machine operations and also new technical developments which is much needed for the coming high power proton hadron accelerators.

As LHC, J-PARC, SNS,PSI cyclotrons and other well-established facilities continue to improve or keep their performance, during the last years, we have also seen important advancements in new facilities that are in the construction phase or design phase. For example, SPIRAL2 at GANIL and PEFP at KAERI are well advanced in their constructions. At IHEP, the CSNS construction was started in September 2011; the new project China-ADS was launched officially in the beginning 2011 with IHEP and IMP collaborating on the design and R&D of the CW high power proton linac. Several major projects are well-prepared for construction, such as FRIB at MSU, ESS in Lund with many European laboratories collaborating together, and FAIR at GSI. As an experimental setup for the critical front-end part of Project-X, several US laboratories are collaborating on the PXIE, while continuing the design and key technology R&D. The similar situation is for EVEDA-IFMIF linac in Europe. The upgrading designs for the proton accelerator chain at CERN, the injector for ISIS and other aged accelerators are also in the course. Whilst all these large facilities contributed to the workshop by participants and presentations, small facilities in universities also showed their significant presence at the workshop.

Table 1: Working Groups at HB2012

Working Group	Convener	No. Talks
WG-A: Beam dynamics in high-intensity circular machines	G. Franchetti (GSI) J. Holmes (SNS) E. Metral (CERN)	29
WG-B: Beam dynamics in high-intensity linacs	P.A.P. Nghiem (CEA-Saclay) D. Raparia (BNL) Z.H. Li (IHEP)	17
WG-C: Accelerator system design, injection, extraction, beam-material interaction	N. Mokhov (FNAL) H.W. Zhao (IMP) D. Li (LBNL)	20
WG-D: Commissioning, operations and performance	M. Plum (SNS) Y. Sato (J-PARC) R. Schmidt (CERN)	12
WG-E: Beam diagnostics and instrumentation for high-intensity beams	R. Doelling (PSI) N. Hayashi (J-PARC) V. Scarpine (FNAL)	12

4.1.3 **Conclusion**

Following its precedent HB workshops, HB2012 proved to be a successful and fruitful workshop that highlighted the rapid and comprehensive progress made in high-intensity hadron accelerators from around the world. With new projects evolving, the growing interest in the field is further made evident by high participation at the HB series.

Preliminary proceedings, which include copies of presentations are available on the IHEP website of the workshop [1], and will be on the JACoW [2]. Selected papers in extended versions after peer-reviews are to be published in a special edition of *Physical Review Special Topics – Accelerators and Beams* [3].

During the IOC meeting at HB2012, the next HB workshop (HB2014) was determined to be held in October or November 2014 in MSU, East Lansing, USA. It follows the tradition of the HB workshop in every two years and rotating among three regions: Europe, Asia and North-America.

4.1.4 **References**

1. HB2012 website with preliminary proceedings: http://hb2012.ihep.ac.cn
2. JACoW website (see “ABDW”): http://www.jacow.org/
3. PRST-AB special edition website: http://prst-ab.aps.org/speced/

5 Recent Doctorial Theses Abstracts

5.1 Machine Induced Experimental Background Conditions in the LHC

Yngve Inntjore Levinsen
Mail to: Yngve.Inntjore.Levinsen@cern.ch

Graduation date: 19 September, 2012
University: University of Oslo
Supervisors: Dr. Helmut Burkhardt and Dr. Steinar Stapnes
URL: http://cdsweb.cern.ch/record/1482357

Abstract:

The Large Hadron Collider set a new energy record for particle accelerators in late 2009, breaking the previous record held by Tevatron of 2 TeV collision energy. The LHC today operates at a collision energy of 7 TeV. With higher beam energy and intensity, measures have to be taken to ensure optimal experimental conditions and safety of the machine and detectors. Machine induced experimental background can severely reduce the quality of experimental triggers and track reconstruction. In a worst case, the radiation levels can be damaging for some of the subdetectors.

The LHC is a particular challenge in this regard due to the vastly different operating conditions of the different experiments. The nominal luminosity varies by four orders of magnitude. The unprecedented stored beam energy and the amount of superconducting elements can make it challenging to protect the accelerator itself as well.

In this work we have simulated and measured the machine induced background originating from various sources: the beam colliding with rest-gas, collision residues that are transported between the experiments, and from beam halo impacting on aperture restrictions. The aim of the work has been to get a first complete overview of all background sources, in order to better understand how we can optimise the running conditions for the LHC experiments.

We have found that the most important background source is beam-gas background, with an expected background rate towards the experiments for the nominal machine on the order of MHz. Other sources of background have been carefully considered and are found to pose less of a challenge under normal running conditions.

5.2 Longitudinally Coherent Single-Spike Radiation from a Self-Amplified Spontaneous Emission Free-Electron Laser

Gabriel Andrew Marcus
Mail to: gmarcus@lbl.gov

Graduation date: August 29, 2012
University: University of California Los Angeles
Supervisor: Professor James B. Rosenzweig

Abstract:

This work studies the production and measurement of longitudinally coherent, ultrashort pulses of light from a self-amplified spontaneous emission free-electron laser (SASE FEL) by using an energy-chirped electron beam in conjunction with a tapered undulator. This scheme effectively preserves the FEL gain only where an appropriate undulator taper compensates for the detuning experienced by an amplifying radiation spike as it slips forward in the electron beam rest frame. The simultaneous time and frequency-domain measurement of ultrashort pulses of light generated in this manner were made with an advanced transient-grating frequency-resolved optical gating (TG FROG) diagnostic, which has the potential to push ultrashort light pulse measurement at FEL facilities to shorter wavelength regimes.

The experimental work was conducted at the SPARC FEL test facility in Frascati, Italy. Electron beams were accelerated and compressed using the velocity bunching technique, which leaves a residual energy-chirp in the longitudinal phase space. The energy-chirp was compensated by appropriately tapering individual undulator sections. This process was optimized at a resonant wavelength of $\lambda = 530$ nm. The ultrashort light pulses that were generated had a temporal full-width at half-maximum of $\delta\tau_{FWHM} = 98$ fs and a time-bandwidth product of $TBP \approx 1.2$, indicating that the Fourier limit was nearly achieved. This experiment provides further insight into methods that can be used to shape the SASE FEL longitudinal profile and enhance coherence properties. In addition, the measurements were taken with an advanced, and relatively simple, TG FROG diagnostic that can potentially be used to measure ultrashort UV pulses at FEL facilities.

5.3 Study of the Thermal Emittance of Photocathode RF Guns

Houjun Qian
Mail to: hqian@lbl.gov

Graduation date: 3 July, 2012
University: Tsinghua University
Supervisors: Prof. Chuanxiang Tang and Prof. Xijie Wang

Abstract:

The emittance of a photocathode RF gun is one of major factors in determining the performance and size of x-ray source. Smaller emittance will reduce the size of the X-ray Free Electron Laser (XFEL) facility and increase the X-ray brightness of Thomson scattering sources. Reduction of the gun emittance has been studied for decades with notable advances in emittance compensation in photoinjectors, laser shaping, and high gradient RF gun. To reach even lower emittance low bunch charge and low thermal emittance are required. Previous experimental studies of thermal emittance showed inconsistent results compared with theoretical predictions, and have not yet been explained. In this thesis, I experimentally studied the thermal emittance of metal photocathodes (Copper and Magnesium), and analyzed mechanisms for formation of thermal emittance formation. Peak gradients of the Tsinghua Photocathode RF guns were limited to ~75 MV/m due to RF breakdowns, and become the bottleneck of emittance optimization. In order to get the emittance of an high charge beam (0.5-1 nC) below 2 mm.mrad, which is required by both Tsinghua Thomson scattering (TTX)

facility and Shanghai soft X-ray FEL (SXFEL) project, the gun gradient of 100 MV/m or more is necessary, so a new photocathode RF gun is designed to increase the gun gradient.

Based on the BNL/KEK/SHI type gun, the new Tsinghua photocathode RF gun was optimized to reduce RF breakdown, zero mode excitation and nonaxisymmetry of π mode field, and reached ~120 MV/m with a RF pulse width of 1.7 μs after high power conditioning. By improving the cathode processing technique, the dark current is also greatly reduced and of the similar level as that of LCLS gun. The correlation between multipole field emittance and monopole field emittance, and the beam dynamics due to single RF feed are analyzed by Panofsky-Wenzel theory, and the analysis results are verified by PARMELA simulations.

In the thermal emittance study of Copper cathode, the thermal emittance due to roughness effect and excess photon energy are assumed to be uncorrelated and added quadratically. The electric field dependences of total thermal emittance and quantum efficiency are used to fit work function, field enhancement factor and roughness emittance. The experiment results revealed a work function (4.16 eV) much lower than literature value (4.65 eV), and a big roughness emittance (0.92 mm.mrad/mm at 50 MV/m) was measured for the first time. The cathode surface morphology was characterized by white light interferometer, and severe surface damge was found. The theorectical calculation of roughness emittance with the actual surface profile is consistent with experimental results on the first order, which verifies the role of surface roughness in thermal emittance formations.

The inconsistencies between experimental results and theoretical predictions for Mg cathode cannot be explained by roughness emittance because measurement results are smaller than theoretical predictions. By reviewing the mechanism of photoexcitation, it is found one assumption in Dowell's theory, i.e. isotropic distribution of electron momentum after photoexcitation, is not right in surface photoemission. Surface Plasmon mediated surface photoemission can be excited on Mg cathode with surface roughness on the order of ~10 nm, even when UV light (266 nm) is normal incident. By laser cleaning, thermal emittance of ~0.5 mm.mrad/mm is measured with QE variation as much as a factor of 10. Besides, vectorial photoelectric effect is measured at oblique incidence, and vector ratio of 1.5 is measured. Both experimental results are inconsistent with volume photoemission theories, and can be explained by surface photoemission excited by surface Plasmons. Surface photoemission breaks Dowell's prediction of higher thermal emittance with higher QE for a metal cathode, and explains that Mg is a low thermal emittance cathode.

5.4 Collective Dynamics and Coherent Diagnostics of Microbunched Relativistic Electron Beams

Agostino Marinelli
Mail to: ago9582@SLAC.Stanford.EDU

Graduation date: September, 2012
University: University of California, Los Angeles
Supervisor: Prof. James Rosenzweig

Abstract:

The x-ray free-electron laser has been established as the brightest available source of x-rays, extending the coherence and brilliance properties of conventional atomic lasers down to the sub-Angstrom level. The high-brightness electron beams that are used to drive the free-electron laser process, undergo a number of collective instabilities that can generate complex phase-space structures and induce the emission of coherent radiation, an effect that is generally termed microbunching instability.

The main subject of this dissertation is the collective evolution of beam microbunching under the effect of longitudinal space-charge forces. We develop a three-dimensional kinetic theory of space-charge effects leading to collective suppression and amplification of beam microbunching. This model gives, for the first time, a fully self-consistent description of the space-charge instability, with the inclusion of three-dimensional and thermal effects. After establishing a self-consistent theoretical foundation for space-charge effects, we present two experiments related to the space-charge instability. The generation of broad- band coherent undulator radiation with a longitudinal space-charge amplifier is demonstrated experimentally for the first time. This experiment extends the capabilities of free-electron laser facilities by allowing the generation of coherent broadband radiation pulses, thus accessing regimes of operation currently unavailable for fourth generation light sources. Finally a coherent diffraction imaging technique for the reconstruction of beam microbunching is designed and experimentally tested. This technique is based on the application of an oversampling phase-retrieval method to the far-field coherent transition radiation emitted by a microbunched electron beam and has applications in the diagnostic of compressed electron beams and free-electron lasers.

While the microbunching instability is generally regarded as a detrimental effect, this work shows that the coherent effects associated with the induced microbunching can be optimized and used to our advantage for the development of new coherent radiation sources and advanced beam diagnostics.

6 Forthcoming Beam Dynamics Events

6.1 ICFA Mini-Workshop on Beam-Beam Effects in Hadron Colliders (BB2013)

We are pleased to announce that an ICFA mini-workshop on "Beam-Beam Effects in Hadron Colliders" will be held at CERN in Geneva, Switzerland from March 18th to 22nd, 2013. This workshop is a successor and follow up to similar workshops held at CERN in April 1999, at Fermilab in June 2001 and in Montauk 2003. It is motivated by the successful start of the LHC and the emergence of a vast amount of beam-beam observations in the LHC as well as from the Tevatron and RHIC. We feel the need to review the progress made since the last workshop on beam-beam effects.

The purpose of this workshop is to review the present knowledge and compare with the observations, and to discuss and plan future research work, with special emphasis on the performance of the LHC after the first long shutdown as well as on studies needed for the planned LHC upgrade projects.

In this context we plan to review experience from lepton colliders where relevant, such as the use of crab cavities and crabbed waist collision schemes. One of the sessions will be dedicated to discuss the progress and the understanding of the various beam-beam compensation schemes.

Workshop Website: We shall use the Indico page http://indico.cern.ch/event/beam-beam-2013 for managing the information and the meeting and you can find more details and the registration procedure as well as the abstract submission on this site.

Registration: The registration to participate in this workshop can be made through the above website in the period from November 1st 2012 to January 31st 2013.

Abstract submission: The website will be open for the submission of abstracts from November 1st until January 31st 2013.

Visa: For those of you who need visas to enter France or Switzerland, please consult the above website and send us the necessary information via e-mail to: Delphine.Rivoiron@cern.ch or Laurie.Hemery@cern.ch.

Accommodation: Depending on the number of participants, we shall book a block of rooms in the CERN hostel.

For more information please send an e-mail to: Delphine.Rivoiron@cern.ch or Laurie.Hemery@cern.ch or visit the workshop website.

Workshop sessions: The workshop will consist of two types of sessions,

1. Plenary sessions with invited presentations and other oral contributions.
2. We plan to reserve some time for discussion sessions on specific topics. These can include any types of contributions. We should also like to encourage informal as well as ad hoc presentations on issues identified during the workshop.

The last day of the workshop will be dedicated to summarize and conclude the workshop in a plenary session.

Presentations: If you plan a presentation, please use the Indico website to submit a title and abstract. Alternatively you can send your proposal as an e-mail to a member of the Organizing Committee or the Local Organizing Committee. For oral presentations, the meeting room is equipped with a PC, computer projector for Powerpoint and PDF presentations as well as wireless LAN and a blackboard. There will be no slide projector of overhead projector.

Proceedings: They will be published on the Indico website as well as in paper form.

Workshop fee: There is no workshop fee. Coffee and tea will be served during the coffee breaks. Lunch can be taken at one of the CERN restaurants. A workshop dinner will be offered to all workshop participants. Accompanying persons not attending the workshop are expected to cover their cost of the workshop dinner.

WLAN and Indico access: An internet connection by WLAN will be available during the workshop. To access the wireless LAN at CERN, a registration at CERN is required. Please follow the instructions on the website. For help or more information please send an e-mail to: Delphine.Rivoiron@cern.ch or Laurie.Hemery@cern.ch.

Contact: For any questions, comments or special requests, please send an e-mail to a member of the Local Organizing Committee.

We hope that many of you can join this workshop to share the present knowledge on this topic and discuss new ideas. We are looking forward to see you at CERN next spring.

Sincerely,

Werner Herr (CERN)	Elias Metral (CERN)
Workshop Chair	ICFA, Beam Dynamics Panel

Workshop Outline

Dates: From March 18th to March 22nd, 2013.
Place: CERN, plenary sessions in CERN BE Auditorium, Meyrin.
Sessions: A tentative layout of the plenary sessions and discussion sessions can be found on the workshop website under "tentative programme". The schedule will be finalized after the scientific programme is set up.

Workshop Chairs:
Werner Herr (CERN)
Elias Metral (CERN)

International Organizing Committee:
Yunhai Cai (SLAC): yunhai@slac.stanford.edu.
Alexander Chao (SLAC): achao@slac.stanford.edu.
Wolfram Fischer (BNL): Wolfram.Fischer@bnl.gov.
Werner Herr (CERN): Werner.Herr@cern.ch.
Elias Metral (CERN): Elias.Metral@cern.ch.
Bruno Muratori (STFC): bruno.muratori@stfc.ac.uk.
Kazunobu Oide (KEK): katsunobu.oide@kek.jp.
Ji Qiang (LBNL): jqiang@lbl.gov.
Leonid Rivkin (EPFL): leonid.rivkin@psi.ch.
David L. Rubin (Cornell): dlr10@cornell.edu.
Tanaji Sen (FNAL): tsen@fnal.gov.
Dmitry Shatilov (BINP): shatilov@inp.nsk.su.
Vladimir Shiltsev (FNAL): shiltsev@fnal.gov.
Alexander Valishev (FNAL): valishev@fnal.gov.
Matthias Vogt (DESY): vogtm@mail.desy.de.
Andrzej Wolski (Univ. Liverpool): a.wolski@liverpool.ac.uk.
Mikhail Zobov (INFN): mikhail.zobov@lnf.infn.it.

Local Organizing Committee:
Xavier Buffat (EPFL): Xavier.Buffat@cern.ch.
Rossano Giachino (CERN): Rossano.Giachino@cern.ch.
Laurie Hemery (CERN): Laurie.Hemery@cern.ch.
Werner Herr (CERN): Werner.Herr@cern.ch.
Elias Metral (CERN): Elias.Metral@cern.ch.
Giulia Papotti (CERN): Giulia.Papotti@cern.ch.
Tatiana Pieloni (CERN): Tatiana.Pieloni@cern.ch.
Delphine Rivoiron (CERN): Delphine.Rivoiron@cern.ch.

Workshop administration:
Delphine Rivoiron
Laurie Hemery

Scientific Programme (sessions):

Welcome and introduction
Chairpersons: W. Herr + E. Metral (CERN)

Experience in hadron colliders
Chairperson and Convener: O. Bruening (CERN)

Experience from lepton colliders
Chairperson and Convener: J. Seeman (SLAC)

Single particle effects I - head on beam-beam effects
Chairperson and Convener: K. Oide (KEK)

Single particle effects II - parasitic beam-beam effects
Chairperson and Convener: V. Shiltsev (FNAL)

Strong - strong interactions
Chairperson and Convener: L. Rivkin (EPFL)

Theory and simulations, beam-beam models
Chairperson and Convener: T. Pieloni (CERN)

Beam-beam effects and operational aspects
Chairperson and Convener: G. Papotti (CERN)

Beam-beam compensations schemes
Chairperson and Convener: W. Fischer (BNL)

Beam-beam Studies for future projects
Chairperson and Convener: A. Valishev (FNAL)

Summary and conclusion
Chairperson: A. Chao (SLAC and Stanford University)

6.2 UCLA Higgs Factory Workshop

With interest building after the apparent discovery of a particle consistent with the Higgs boson, doors are opening to a new range of questions and discussions. A collider with its clean and controlled collisions could be the key to future research.

The UCLA Physics & Astronomy Department will sponsor a workshop on the Higgs boson and the development of a Higgs factory collider. The meeting will be held at the UCLA Faculty Center on Thursday March 21 and Friday March 22, 2013. The workshop website is available here:

https://hepconf.physics.ucla.edu/higgs2013/

Topics to be covered include:

- Latest results from the Large Hadron Collider
- S-channel muon collider Higgs
- Factory status of muon cooling and collider research
- h^0 factory, A/H factory
- Calculations of the Higgs branching ratios

Abstracts are now being accepted. Registration for the two-day workshop will begin in December 2012. We invite you to forward this message to anyone who may be interested in participating.

David B. Cline
on behalf of the Organizing Committee

6.3 COOL'13

We are pleased to announce that the next International Workshop on Beam Cooling and Related Topics, COOL'13, will take place at the Alpin Palace Hotel in Murren, Switzerland from 10th to 14th June 2013.

This is the 9th workshop in the series which was first held in Montreux, Switzerland in 1993 and has been a bi-annual event since 2001. The workshop will highlight the latest developments in the field of particle beam cooling and will provide a perfect opportunity for accelerator physicists, engineers and students to meet and interact in a quiet and relaxed environment.

At an elevation of 1650 m, perched on a high, sunny terrace facing the famous Eiger, Monch and Jungfrau, Murren is located amidst some of the world's most spectacular scenery. Coming by train from one of the airports (Bern, Zurich, Basel, Geneva) Murren is reached by a mountain railway or by aerial cableways running from the Lauterbrunnen valley into the centre of the car-free village. Murren has remained a charming little village rich of traditions and has managed to escape over-development despite being famous in the history of winter sports.

A program of invited oral presentations is being developed by the International Program Committee and will be published in due course at the workshop website

https://cool-13.web.cern.ch/COOL-13

Please bookmark the site and visit it regularly for updates on the program and for useful information concerning the workshop.

Prospective participants should take note of the deadlines for abstract submission (15th February 2013), early registration (3rd May 2013) and hotel reservation (10th May 2013). Delegate registration will open in January and proposals for hotel accommodation will be published on our website.

Abstract and paper submission as well as delegate registration will be handled via the JACoW Scientific Programme Management System (SPMS) at

https://oraweb.cern.ch/pls/cool2013/profile.html

The proceedings will be published at the JACoW site

http://www.jacow.org

shortly after the workshop. We would like to take the opportunity to invite you to update your JACoW profile if you no longer wish to receive communications on this and future COOL workshops.

We are excited to welcome you to this unique location for COOL?13 and are looking forward to meeting you at the workshop.

The Local Organising Committee:

Pavel Belochitskii
Flora Berrenger
Madeleine Catin (Secretary)
Tommy Eriksson
Alexandre Frassier
Lars Varming Joergensen (Editor)
Bertrand Lefort
Gerard Tranquille (Chair)

6.4 SRF 2013

We are pleased to invite you to attend the 16th International Conference on RF Superconductivity, SRF 2013, to take place on September 23-27, 2013 in Cite Universitaire, downtown Paris, France. Please note this important conference in your calendar and bookmark the conference website.

http://www.srf2013.fr/

RF superconductivity is now the key technology of many accelerators for particle physics, nuclear physics and, increasingly, light sources. SRF 2013 will cover the latest advances in the science, technology, and applications of superconducting RF. The program will consist of invited review talks, poster sessions and 'hot-topic' discussion sessions (and also our traditional boat tour, trademark of this conference). An industrial exhibition will also take place during the conference.

We will continue the tradition of providing a vivid forum for SRF scientists, engineers, students and industrial partners to present and discuss the latest developments in the science and technology of superconducting RF for particle accelerators.

Special tutorials will be held from Sept. 19-21 in GANIL, Caen. These are designed to provide an in-depth overview of SRF related subjects for scientists and engineers new to the field. It will also give the attendees a unique opportunity of visiting the GANIL accelerator facilities, especially the Spiral2 linac which will be under assembly at this time.

The proceedings will be published through JACoW. Only contributions presented as a talk or in the poster sessions will be included in the proceedings.

We invite you to log on to your JACOW account and activate the SRF mailing-list checkbox in your personal profile to ensure that you will receive updates on the SRF Conference in the future.

https://oraweb.cern.ch/pls/jacow/profile.new_account

Registration and call for contribution will open 1st February 2013. We invite you to visit regularly www.srf2013.fr website to find latest information.

Conference Chairwoman: Claire Antoine
Conference Chairman: Sebastien Bousson
Conference contact: contact@srf2013.fr

6.5 ICFA Mini-Workshop on Space Charge (SPACE CHARGE 2013)

This workshop will be held at CERN in Geneva, Switzerland from 15-19 April, 2013. High intensity beams have always caught the attention of the accelerator community. The present development of the field is being pushed by projects and major upgrade programs to existing facilities. We refer for example to the FAIR project at GSI, and the LIU upgrade at CERN. The need for advanced understanding of space charge dominated machines and the unavailability of both CERN and GSI accelerators as of early 2013, sets a convenient time window (April 2013) to organize a meeting of reviewing the state of the art in our field. This workshop would serve as a forum for the urgent issues of the upcoming year.

The workshop web site is:

https://indico.cern.ch/conferenceDisplay.py?confId=221441

Workshop chair: G. Franchetti (GSI) g.franchetti@gsi.de,
F. Schmidt (CERN) frank.schmidt@cern.ch

7 Announcements of the Beam Dynamics Panel

7.1 ICFA Beam Dynamics Newsletter

7.1.1 Aim of the Newsletter

The ICFA Beam Dynamics Newsletter is intended as a channel for describing

unsolved problems and highlighting important ongoing works, and not as a substitute for journal articles and conference proceedings that usually describe completed work. It is published by the ICFA Beam Dynamics Panel, one of whose missions is to encourage international collaboration in beam dynamics.

Normally it is published every April, August and December. The deadlines are 15 March, 15 July and 15 November, respectively.

7.1.2 Categories of Articles

The categories of articles in the newsletter are the following:

1. Announcements from the panel.
2. Reports of beam dynamics activity of a group.
3. Reports on workshops, meetings and other events related to beam dynamics.
4. Announcements of future beam dynamics-related international workshops and meetings.
5. Those who want to use newsletter to announce their workshops are welcome to do so. Articles should typically fit within half a page and include descriptions of the subject, date, place, Web site and other contact information.
6. Review of beam dynamics problems: This is a place to bring attention to unsolved problems and should not be used to report completed work. Clear and short highlights on the problem are encouraged.
7. Letters to the editor: a forum open to everyone. Anybody can express his/her opinion on the beam dynamics and related activities, by sending it to one of the editors. The editors reserve the right to reject contributions they judge to be inappropriate, although they have rarely had cause to do so.

The editors may request an article following a recommendation by panel members. However anyone who wishes to submit an article is strongly encouraged to contact any Beam Dynamics Panel member before starting to write.

7.1.3 How to Prepare a Manuscript

Before starting to write, authors should download the template in Microsoft Word format from the Beam Dynamics Panel web site:

http://www-bd.fnal.gov/icfabd/news.html

It will be much easier to guarantee acceptance of the article if the template is used and the instructions included in it are respected. The template and instructions are expected to evolve with time so please make sure always to use the latest versions.

The final Microsoft Word file should be sent to one of the editors, preferably the issue editor, by email.

The editors regret that LaTeX files can no longer be accepted: a majority of contributors now prefer Word and we simply do not have the resources to make the conversions that would be needed. Contributions received in LaTeX will now be returned to the authors for re-formatting.

In cases where an article is composed entirely of straightforward prose (no equations, figures, tables, special symbols, etc.) contributions received in the form of plain text files may be accepted at the discretion of the issue editor.

Each article should include the title, authors' names, affiliations and e-mail addresses.

7.1.4 **Distribution**

A complete archive of issues of this newsletter from 1995 to the latest issue is available at

http://icfa-usa.jlab.org/archive/newsletter.shtml.

This is now intended as the primary method of distribution of the newsletter.

Readers are encouraged to sign-up for electronic mailing list to ensure that they will hear immediately when a new issue is published.

The Panel's Web site provides access to the Newsletters, information about future and past workshops, and other information useful to accelerator physicists. There are links to pages of information of local interest for each of the three ICFA areas.

Printed copies of the ICFA Beam Dynamics Newsletters are also distributed (generally some time after the Web edition appears) through the following distributors:

Weiren Chou	chou@fnal.gov	North and South Americas
Rainer Wanzenberg	rainer.wanzenberg@desy.de	Europe[++] and Africa
Toshiyuki Okugi	toshiyuki.okugi@kek.jp	Asia[**] and Pacific

++ Including former Soviet Union.

** For Mainland China, Jiu-Qing Wang (wangjq@mail.ihep.ac.cn) takes care of the distribution with Ms. Su Ping, Secretariat of PASC, P.O. Box 918, Beijing 100039, China.

To keep costs down (remember that the Panel has no budget of its own) readers are encouraged to use the Web as much as possible. In particular, if you receive a paper copy that you no longer require, please inform the appropriate distributor.

7.1.5 **Regular Correspondents**

The Beam Dynamics Newsletter particularly encourages contributions from smaller institutions and countries where the accelerator physics community is small. Since it is impossible for the editors and panel members to survey all beam dynamics activity worldwide, we have some Regular Correspondents. They are expected to find interesting activities and appropriate persons to report them and/or report them by themselves. We hope that we will have a "compact and complete" list covering all over the world eventually. The present Regular Correspondents are as follows:

Liu Lin	Liu@ns.lnls.br	LNLS Brazil
Sameen Ahmed Khan	Rohelakan@yahoo.com	SCOT, Oman
Jacob Rodnizki	Jacob.Rodnizki@gmail.com	Soreq NRC, Israel
Rohan Dowd	Rohan.Dowd@synchrotron.org.au	Australian Synchrotron

We are calling for more volunteers as Regular Correspondents.

7.2 ICFA Beam Dynamics Panel Members

Name	eMail	Institution
Rick Baartman	baartman@lin12.triumf.ca	TRIUMF, 4004 Wesbrook Mall, Vancouver, BC, V6T 2A3, Canada
Marica Biagini	marica.biagini@lnf.infn.it	LNF-INFN, Via E. Fermi 40, C.P. 13, Frascati, Italy
John Byrd	jmbyrd@lbl.gov	Center for Beam Physics, LBL, 1 Cyclotron Road, Berkeley, CA 94720-8211, U.S.A.
Yunhai Cai	yunhai@slac.stanford.edu	SLAC, 2575 Sand Hill Road, MS 26 Menlo Park, CA 94025, U.S.A.
Swapan Chattopadhyay	swapan@cockroft.ac.uk	The Cockcroft Institute, Daresbury, Warrington WA4 4AD, U.K.
Weiren Chou (Chair)	chou@fnal.gov	Fermilab, MS 220, P.O. Box 500, Batavia, IL 60510, U.S.A.
Wolfram Fischer	wfischer@bnl.gov	Brookhaven National Laboratory, Bldg. 911B, Upton, NY 11973, U.S.A.
Yoshihiro Funakoshi	yoshihiro.funakoshi@kek.jp	KEK, 1-1 Oho, Tsukuba-shi, Ibaraki-ken, 305-0801, Japan
Jie Gao	gaoj@ihep.ac.cn	Institute for High Energy Physics, P.O. Box 918, Beijing 100039, China
Ajay Ghodke	ghodke@cat.ernet.in	RRCAT, ADL Bldg. Indore, Madhya Pradesh, 452 013, India
Ingo Hofmann	i.hofmann@gsi.de	High Current Beam Physics, GSI Darmstadt, Planckstr. 1, 64291 Darmstadt, Germany
Sergei Ivanov	sergey.ivanov@ihep.ru	Institute for High Energy Physics, Protvino, Moscow Region, 142281 Russia
In Soo Ko	isko@postech.ac.kr	Pohang Accelerator Lab, San 31, Hyoja-Dong, Pohang 790-784, South Korea
Elias Metral	elias.metral@cern.ch	CERN, CH-1211, Geneva 23, Switzerland
Yoshiharu Mori	mori@rri.kyoto-u.ac.jp	Research Reactor Inst., Kyoto Univ. Kumatori, Osaka, 590-0494, Japan
George Neil	neil@jlab.org	TJNAF, 12000 Jefferson Ave., Suite 21, Newport News, VA 23606, U.S.A.
Toshiyuki Okugi	toshiyuki.okugi@kek.jp	KEK, 1-1 Oho, Tsukuba-shi, Ibaraki-ken, 305-0801, Japan
Mark Palmer	mark.palmer@cornell.edu	Wilson Laboratory, Cornell University, Ithaca, NY 14853-8001, USA
Chris Prior	chris.prior@stfc.ac.uk	ASTeC Intense Beams Group, STFC RAL, Chilton, Didcot, Oxon OX11 0QX, U.K.
Yuri Shatunov	Yu.M.Shatunov@inp.nsk.su	Acad. Lavrentiev, Prospect 11, 630090 Novosibirsk, Russia
Jiu-Qing Wang	wangjq@ihep.ac.cn	Institute for High Energy Physics, P.O. Box 918, 9-1, Beijing 100039, China
Rainer Wanzenberg	rainer.wanzenberg@desy.de	DESY, Notkestrasse 85, 22603 Hamburg, Germany